Unified probabilistic and interval analysis of structures with hybrid uncertainties

Author:
Feng, Jinwen

Publication Date:
2019

DOI:
https://doi.org/10.26190/unsworks/21423

Unified probabilistic and interval analysis of structures with hybrid uncertainties

By

Jinwen Feng

A thesis in fulfilment of the requirement for the degree of Doctor of Philosophy

School of Civil and Environmental Engineering

The University of New South Wales

Sydney, Australia

2019

This page is left as blank.

Thesis/Dissertation Sheet

Surname/Family Name	:	**Feng**
Given Name/s	:	**Jinwen**
Abbreviation for degree as give in the University calendar	:	**PhD**
Faculty	:	**Engineering**
School	:	**Civil & Environmental Engineering**
Thesis Title	:	**Unified probabilistic and interval analysis of structures with hybrid uncertainties**

Abstract 350 words maximum: (PLEASE TYPE)

In modern engineering analysis and design, it is well recognized that fluctuations exist in the material properties, geometric characteristics and externally applied loadings. These uncertainties, which are either resulted from the variation of system parameters or the lack of knowledge or information, can significantly affect the performance of engineering systems. Recently, the study in hybrid uncertainty analysis is gaining increasingly popularity duo to the advantage in evaluating the effect of various types of uncertainties in a unified approach. Despite of the availability, the existing methods are developed with strengths in particular engineering applications. Thus, there is a continuous demand on enhancing the reliability, accuracy, computational efficiency and robustness of hybrid uncertainty analysis.

This dissertation aims at providing a series of uncertainty analysis approaches for engineering structures with both random and interval uncertain parameters, which can be applied to investigation on various engineering problems. Firstly, the uncertain linear static analysis of discrete structures with hybrid random and interval variables is investigated by using a novel perturbation-based mathematical programming approach. For the structures with non-random and spatially variant uncertainties, a novel interval field concept is adopted to model such uncertainties. Then, the natural frequencies of structures with both random and interval fields are studied for the first time by using the extended unified interval stochastic sampling (X-UISS) method. Finally, a brand-new dynamic reliability analysis through an advanced machine learning algorithm, namely the extended support vector regression (X-SVR), is proposed. Various numerical examples, including both academic-sized and engineering motivated, have been elaborately selected for demonstrating the accuracy, efficiency and applicability of the proposed methods.

The computational schemes developed in this dissertation offer new yet efficient strategies for analysing the performance of engineering systems with various uncertain system parameters. Since that the proposed methods are all based on finite element analysis, either intrusively or non-intrusively, it is possible to integrate the introduced approaches with the finite element software. Thus, the methods developed in this research project have the potential to be applied in practical engineering analysis and design.

FOR OFFICE USE ONLY Date of completion of requirements for Award:

Original Statement

‘I hereby declare that this submission is my own work and to the best of my knowledge it contains no materials previously published or written by another person, or substantial proportions of material which have been accepted for the award of any other degree or diploma at UNSW or any other educational institution, except where due acknowledgement is made in the thesis. Any contribution made to the research by others, with whom I have worked at UNSW or elsewhere, is explicitly acknowledged in the thesis. I also declare that the intellectual content of this thesis is the product of my own work, except to the extent that assistance from others in the project's design and conception or in style, presentation and linguistic expression is acknowledged.’

Signed ……

Date ……

Copyright Statement

Authenticity Statement

‘I certify that the Library deposit digital copy is a direct equivalent of the final officially approved version of my thesis. No emendation of content has occurred and if there are any minor variations in formatting, they are the result of the conversion to digital format.’

Signed …….....

Date …….....

Inclusion of Publications Statement

UNSW is supportive of candidates publishing their research results during their candidature as detailed in the UNSW Thesis Examination Procedure.

Publications can be used in their thesis in lieu of a Chapter if:

- The student contributed greater than 50% of the content in the publication and is the "primary author", ie. the student was responsible primarily for the planning, execution and preparation of the work for publication
- The student has approval to include the publication in their thesis in lieu of a Chapter from their supervisor and Postgraduate Coordinator.
- The publication is not subject to any obligations or contractual agreements with a third party that would constrain its inclusion in the thesis

Please indicate whether this thesis contains published material or not.

☐ *This thesis contains no publications, either published or submitted for publication (if this box is checked, you may delete all the material on page 2)*

☐ *Some of the work described in this thesis has been published and it has been documented in the relevant Chapters with acknowledgement (if this box is checked, you may delete all the material on page 2)*

☒ *This thesis has publications (either published or submitted for publication) incorporated into it in lieu of a chapter and the details are presented below*

CANDIDATE'S DECLARATION

I declare that:

- I have complied with the Thesis Examination Procedure
- where I have used a publication in lieu of a Chapter, the listed publication(s) below meet(s) the requirements to be included in the thesis.

Name	Signature	Date (dd/mm/yy)
Jinwen Feng		

Postgraduate Coordinator's Declaration (to be filled in where publications are used in lieu of Chapters)

I declare that:

- the information below is accurate
- where listed publication(s) have been used in lieu of Chapter(s), their use complies with the Thesis Examination Procedure
- the minimum requirements for the format of the thesis have been met.

PGC's Name	PGC's Signature	Date (dd/mm/yy)

Hamid Valipour		

For each publication incorporated into the thesis in lieu of a Chapter, provide all of the requested details and signatures required

Details of publication #1:
Full title: Uncertainty analysis for structures with hybrid random and interval parameters using mathematical programming approach
Authors: Jinwen Feng, Di Wu, Wei Gao, Guoyin Li
Journal or book name: Applied Mathematical Modelling
Volume/page numbers: 48/ 208-232
Date accepted/ published:05/04/2017

Status	*Published*	☒	*Accepted and In press*		*In progress (submitted)*	

The Candidate's Contribution to the Work
The candidate was the primary author for this publication. The candidate was responsible primarily for the planning, execution and preparation of the work for publication.

Location of the work in the thesis and/or how the work is incorporated in the thesis:
Chapter 3

Primary Supervisor's Declaration
I declare that:
- the information above is accurate
- this has been discussed with the PGC and it is agreed that this publication can be included in this thesis in lieu of a Chapter
- All of the co-authors of the publication have reviewed the above information and have agreed to its veracity by signing a 'Co-Author Authorisation' form.

Supervisor's name	*Supervisor's signature*	*Date (dd/mm/yy)*
Wei Gao		

Co-Author's Declaration
I authorise the inclusion of this publication in the student's thesis and certify that:
- the declaration made by the student on the Declaration for a thesis with publication form correctly reflects the extent of the student's contribution to this work;
- the student contributed greater than 50% of the content of the publication and is the "primary author" i.e. the student was responsible primarily for the planning, execution and preparation of the work for publication

Co-Author's name	*Co-author's signature*	*Date (dd/mm/yy)*
Di Wu		
Wei Gao		
Guoyin Li		

Details of publication #2:
Full title: Uncertain structural free vibration analysis with non-probabilistic spatially varying parameters

Authors: Jinwen Feng, Qingya Li, Alba Sofi, Guoyin Li, Di Wu, Wei Gao *Journal or book name: ASCE-ASME Journal of Risk and Uncertainty in Engineering Systems, Part B: Mechanical Engineering* *Volume/page numbers: N/A* *Date accepted/ published: 13/06/2018*						
Status	*Published*	☒	*Accepted and In press*		*In progress (submitted)*	
The Candidate's Contribution to the Work The candidate was the primary author for this publication. The candidate was responsible primarily for the planning, execution and preparation of the work for publication.						
Location of the work in the thesis and/or how the work is incorporated in the thesis: Chapter 4						
Primary Supervisor's Declaration I declare that: • the information above is accurate • this has been discussed with the PGC and it is agreed that this publication can be included in this thesis in lieu of a Chapter • All of the co-authors of the publication have reviewed the above information and have agreed to its veracity by signing a 'Co-Author Authorisation' form.						
Supervisor's name	*Supervisor's signature*	*Date (dd/mm/yy)*				
Wei Gao						
Co-Author's Declaration I authorise the inclusion of this publication in the student's thesis and certify that: • the declaration made by the student on the Declaration for a thesis with publication form correctly reflects the extent of the student's contribution to this work; • the student contributed greater than 50% of the content of the publication and is the "primary author" i.e. the student was responsible primarily for the planning, execution and preparation of the work for publication						
Co-Author's name	*Co-Author's signature*	*Date (dd/mm/yy)*				
Qingya Li						
Alba Sofi						
Guoyin Li						
Di Wu						
Wei Gao						

Details of publication #3: *Full title: Hybrid uncertain natural frequency analysis for structures with random and interval fields* *Authors: Jinwen Feng, Di Wu, Wei Gao, Guoyin Li*

Journal or book name: Computer Methods in Applied Mechanics and Engineering *Volume/page numbers: 328/ 365-389* *Date accepted/ published: 01/09/2017*						
Status	*Published*	☒	*Accepted and In press*		*In progress (submitted)*	
The Candidate's Contribution to the Work The candidate was the primary author for this publication. The candidate was responsible primarily for the planning, execution and preparation of the work for publication.						
Location of the work in the thesis and/or how the work is incorporated in the thesis: Chapter 5						
Primary Supervisor's Declaration I declare that: • the information above is accurate • this has been discussed with the PGC and it is agreed that this publication can be included in this thesis in lieu of a Chapter • All of the co-authors of the publication have reviewed the above information and have agreed to its veracity by signing a 'Co-Author Authorisation' form.						
Supervisor's name	*Supervisor's signature*			*Date (dd/mm/yy)*		
Wei Gao						
Co-Author's Declaration I authorise the inclusion of this publication in the student's thesis and certify that: • the declaration made by the student on the Declaration for a thesis with publication form correctly reflects the extent of the student's contribution to this work; • the student contributed greater than 50% of the content of the publication and is the "primary author" i.e. the student was responsible primarily for the planning, execution and preparation of the work for publication						
Co-Author's name	*Co-Author's signature*			*Date (dd/mm/yy)*		
Di Wu						
Wei Gao						
Guoyin Li						

Details of publication #4: *Full title: Dynamic reliability analysis using the extended support vector regression (X-SVR)* *Authors: Jinwen Feng, Lei Liu, Di Wu, Guoyin Li, Michael Beer, Wei Gao* *Journal or book name: Mechanical Systems and Signal Processing* *Volume/page numbers: 126/368-391* *Date accepted/ published: 14/02/2019*						
Status	*Published*	☒	*Accepted and In press*		*In progress (submitted)*	
The Candidate's Contribution to the Work						

The candidate was the primary author for this publication. The candidate was responsible primarily for the planning, execution and preparation of the work for publication.		
Location of the work in the thesis and/or how the work is incorporated in the thesis: Chapter 6		
Primary Supervisor's Declaration I declare that: • the information above is accurate • this has been discussed with the PGC and it is agreed that this publication can be included in this thesis in lieu of a Chapter • All of the co-authors of the publication have reviewed the above information and have agreed to its veracity by signing a 'Co-Author Authorisation' form.		
Supervisor's name	*Supervisor's signature*	*Date (dd/mm/yy)*
Wei Gao		
Co-Author's Declaration I authorise the inclusion of this publication in the student's thesis and certify that: • the declaration made by the student on the Declaration for a thesis with publication form correctly reflects the extent of the student's contribution to this work; • the student contributed greater than 50% of the content of the publication and is the "primary author" i.e. the student was responsible primarily for the planning, execution and preparation of the work for publication		
Co-Author's name	*Co-Author's signature*	*Date (dd/mm/yy)*
Lei Liu		
Di Wu		
Guoyin Li		
Michael Beer		
Wei Gao		

Abstract

In modern engineering analysis and design, it is well recognized that fluctuations exist in the material properties, geometric characteristics and externally applied loadings. These uncertainties, which are either resulted from the variation of system parameters or the lack of knowledge or information, can significantly affect the performance of engineering systems. Recently, the study in hybrid uncertainty analysis is gaining increasingly popularity duo to the advantage in evaluating the effect of various types of uncertainties in a unified approach. Despite of the availability, the existing methods are developed with strengths in particular engineering applications. Thus, there is a continuous demand on enhancing the reliability, accuracy, computational efficiency and robustness of hybrid uncertainty analysis.

This dissertation aims at providing a series of uncertainty analysis approaches for engineering structures with both random and interval uncertain parameters, which can be applied to investigation on various engineering problems. Firstly, the uncertain linear static analysis of discrete structures with hybrid random and interval variables is investigated by using a novel perturbation-based mathematical programming approach. For the structures with non-random and spatially variant uncertainties, a novel interval field concept is adopted to model such uncertainties. Then, the natural frequencies of structures with both random and interval fields are studied for the first time by using the extended unified interval stochastic sampling (X-UISS) method. Finally, a brand-new dynamic reliability analysis through an advanced machine learning algorithm, namely the extended support vector regression (X-SVR), is proposed. Various numerical examples, including both academic-sized and engineering motivated, have been elaborately selected for demonstrating the accuracy, efficiency and applicability of the proposed methods.

The computational schemes developed in this dissertation offer new yet efficient strategies for analysing the performance of engineering systems with various uncertain system parameters. Since that the proposed methods are all based on finite element analysis, either intrusively or non-intrusively, it is possible to integrate the introduced approaches with the finite element software. Thus, the methods developed in this research project have the potential to be applied in practical engineering analysis and design.

Acknowledgement

First of all, I would like to express my sincere gratitude to Prof. Wei Gao who has been consistently supporting me since my undergraduate study to the finish of my PhD study. His expertise in the research of uncertainty analysis allowed me quickly learning the essentials and also gave me ideal guidelines in my research and career development. Additionally, I sincerely thank my joint supervisor, A/Prof. Guoyin Li, for his continues assistance, guidance and support during my PhD study, especially in the area of mathematics. Their prospective advises and thoughts truly broaden my horizon in research.

Meanwhile, I would like to specially thank Dr. Di Wu who is the postdoctoral research fellow working with Prof. Wei Gao. During my four-year PhD study, Dr. Di Wu spent countless hours on educating me the details in every aspect in research, such as numerical modelling, presentation preparation and paper writing. My thank also includes my collaborator and good friend Dr. Lei Liu who spent three years' time with me until he achieved his PhD degree.

Last but not least, I thank my family including my parents-in-law, my parents and my wife for the countless support that I obtained throughout my studies and particularly during my PhD. It is impossible for me finish the thesis without them.

Table of Contents

List of Figures

List of Tables

Nomenclature

Greek letter

α_i , $\hat{\alpha}_i$	*i*th Lagrange multiplier
$\tilde{\alpha}$	Polynomial parameter for Gegenbauer polynomial
$\boldsymbol{\alpha}$, $\hat{\boldsymbol{\alpha}}$	Vector of Lagrange multiplier
δ_E	The magnitude of the increase of $\hat{\mathbf{I}}_E$
δ_{kl}	Kronecker delta
δ_ρ	The magnitude of the increase of $\hat{\mathbf{I}}_\rho$
γ	Bias parameter
Γ	Gamma function
$\tilde{\Gamma}$	Intrinsic degree
ε	Tolerable deviation between actual and predicted output
ε_{p_f}	Relative difference between $\hat{p}_f$ and $\tilde{p}_f$
ζ	Interval variable
$\overline{\zeta}$, $\underline{\zeta}$	Upper and lower bounds of ζ

$\boldsymbol{\zeta}$	Vector of interval variables
$\boldsymbol{\eta}$	The vector of concerned non-probabilistic and spatially uncertain system parameters
θ	An arbitrary sampling point in the sample space $\boldsymbol{\Omega}$
$\boldsymbol{\kappa}$	Empirical feature vector
K	Kernel function
K_{GGK}	Generalized Gegenbauer kernel function
$\mathbf{K}$, $\mathbf{K}_{train}$	Kernel matrix
λ	Generic penalty variable applied on $\mathbf{w}$
λ_a , λ_b	Penalty parameters applied on DrSVM and X-SVR
$\hat{\lambda}_v$	The approximation of the vth eigenvalue of a structural system
$\lambda_{\min}^{w}$	Minimum wave length
$\mu(\boldsymbol{\chi})$	Mean of Gaussian random field
μ_f	Mean of the output samples
μ_{input}	Mean of the input random variable

$\mu_{\log}(\boldsymbol{\chi})$	Mean od lognormal random field
$\mu_{(\bullet)}$	Mean of $(\bullet)$
$\overline{\mu_{(\bullet)}}$, $\underline{\mu_{(\bullet)}}$	Upper and lower bounds of $\mu_{(\bullet)}$
$\boldsymbol{\mu}_{(\bullet)}$	Vector contains all the mean of $(\bullet)$
ν	Poisson's ratio
ξ , $\hat{\xi}$	Slack variables for deviation allowance in prediction
$\boldsymbol{\xi}$, $\hat{\boldsymbol{\xi}}$	Vectors of slack variables
ρ	Mass density
$\rho^{\tilde{\alpha}}(x)$	Weight function for one-dimensional Gegenbauer polynomial with input variable x
$\sigma(\boldsymbol{\chi})$	Standard deviation of Gaussian random field
σ_{input}	standard deviation of the input random variable
σ_{K}	Kernel scale
$\sigma_{\log}(\boldsymbol{\chi})$	Standard deviation of lognormal random field
$\sigma_{(\bullet)}$	Standard deviation of $(\bullet)$

$\overline{\sigma_{(\bullet)}}$, $\underline{\sigma_{(\bullet)}}$	Upper and lower bounds of $\sigma_{(\bullet)}$
$\boldsymbol{\sigma}_{(\bullet)}$	Vector contains all standard deviations of $(\bullet)$
$\boldsymbol{\Phi}$	Intrinsic mapping function
$\boldsymbol{\Phi}_v$	The *v*th eigenvector
$\hat{\boldsymbol{\Phi}}_v$	The eigenvector associated with $\hat{\omega}_v$
$\boldsymbol{\chi}$	Generic continuous parameter
$\boldsymbol{\chi}_p$	A specific location of $\boldsymbol{\chi}$
ψ	Random variable
$\boldsymbol{\psi}$	Vector contains random variables
$\boldsymbol{\Psi}$	Domain of the entire structural system
$\boldsymbol{\Psi}_{i_e}$	The domain of the i_ℓ th structural element
$\lvert\boldsymbol{\Psi}_{i_e}\rvert$	The area of the i_ℓ th structural element
ω_d	Dimensionless frequency
$\omega_{d,\max}$	Highest frequency of ω_d
ω_v	The *v*th ($v = 1,\ldots,d_s$) natural frequency

$\hat{\omega}_v$	The approximation of ω_v
$\overline{\hat{\omega}_v}$, $\underline{\hat{\omega}_v}$	Upper and lower bounds of $\hat{\omega}_v$
ω_v^*	The constraint of the *v*th natural frequency
$\mathbf{\Omega}$	The probabilistic sample space
$\tilde{\mathbf{\Omega}}$	The interval space

English letter

a_v , $a_{1,v}$, $a_{2,v}$	Auxiliary variables
b_v , $b_{1,v}$, $b_{2,v}$	Auxiliary variables
A	Cross-sectional area of a structural memeber
A_B	Cross-sectional area of beam elements
A_C	Cross-sectional area of column elements
$\mathbf{A}$	Auxiliary matrix
$\mathbf{A}_i$	Auxiliary vector
$\hat{\mathbf{A}}$, $\hat{\mathbf{A}}_k$	Auxiliary matrices used for X-SVR

$\tilde{b}_1$	Upper threshold of dynamic response
$\tilde{b}_2$	Lower threshold of dynamic response
$\mathbf{b}$, $\mathbf{b}_k$	Auxiliary vectors used for X-SVR
$\mathbf{B}$	Auxiliary matrix
$\mathbf{B}_i$	Auxiliary vector
c	Penalty constant for support vector machine/ regression
c_{sound}	Sound speed
$\hat{c}$	Nominal value of c_{sound}
$\mathbf{C}$	Compatibility matrix
$\mathbf{C}_G^a$	Global damping matrix of acoustic
$C_H(\boldsymbol{\chi}, \hat{\boldsymbol{\chi}})$	Covariance function
$\mathbf{C}_s$	Damping matrix of structure
$\hat{\mathbf{C}}$, $\hat{\mathbf{C}}_k$	Auxiliary matrices used for X-SVR
d	Order of polynomial
d_s	Number of degrees of freedom of a structure

$\hat{\mathbf{d}}$, $\hat{\mathbf{d}}_k$	Auxiliary vectors used for X-SVR
$\mathbf{D}$	Flexibility matrix of a structure
$\mathbf{D}_i$	Derivative of $\mathbf{D}$ with respect to ψ_i
$\mathbf{D}_{pq}$	Diagonal matrix which contains all labels associated with training dataset
err_i	mean squared error between predicted and true outputs in the *i*th fold
$\mathbf{e}$	Generalized stress vector
$\mathbf{e}_n$	Unit vector in $\Re^n$
$\mathbf{e}_{\mathbf{A}_i}$, $\mathbf{e}_{\mathbf{B}_i}$, $\mathbf{e}_{\hat{\mathbf{m}}}$	Auxiliary vectors
$\hat{\mathbf{e}}$, $\hat{\mathbf{e}}_k$	Auxiliary vectors used for X-SVR
E	Young's modulus of a structural member
E[•]	Expectation operator for [•]
Err_{5CV}	5-fold cross-validation error
$f(\mathbf{x})$	True function/ model
$\hat{f}(\mathbf{x})$	Predicted function/ model

$f_s(t)$	Transient acoustic flux
$f_{\psi_i}(x)$	Probability density function of ψ_i
$f_{(\bullet)}^{CDF}$	The true cumulative distribution function of $(\bullet)$
$\tilde{f}_{(\bullet)}^{CDF}$	The true cumulative distribution function of $(\bullet)$
$f_{(\bullet)}^{PDF}$	The true probability density function of $(\bullet)$
$\tilde{f}_{(\bullet)}^{PDF}$	The estimated probability density function of $(\bullet)$
$\mathbf{f}$	Vector contains elemental forces
F	Load applied on a structural node
F_0	Amplitude of the harmonic excitation
$F_s(\omega)$	Fourier transform of the flux $f_s(t)$
F_{st}	Peak magnitude of $f_s(t)$
F^*	Hilbert feature space/ Intrinsic vector space
$\tilde{F}$	σ-algebra that contains all events
$\mathbf{F}$	Externally applied static load
$\mathbf{F}_i$	The derivative of $\mathbf{F}$ with respect to ψ_i

$\mathbf{F}(t)$	Time-dependent external excitation vector
$g(\mathbf{x})$	True limit state function
$\hat{g}(\mathbf{x})$	Limit state function approximated by surrogate model
$\hat{\mathbf{G}}$, $\hat{\mathbf{G}}_k$	Auxiliary matrices used for X-SVR
h	Vapnik Chervonenkis (VC) dimension
$\tilde{h}(\mathbf{x})$	Arbitrary squared integrable function
$H(\mathbf{x},\theta)$	Random field
$\hat{H}^d(\chi,\theta)$	dth order approximation of the random field
$\mathbf{H}$	Deterministic operator
$I(\chi)$	Interval field as a function of continuous parameter χ
$I^C(\chi)$	Mid-point function of interval field
$I_E(\chi)$	Interval field of Young's modulus
$\overline{I_E}(\chi)$, $\underline{I_E}(\chi)$	The upper and lower bound function of Young's modulus
$I_r(\chi)$	Sample function of the interval field $I(\chi)$
$I_\rho(\chi)$	The interval field of mass density

$\overline{I_\rho}(\chi)$, $\underline{I_\rho}(\chi)$	The upper and lower bound functions of mass density
$I^W(\chi)$	Half-width function of interval field
$\overline{I}(\chi)$, $\underline{I}(\chi)$	Upper and lower bound functions of $I(\chi)$
$\hat{I}(\chi)$	Discretized interval field
I[•]	Indicator function of [•]
$\mathbf{I}_{(2m+2n)\times(2m+2n)}$	Identity matrix in $\Re^{(2m+2n)\times(2m+2n)}$
$\mathbf{I}(\Re)$	Closed set for all real intervals
$\hat{\mathbf{I}}_E$	The discretisation of $I_E(\chi)$
$\Delta\hat{\mathbf{I}}_E$	Incremental vector of $\hat{\mathbf{I}}_E$
$\hat{\mathbf{I}}_{\hat{i}}$	An approximation of the θth interval field
$\overline{\hat{\mathbf{I}}_{\hat{i}}}$, $\underline{\hat{\mathbf{I}}_{\hat{i}}}$	Upper and lower bound vectors of $\hat{\mathbf{I}}_\theta$
$\hat{\mathbf{I}}_{\hat{i}}^C$	Mid-point vector of $\hat{\mathbf{I}}_\theta$
$\hat{\mathbf{I}}_{\hat{i}}^H$	Half-width vector of $\hat{\mathbf{I}}_\theta$
$\hat{\mathbf{I}}_\rho$	The discretisation of $I_\rho(\chi)$

$\Delta\hat{\mathbf{I}}_{\rho}$	Incremental vector of $\hat{\mathbf{I}}_{\rho}$
$\mathbf{I}_{i_e}^{e}$	Elemental interval vector collecting all interval variables from discretising interval field
$\overline{\hat{\mathbf{I}}_{i_e}^{e}}$, $\underline{\hat{\mathbf{I}}_{i_e}^{e}}$	Upper and lower bound vectors of $\mathbf{I}_{v}^{e}$
J	Confidence interval (VC confidence)
$\mathbf{K}_{G}^{a}$	Global stiffness matrix of acoustic
$\mathbf{K}_{i}$	The derivative of $\mathbf{K}_{s}$ with respect to ψ_{i}
$\mathbf{K}_{s}$	Global stiffness matrix of structure
$\mathbf{K}_{i_e}^{e}$	The elemental stiffness matrix of the *v*th element
$l(\bullet)$	Generic loss function of $(\bullet)$
$l^{\varepsilon}(\bullet)$	ε-insensitive loss function
l_{2}^{ε}	quadratic ε-insensitive loss function
l_{e}	Length of a structural member
L	Lagrange function
L_{x}, L_{y}	Correlations lengths in x - and y - direction

m	Number of random variables
m_f	Number of samples that result in the failure of the structure
m_i	Number of training samples in the *i*th fold
m^I	Number of interval variables
m_{train}	Number of training samples
m_{MCS}	Number of samples generated by MCS
$\mathbf{m}$, $\mathbf{m}_k$	Auxiliary vectors used for X-SVR
$\hat{\mathbf{m}}$	Auxiliary vector
$\mathbf{M}_G^a$	Global mass matrix of acoustic
$\mathbf{M}_s$	Global mass matrix of structure
$\mathbf{M}_{i_e}^e$	The elemental mass matrix of the *v*th element
n	Number of input variables
$\mathbf{n}_i$	Auxiliary vector
n_s	Number of elements in a structural system
$P_d^{\tilde{\alpha}}$	Gegenbauer polynomial with degree d

p_f	Probability of failure
$p_{f,ins}(t)$	Instantaneous probability of failure at time t
$\hat{p}_f$	Estimated probability of failure
$\tilde{p}_f$	Probability of failure computed by MCS
p_j, q_j	jth element of $\mathbf{p}$ and $\mathbf{q}$, respectively
$\mathbf{p}$, $\mathbf{p}_k$	Non-negative auxiliary vectors for *pq*-SVM and X-SVR
$\mathbf{p}(t)$	Time-dependent nodal acoustic pressure
P	Probability measure
$p_O(t)$	Time-dependent acoustic pressure at point O
$\overline{\hat{p}_O}$	The ultimate capacity of acoustic pressure at point O
$\overline{P_r}$, $\underline{P_r}$	Upper and lower bounds of structural reliability
$\Pr\{\bullet\}$	Probability of $\{\bullet\}$
q	Total number of interval fields in an engineering system
$\mathbf{q}$, $\mathbf{q}_k$	Non-negative auxiliary vectors for kernelized X-SVR
$\mathbf{q}_{\mathbf{A}_i}$, $\mathbf{q}_{\mathbf{B}_i}$, $\mathbf{q}_{\dot{\mathbf{m}}}$, $\mathbf{q}_{\mathbf{n}_i}$	Auxiliary vectors

$\mathbf{q}_s$	Generalized stress vector of the structure
$\mathbf{Q}$, $\mathbf{Q}_k$	Auxiliary matrices used for X-SVR
r_0 , r_1	Inner and outer radii of open hollow sphere
R	Structural risk
RR	Relative difference between proposed method and reference method
R_{emp}	Empirical risk
RMSE	Root mean square error
R^2	Coefficient of determination
$\mathbf{Re}_{(\bullet)}$	the high-order terms of the Taylor expansion for the uncertain parameter $(\bullet)$
$\mathbf{S}$	Matrix which collects all elemental stiffness
t	Time
t_{com}	Computational time
t_d	Dimensionless time
T	Kinetic energy

$\overline{u_1}$	Allowable displacement of element 1
u_v	Static displacement at vth degree-of-freedom
$u_{v,x}$, $u_{v,y}$	Displacement in x and y direction at vth degree-of-freedom
$\mathbf{u}$, $\mathbf{u}_k$	Vectors of non-negative Lagrange multiplier for X-SVR
$\mathbf{u}^*$, $\mathbf{u}_k^*$	Obtained solution for by soling optimization problems.
$\mathbf{u}_s$	Vector of all nodal displacement
$\mathbf{u}(t)$	Time-dependent displacement vector
$\mathbf{u}(0)$, $\mathbf{u}_0$	Initial displacement at $t=0$
$\dot{\mathbf{u}}(t)$	Time-dependent velocity vector
$\dot{\mathbf{u}}(0)$, $\dot{\mathbf{u}}_0$	Initial velocity at $t=0$
$\ddot{\mathbf{u}}(t)$	Time-dependent acceleration vector
$\hat{\mathbf{u}}$	Unit vector
U	Strain energy
$v^+(t)$	Out-crossing rate
$\mathbf{v}$	Non-negative auxiliary vector

Var[•]	Variance operator for [•]
w	Total number of generalized stress/strain in a structural system
w_j	jth element of $\mathbf{w}$
$w(\chi)$	Mean function of the random field
$\mathbf{w}$	Weighted vector in $\Re^n$
x	Generic input variable
x_i	ith generic input variable
$\mathbf{x}$	Generic input vector
$\mathbf{x}_i$	Vector of ith input sample
$\mathbf{x}_{train}$	Matrix of input samples of training dataset
y^i_{train}	ith output sample of training dataset
$\mathbf{y}_{train}$	Vector of output samples of training dataset
$\mathbf{z}$, $\mathbf{z}_k$	Auxiliary vectors used for X-SVR
$\mathbf{z}_G(t)$	Vector of all nodal pressures

Chapter 1 . Introduction

1.1 Motivation of research

In order to achieve trustworthy predictions with respect to the behaviour, performance and safety of engineering systems, the numerical modelling of the physical and mechanical properties should be realistic [1]. Despite of the wide implementation of deterministic numerical models, uncertainties inevitably exist in most engineering applications and affect the design of structural system and operating performance [2]. For structural engineering, uncertainty analysis [3] could provide rational assessment of the effects of variation of system parameters on structural response. Therefore, by incorporating the uncertainty analysis into the process of structural analysis and optimization, more reliable and economic optimal designs will be achieved [4].

Traditionally, probabilistic methods have been widely applied in uncertainty analysis and structural reliability analysis. Within the probabilistic analysis framework, all uncertain parameters are modelled as either random variables or fields with associated statistical information [1, 5]. Consequently, by combining the FEM with the well-established theories on probability and statistics, the stochastic finite element method (SFEM) has been innovatively established with extensive application across wide range of engineering disciplines [6–8]. Subsequently, a probability profile can be constructed for the concerned engineering system output, such as structural displacement, as the discrption of the variation caused by uncertain input variables. For practical application, sufficient statistical information may be unavailable or very expensive to obtain in real engineering problems. It has been shown that even small variations in the real statistical characteristics from the assumed one could lead to relatively large errors in the probability file of the output [9].

In order to achieve valid uncertainty analysis for situations where stochastic approaches are prohibited, the non-probabilistic approaches, such as the convex model, fuzzy set theory and interval analysis, have been developed as alternatives. By using convex sets to describe uncertain parameters, such non-stochastic modelling technique has been applied in uncertainty propagation analysis, reliability analysis and engineering optimizations involving uncertain system inputs [10–12]. The fuzzy analysis, stemming from the fuzzy set theory, incorporates membership functions to represent the possibility distributions of uncertain variables [13, 14]. Among the non-probabilistic approaches, interval method is the most widely adopted computational strategy due to the conceptual simplicity, which only requires the upper and lower bounds of the uncertain parameters rather than the probability profiles. The interval model is also regarded as a special case of the convex model analsys.

In real engineering problems, it is recently recognized that both probabilistic and non-probabilistic uncertainties can exist simultaneously. By unifying a mixture of uncertain parameters into one computational approach, it would enhance the robustness and applicability of the algorithm considering the diverse natural of practical situation. Within such framework, the concept of probabilistic interval analysis is widely implemented in the investigation of static response [7, 15], acoustic fields [16, 17] and structural-acoustic interaction system [18, 19] and structural reliability [20, 21] with spatially independent random and interval uncertain variables. The combination of multi-types of uncertainties in one approach cerntainty brings the complexity existing in each approach to the hybrid analysis. Therefore, the study of hybrid uncertainty analysis and reliability analysis considering mixed uncertainties have received increasingly amount of attention in the past decade.

At the time of the start of this research project, there have been many numerical methods developed within each of the uncertainty analysis category. Obviously, the mentioned three types of uncertainty analysis are proposed with distinctive concerns of the practical situation and the every uncertainty analysis approach has individual advantages in particular engineering applications. At current stage, there is still a lack of single uncertainty analysis approach which is effective and applicable for all scenarios. Thus, there are always enquires on developing novel approaches and improving the currently available methods of uncertainty analysis for the increasingly more complicated engineering applications.

1.2 Research objectives

The aim of the research is to propose a series of new uncertainty analysis methods which can be effectively and efficiently integrated into the practical engineering applications. More explicitly, this research encompasses the following key objectives:

1. Develop new formulations and computational methods for static analysis of structures (i.e. truss and frame) with hybrid uncertainties. In this thesis, a novel unified perturbation mathematical programming approach is proposed, which combines the advantages of both perturbation method and mathematical programming approach.
2. Propose a new non-deterministic free vibration analysis scheme for continuous structures with hybrid probabilistic and interval uncertainties. Firstly, formulations and computational methods for interval analysis with spatially dependent uncertain parameters will be developed. Then this method will be adopted and extended to a hybrid analysis to include both random and interval fields.

3. Propose new efficient approach for dynamic reliability analysis of structures against various uncertainties. For this target, a new machine learning based surrogate model will be developed to have the capability in considering relatively large number of (more than several) random variables. Then this method will be applied into dynamic reliability analysis with random uncertainties.

The main contribution of the research is to provide a collection of uncertain analysis methods for engineering structures with considerations of hybrid uncertain parameters, which can be implemented into modern engineering applications. The robustness of the framework is another key factor considered in this research, which enable the further extension of the proposed method into other engineering applications in addition to structural engineering.

1.3 Outline of the thesis

The thesis is organized in seven chapters. The contents included in each chapter are briefly presented in the following.

Chapter 1 presents the motivation and objective of the research. The structure of this dissertation and achieved journal and conference publications are also included in this chapter.

Chapter 2 provides a literature review of the uncertainty analysis strategies adopted in structural engineering. The probabilistic analysis, non-probabilistic methods and hybrid probabilistic and non-probabilistic models are discussed in details. The reliability analyses based on the aforementioned three theories are also presented in corresponding sections.

Chapter 3 demonstrates the static response analysis of linear engineering structures with hybrid random and interval uncertainties. In this chapter, a novel unified perturbation mathematical programming (UPMP) approach is proposed for the hybrid static response analysis. As a combination of perturbation method and mathematical programming, the proposed method enables the obtained of the bounds of mean and standard deviations of static structural response by solving nonlinear programming problems (NPLs).

Chapter 4 investigates the effect of spatial-variant non-probabilistic uncertainties on structural natural frequencies. Such uncertainties are modelled by adopting a recently introduced interval field concept. An efficient computational strategy is proposed such that the extreme bounds of natural frequencies of the structure involving interval fields can be rigorously computed by performing two independent eigen-analyses. The effectiveness of the proposed method is validated by comparing with the conventional Monte Carlo simulation.

Chapter 5 extends the uncertain natural frequency analysis with interval field to the hybrid analysis with both random and interval fields, which is distinguished from the conventional hybrid analysis. By combining the interval eigenvalue analysis proposed in Chapter 4 with stochastic sampling techniques, a large number of samples can be collected for the upper and lower bounds of structural natural frequencies. The stochastic characteristics of the extreme bounds of the structural natural frequencies can be obtained by utilizing the adequate statistical inference methods.

Chapter 6 provides the dynamic reliability analysis of engineering systems. The reliability analysis is conducted by using a new machine learning based surrogate model, namely the extended support vector regression (X-SVR). Additionally, a new orthogonal

polynomial kernel is proposed to enhance the performance of the proposed metamodel. The efficiency and effectiveness of the proposed method is verified by two benchmark functions and two engineering motivated models.

Chapter 7 presents the conclusions and further development recommendations.

1.4 List of publications

By the completion of this dissertation, there have been a number of journal and conference papers which have been published or submitted for publication. The details of the publications are:

Journal publications:

1. Wu, D., Gao, W., Feng, J., & Luo, K. (2016). Structural behaviour evolution of composite steel-concrete curved structure with uncertain creep and shrinkage effects. *Composites Part B: Engineering*, *86*, 261-272. https://doi.org/10.1016/j.compositesb.2015.10.004
2. Feng, J., Wu, D., Gao, W., & Li, G. (2017). Uncertainty analysis for structures with hybrid random and interval parameters using mathematical programming approach. *Applied Mathematical Modelling*, *48*, 208-232. https://doi.org/10.1016/j.apm.2017.03.066
3. Feng, J., Wu, D., Gao, W., & Li, G. (2018). Hybrid uncertain natural frequency analysis for structures with random and interval fields. *Computer Methods in Applied Mechanics and Engineering*, *328*, 365-389. https://doi.org/10.1016/j.cma.2017.09.004
4. Feng, J., Li, Q., Sofi, A., Li, G., Wu, D., & Gao, W. (2018). Uncertain structural free vibration analysis with non-probabilistic spatially varying parameters. *ASCE-*

ASME Journal of Risk and Uncertainty in Engineering Systems, Part B: Mechanical Engineering. https://doi.org/10.1115/1.4041501

5. Feng, J., Liu, L., Wu D., Li, G., Gao, W., & Beer M. (2019). Dynamic reliability analysis using the extended support vector regression (X-SVR). *Mechanical Systems and Signal Processing*, *126*, 368-391. https://doi.org/10.1016/j.ymssp.2019.02.027

Conference publications:

1. Gao, W., Feng, J. & Wang, C. (2015). Nondeterministic dynamic characteristics of structures with mixed uncertainties, *Proceedings of 23rd Annual International Conference on Composites or Nano Engineering, July 12-18, 2015, Chengdu, China*
2. Feng, J., Wu, D., Gao, W., & Li, G. (2015). Structural behaviour analysis of truss structure with mixed uncertainties, *Proceedings of 2nd Australasian Conference on Computational Mechanics, Nov 30-Dec 1, Brisbane*.
3. Feng, J., Wu, D., Gao, W., & Li, G. (2016). Static response of frame structure in the presence of hybrid uncertainties, *Proceedings of 6th Asian-Pacific Symposium on Structural Reliability and Its Application, May 28-30, 2016, Shanghai, China.*
4. Feng, J., Wu, D., Gao, W., & Li, G. (2016). Unified stochastic and non-stochastic free vibration analysis of structures, *Proceedings of 24th Australasian Conference on the Mechanics of Structures and Materials, December 6-9, 2016, Perth.*
5. Feng, J., Wu, D., Gao, W., & Li, G. (2017). Non-deterministic free vibration analysis of structures with random and fuzzy parameters, *Proceedings of International Mechanical Engineering Congress and Exposition, November 3-9, 2017, Tampa, USA*

Chapter 2 . Literature review on uncertainty analysis in structural engineering

Despite that the system variables of the concerned structures are widely assumed as deterministic, it has been illustrated that the fluctuation, or so-called uncertainties, of these parameters inherently associates with the structures as well as the modelling process [22–24]. Uncertainties are contributed from wide ranges of resources, such as manufacturing imperfection, random environmental attacks, measurement errors and human faults. Depending on the originality, the uncertainties can be generally divided into two categories: aleatory and epistemic uncertainties [25]. The aleatory uncertainty is resulted from the inherent variations associated with the engineering systems or environment. Thus, probabilistic theories are adopted by modelling the aleatory uncertainty as random variables. The epistemic uncertainty is considered as the consequence of the ignorance or incomplete information of the engineering systems or environment and thus usually described by interval, convex or fuzzy variables and so on.

The analysis approaches are usually categorised into three groups: (1) probabilistic approach, such as Monte-Carlo simulation, perturbation techniques and spectral methods; (2) non-probabilistic approaches including interval models, convex methods and fuzzy analysis; (3) hybrid uncertainty analysis which unifies a mixture of uncertainties (i.e. random and interval) into a single numerical strategy. In this section, the overviews of the methodologies that can be incorporated in uncertainty analysis are discussed.

2.1 Probabilistic analysis of structures

Probabilistic approach has been widely used for analysing structural responses with uncertainties when sufficient stochastic information is available. By adopting this concept, uncertain parameters are modelled as random variables or random fields which enable the computation of statistical characteristics, such as mean and standard deviation, of the structural response. Different engineering variables, such as Young's modulus and loading regimes, can be modelled as different probability distributions, which is comprehensively summarised in the reference [26]. Generally, the implementation of SFEM can be classified into two categories: the simulative approaches (e.g., direct Monte-Carlo simulation (MCS)) which are capable in offering the probabilistic features of the concerned structural responses based on the collection of samples obtained from the simulation [2, 27–30]; and the non-simulative strategies which approximate the statistical characteristics of the structural system outputs by implementing various numerical methods [31–35].

The sampling approaches, such as Monte-Carlo simulation (MCS), have been widely used in the probabilistic analysis. Within this framework, a large number of samples of the uncertain variables are generated based on the given statistical information. Then, deterministic analysis is repeated for each set of samples. The advantage of MCS is its robustness, which means that it can be extensively adapted to a variety of engineering analysis models [24]. By combining MCS with Abaqus, the effect of uncertain material properties on the structural response of composite steel-concrete beams is obtained [36]. To select the best-fit distributions, some statistical analysis methods, such as Anderson-Darling test, Chi-square test and Kolmogorov-Smirnov test, can be applied to the samples from MCS [37]. The MCS is also capable to be combined with

extended finite element method (XFEM) in the uncertainty analysis of composite structures [30].

However, to reach an acceptable level of accuracy, a large number of simulations are necessary which requires excessive computational efforts. Hence, a Monte-Carlo simulation method is often used as a reference approach to validate the accuracy of other approach. For increasing the computational efficiency for calculating the eigenvalues and eigenvectors of complex stochastic structures, Székely & Schuëller [38] combines the subspace iteration method with the parallel computing such that the practical application of MCS is enabled. Latin Hypercube Sampling (LHS) method is an alternative of MCS. This method will generate samples which are equally distributed according to the cumulative distribution functions of the input uncertain parameters [39]. Line sampling and Adaptive Line Sampling methods can improve the simulation efficiency as well [40].

Perturbation method has been widely applied to formulate the finite element matrices for stochastic engineering systems. By using Taylor expansion to the stochastic matrices and structural response vector, the uncertain property of the structures is discretised as a function of partial derivative of the input random parameters. Generally, the Taylor expansions are truncated at first or second-order since higher order terms will result in a significant increase in computational effect [41]. Accordingly, a random variable functional moment method is proposed by Gao et al. [15] up to the second-order Taylor expansion for linear analysis of truss and frame structures. This method is extended to hybrid random and interval uncertainty analysis. Kaminski et al proposed a generalised stochastic finite element method and applied it to the elastic buckling analysis of structures [42]. The perturbation-based method is capable in uncertain dynamic analysis of laminated plate as well [43]. The key advantage of this method is that the

means and standard deviations of the structural output can be obtained without running simulations with a large number of samples. Hence, the efficiency is increased dramatically comparing with sampling method. However, the accuracy of this approach is affected by the coefficient of variation of the input variables [44] due to neglect of higher order terms. Therefore, improved perturbation methods for stochastic finite element analysis are developed to increase the accuracy [41, 45]. For large-scale random eigenvalue problem, a reduced basis formulation is proposed aiming on improving the accuracy of the first order perturbation method [46]. By adopting this method, the original random eigenvalue problem is transferred into a series of reduced order random eigenvalue problem for each interested mode and thus the computational efficiency is also increased. Adhikari & Friswell [47] propose a modification of the conventional perturbation method. Instead of applying the Taylor's expansion at the mean of random variables, the proposed method applied the perturbation expansion at the so-called optimal point, which enhances the performance of perturbation method in the presence of non-Gaussian random variables. To overcome the drawback that the traditional perturbation-based SFEM can only estimate the probability density function of structural responses with Gaussian distributed input variables, Xia et al. [48] integrate the change-of-variable technique into the perturbation method and applied to the static response analysis of structures. Subsequently, the cumulative distribution function of the stochastic structural response can be achieved.

Instead of using the conventional finite element method, Long et al. [49] combine the perturbation concept with the scaled boundary finite element method (SBFEM) for the stochastic analysis of the orthotropic and cracked structures with random variables. Such stochastic SBFEM is then extended by considering the material properties as

random fields which are discretised by Karhunen–Loève (KL) expansion [50]. In this context, the first-order Taylor series expansion is applied by using the independent random variables resulted from the KL expansion. This method takes the advantage of the SBFEM in fracture mechanics and thus extended the applicability of the perturbation method.

With the progressive development of uncertainty analysis, SFEM has been escalated with the consideration of the spatial dependency of uncertain system parameters by incorporating the theory of random field. The spectral stochastic finite element method (SSFEM) is another type of non-simulative approaches, which was introduced by [32] by describing the spatial random variables of structure as random field. The core concept of SSFEM is to establish a valid surrogate model by implementing various series expansion schemes (e.g., the Karhunen–Loève expansion) such that the statistical characteristics (i.e., mean and variance) of the structural responses can be effectively calculated [51]. Instead of assuming the independency of random variables, the spatial correlation of random variables is considered in SSFEM as the covariance between the variables at any two locations within the spatial domain of the structures [52]. In additional to the static analysis, the SSFEM is implemented on random eigenvalue problem where the stochastic natural frequencies and mode shapes are represented by polynomial expansion [53] with respect to the random variables resulted from the Karhunen-Loève discretization.

The performance of the SSFEM is affected the inherent defect of the tradition FEM which can only approximate the geometry of the physical domain of structures to a certain extent. This negative effect would lead to numerical errors in the case that the structural systems are sensitive to geometric fluctuation. Stimulated by such imperfection of the traditional FEM, Li et al. [54] introduced a spectral stochastic isogeometric analysis

(SSIGA) which combines the spectral representation of random field with the novel isogeometric analysis. This method allows the complex geometries of structures to be exactly represented with relatively coase discretization comparing with the traditional FEM. Moreover, the quality of approximating the covariance function of random field is improved by integrating the NURBS and T-spline with the KL expansion.

Theoretically, the results estimated by the SSFEM can converge to the "exact" solution if the number of terms in the polynomial expansion increases to infinity. It is admitted that the accuracy will be increased with more terms involved, but the computational burden will be significantly heavy which prevents the SSFEM to be applied in the uncertainty problems with a large number of random variables.

Additionally, other types of stochastic methods have been proposed. Di Paola [55] proposed a virtual distortion method for investigating the static response of truss structures with stochastic uncertainties. By using the superposition principle, the explicit expression of structural response as a function of input random variables could be obtained in an asymptotic series expansion format. Due to the adoption of an alternative finite element formulation, the applicability of this approach is rather limited. A random eigenfunction expansion method is proposed by [56] for the response of stochastic finite element analysis of elliptical partial differential equations. The eigenvalues and eigenvectors used for constructing the expansion are computed by the eigendecomposition of the stiffness matrix of the investigated structures. Similar as other series expansion method, the proposed eigenfunction expansion approach requires truncation and approximation. The associated error is minimized by adopting the Galerkin error minimization approach. However, the computational efficient is significantly reduced by this error reduction strategy as discussed by the authors.

Surrogate models have been widely employed as computationally highly efficient approach for reliability assessments and uncertainty quantifications. The core concept of the metamodel technique is to establish an explicit formulation to approximate the relationship between the inputs and outputs of the concerned structural analyses with limit number of running the original model based on the Design of Experiments (DOE) and then the conventional MCS will be performed on the constructed metamodel [57]. Impollonia & Sofi [58] proposed a response surface method for analysing the stochastic static response of structures with geometrical nonlinearities. Although this approach is developed based on the first-order perturbation method, it offers a closed-form expression that approximates the relationship between the stochastic responses and input random variables. However, due to existence of computing the derivative of stiffness matrix with respect to random variables and the calculation of eigenvalues and eigenvectors, the applicability of such method would be limited to specific cases such as truss structures. In terms of using surrogate models for reliability analysis, the polynomial-based classical response surface method (RSM) was first employed [59, 60] and received further improvement upon in various applications [61, 62]. Polynomial chaos expansion (PCE) is another widely adopted non-intrusive method such that the stochastic system output is represented by a collection of orthogonal polynomial basis functions [54, 63]. To reduce the effect of "curse of dimensionality" issue associated with PCE, a sparse polynomial chaos expansion approach was introduced [64, 65] such that only a subset of PC terms is involved in the expansion. The PCE technique is recently extended to the generalized polynomial chaos (gPC) [66] and arbitrary polynomial chaos (aPC) [67, 68] methods, which enable the strategy to be applied to the problems with non-Gaussian distributions. A Chebyshev method is proposed for the dynamic uncertainty analysis of multibody

mechanical systems and extended for analyzing the dynamic responses of structures with uncertain variables [69, 70].

Aside from the aforementioned surrogate models, Kriging model which is a performance promising spatial interpolation technique has been extensively applied in uncertainty quantification and reliability analysis [71–74]. As a mathematical model constructed based on Gaussian process, Kriging can not only offer the unbiased predictive value but also uncertainty of the prediction measured by the Kriging variance [75]. Via utilizing the Kriging technique, a nested extreme response surface (NERS) method was developed to efficiently identify the extreme time responses as the dynamic reliability analysis can be conducted using static reliability analysis methods [76]. Other Kriging-based reliability analysis approaches for dynamics are also developed for various engineering applications [77, 78].

The artificial neural network (ANN) and its variations, benefitted from the capability in capturing the complex nonlinear relationship between the inputs and outputs, are increasingly applied as surrogate models for structural reliability analysis [79–81] and other engineering applications [82, 83]. Another machine learning technique, the support vector machine (SVM), has also been extensively studied in the structural reliability assessments. For example, the least squares support vector machine has been utilized for the dynamic reliability analysis of turbomachinery in [84]. Unlike the surrogate models based on the polynomial chaos expansion (PCE), the SVM is capable to bypass the curse of dimensionality and can also handle nonlinear problems effectively.

Even though the probabilistic approach of uncertainty analysis has been prevalently implemented in practical engineering applications, the applicability of such

methodology strongly depends on the availability of the information of uncertain parameters [85].

2.2 Non-probabilistic analysis of structures

In practical engineering applications, sufficient probabilistic information may not be available under particular circumstance. Therefore, non-probabilistic approaches are implemented as an alternative of the probabilistic methods for uncertainty analysis. Among which, the uncertainties are generally either described as fuzzy, convex or interval parameters.

The fuzzy set theory was introduced by [86] firstly in 1965. The importance of this theory is its capability of describing the incomplete information by using the fuzzy set which is generally defined by its membership function [87]. The membership function can be interpreted as a distribution of uncertainty. In practice, the α-level strategy is used so that the membership function is subdivided into series α-sublevels [88]. Each α-sublevel will generate a closed interval. Therefore, the α-sublevel approach actually transfers the fuzzy analysis into a number of interval analyses [87] and the membership function of the output of structures can be obtained. By using this strategy, a novel mathematical programming approach is proposed for robust fuzzy structural safety assessment [89]. The fuzzy membership function is constructed by performing a series of interval limit analyses using the concept of robust and optimistic optimizations. Recently, a novel fuzzy reliability model is from the viewpoint of probability theory [90]. In this theory, the membership levels of different variables are treated as independent standard uniform distributions. Inspired by the SSFEM, Adhikari & Khodaparast [91] proposed a spectral fuzzy finite element method based on Legendre polynomial expansion. Accordingly, the fuzzy variables are transferred into the standard interval variables vary

within $[-1,1]$. Similar as the SSFEM, the structural response is expressed as a function in the basis of multivariate orthogonal polynomials. This method extends the concept of SSFEM to non-stochastic analysis while maintains the same drawback which limits the number of fuzzy variables to be relatively small.

Convex model which was introduced in early 1990s [9] is another non-probabilistic methodology for uncertainty analysis. In this method, the uncertain variables are assumed to vary within a non-stochastic convex set, such as multidimensional ellipsoid. The interval analysis can be regarded as a special case of convex analysis with uncertainties varying within a multidimensional solid box. Comparing with the probabilistic analysis, the convex model has weak dependency on the number of samples [92]. In order to develop an effective approach for constructing the multidimensional ellipsoids for describing uncertainties, Jiang et al. [93] created a correlation analysis strategy. Accordingly, mathematical definitions are provided for the marginal convex model which represents the variation range of each uncertain parameter, and a covariance which describes the correlation degree between two variables. This approach is combined with the reliability index method and applied on the non-probabilistic structural analysis. The introduced correlation analysis offers the first attempt for defining the concept of correlation within the framework of non-probabilistic analysis of engineering structures. The degree of the correlation is represented by the shape of the ellipsoid. To improve the conventional convex model in considering both independent and correlated variables, a novel multidimensional parallelepiped model is developed with the introduction of correlation angle [94]. In this method, both positive and negative correlation between two uncertain variables can be represented. Assitionally, the parallelepiped model in the original parameter space is transferred into the affine space by using the affine coordinates,

which simplified the subsequent computation. Comparing with the conventional ellipsoid model, the multidimensional parallelepiped model extends the convex strategy to a more general manner. However, this model cannot provide an explicit formulation for describing the uncertainties and the complex affine transformation prevents the practical implementation in structural uncertainty analysis. To enhance the applicability of this approach, an improved multidimensional parallelepiped model is then developed to fix the aformentioned defects [10].

The interval analysis was developed based on the interval arithmetic [95], which simply requires the upper and lower bounds of the uncertain variables. Comparing with the probabilistic analysis and fuzzy method, the interval analysis takes the advantage of the conceptual simplicity and thus has been extensively implemented as an alternative to the probabilistic methods. Similar as the probabilistic approaches, sampling methods which include Monte-Carlo simulation (MCS) and Quasi-MCS are widely adopted for interval analysis of structures. Comparing with MCS, the samples generated by Quasi-MCS are relatively more equally distributed within the upper and lower bounds of the interval variables [96]. The disadvantage of this method is same as demonstrated previously that huge computation cost is requires, especially for complex structures.

In the light of pursuing a more accurate estimation of the bounds of natural frequencies, different numerical strategies have been developed, such as perturbation method, vertex method, interval factor method and others [97–100]. The accuracy of these numerical approaches is conditional to specified assumptions and types of structures. Among these methods, the perturbation method can be applied without the limit of the type of structures or where the interval uncertainty exists. Chen et al. [101] applied the first-order perturbation method with finite element method in static response analysis

with interval parameters within the frame work of interval arithmetic. However, the drawback of the traditional interval finite element analysis is the so-called dependency issue [102, 103] which may result in the overestimation of upper and lower bounds of structural response.

For the purpose of addressing this problem, different approaches have proposed for within the framework of interval finite element method. Guo et al. [104] applied linear mixed 0-1 programming for structural response analysis of truss structures with interval material properties. Affine arithmetic is another effective approach which is capable to track the dependency between interval variables [105]. Additionally, Interval Rational Series Expansion [106] is proposed and later on combined into the optimization and anti-optimization approach for interval analysis of structures [107]. A novel mathematical programming (MP) based formulation within the framework of FEM is developed which is capable for completely eliminating the dependency issue [108]. With the reformulation, the traditional governing equation of finite element method is decomposed into equilibrium equation, compatibility equation and elastic constitutive equation. This reformulation enables the upper and lower bounds of structural response to be solved as nonlinear programming problems. Recently, this approaches have extend to structural stability analysis [109] and elastoplastic analysis [110]. Within the framework of improved interval analysis via extra unitary interval, an interval finite element analysis is proposed by [111] to associate an extra unitary interval to each uncertain variable. Subsequently, the dependency between interval variables can be tracked in both assembly and solution stage of the finite element analysis. However, this method is limited to analyse with interval uncertainties existing in Young's modulus.

For interval eigenvalue problems, under the circumstance that only the structural stiffness is affected by interval variables, the exact bounds of natural frequencies are firstly proved by [112] to be achievable by implementing two deterministic finite element analyses. Recently, pioneering work has been accomplished [113] that the sensitivity analysis of eigenvalue is implemented with regarding to the interval system variables. By evaluating the first-order derivative of eigenvalues with respect to interval variables, monotonic relationship between the natural frequencies and input variables can be indicated. In such way, the combinations of the extreme values of interval parameters that lead to the exact bounds of eigenvalues can be identified. The combination of mathematical programming and perturbation method is also implemented for interval eigenvalue problems. Since that the perturbation method based on the second-order Taylor expansion can increase the accuracy in interval analysis, Li et al. [114] reformulated the Taylor expansion of eigenvalues as a quadratic programming problem and employed the difference of convex functions algorithm (DCA) to obtain the optimal solutions. Although extra computational time is required comparing with the first-order Taylor expansion method, this approach allows the eigenvalue analysis with large interval uncertainties.

A common assumption enclosed in the discussed interval analyses is that the interval parameters exist in the structural system are spatially independent. The consistency between the numerical analysis and general engineering practice is not fully addressed by such hypothesis [85]. To realistically describe the spatial dependencies of interval parameters, the concept of interval field is innovatively proposed as an extension of conventional random model by Verhaeghe et al. [115] who have suggested two models, namely explicit and implicit interval fields, for the static analysis of engineering

structures. Such novel concept is reinvented by implementing the Karhunen-Loeve-like decomposition of the bounded spatial fluctuation of Young's modulus for the static response analysis of an Euler-Bernoulli beam [116]. A comparative study on random and interval field models based on a one-dimensional beam structure is conducted by [117]. The introduction of interval field concept provides an innovative point of view for interval structural analysis. In addition, a non-probabilistic convex process model is introduced for time-variant uncertainty analysis and dynamic reliability analysis [118]. Accordingly, an interval process model is constructed to describe the non-random excitation applied on structures [119]. Comparing with the conventional random vibration analysis, only the upper and lower bounds functions are required for the time-variant excitation rather than the precise probability distribution. Wu & Gao [120] proposed another interval field model which is applied on both 1D and 2D static plain stress problem. The input interval parameters are described by upper and lower bound spatial-variant functions. By adopting the spatial average discretization scheme which was originally proposed for random field [121], the interval field is discretised into a vector of interval variables. Subsequently, the conventional interval finite element methods can be employed to solve the uncertainty problem with interval field. The aforementioned non-random field/process models enrich the theories of non-probabilistic analysis for engineering applications by offering practically applicable representations of the spatial/time variabilities of system parameters when information of the uncertain variables is insufficient for stochastic analysis.

2.3 Hybrid probabilistic and non-probabilistic uncertainty analysis

Considering that the modern engineering applications are advancing with increasing complexity in terms of materials, geometric properties and loading regimes, it is realized

by researchers that the aforementioned single uncertainty modelling techniques are inadequate for representing all the uncertain system parameters [122]. In this context, the hybrid uncertainty analysis approaches are developed to unify the diverse types of uncertainty modelling strategies (typically the probabilistic and non-probabilistic) into a single computational scheme.

Gao et al. [15] developed a random interval moment method based on the perturbation theory by taking Taylor expansion and the mean of random variables and mid-point values of interval parameters. In these studies, the upper and lower bounds of means and variances of system responses are explicitly formulated, such that the computational efficiency of this type of approach can be well preserved. The main advantage of this method is that mean and standard deviation of structural responses can be obtained with relatively less computational cost comparing with the sampling approaches. In addition to the static response analysis, the random interval moment method has been extended to natural frequency and mode shape analysis [123]. To avoid the interval dependency issue, the Monte Carlo simulation is used for computing the upper and lower bounds of mean and variance instead of using the interval perturbation method [6]. However, the computational efficiency is significantly reduced and the achievement of the exact upper and lower bounds is not promised. The random interval moment method is extended to the analysis of acoustic field with both random and interval uncertainties [17, 18, 124].

Semi-sampling approach combines the advantages of sampling method for stochastic analysis and non-simulative methods for interval analysis. Wu et al. [125] proposed a unified interval stochastic sampling (UISS) approach for the probabilistic interval limit analysis of structures. Firstly, a large number of samples for the input

random variables are generated according to the corresponding statistical information. Then, for each sample, an interval limit analysis is performed to obtain the upper and lower bounds of the collapse load factor. Thus, the statistical analysis can be conducted based on the collected samples to estimate the PDFs and CDFs of the bounds of collapse load factor. Assisted by the samples, the bounds of structural reliability against plastic collapse can be conveniently evaluated. The UISS method is also implemented on the uncertain stability analysis of structures with mixed random and interval variables [7]. The UISS approach offers a semi-sampling computational scheme which can be combined with the advanced sampling strategies in addition to the conventional MCS and also other non-simulative interval analysis approaches. For example, Wu et al. [126] incorporated the UISS method with a unified Chebyshev surrogate model for geometrically nonlinear analysis of structures with random and interval variables.

The dynamic response of structures with interval system parameters under random excitations has been investigated as a special case of hybrid uncertainty problem. Muscolino & Sofi [127] improved the interval perturbation method by using the affine arithmetic which introduces a unitary interval. The random dynamic response in time domain is approximated by the first-order Taylor expansion by assuming the stochastic response can be expressed as sum of midpoint solution and a deviation. This method is also applied to the frequency domain analysis [128] and dynamic reliability analysis of linear structures under stationary Gaussian excitation [129]. Do et al. [130] investigate the bounds of dynamic reliability of structures based on the first-passage failure probability. In this study, the boundary governing the first-passage failure is considered as interval variables in addition to the structural system parameters. Instead of evaluating the upper and lower bounds of the time-variant stochastic response, the proposed method

investigates the variations of the mean of structural response/ stress. Due to the complexity of the problem, an improved particle swarm optimization method is adopted to efficiently obtain the bounds of structural reliability and the mean of nodal structural responses.

For the hybrid uncertainty analysis involving spatial dependency, the static plane stress problem is investigated by either extending the spectral SFEM with interval variables [131]. In this study, the SSFEM is combined with interval analysis to calculate the bounds of the first two moment, mean and standard deviations, of the static structural responses. The mean and standard deviations are expressed as complicated polynomials of interval variables, which prevents the achievement of upper and lower bounds by simple interval arithmetic. Thus, an improved particle swarm optimization (PSO) method is adopted for efficiently computing the extreme bounds. An imprecise random field model is proposed by [132] by incorporating the uncertain-but-bounded values into the mean and standard deviations. Specifically, the Young's modulus and body force of structures are modelled as imprecise random fields which are discretised by KL expansion. This special case leads to the monotonic relationship between the structural response and the interval parameters. Therefore, the exact upper and lower bounds of statistical characteristics of the responses can be obtained by using the combinatorial approach. The uncertain static analysis with hybrid random and interval fields is conducted by [133] for the first time by a semi-sampling approach. Firstly, the random field is discretised by using the KL expansion and then a large number of samples for the random field are generated. At each sampling point, an interval analysis is conducted by using mathematical programming method. Subsequently, the collections of upper and lower bound samples are obtained, and the corresponding PDFs and CDFs can be constructed.

For representing the variabilities existing in fibre composites, a novel fuzzy-stationary random field model is proposed [134] by calibrating the random fields with fuzzy variables. Accordingly, a global-local multiscale algorithm is constructed by adopting the concept of representative volume element (RVE) and homogenization. At current stage, this model has only been applied on one-dimensional problem.

The hybrid uncertainties are also considered in the reliability analysis. For the First Order Reliability Analysis (FORM), a unified uncertainty analysis approach is introduced for considering a mixture of random and interval variables [135]. Thus, the probability of failure varies within a range instead of a constant value. In this study, the upper and lower bounds of the probability of failure are defined plausibility and belief according to both evidence and probability theory. This method is later on extended to reliability sensitivity analysis with both random and interval parameters [136]. Luo et al. [21] proposed a hybrid probabilistic and convex approach for structural reliability analysis. Due to existence of the uncertain-but-bounded parameters, the points that can lead to the structural failure form a bounded region, namely the critical region, rather than a multi-dimensional surface in the traditional probabilistic reliability analysis. For sake of conservation, this method is developed for searching the most probable failure point which has the shortest distance from origin to the critical region. For the structural reliability analysis with imprecise random distribution, Jiang et al. [137] proposed two models based on the reliability index approach (RIA) and performance measurement approach (PMA), which can be solved as two-layer nesting optimization problems. To increase the computational efficiency, a monotonicity analysis is conducted based on the two proposed approaches. As shown in this study, monotonicity of CDF can be observed for several commonly used probability distributions, such as Gaussian, lognormal,

extreme value distribution. The concern raised is that the first-order Taylor expansion is adopted in the inner-layer optimization problem, which could affect the accuracy of the proposed models. The perturbation-based random interval moment method is also extended to the reliability analysis of homogeneous and biomaterial cracked structures [138]. In this method, the elastic properties, externally applied loads and material fracture resistance are modelled as random variables, and the crack geometry is represented by interval variables. The upper and lower bounds of the reliability index are defined as functions of the bounds of mean and standard deviations of structural response.

Recently, the non-intrusive approaches are gaining increasingly popularity for the application in the hybrid uncertainty analysis and reliability analysis. By integrating the Polynomial Chaos expansion (PCE) method with the Chebyshev inclusion theory, a Polynomial-Chaos-Chebyshev-Interval (PCCI) method is proposed for the vehicle dynamics involving hybrid random and interval variables [139]. This method is capable in providing two types of hybrid analysis outcomes: (1) the interval mean and standard deviations; (2) the mean and standard deviations of upper and lower bounds of. The PCCI method can be regarded as the first non-intrusive approach for hybrid uncertainty analysis. In addition to the Chebyshev polynomial, the Legendre polynomial is also combined with the PCE and implemented for the time response of structures with hybrid uncertainties [140]. A Gegenbauer series expansion method (GSEM) is introduced by [141] for approximating the response of structural-acoustic systems with bounded hybrid random and interval variables. In this method, the expansion coefficients are obtained by the Gauss-Gegenbauer integration method. These methods share the same concept by using sampling approaches, either scanning method or Monte Carlo simulation, to obtained the

upper and lower bounds. Theoretically, the results can converge to the exact solution if sufficient number of samples is used.

Surrogate models have also been applied in the reliability analysis of structures with hybrid uncertainties. Balu & Rao [142] applied the Multicut-High Dimensional Model Representation (MHDMR) method in evaluating the bounds on structural reliability involving a mixture of random and fuzzy parameters. In this method, the probability distribution function of the approximated limit state function is estimated by using fast Fourier transform (FFT). An active learning Kriging model is proposed and implemented for reliability analysis with hybrid random and convex variables [143]. By iteratively adding the training point which is least likely to be correctly predicted, the accuracy of the Kriging model can be gradually increased. Comparing with the perturbation-based method and other intrusive approaches for hybrid analysis, the surrogate model based strategies eliminated the reformulation of the governing equations of the computational model which are usually complex. Thus, the implementation of metamodeling techniques in practical applications is expected to be more straightforward.

Chapter 3 . Uncertainty analysis for structures with hybrid random and interval parameters using mathematical programming approach

3.0 Summary

A novel computational method, namely the unified perturbation mathematical programming (UPMP) approach, for hybrid uncertainty analysis of engineering structures is proposed in this paper. The presented study considers a mixture of random and interval system parameters which are frequently encountered in engineering applications. Within the UPMP approach, matrix perturbation theory is adopted in combination with the mathematical programming approach. The proposed computational method provides a non-simulative hybrid uncertainty analysis framework, which is competent to offer the extreme bounds of the statistical characteristics (i.e., mean and variance) of any concerned structural responses in computationally tractable fashion. In order to thoroughly explore various intricate aspects of the engineering system involving hybrid uncertainties, systematic numerical experiments have also been conducted. Diverse statistical analyses are implemented to identify the bounded probability profile of the uncertain structural responses. Both academic and practical engineering structures are investigated to justify the applicability, accuracy and efficiency of the proposed UPMP approach.

The Chapter 3 is organised as follows. Section 3.1 introduces the background of static structural analysis with uncertainties. In Section 3.2, the formulations for static structural response analysis with hybrid uncertainties are presented. The proposed UPMP scheme is formally presented in Section 3.3. Furthermore, both academic sized and practically motivated numerical examples are investigated by the proposed UPMP

approach and then critically compared with either analytical solution or exhausted simulation approach in Section 3.4. Finally, some concluding remarks are drawn in Section 3.5.

The research work developed in this chapter has produced one journal paper which has been published in *Applied Mathematical Modelling*. The detail of the publication is: Feng, J., Wu, D., Gao, W., & Li, G. (2017). Uncertainty analysis for structures with hybrid random and interval parameters using mathematical programming approach. *Applied Mathematical Modelling*, *48*, 208-232. https://doi.org/10.1016/j.apm.2017.03.066

3.1 Introduction

Uncertainties, such as variations in material properties, cross-sectional geometry as well as loading regimes, inherently exist in practical engineering applications [144]. Such variabilities can result in significant effect on the structural response [2, 145]. Therefore, it is essential to incorporate the uncertain parameters into structural analyses.

Regarding the traditional uncertainty analysis, probabilistic/stochastic approaches are frequently implemented in the uncertain structural analysis due to the solid theoretical foundation associated with uncertainty modelling. Within the framework of the stochastic finite element method (SFEM), the well-known Monte-Carlo simulation (MCS) method is one of the most straightforward procedures, which has been pervasively implemented in a variety of stochastic problems [23, 27, 28]. In addition, the computational stochastic analysis, which has been developed basing on the theory of general matrix perturbation, offers an advantageous non-simulative strategy for uncertainty analysis on engineering structures involving random variables [48, 146–148]. Furthermore, the spectral stochastic

finite element method (SSFEM) was introduced to address the spatially dependent uncertain system parameters in structural engineering problems [22, 32, 149].

However, accumulated experiences from engineering practice have repeatedly revealed that the requirement for the implementation of the probabilistic analysis cannot be always fulfilled due to the issue of information deficiency on the uncertain system parameters [150]. In this context, the interval models are gaining popularity because of the conceptual simplicity [151]. By implementing the concept of interval analysis within the framework of the FEM, various computational algorithms with specific emphasises have been explicitly developed for tackling intricate engineering problems with enhanced capability and accuracy [103, 104, 107, 109, 152].

In modern engineering applications, it is frequently encountered that both probabilistic and non-probabilistic uncertainties exist simultaneously [153]. Therefore, a computational scheme which is capable of estimating the effect of diverse types of uncertainties on engineering system is inevitably necessary. A random interval perturbation method has been developed for static response analysis [15], and free vibration analysis [123] of structures with both stochastic and non-stochastic uncertainties. Also, the perturbation based computational method is extended to the dynamic response analysis of acoustic field and structural-acoustic interaction system with hybrid uncertain parameters [124].

By thoroughly examining on the literatures regarding the perturbation theory based hybrid uncertainty analysis with random and interval variables, it is realized that either series expansion or numerical approximation has been implemented to derive explicit formulations for the upper and lower bounds of the statistical characteristics of the considered structural responses. The advantage of such prevalently employed

technique is that explicit formulations on the bounded statistical characteristics of structural responses can be explicitly formulated. However, the drawback of such analysis is that the overestimation on the bounded statistical characteristics of system output cannot be completely exempted due to the issue of interval dependency. As clearly demonstrated in the previous studies [103, 104, 107, 109, 152], the issue of interval dependency can significantly affect the accuracy of the interval analysis, which is mainly attributed by the multiple occurrences of the same interval parameter at various locations. The general rule is that the more numbers of interval parameters appear in the system, the more likely the bounded results are suffering from overestimation.

In the light of achieving valid hybrid uncertainty analysis with the least overestimation due to interval dependency, a novel computational method, namely the *unified perturbation mathematical programming* (UPMP) method, is proposed for static analysis of engineering structures with a mixture of random and interval uncertain parameters. Within the proposed computational scheme, the matrix perturbation theory and mathematical programming (MP) approach are integrated in conjunction with an alternative FEM modelling technique. Such novel integration reformulates the hybrid probabilistic interval static analysis into a series of nonlinear programming (NLPs) problems. Consequently, the upper and lower bounds of the mean and variance of the concerned structural response can be explicitly determined by solving the corresponding NLPs. Some core advantages of UPMP are including:

1. The superior computational efficiency of the non-simulative method is fully inherited by the UPMP approach, which significantly enhances the applicability of the proposed scheme in the context of analysing modern complex engineering structures.

2. The physical feasibility of all interval parameters can be rigorously maintained throughout the entire hybrid probabilistic interval analysis. Thus, the determined system outputs are fully liberated from the overestimation caused by the issue of interval dependency.
3. The critical values of the interval parameters responsible for the extremities of statistical information of structural response can be effectively retrieved as by-products of the uncertainty analysis.

In order to evidently illustrate the applicability and effectiveness of the proposed UPMP approach, both academic sized and practically motivated structures have been investigated in this chapter. For the purpose of results verification, all computational results provided by the UPMP approach are rigorously testified against either analytical solution (for academic sized example) or results obtained from exhausted simulation approach (for practically motivated example). In addition to the proposition of the UPMP approach, supplementary numerical experiments have been conducted to further explore some important aspects on the hybrid uncertain static analysis with random and interval variables.

3.2 Non-deterministic static analysis of structures with hybrid uncertainties

For the non-deterministic analysis, the system parameters such as material properties, cross-sectional geometries and loading regimes are considered as uncertain variables. In general engineering practice, the availability and sufficiency of information of uncertain system parameters are strongly situational dependent [6, 7]. Therefore, it is rational and necessary to develop a hybrid uncertainty analysis scheme which can adopt as many different uncertainty modelling techniques as possible in a single framework of analysis.

3.2.1 Generalized hybrid random interval static analysis of structures

Without loss of generality, ψ is defined as a random variable in a probability space $\left(\mathbf{\Omega}, \tilde{F}, P\right)$ and $\Re$ denotes the set collects all real numbers; and ζ denotes an interval variable, such that $\zeta = [\underline{\zeta}, \overline{\zeta}] = \{\zeta \in \Re \mid \underline{\zeta} \le \zeta \le \overline{\zeta}\}$, where $\underline{\zeta}$ an $\overline{\zeta}$ represent the lower and upper bounds of ζ, respectively. For maintaining the consistency of formulations throughout this paper, $(\bullet)^R$ denotes that the parameter $(\bullet)$ is a random variable/vector, $(\bullet)^I$ denotes that the parameter $(\bullet)$ is an interval variable/vector, and $(\bullet)^{RI}$ denotes that the parameter $(\bullet)$ is a variable/vector which includes both random and interval characteristics. Thus, the non-deterministic linear static response analysis of a structure with d_s degrees-of-freedom (DOFs) is expressed as:

$$\mathbf{K}_s(\boldsymbol{\psi}, \boldsymbol{\zeta})\mathbf{u}_s^{RI} = \mathbf{F}(\boldsymbol{\psi}, \boldsymbol{\zeta}) \tag{3.1}$$

such that

$$\boldsymbol{\psi} \in \mathbf{\Omega} := \{\boldsymbol{\psi} \in \Re^m \mid \psi_i \sim f_{\psi_i}(x), \text{ for } i = 1,...,m\} \tag{3.2}$$

$$\boldsymbol{\zeta} \in \tilde{\mathbf{\Omega}} := \{\boldsymbol{\zeta} \in \Re^{m^I} \mid \underline{\zeta_j} \le \zeta_j \le \overline{\zeta_j}, \text{ for } j = 1,...,m^I\} \tag{3.3}$$

where $\mathbf{K}_s(\boldsymbol{\psi}, \boldsymbol{\zeta}) \in \Re^{d_s \times d_s}$ denotes the non-deterministic stiffness matrix of the structure; $\mathbf{u}_s^{RI} \in \Re^{d_s}$ is the vector that contains the non-deterministic displacements at all DOFs; and $\mathbf{F}(\boldsymbol{\psi}, \boldsymbol{\zeta}) \in \Re^{d_s}$ denotes the non-deterministic externally applied forces; $\boldsymbol{\psi}$ denotes the random vector which collects all the m probabilistic uncertain system parameters; $f_{\psi_j}(x)$ denotes the probability density function of the random variable ψ_j; $\boldsymbol{\zeta}$ denotes the interval vector which contains all the m^I interval variables presented in the system;

$\underline{\zeta_j}$ and $\overline{\zeta_j}$ denote the lower and upper bounds of ζ_j, respectively. It is worth to notice that due to the presence of hybrid uncertainties, the stiffness matrix and force vector are functions of both random and interval variables.

The consideration of hybrid stochastic and non-stochastic uncertainties within the structural system dramatically increases the complexity of the static analysis problem. Due to the simultaneous existence of both random and interval variables, the behaviour of structural responses including nodal displacement and elemental force could have both probabilistic and interval characteristics. Moreover, for complex structural systems, the relation between each input variable and the structural output (i.e. nodal displacement and elemental force) cannot be analytically determined such that the exact prediction on the mercurial characteristics of structural behaviour is prohibited. Being conceptually different with the theories of imprecise probabilities [154], the random and interval uncertainties considered in this study are mutually independent rather than inclusive.

3.2.2 Hybrid uncertainty analysis by using moment method

By implementing the concept of the random moment method [7, 123] combined with the probabilistic theory, the means and standard deviations of the structural responses can be explicitly reformulated. Without loss of generality, multiple random and interval variables are respectively represented by random vector $\boldsymbol{\psi} \in \Re^m$ and interval vector $\boldsymbol{\zeta} \in \Re^{m^I}$. Within the framework of finite element method, the structural stiffness matrix $\mathbf{K}_s(\boldsymbol{\psi}, \boldsymbol{\zeta})$ and the applied load vector $\mathbf{F}(\boldsymbol{\psi}^R, \boldsymbol{\xi}^I)$, which are the functions of random and interval parameters, can be expanded by implementing the random moment method as:

$$\mathbf{K}_s(\boldsymbol{\psi},\boldsymbol{\zeta}) = \mathbf{K}_s(\boldsymbol{\mu}_\psi,\boldsymbol{\zeta}) + \sum_{i=1}^{m}\left[\left.\frac{\partial \mathbf{K}_s(\boldsymbol{\psi},\boldsymbol{\zeta})}{\partial \psi_i}\right|_{\boldsymbol{\psi}=\boldsymbol{\mu}_\psi}\right]\{\psi_i - \mu_{\psi_i}\} + \frac{1}{2}\sum_{i=1}^{m}\sum_{k=1}^{m}\left[\left.\frac{\partial^2 \mathbf{K}_s(\boldsymbol{\psi},\boldsymbol{\zeta})}{\partial \psi_i \partial \psi_k}\right|_{\boldsymbol{\psi}=\boldsymbol{\mu}_\psi}\right]\{\psi_i - \mu_{\psi_i}\}\{\psi_k - \mu_{\psi_k}\} + \mathbf{Re}_{(\mathbf{K}_s)} \tag{3.4}$$

$$\mathbf{F}(\boldsymbol{\psi},\boldsymbol{\zeta}) = \mathbf{F}(\boldsymbol{\mu}_\psi,\boldsymbol{\zeta}) + \sum_{i=1}^{m}\left[\left.\frac{\partial \mathbf{F}(\boldsymbol{\psi}^R,\boldsymbol{\zeta})}{\partial \psi_i}\right|_{\boldsymbol{\psi}=\boldsymbol{\mu}_\psi}\right]\{\psi_i - \mu_{\psi_i}\} + \frac{1}{2}\sum_{i=1}^{m}\sum_{k=1}^{m}\left[\left.\frac{\partial^2 \mathbf{F}(\boldsymbol{\psi},\boldsymbol{\zeta})}{\partial \psi_i \partial \psi_k}\right|_{\boldsymbol{\psi}=\boldsymbol{\mu}_\psi}\right]\{\psi_i - \mu_{\psi_i}\}\{\psi_k - \mu_{\psi_k}\} + \mathbf{Re}_{(\mathbf{F})} \tag{3.5}$$

where $\boldsymbol{\mu}_\psi = [\mu_{\psi_1},...,\mu_{\psi_i},...,\mu_{\psi_m}]$ is the vector collects the means of all random variables; μ_{ψ_i} denotes the mean of the *i*th random variable ψ_i ; $\mathbf{Re}_{(\bullet)}$ is the high-order terms of the Taylor expansion for the uncertain parameter $(\bullet)$.

From the theory of first-order matrix perturbation, the governing equation for linear static analysis of the structure involving various uncertain parameters can be formulated as:

$$[\mathbf{K}_0 + \Delta_1\mathbf{K}_s][\mathbf{u}_0 + \Delta_1\mathbf{u}] = \mathbf{F}_0 + \Delta_1\mathbf{F} \tag{3.6}$$

where

$$\mathbf{K}_0 = \mathbf{K}_s(\boldsymbol{\mu}_\psi,\boldsymbol{\zeta}) \tag{3.7}$$

$$\Delta_1\mathbf{K}_s = \sum_{i=1}^{m}\left[\left.\frac{\partial^2 \mathbf{K}_s(\boldsymbol{\psi},\boldsymbol{\zeta})}{\partial \psi_i}\right|_{\boldsymbol{\psi}=\boldsymbol{\mu}_\psi}\right]\{\psi_i - \mu_{\psi_i}\} = \sum_{i=1}^{m}\mathbf{K}_i\{\psi_i - \mu_{\psi_i}\} \tag{3.8}$$

$$\mathbf{F}_0 = \mathbf{F}(\boldsymbol{\mu}_\psi,\boldsymbol{\zeta}) \tag{3.9}$$

$$\Delta_1\mathbf{F} = \sum_{i=1}^{m}\left[\left.\frac{\partial^2\mathbf{F}(\boldsymbol{\psi},\boldsymbol{\zeta})}{\partial\psi_i}\right|_{\boldsymbol{\psi}=\boldsymbol{\mu}_\psi}\right]\{\psi_i - \mu_{\psi_i}\} = \sum_{i=1}^{m}\mathbf{F}_i\{\psi_i - \mu_{\psi_i}\} \tag{3.10}$$

By neglecting the high-order terms, the random interval structural displacement based on the first-order perturbation is calculated as:

$$\begin{aligned}
\mathbf{u}^{RI} &= \mathbf{u}_0 + \Delta_1\mathbf{u} \\
&= \mathbf{K}_0^{-1}\mathbf{F}_0 + \mathbf{K}_0^{-1}\left\{\sum_{i=1}^{m}\left[\left.\frac{\partial\mathbf{F}(\boldsymbol{\psi},\boldsymbol{\zeta})}{\partial\psi_i}\right|_{\boldsymbol{\psi}=\boldsymbol{\mu}_\psi}\right]\{\psi_i - \mu_{\psi_i}\}\right. \\
&\quad \left. - \left[\sum_{i=1}^{m}\left[\left.\frac{\partial\mathbf{K}_s(\boldsymbol{\psi},\boldsymbol{\zeta})}{\partial\psi_i}\right|_{\boldsymbol{\psi}=\boldsymbol{\mu}_\psi}\right]\{\psi_i - \mu_{\psi_i}\}\right]\mathbf{K}_0^{-1}\mathbf{F}_0\right\} \\
&= \mathbf{K}_0^{-1}\mathbf{F}_0 \\
&\quad + \sum_{i=1}^{m}\left\{\mathbf{K}_0^{-1}\left[\left.\frac{\partial\mathbf{F}(\boldsymbol{\psi},\boldsymbol{\zeta})}{\partial\psi_i}\right|_{\boldsymbol{\psi}=\boldsymbol{\mu}_\psi}\right] - \mathbf{K}_0^{-1}\left[\left.\frac{\partial\mathbf{K}_s(\boldsymbol{\psi},\boldsymbol{\zeta})}{\partial\psi_i}\right|_{\boldsymbol{\psi}=\boldsymbol{\mu}_\psi}\right]\mathbf{K}_0^{-1}\mathbf{F}_0\right\}\{\psi_i - \mu_{\psi_i}\} \\
&= \mathbf{K}_0^{-1}\mathbf{F}_0 + \sum_{i=1}^{m}\left[\mathbf{K}_0^{-1}\mathbf{F}_i - \mathbf{K}_0^{-1}\mathbf{K}_i\mathbf{K}_0^{-1}\mathbf{F}_0\right]\{\psi_i - \mu_{\psi_i}\}
\end{aligned} \tag{3.11}$$

Subsequently, the mean and standard deviation of the random interval structural displacement responses $\mathbf{u}^{RI}$ based on the first-order matrix perturbation [123] can be obtained by taking the mean and variance operation on Eq. (3.11), which leads to:

$$\boldsymbol{\mu}_{\mathbf{u}^{RI}} = \mathbf{K}_0^{-1}\mathbf{F}_0 \tag{3.12}$$

$$\begin{aligned}
\boldsymbol{\sigma}_{\mathbf{u}^{RI}} \circ \boldsymbol{\sigma}_{\mathbf{u}^{RI}} &= \sum_{i=1}^{m}\sum_{k=1}^{m}\left[\mathbf{K}_0^{-1}\mathbf{F}_i - \mathbf{K}_0^{-1}\mathbf{K}_i\mathbf{K}_0^{-1}\mathbf{F}_0\right] \\
&\quad \circ \left[\mathbf{K}_0^{-1}\mathbf{F}_k - \mathbf{K}_0^{-1}\mathbf{K}_k\mathbf{K}_0^{-1}\mathbf{F}_0\right]\mathrm{cov}(\psi_i, \psi_k)
\end{aligned} \tag{3.13}$$

where $\boldsymbol{\mu}_{\mathbf{u}^{RI}} \in \Re^{d_s}$ and $\boldsymbol{\sigma}_{\mathbf{u}^{RI}} \in \Re^{d_s}$ denote the vectors which collect the mean and standard deviation of the displacement responses at all d_s degrees-of-freedom, respectively; $\mathrm{cov}(\psi_i, \psi_k)$ denotes the covariance between the *i*th and *k*th random variables ψ_i and ψ_k;

the operator "$\circ$" denotes the Hadamard product of two matrices with equal dimension [155]. As indicated by Eqs. (3.12) and (3.13), the hybrid random interval problem has been transferred into two explicit interval analyses such that the statistical characteristics of the structural displacements are uncertain-but-bounded which can be further expressed as:

$$\boldsymbol{\mu}_{\mathbf{u}^{RI}} \in \tilde{\boldsymbol{\Omega}} := \{\boldsymbol{\mu}_{\mathbf{u}^{RI}} \in \Re^{d_s} \mid \underline{\mu_{u_v^{RI}}} \le \mu_{u_v^{RI}} \le \overline{\mu_{u_v^{RI}}}, \ \text{for } v = 1,...,d_s\} \tag{3.14}$$

$$\boldsymbol{\sigma}_{\mathbf{u}^{RI}} \in \tilde{\boldsymbol{\Omega}} := \{\boldsymbol{\sigma}_{\mathbf{u}^{RI}} \in \Re^{d_s} \mid \underline{\sigma_{u_v^{RI}}} \le \sigma_{u_v^{RI}} \le \overline{\sigma_{u_v^{RI}}}, \ \text{for } v = 1,...,d_s\} \tag{3.15}$$

where $\mu_{u_v^{RI}}$ and $\sigma_{u_v^{RI}}$ denote the mean and standard deviation of the structural displacement (u_v^{RI}) at vth degree-of-freedom, respectively; $\overline{\mu_{u_v^{RI}}}$ and $\underline{\mu_{u_v^{RI}}}$ denote the upper and lower bounds of $\mu_{u_v^{RI}}$, respectively; $\overline{\sigma_{u_v^{RI}}}$ and $\underline{\sigma_{u_v^{RI}}}$ denote the upper and lower bounds of $\sigma_{u_v^{RI}}$, respectively.

In addition, the elemental force denoted by $\mathbf{f}^{RI} \in \Re^{w}$, can be explicitly formulated as:

$$\mathbf{f}^{RI} = \mathbf{D}(\boldsymbol{\psi},\boldsymbol{\zeta})\mathbf{u}^{RI} = \mathbf{D}(\boldsymbol{\psi},\boldsymbol{\zeta})\mathbf{K}(\boldsymbol{\psi},\boldsymbol{\zeta})^{-1}\mathbf{F}(\boldsymbol{\psi},\boldsymbol{\zeta}) \tag{3.16}$$

where $\mathbf{D}(\boldsymbol{\psi},\boldsymbol{\zeta}) \in \Re^{w\times d_s}$ can be defined as:

$$\begin{aligned}\mathbf{D}(\boldsymbol{\psi},\boldsymbol{\zeta}) &= \mathbf{D}(\boldsymbol{\mu}_{\boldsymbol{\psi}},\boldsymbol{\zeta}) + \sum_{i=1}^{m}\left[\left.\frac{\partial \mathbf{D}(\boldsymbol{\psi},\boldsymbol{\zeta})}{\partial \psi_i}\right|_{\boldsymbol{\psi}=\boldsymbol{\mu}_{\boldsymbol{\psi}}}\right]\{\psi_i - \mu_{\psi_i}\} \\ &\quad + \frac{1}{2}\sum_{i=1}^{m}\sum_{k=1}^{m}\left[\left.\frac{\partial^2 \mathbf{D}(\boldsymbol{\psi},\boldsymbol{\zeta})}{\partial \psi_i \partial \psi_k}\right|_{\boldsymbol{\psi}=\boldsymbol{\mu}_{\boldsymbol{\psi}}}\right]\{\psi_i - \mu_{\psi_i^i}\}\{\psi_k - \mu_{\psi_k}\} + \mathbf{Re}_{(\mathbf{D})} \\ &= \mathbf{D}_0 + \sum_{i=1}^{m}\mathbf{D}_i\{\psi_i - \mu_{\psi_i}\} + \frac{1}{2}\sum_{i=1}^{m}\sum_{k=1}^{m}\mathbf{D}_{i,k}\{\psi_i - \mu_{\psi_i}\}\{\psi_k - \mu_{\psi_k}\} + \mathbf{Re}_{(\mathbf{D})}\end{aligned} \tag{3.17}$$

Once again, by implementing the random moment method combined with the theory of matrix perturbation, the mean and standard deviation of elemental force can be explicitly formulated as:

$$\boldsymbol{\mu}_{\mathbf{f}^{RI}} = \mathbf{D}_0\mathbf{K}_0^{-1}\mathbf{F}_0 \tag{3.18}$$

$$\begin{aligned}\boldsymbol{\sigma}_{\mathbf{f}^{RI}} \circ \boldsymbol{\sigma}_{\mathbf{f}^{RI}} = &\sum_{i=1}^{m}\sum_{k=1}^{m}\{\mathbf{D}_0[\mathbf{K}_0^{-1}\mathbf{F}_i - \mathbf{K}_0^{-1}\mathbf{K}_i\mathbf{K}_0^{-1}\mathbf{F}_0] + \mathbf{D}_i\mathbf{K}_0^{-1}\mathbf{F}_0\} \\ &\circ\{\mathbf{D}_0[\mathbf{K}_0^{-1}\mathbf{F}_k - \mathbf{K}_0^{-1}\mathbf{K}_k\mathbf{K}_0^{-1}\mathbf{F}_0] + \mathbf{D}_k\mathbf{K}_0^{-1}\mathbf{F}_0\}\operatorname{cov}(\psi_i, \psi_k)\end{aligned} \tag{3.19}$$

where $\boldsymbol{\mu}_{\mathbf{f}^{RI}} \in \Re^w$,and $\boldsymbol{\sigma}_{\mathbf{f}^{RI}} \in \Re^w$ denote the vectors which collect the mean and standard deviation of the elemental force, respectively. Subsequently considering the effects of interval uncertainties, the mean and standard deviation of the elemental force become uncertain-but-bounded which can be further expressed as:

$$\boldsymbol{\mu}_{\mathbf{f}^{RI}} \in \tilde{\boldsymbol{\Omega}} := \{\boldsymbol{\mu}_{\mathbf{f}^{RI}} \in \Re^w \mid \underline{\mu_{f_z^{RI}}} \le \mu_{f_z^{RI}} \le \overline{\mu_{f_z^{RI}}},\ \text{for z} = 1,...,w\} \tag{3.20}$$

$$\boldsymbol{\sigma}_{\mathbf{f}^{RI}} \in \tilde{\boldsymbol{\Omega}} := \{\boldsymbol{\sigma}_{\mathbf{f}^{RI}} \in \Re^w \mid \underline{\sigma_{f_z^{RI}}} \le \sigma_{f_z^{RI}} \le \overline{\sigma_{f_z^{RI}}},\ \text{for z} = 1,...,w\} \tag{3.21}$$

where $\mu_{f_z^{RI}}$ and $\sigma_{f_z^{RI}}$ denotes the mean and standard deviation of f_z^{RI} which is the *z*th component of the elemental force vector, respectively; $\overline{\mu_{f_z^{RI}}}$ and $\underline{\mu_{f_z^{RI}}}$ denote the upper and lower bounds of $\mu_{f_z^{RI}}$, respectively; $\overline{\sigma_{f_z^{RI}}}$ and $\underline{\sigma_{f_z^{RI}}}$ denote the upper and lower bounds of $\sigma_{f_z^{RI}}$, respectively; w denotes the total number of elemental force in the structural system.

Eqs. (3.14) - (3.15) and (3.20) - (3.21) indicate that the implementation of the random moment method meticulously transforms the hybrid random interval static analysis of linear structures into a series of interval problems, which provide an efficient

yet systematic scheme for solving uncertainty analysis of structures with a mixture of random and interval variables. The explicit reformulations on the mean and standard deviation of the nodal displacement and elemental force offer preliminary information for analysing the uncertain structural behaviour under static loads. However, the calculation of the uncertain-but-bounded statistical characterises remains a computational challenge which is dominated by the aforementioned interval dependency issue. In this context, the interval arithmetic-based approaches could lead to overestimation of the bounded stochastic characteristic while sampling method would be computational expensive for complex hybrid uncertainty analysis. Therefore, it is necessary to develop a more computational tractable approach such that the bounded means and standard deviations of the structural responses can be efficiently calculated without the interference of the issue of interval dependency.

3.3 The unified perturbation mathematical programming (UPMP) approach

In this section, a new computational approach, namely the *unified perturbation mathematical programming* (UPMP) approach, is proposed to investigate the hybrid uncertain static response analysis with random and interval parameters. The UPMP approach offers a non-sampling computational strategy which can efficiently determine the mean and standard deviations of the structural responses. Furthermore, by adopting the alternative finite element (FE) formulation, the upper and lower bounds of the means and standard deviations of the structural responses can be explicitly formulated into standard nonlinear programming problems (NLPs). Consequently, the extreme bounds of all statistical characteristics (i.e. means and standard deviations) of either nodal displacements or elemental forces can be efficiently obtained by solving eight standard NLPs.

3.3.1 Alternative finite element formulation

As previously emphasized, the issue of interval dependency is always present in assembling global stiffness matrix with interval variables through the interval arithmetic approach. Even though the interval stiffness matrix can be easily assembled, it is highly likely that the final computational results are over-estimated due to the inappropriate manipulation of interval algebra. In the light of eliminating the interference on the system outputs caused by the interval dependency, an alternative FE formulation [108, 109] is implemented in interval analysis of engineering structures. Within the studies reported in [108, 109], the structural response analysis and linear bifurcation buckling analysis with interval uncertain parameters are transformed into mathematical programming problems. Subsequently, the interval analyses are processed directly via NLP solver by modelling the interval parameters as inequality constraints of the NLPs while the originality of the FE governing equations is thoroughly maintained. In this context, the interval arithmetic and the associated dependency issue are completely eliminated from the analysis such that the sharpness of results is improved. Therefore, such FE reformulation is meticulously adopted in this hybrid uncertainty analysis and briefly demonstrated in this subsection.

By implementing this alternative FE modelling, the governing equations of linear elastic analysis of a structure which consist n_s elements, d_s degrees of freedom and w generalized stress/strain, are composed by the equilibrium condition, the compatibility condition and the elastic constitutive condition. The three governing equations can be explicitly expressed as:

$$\mathbf{C}^T \mathbf{q}_s = \mathbf{F} \tag{3.22}$$

$$\mathbf{C}\mathbf{u}_s = \mathbf{e} \tag{3.23}$$

$$\mathbf{S}\mathbf{e} = \mathbf{q}_s \tag{3.24}$$

where $\mathbf{q}_s \in \Re^w$ denotes the generalized stress vector of the structure; $\mathbf{e} \in \Re^w$ denotes the generalized strain vector corresponding to $\mathbf{q}_s$; $\mathbf{C} \in \Re^{w \times d_s}$ denotes the compatibility matrix which physically correlates the global displacement with generalised strain, and its transpose is the equilibrium matrix which maintains the balance between the externally applied force $\mathbf{F} \in \Re^{d_s}$ and the generalised stresses $\mathbf{q}_s$; $\mathbf{S} \in \Re^{\mathrm{w} \times \mathrm{w}}$ is a block diagonal matrix which collects all elemental stiffness. Readers who are interested in the detailed alternative FE formulations of the 2D truss and frame structures can refer to [108].

When the hybrid random and interval uncertainties of system parameters are considered, the non-deterministic analysis expressed in Eq. (3.1) can be reformulated into:

$$\mathbf{C}^T \mathbf{q}_s^{RI} = \mathbf{F}(\boldsymbol{\psi}, \boldsymbol{\zeta}) \tag{3.25}$$

$$\mathbf{C}\mathbf{u}_s^{RI} = \mathbf{e}^{RI} \tag{3.26}$$

$$\mathbf{S}(\boldsymbol{\psi}, \boldsymbol{\zeta})\mathbf{e}^{RI} = \mathbf{q}_s^{RI} \tag{3.27}$$

where $\mathbf{q}_s^{RI}, \mathbf{e}^{RI} \in \Re^w$ denote the non-deterministic generalized stress and strain vectors respectively. By substituting Eqs. (3.26) and (3.27) into Eq. (3.25), the resultant equation becomes:

$$\mathbf{C}^T \mathbf{q}_s^{RI} = \mathbf{C}^T \mathbf{S}(\boldsymbol{\psi}, \boldsymbol{\zeta})\mathbf{e}^{RI} = \mathbf{C}^T \mathbf{S}(\boldsymbol{\psi}, \boldsymbol{\zeta})\mathbf{C}\mathbf{u}_s^{RI} = \mathbf{K}_s(\boldsymbol{\psi}, \boldsymbol{\zeta})\mathbf{u}_s^{RI} = \mathbf{F}(\boldsymbol{\psi}, \boldsymbol{\zeta}) \tag{3.28}$$

It is easily recognized that Eq. (3.28) is exactly same as Eq. (3.1) with:

$$\mathbf{K}_s(\boldsymbol{\psi}, \boldsymbol{\zeta}) = \mathbf{C}^T \mathbf{S}(\boldsymbol{\psi}, \boldsymbol{\zeta})\mathbf{C} \tag{3.29}$$

Additionally, the elemental force of the structure can be obtained from the generalized stress vector as:

$$\mathbf{q}_s^{RI} = \mathbf{S}(\boldsymbol{\psi},\boldsymbol{\zeta})\mathbf{e}^{RI} = \mathbf{S}(\boldsymbol{\psi},\boldsymbol{\zeta})\mathbf{C}\mathbf{u}_s^{RI} \tag{3.30}$$

Eqs. (3.25) - (3.27) are the general governing equations for linear elastic analyses of structures involving hybrid random and interval uncertainties, which should be satisfied regardless of element types.

3.3.2 Upper and lower bounds of mean of nodal displacement

By implementing the alternative FE formulation as illustrated in Eqs. (3.28) and (3.29), the mean of nodal displacement as expressed in Eq. (3.14) can be reformulated as:

$$\mathbf{C}^T\mathbf{S}(\boldsymbol{\mu}_{\boldsymbol{\psi}},\boldsymbol{\zeta})\mathbf{C}\boldsymbol{\mu}_{\mathbf{u}_s^{RI}} = \mathbf{F}_0 \tag{3.31}$$

Thus, the formulation of mean of nodal displacement can be alternative expressed by the format introduced in Eqs. (3.25) - (3.27). Mathematically, all the interval uncertain parameters can be treated as inequality constraints, and the equilibrium condition, the compatibility condition and the elastic constitutive condition are considered as equality constraints. Subsequently, the upper bound of the mean of the displacement response at vth ($v = 1,...,d_s$) degree-of-freedom can be obtained by solving the following NLP:

(P_1):

$$\overline{\mu_{u_v^{RI}}} = \text{maximise}\{\mu_{u_v^{RI}}\} \tag{3.32a}$$

subject to:

$$\mathbf{C}^T\mathbf{q}_s = \mathbf{F}_0 \tag{3.32b}$$

$$\mathbf{C}\boldsymbol{\mu}_{\mathbf{u}_s^{RI}} = \mathbf{e} \tag{3.32c}$$

$$\mathbf{S}(\boldsymbol{\mu}_{\psi}, \boldsymbol{\zeta})\mathbf{e} = \mathbf{q}_s \tag{3.32d}$$

$$\boldsymbol{\zeta} \in \tilde{\boldsymbol{\Omega}} := \{\boldsymbol{\zeta} \in \Re^{\mathrm{m}^I} \mid \underline{\zeta_j} \le \zeta_j \le \overline{\zeta_j}, \ \text{ for } j = 1,...,\mathrm{m}^I\} \tag{3.32e}$$

Similarly, the lower bound of the mean of the displacement response at *v*th ($v = 1,...,d_s$) degree-of-freedom is calculated by solving the following problem:

(P_2):

$$\underline{\mu_{\mathrm{u}_v^{\mathrm{RI}}}} = \text{minimise}\{\mu_{u_v^{RI}}\} \tag{3.33a}$$

subject to:

$$\text{Eqs.}\,(3.32\,\text{b})\text{-}(3.32\,\text{e}) \tag{3.33b}$$

Eqs. (3.32) and (3.33) indicate that by introducing the alternative finite element model into the matrix perturbation, the upper and lower bounds of the mean of the nodal displacement can be determined without the implementation of interval arithmetic. Consequently, the extremities of the mean of the structural displacement at any degree of freedom can be rigorously established by completely eliminating the effects of interval dependency.

3.3.3 Upper and lower bounds of standard deviation of nodal displacement

Similarly, by adopting the alternative FE model introduced in Section 3.3.1, the bounds of standard deviation of the nodal displacement at the *v*th degree-of-freedom can be also calculated by solving two standard NPLs. To further simplify Eq. (3.13), additional auxiliary variables $\mathbf{A}_i \in \Re^{d_s}$, $\mathbf{B}_i \in \Re^{d_s}$, $\hat{\mathbf{m}} \in \Re^{d_s}$ and $\mathbf{n}_i \in \Re^{d_s}$ for $i = 1, 2, ..., m$, are introduced, thus the variance of displacement can be expressed as:

$$\boldsymbol{\sigma}_{\mathbf{u}^{RI}} \circ \boldsymbol{\sigma}_{\mathbf{u}^{RI}} = \sum_{i=1}^{m}\sum_{k=1}^{m}[\mathbf{A}_i - \mathbf{B}_i] \circ [\mathbf{A}_k - \mathbf{B}_k]\mathrm{cov}(\psi_i, \psi_k) \tag{3.34}$$

where

$$\mathbf{A}_i = \mathbf{K}_0^{-1}\mathbf{F}_i \tag{3.35}$$

$$\mathbf{B}_i = \mathbf{K}_0^{-1}\mathbf{K}_i\mathbf{K}_0^{-1}\mathbf{F}_0 = \mathbf{K}_0^{-1}\mathbf{K}_i\hat{\mathbf{m}} = \mathbf{K}_0^{-1}\mathbf{n}_i \tag{3.36}$$

such that

$$\hat{\mathbf{m}} = \mathbf{K}_0^{-1}\mathbf{F}_0 \tag{3.37}$$

$$\mathbf{n}_i = \mathbf{K}_i\hat{\mathbf{m}} \tag{3.38}$$

The introduction of these auxiliary variables enables the adoption of the alternative FE model to reformulate the standard deviation of nodal displacement. Thus, by implementing the concept expressed in Eqs. (3.28) and (3.29), Eqs. (3.35) - (3.38) can be explicitly reformulated. Subsequently, the determinations of the extreme bounds of standard deviation of nodal displacement could be achieved through solving two explicit NLPs. By treating interval uncertainties as bounded variables, the upper bound of the standard deviation of displacement response at the *v*th degree-of-freedom is calculated by solving the NLP defined by Eq. (3.39). Due to the non-negative property of standard deviation, $(\overline{\sigma_{u_v^{RI}}})^2 = \overline{\sigma^2_{u_v^{RI}}}$ and $(\underline{\sigma_{u_v^{RI}}})^2 = \underline{\sigma^2_{u_v^{RI}}}$ such that the validity of the proposed UPMP approach for obtaining the bounds of standard deviation through the calculation on the bounds of variance is ensured. Consequently, the upper bound of the variance of the *v*th structural displacement can be explicitly formulated as the NLP problem (P_3):

(P_3):

$$\overline{\sigma_{u_v^{RI}}}^2 = \text{maximise}\{\sigma^2_{u_v^{RI}}\} \tag{3.39a}$$

subject to:

$$\boldsymbol{\sigma}_{\mathbf{u}^{RI}} \circ \boldsymbol{\sigma}_{\mathbf{u}^{RI}} = \sum_{i=1}^{m}\sum_{k=1}^{m}[\mathbf{A}_i - \mathbf{B}_i]\circ[\mathbf{A}_k - \mathbf{B}_k]\text{cov}(\psi_i, \psi_k) \tag{3.39b}$$

$$\mathbf{C}^T\mathbf{q}_{\mathbf{A}_i} = \mathbf{F}_i\ ,\ i = 1,...,m \tag{3.39c}$$

$$\mathbf{C}\mathbf{A}_i = \mathbf{e}_{\mathbf{A}_i}\ ,\ i = 1,...,m \tag{3.39d}$$

$$\mathbf{S}(\boldsymbol{\mu}_{\boldsymbol{\psi}}, \boldsymbol{\zeta})\mathbf{e}_{\mathbf{A}_i} = \mathbf{q}_{\mathbf{A}_i}\ ,\ i = 1,...,m \tag{3.39e}$$

$$\mathbf{C}^T\mathbf{q}_{\mathbf{B}_i} = \mathbf{n}_i\ ,\ i = 1,...,m \tag{3.39f}$$

$$\mathbf{C}\mathbf{B}_i = \mathbf{e}_{\mathbf{B}_i}\ ,\ i = 1,...,m \tag{3.39g}$$

$$\mathbf{S}(\boldsymbol{\mu}_{\boldsymbol{\psi}}, \boldsymbol{\zeta})\mathbf{e}_{\mathbf{B}_i} = \mathbf{q}_{\mathbf{B}_i}\ ,\ i = 1,...,m \tag{3.39h}$$

$$\mathbf{C}^T\mathbf{q}_{\hat{\mathbf{m}}} = \mathbf{F}_0 \tag{3.39i}$$

$$\mathbf{C}\hat{\mathbf{m}} = \mathbf{e}_{\hat{\mathbf{m}}} \tag{3.30j}$$

$$\mathbf{S}(\boldsymbol{\mu}_{\boldsymbol{\psi}}, \boldsymbol{\zeta})\mathbf{e}_{\hat{\mathbf{m}}} = \mathbf{q}_{\hat{\mathbf{m}}} \tag{3.39k}$$

$$\mathbf{C}^T\mathbf{q}_{\mathbf{n}_i} = \mathbf{n}_i\ ,\ i = 1,...,m \tag{3.39l}$$

$$\left[\left.\frac{\partial \mathbf{S}(\boldsymbol{\psi}, \boldsymbol{\zeta})}{\partial \psi_i}\right|_{\boldsymbol{\psi}=\boldsymbol{\mu}_{\boldsymbol{\psi}}}\right]\mathbf{e}_{\hat{\mathbf{m}}} = \mathbf{q}_{\mathbf{n}_i}\ ,\ i = 1,...,m \tag{3.39m}$$

$$\boldsymbol{\zeta} \in \tilde{\boldsymbol{\Omega}} := \{\boldsymbol{\zeta} \in \Re^p \mid \underline{\zeta_j} \le \zeta_j \le \overline{\zeta_j},\ \text{ for } j = 1,...,\mathrm{m}^I\} \tag{3.39n}$$

Furthermore, the lower bound of the variance of displacement response at the *v*th ($v = 1,...,d_s$) degree-of-freedom is calculated by solving the following NLP:

(P_4):

$$\underline{\sigma_{u_v^{RI}}}^2 = \text{minimise}\{\sigma_{u_v^{RI}}^2\} \tag{3.40a}$$

subject to:

$$\text{Eqs.}\,(3.39\,\text{b})\text{-}(3.39n) \tag{3.40b}$$

The details of the reformulation of Eqs. (3.35) - (3.38) are illustrated by the following proof, which provides a reference for the construction of the two NLP problems indicated by Eqs. (3.39) and (3.40).

Proof.

By implementing the alternative FE formulation presented in Section 3.3.1, the reformulation of Eq. (3.35) is demonstrated as:

$$\mathbf{A}_i = \mathbf{K}_0^{-1}\mathbf{F}_i \Rightarrow \mathbf{C}^T\mathbf{S}(\boldsymbol{\mu}_\psi,\boldsymbol{\zeta})\mathbf{C}\mathbf{A}_i = \mathbf{F}_i \Rightarrow \begin{cases} \mathbf{C}^T\mathbf{q}_{\mathbf{A}_i} = \mathbf{F}_i \\ \mathbf{C}\mathbf{A}_i = \mathbf{e}_{\mathbf{A}_i} \\ \mathbf{S}(\boldsymbol{\mu}_\psi,\boldsymbol{\zeta})\mathbf{e}_{\mathbf{A}_i} = \mathbf{q}_{\mathbf{A}_i} \end{cases} \tag{3.41}$$

where $\mathbf{q}_{\mathbf{A}_i} \in \Re^w$ and $\mathbf{e}_{\mathbf{A}_i} \in \Re^w$ denote the two pseudo-vectors corresponding to $\mathbf{A}_i$. The two pseudo-vectors are introduced here for numerical decomposition purpose.

By adopting the same concept, Eq. (3.36) can be decomposed as:

$$\mathbf{B}_i = \mathbf{K}_0^{-1}\mathbf{n}_i \Rightarrow \mathbf{C}^T\mathbf{S}(\boldsymbol{\mu}_\psi,\boldsymbol{\zeta})\mathbf{C}\mathbf{B}_i = \mathbf{n}_i \Rightarrow \begin{cases} \mathbf{C}^T\mathbf{q}_{\mathbf{B}_i} = \mathbf{n}_i \\ \mathbf{C}\mathbf{B}_i = \mathbf{e}_{\mathbf{B}_i} \\ \mathbf{S}(\boldsymbol{\mu}_\psi,\boldsymbol{\zeta})\mathbf{e}_{\mathbf{B}_i} = \mathbf{q}_{\mathbf{B}_i} \end{cases} \tag{3.42}$$

where $\mathbf{q}_{\mathbf{B}_i} \in \Re^w$ and $\mathbf{e}_{\mathbf{B}_i} \in \Re^w$ denotes the two pseudo-vectors corresponding to $\mathbf{B}_i$.

Similarly, Eq. (3.37) is reformulated as Eq. (3.43) by adding two pseudo-vectors $\mathbf{q}_{\hat{\mathbf{m}}} \in \Re^w$ and $\mathbf{e}_{\hat{\mathbf{m}}} \in \Re^w$. That is,

$$\hat{\mathbf{m}} = \mathbf{K}_0^{-1}\mathbf{F}_0 \Rightarrow \mathbf{C}^T\mathbf{S}(\boldsymbol{\mu}_\psi, \boldsymbol{\zeta})\mathbf{C}\hat{\mathbf{m}} = \mathbf{F}_0 \Rightarrow \begin{cases} \mathbf{C}^T\mathbf{q}_{\hat{\mathbf{m}}} = \mathbf{F}_0 \\ \mathbf{C}\hat{\mathbf{m}} = \mathbf{e}_{\hat{\mathbf{m}}} \\ \mathbf{S}(\boldsymbol{\mu}_\psi, \boldsymbol{\zeta})\mathbf{e}_{\hat{\mathbf{m}}} = \mathbf{q}_{\hat{\mathbf{m}}} \end{cases} \tag{3.43}$$

Then, Eq. (4.38) could be decomposed into Eq. (3.44) by introducing a pseudo-vector $\mathbf{q}_{\mathbf{n}_i} \in \Re^w$, such that:

$$\mathbf{n}_i = \mathbf{K}_i\hat{\mathbf{m}} \Rightarrow \mathbf{C}^T\mathbf{S}_i\mathbf{C}\hat{\mathbf{m}} = \mathbf{n}_i \Rightarrow \begin{cases} \mathbf{C}^T\mathbf{q}_{\mathbf{n}_i} = \mathbf{n}_i \\ \mathbf{C}\hat{\mathbf{m}} = \mathbf{e}_{\hat{\mathbf{m}}} \\ \mathbf{S}_i\mathbf{e}_{\hat{\mathbf{m}}} = \mathbf{q}_{\mathbf{n}_i} \end{cases} \tag{3.44a}$$

where

$$\mathbf{S}_i = \left.\frac{\partial \mathbf{S}(\boldsymbol{\psi}, \boldsymbol{\zeta})}{\partial \psi_i}\right|_{\boldsymbol{\psi}=\boldsymbol{\mu}_\psi} \tag{3.44b}$$

The combination of Eqs. (3.41) - (3.44) constructs the equality constraints listed as Eqs. (3.39c) - (3.39m).

This completes the proof. □

The proposed UPMP approach transformed the computation of bounded standard deviation of nodal displacement into two NLP problems under same constraints, such that the interval arithmetic procedure is eliminated throughout the hybrid random interval analysis. The integration of the alternative FE formulation and mathematical

programming approach advantageously accommodates the dependency of interval uncertain variables.

3.3.4 Upper and lower bounds of mean of elemental force

Within the framework of the proposed UPMP approach, the expression of mean of elemental force (Eq. (3.18)) is reformulated by adopting the alternative FE formulation indicated by Eq. (3.30) as following:

$$\begin{aligned} \boldsymbol{\mu}_{\mathbf{f}^{RI}} &= \mathbf{D}_0 \mathbf{K}_0^{-1} \mathbf{F}_0 \\ &= \mathbf{S}(\boldsymbol{\mu}_{\boldsymbol{\psi}}, \boldsymbol{\zeta}) \mathbf{C} \boldsymbol{\mu}_{\mathbf{u}^{RI}} \\ &= \mathbf{q}_s \end{aligned} \tag{3.45}$$

where $\mathbf{q}_s$ has been defined as in Eqs. (3.32b) - (3.32d) such that

$$\mathbf{D}_0 = \mathbf{S}(\boldsymbol{\mu}_{\boldsymbol{\psi}}, \boldsymbol{\zeta}) \mathbf{C} \tag{3.46}$$

Therefore, the upper bound of mean of the *z*th ($z = 1, \ldots, w$) force response can be obtained by solving the NLP problem (P_5) expressed as Eq. (3.47):

(P_5):

$$\overline{\mu_{f_z^{RI}}} = \text{maximise}\{q_z\} \tag{3.47a}$$

subject to:

$$\text{Eqs. (3.32b)-(3.32e)} \tag{3.47b}$$

and the calculation of the lower bound of mean of the *z*th ($z = 1, \ldots, w$) force response is summarised as the following NLP (P_6):

(P_6):

$$\underline{\mu_{f_z^{RI}}} = \text{minimise}\{q_z\} \tag{3.48a}$$

subject to:

$$\text{Eqs. (3.32b)-(3.32e)} \tag{3.48b}$$

The Eqs. (3.47) and (3.48) indicate that the computation of upper and lower bounds of the mean of elemental force are based on solving two NLP problems with same constraints as in the calculation of bounded mean of nodal displacement which saves the computational effort in the hybrid random interval uncertainty analysis.

3.3.5 Upper and lower bounds of standard deviation of elemental force

The expression of the standard deviation of elemental force for the hybrid uncertainty analysis can be reformulated by utilising the proposed UPMP approach as Eq. (3.49):

$$\begin{aligned}
\boldsymbol{\sigma}_{\mathbf{f}^{RI}} \circ \boldsymbol{\sigma}_{\mathbf{f}^{RI}} &= \sum_{i=1}^{m}\sum_{k=1}^{m}\{\mathbf{D}_0[\mathbf{A}_i - \mathbf{B}_i] + \mathbf{D}_i\mathbf{m}\} \circ \{\mathbf{D}_0[\mathbf{A}_k - \mathbf{B}_k] + \mathbf{D}_k\mathbf{m}\}\operatorname{cov}(\psi_i, \psi_k) \\
&= \sum_{i=1}^{m}\sum_{k=1}^{m}\{\mathbf{S}(\boldsymbol{\mu}_{\boldsymbol{\psi}}, \boldsymbol{\zeta})\mathbf{C}[\mathbf{A}_i - \mathbf{B}_i] + \mathbf{D}_i\mathbf{m}\} \\
&\quad \circ \{\mathbf{S}(\boldsymbol{\mu}_{\boldsymbol{\psi}}, \boldsymbol{\zeta})\mathbf{C}[\mathbf{A}_k - \mathbf{B}_k] + \mathbf{D}_k\mathbf{m}\}\operatorname{cov}(\psi_i, \psi_k) \\
&= \sum_{i}^{m}\sum_{k}^{m}\{\mathbf{q}_{\mathbf{A}_i} - \mathbf{q}_{\mathbf{B}_i} + \mathbf{q}_{\mathbf{n}_i}\} \circ \{\mathbf{q}_{\mathbf{A}_k} - \mathbf{q}_{\mathbf{B}_k} + \mathbf{q}_{\mathbf{n}_k}\}\operatorname{cov}(\psi_i, \psi_k)
\end{aligned} \tag{3.49}$$

where $\mathbf{A}_i \in \Re^{d_s}$, $\mathbf{B}_i \in \Re^{d_s}$, $\hat{\mathbf{m}} \in \Re^{d_s}$ are the auxiliary variables and $\mathbf{q}_{\mathbf{A}_i} \in \Re^{w}$, $\mathbf{q}_{\mathbf{B}_i} \in \Re^{w}$, $\mathbf{q}_{\mathbf{n}_i} \in \Re^{w}$ are the pseudo-vectors introduced in the reformulation for standard deviation of nodal displacement. By adopting the same concept of numerical decomposition for the calculation of the bounds of the standard deviation of nodal displacement, the general computational formulation of UPMP for the calculation of the upper bound of the standard deviation of the *s*th ($z = 1,...,w$) elemental force response can be explicitly formulated into a NLP, such that:

(P_7):

$$\overline{\sigma_{f_z^{RI}}}^2 = \text{maximise}\{\sigma^2_{f_z^{RI}}\} \tag{3.50a}$$

subject to:

$$\boldsymbol{\sigma}_{\mathbf{f}^{RI}} \circ \boldsymbol{\sigma}_{\mathbf{f}^{RI}} = \sum_i^m \sum_k^m \{\mathbf{q}_{\mathbf{A}_i} - \mathbf{q}_{\mathbf{B}_i} + \mathbf{q}_{\mathbf{n}_i}\} \circ \{\mathbf{q}_{\mathbf{A}_k} - \mathbf{q}_{\mathbf{B}_k} + \mathbf{q}_{\mathbf{n}_k}\} \text{cov}(\psi_i, \psi_k) \tag{3.50b}$$

$$\text{Eqs. (3.39c)-(3.39n)} \tag{3.50c}$$

and the calculation of the lower bound of the standard deviation of the *z*th elemental force response can be explicitly expressed as:

(P_8):

$$\underline{\sigma_{f_z^{RI}}}^2 = \text{minimise}\{\sigma^2_{f_z^{RI}}\} \tag{3.51a}$$

subject to:

$$\text{Eqs. (3.50b)} \tag{3.51b}$$

$$\text{Eqs. (3.39c)-(3.39n)} \tag{3.51c}$$

Eqs. (3.50) and (3.51) comprise the general formulations of the proposed UPMP approach for calculating the upper and lower bounds of standard deviation of elemental force of linear structures. The proposed computational scheme rigorously transforms a complicated hybrid random interval analysis of elemental force into four NLP problems (P_5 - P8) which could be solved by any available NLP solver. Additionally, the constraints for the calculation of standard deviation of nodal displacement and elemental force are identical such that only the objective functions of NLP problems are necessarily to be modified.

3.3.6 The implementation of the UPMP approach

The proposed UPMP approach transforms the uncertain structural responses analysis with hybrid random and interval parameters into mathematical programming problems. In this context, the means and standard deviations of random variables become deterministic inputs. Furthermore, by modelling the interval uncertain parameters as inequality constraints, the extreme bounds of the stochastic characteristic of structural responses are directly obtained by respectively solving the NLP problems P_1 - P_8. The solution algorithm of the proposed UPMP methods is summarised by a flowchart shown in Figure. 3.1.

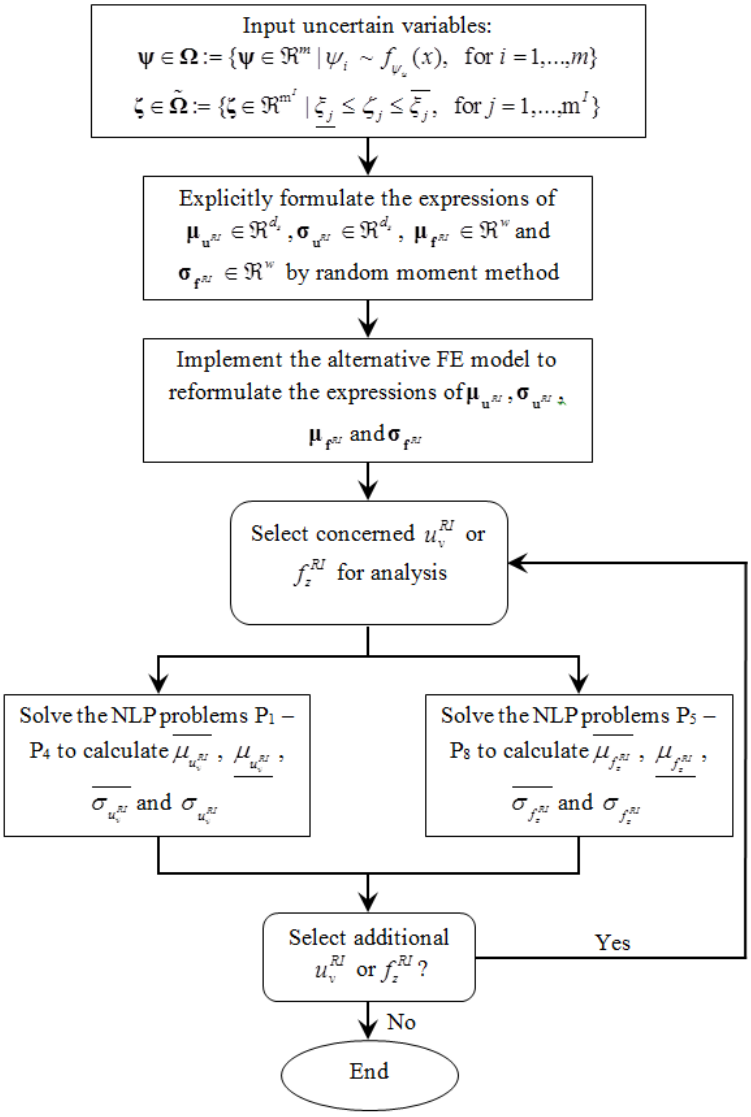

Figure 3.1 Flowchart of the solution algorithm of UPMP approach

As a combination of perturbation method and mathematical programming approach, the proposed UPMP method offers a computational framework which contains the advantages of both approaches. By employing the perturbation-based random moment method with respect to random variables, the explicit expressions of first two moments of structural responses are respectively formulated such that only the means and standard deviations of random variables are enclosed. Thus, the achievement of means and standard deviations of system outputs is no longer rely on generating a large number of samples for random variables. Furthermore, the adoption of the alternative FE modelling technique conveniently reformulated the expressions of the statistical characteristics of structural responses into the NLP format. Subsequently, the hybrid uncertain structural response analysis with random and interval variables can be efficiently processed by any available NLP solver. Consequently, the interval arithmetic is completely eliminated throughout the proposed computational strategy.

3.4 Numerical examples

In this section, the applicability, accuracy and efficiency of the proposed UPMP approach are critically justified through investigations on both academic sized and practically motivated engineering structures. For the simple academic sized examples, the accuracy of the proposed UPMP approach can be rigorously justified by comparing with some analytical solutions, whereas the applicability of the proposed approach can be illustrated by analysing the practically motivated examples.

Within the context of this study, all NLPs involved in the proposed UPMP approach are solved by a commercial NLP solver named CONOPT [156], which is operated within an advanced mathematical modelling environment, namely General

Algebraic Modelling System (GAMS) [157]. For all the numerical examples investigated in this study, uncertain parameters from the same category of different elements are treated as independent to each other. The accuracy of the results is rigorously verified through a number of different approaches. For academic sized examples, the results calculated by the proposed UPMP approach are compared with the analytical solutions where possible. For the circumstance that analytical solution cannot be determined, the computationally exhaustive Monte-Carlo Simulation combined with Quasi-Monte-Carlo Simulation (MCS-QMCS) method is implemented to verify the uncertain-but-bounded statistical characteristics obtained by UPMP approach into certain extent. The realizations for both random and interval variables used in the MCS-QMCS approach are generated by the Statistics toolbox of MATLAB R2015b [158]. For the QMCS scheme, the Halton low discrepancy sequence has been implemented with a dynamic skip and leap scheme combined with a ‘‘RR2” scramble scheme [159]. The presented numerical results are obtained by using a workstation with CPU of Intel Core i7-4770, 32 GB of memory, and 1 TB of hard drive.

3.4.1 Stepped cantilever beam

The first investigation considers a two-stepped cantilever Euler-Bernoulli beam subjected to an external load acting at the right end, as depicted in Figure. 3.2. The Young’s modulus and cross-sectional geometries of the two elements (element 1 is between nodes 1 and 2, and element 2 is between nodes 2 and 3) are different. For this particularly example, the vertical displacements at nodes 2 ($u_{2,y}$) and 3 ($u_{3,y}$) have been analysed by employing the UPMP approach considering three cases of analysis with distinctive mixture of random and interval variables. The information of uncertain parameters of the considered three cases is presented in Table 3.1.

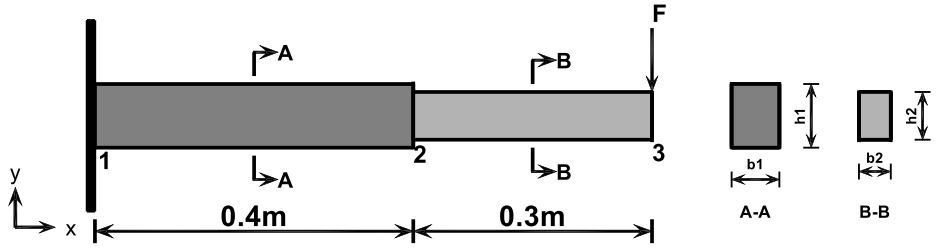

Figure 3.2 Two-stepped cantilever beam

The upper and lower bounds of the stochastic characteristics of $u_{2,y}$ and $u_{3,y}$ of Case 1 obtained by the proposed UPMP approach are presented in Table 3.2. In order to verify the accuracy of the proposed method, the analytical expressions of $u_{2,y}$ and $u_{3,y}$ are respectively obtained as Eqs. (3.52) and (3.53) based on the Euler-Bernoulli beam theory. Subsequently, the analytical solutions for the upper and lower bounds of the means and standard deviations of and $u_{3,y}$ for Case 1 can be calculated as demonstrated in Table 3.2. In such way, the accuracy of the UPMP approach has been evidently justified for this particular case of analysis.

$$u_{2,y} = \left[\frac{4l_{e,1}^3}{E_1 b_1 h_1^3} + \frac{6l_{e,1}^2 l_{e,2}}{E_1 b_1 h_1^3} \right] F \tag{3.52}$$

$$u_{3,y} = \left[\frac{4l_{e,1}^3 + 12l_{e,1}^2 l_{e,2} + 12l_{e,1} l_{e,2}^2}{E_1 b_1 h_1^3} + \frac{4l_{e,2}^3}{E_2 b_2 h_2^3} \right] F \tag{3.53}$$

For the investigations conducted in Cases 2 and 3, the analytical solutions of bounded statistical characteristics of the nodal displacement with hybrid uncertainties cannot be explicitly determined, thus the MCS-QMCS method has been implemented to verify the results obtained from the proposed UPMP approach. Regarding the investigations for Cases 2 and 3, 1,000 realizations have been generated for all the interval variables within the scheme of QMCS, and 10,000 random samples have been explored

at each realization of the interval variable. Therefore, the bounds of stochastic characteristics of $u_{2,y}$ and $u_{3,y}$ obtained by both approaches for Cases 2 and 3 of the cantilever beam are summarised in Table 3.3.

By thoroughly examining Table 3.3, all computational results provided by the proposed UPMP approach are fully enclosing the results reported from the dually simulative MCS-QMCS approach. The reason for such observed incompetence of the simulative approach is that even though extensive amount of sampling points with considerable amount of uniformity have been explored for the interval counterpart, it still remains quite challenging for the global search based method to sample the points at the boundaries of the interval parameters (i.e., the upper and lower bounds of the interval parameters). However, from Eqs. (3.52) and (3.53), monotonic relationship can be observed for the considered interval parameters in Cases 2 and 3 with the concerned structural responses. Consequently, once explicit formulations for the mean and standard deviation for the structural responses are established, the UPMP approach can utilize the computational benefit offered by the mathematical programming approach to search for the extreme bounds of the statistical characteristics in a more appropriate manner.

Table 3.1 Information of uncertain parameters of Example 3.4.1

Parameters	Case 1	Case 2	Case 3
$E_1\,(GPa)$	*Interval* $180 \le E_1 \le 220$	*Normal* $\mu_{E_1} = 200\,,\sigma_{E_1} = 20$	*Same as Case 1*
$E_2\,(GPa)$	*Interval* $62.1 \le E_2 \le 75.9$	*Normal* $\mu_{E_2} = 69\,,\sigma_{E_2} = 6.9$	*Lognormal* $\mu_{E_2} = 69\,,\sigma_{E_2} = 6.9$
$b_1\,(m)$	*Interval* $0.054 \le b_1 \le 0.066$	*Same as Case 1*	*Same as Case 1*
$b_2\,(m)$	*Interval* $0.036 \le b_2 \le 0.044$	*Same as Case 1*	*Normal* $\mu_{b_2} = 0.04\,,\sigma_{b_2} = 0.002$
	Interval	*Same as Case 1*	*Same as Case 1*

$h_1\ (m)$	$0.0736 \le h_1 \le 0.0864$		
$h_2\ (m)$	*Interval* $0.0552 \le h_2 \le 0.0648$	*Same as Case 1*	*Normal* $\mu_{h_2} = 0.06\ , \sigma_{h_2} = 0.003$
$F\ (kN)$	*Lognormal* $\mu_F = 50\ , \sigma_F = 7.5$	*Interval* $42.5 \le F \le 57.5$	*Normal* $\mu_F = 50\ , \sigma_F = 7.5$

Overall, by comparing with both analytical solutions in Case 1 and simulative results provided by the MCS-QMCS approach in Cases 2 and 3, the proposed UPMP approach offers several superiorities over the simulative approach for all the investigated scenarios.

Table 3.2The statistical characteristics of Case 1 of cantilever beam

	UPMP (m)	Analytical solution (m)
$\overline{\mu_{u_{2,y}}}$	7.019×10^{-3}	7.019×10^{-3}
$\overline{\sigma_{u_{2,y}}}$	1.053×10^{-3}	1.053×10^{-3}
$\underline{\mu_{u_{2,y}}}$	2.904×10^{-3}	2.904×10^{-3}
$\underline{\sigma_{u_{2,y}}}$	4.357×10^{-4}	4.357×10^{-4}
$\overline{\mu_{u_{3,y}}}$	3.067×10^{-2}	3.067×10^{-2}
$\overline{\sigma_{u_{3,y}}}$	4.600×10^{-3}	4.600×10^{-3}
$\underline{\mu_{u_{3,y}}}$	1.269×10^{-2}	1.269×10^{-2}
$\underline{\sigma_{u_{3,y}}}$	1.904×10^{-3}	1.904×10^{-3}

Table 3.3 The statistical characteristics of Case 2 and 3 of cantilever beam

	Case 2		Case 3	
	UPMP	MCS-QMCS	UPMP	MCS-QMCS
$\overline{\mu_{u_{2,y}}}\ (m)$	7.265×10^{-3}	6.711×10^{-3}	7.019×10^{-3}	6.442×10^{-3}
$\overline{\sigma_{u_{2,y}}}\ (m)$	7.265×10^{-4}	6.833×10^{-4}	1.053×10^{-3}	9.621×10^{-4}
$\underline{\mu_{u_{2,y}}}\ (m)$	2.716×10^{-3}	2.982×10^{-3}	2.904×10^{-3}	3.142×10^{-3}
$\underline{\sigma_{u_{2,y}}}\ (m)$	2.716×10^{-4}	3.112×10^{-4}	4.357×10^{-4}	4.688×10^{-4}

$\overline{\mu_{u_{3,y}}}\,(m)$	3.174×10^{-2}	2.840×10^{-2}	2.537×10^{-2}	2.432×10^{-2}
$\overline{\sigma_{u_{3,y}}}\,(m)$	2.249×10^{-3}	2.054×10^{-3}	4.165×10^{-3}	4.076×10^{-3}
$\underline{\mu_{u_{3,y}}}\,(m)$	1.187×10^{-2}	1.372×10^{-2}	1.581×10^{-2}	1.660×10^{-2}
$\underline{\sigma_{u_{3,y}}}\,(m)$	8.408×10^{-4}	9.966×10^{-4}	2.914×10^{-3}	3.060×10^{-3}
t_{com} (s)	*1.52*	*230.76*	*1.47*	*253.64*

3.4.2 Three-span truss bridge

In the second example, the hybrid uncertain static analysis of a three-span truss bridge involving both random and interval uncertainties is conducted. The general layout of the structure with the loading regime at reference configuration is shown in Figure. 3.3. The truss bridge consists of 113 elements with 108 degrees-of-freedom. Moreover, the elements of the truss bridge are categorised into four groups with different cross-sectional areas such that A_1 denotes the cross-sectional areas of all the vertical elements, A_2 denotes the cross-sectional areas of all the diagonal elements, A_3 denotes the cross-sectional areas of the elements between nodes 1 and 29, and A_4 denotes the cross-sectional areas of the elements between nodes 30 and 58.

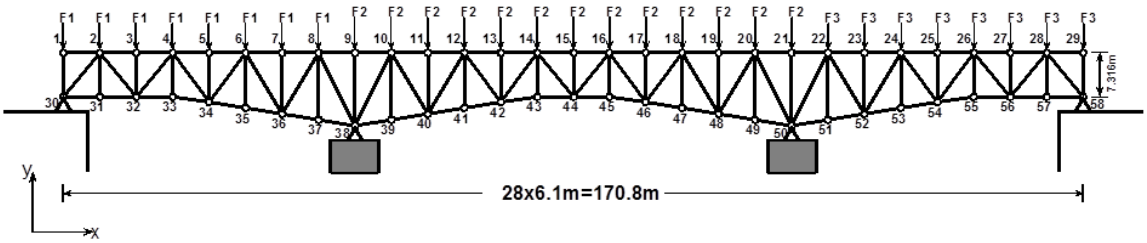

Figure 3.3 Three-span truss bridge

The investigation of structural response of the truss structure involves two distinctive cases with various uncertain situations. The details of the two cases are outlined as follows:

Case 1. The Young's modulus (E^R, unit: GPa) is lognormal random variable and the four different cross-sectional areas (A_1^R, A_2^R, A_3^R and A_4^R, unit: m^2) are normally distributed random variables. The statistical information of random variables are: $\mu_E = 200$ GPa, $\sigma_E = 20$ GPa; $\mu_{A_1} = 1.232\times10^{-2} m^2$, $\sigma_{A_1} = 6.160\times10^{-4} m^2$; $\mu_{A_2} = 1.361\times10^{-2} m^2$, $\sigma_{A_2} = 6.805\times10^{-4} m^2$; $\mu_{A_3} = 1.171\times10^{-2} m^2$, $\sigma_{A_3} = 8.550\times10^{-4} m^2$; $\mu_{A_4} = 1.671\times10^{-2} m^2$, $\sigma_{A_4} = 8.355\times10^{-4} m^2$. The externally applied loads ($\mathbf{F}_1^I$, $\mathbf{F}_2^I$ and $\mathbf{F}_3^I$, units: kN) at reference configuration are interval parameters which have:

$$\mathbf{F}_1^I \in \tilde{\mathbf{\Omega}} := \{\mathbf{F}_1 \in \Re^8 \mid 288 \le F_{1,i_{F_1}} \le 352, \text{ for } i_{F_1} = 1,...,8\} \tag{3.54}$$

$$\mathbf{F}_2^{\mathrm{I}} \in \tilde{\mathbf{\Omega}} := \{\mathbf{F}_2 \in \Re^{13} \mid 360 \le F_{2,i_{F_2}} \le 440, \text{ for } i_{F_2} = 1,...,13\} \tag{3.55}$$

$$\mathbf{F}_3^I \in \tilde{\mathbf{\Omega}} := \{\mathbf{F}_3 \in \Re^8 \mid 288 \le F_{3,i_{F_3}} \le 352, \text{ for } i_{F_3} = 1,...,8\} \tag{3.56}$$

Case 2. The effect of varying degree of uncertainty of system parameters against the structural responses is analysed. The change range (CR) of interval variables is varying between $0.04 \le \mathrm{CR} \le 0.3$ and the coefficient of variation (COV) of random variables is varying between $0.04 \le \mathrm{COV} \le 0.3$. In this case, Young's modulus ($\mathbf{E}^I$, unit: GPa) and cross-sectional areas ($\mathbf{A}_1^I$, $\mathbf{A}_2^I$, $\mathbf{A}_3^I$ and $\mathbf{A}_4^I$, unit: m^2) are interval variables which have the nominal values as: $E^C = 200$ GPa, $A_1^C = 1.232\times10^{-2}\ m^2$, $A_2^C = 1.361\times10^{-2}\ m^2$, $A_3^C = 1.171\times10^{-2}\ m^2$, and $A_4^C = 1.671\times10^{-2}\ m^2$. Thus, the interval parameters can be expressed as:

$$\mathbf{E}^I \in \tilde{\mathbf{\Omega}} := \{\mathbf{E} \in \Re^{113} \mid E^C(1-\mathrm{CR}) \le E_{i_E} \le E^C(1+\mathrm{CR}), \text{ for } i_E = 1,...,113\} \tag{3.57}$$

$$\mathbf{A}_1^I \in \tilde{\mathbf{\Omega}} = \{\mathbf{A}_1 \in \Re^{29} \mid A_1^C(1-\mathrm{CR}) \le A_{1,i_{A_1}} \le A_1^C(1+\mathrm{CR}), \ \text{for } i_{A_1} = 1,...,29\} \quad (3.58)$$

$$\mathbf{A}_2^I \in \tilde{\mathbf{\Omega}} := \{\mathbf{A}_2 \in \Re^{28} \mid A_2^C(1-\mathrm{CR}) \le A_{2,i_{A_1}} \le A_2^C(1+\mathrm{CR}), \ \text{for } i_{A_1} = 1,...,28\} \quad (3.59)$$

$$\mathbf{A}_3^I \in \tilde{\mathbf{\Omega}} := \{\mathbf{A}_3 \in \Re^{28} \mid A_3^C(1-\mathrm{CR}) \le A_{3,i_{A_3}} \le A_3^C(1+\mathrm{CR}), \ \text{for } i_{A_3} = 1,...,28\} \quad (3.60)$$

$$\mathbf{A}_4^I \in \tilde{\mathbf{\Omega}} := \{\mathbf{A}_4 \in \Re^{28} \mid A_4^C(1-\mathrm{CR}) \le A_{4,i_{A_3}} \le A_4^C(1+\mathrm{CR}), \ \text{for } i_{A_3} = 1,...,28\} \quad (3.61)$$

The random variables considered in this case are the normally distributed externally applied loads at reference configuration. The means of the externally applied loads are: $\mu_{F_1} = 320$ kN, $\mu_{F_2} = 400$ kN, and $\mu_{F_3} = 320$ kN.

For Case 1, both UPMP approach and dual simulative MCS-QMCS method are implemented to investigate the structural responses of the truss bridge with hybrid uncertainties specified as above. For the purpose of demonstration, the bounds of statistical characteristics of the horizontal displacement at node 10 ($u_{10,x}$), the vertical displacement at node 44 ($u_{44,y}$) and the internal force of element 69 (f_{69}) obtained by both approaches are reported in Table 3.4. For the MCS-QMCS method, various sample sizes are adopted in calculating the upper and lower bounds of the statistical characteristics. It is evidently illustrated that all the results of MCS-QMCS approach are enclosed within the results obtained by the proposed UPMP approach. From Table 3.4, it can be observed that increasing the initial sample size in MCS-QMCS approach could slightly improve the computational results. However, the computational effort increases dramatically with the increase of sample size. Therefore, the proposed UPMP approach surpassed the performance of MCS-QMCS method in both accuracy and computational efficiency.

Table 3.4 The bounds of statistical characteristics of Case 1 of truss bridge

	UPMP	MCS-QMCS 100 interval 5000 random	500 interval 5000 random	500 interval 10,000 random	1000 interval 10,000 random
$\overline{\mu_{u_{10,x}}}\ (m)$	1.128×10^{-2}	1.048×10^{-2}	1.048×10^{-2}	1.046×10^{-2}	1.069×10^{-2}
$\overline{\sigma_{u_{10,x}}}\ (m)$	1.209×10^{-3}	1.134×10^{-3}	1.134×10^{-3}	1.129×10^{-3}	1.153×10^{-3}
$\underline{\mu_{u_{10,x}}}\ (m)$	7.897×10^{-3}	9.328×10^{-3}	9.141×10^{-3}	9.121×10^{-3}	9.121×10^{-3}
$\underline{\sigma_{u_{10,x}}}\ (m)$	8.419×10^{-4}	9.867×10^{-4}	9.634×10^{-4}	9.661×10^{-4}	9.661×10^{-4}
$\overline{\mu_{u_{44,y}}}\ (m)$	8.305×10^{-2}	7.913×10^{-2}	7.931×10^{-2}	7.934×10^{-2}	8.042×10^{-2}
$\overline{\sigma_{u_{44,y}}}\ (m)$	8.655×10^{-3}	8.418×10^{-3}	8.418×10^{-3}	8.292×10^{-3}	8.375×10^{-3}
$\underline{\mu_{u_{44,y}}}\ (m)$	6.567×10^{-2}	7.150×10^{-2}	7.133×10^{-2}	7.124×10^{-2}	7.124×10^{-2}
$\underline{\sigma_{u_{44,y}}}\ (m)$	6.849×10^{-3}	7.474×10^{-3}	7.425×10^{-3}	7.415×10^{-3}	7.364×10^{-3}
$\overline{\mu_{f_{69}}}$ (kN)	1.731×10^{3}	1.613×10^{3}	1.613×10^{3}	1.614×10^{3}	1.637×10^{3}
$\overline{\sigma_{f_{69}}}$ (kN)	22.580	21.344	21.439	21.282	21.590
$\underline{\mu_{f_{69}}}$ (kN)	1.277×10^{3}	1.464×10^{3}	1.442×10^{3}	1.442×10^{3}	1.442×10^{3}
$\underline{\sigma_{f_{69}}}$ (kN)	17.844	19.386	19.211	19.177	19.177
t_{com} (s)	3.109	679.906	2.856×10^{3}	5.487×10^{3}	1.346×10^{4}

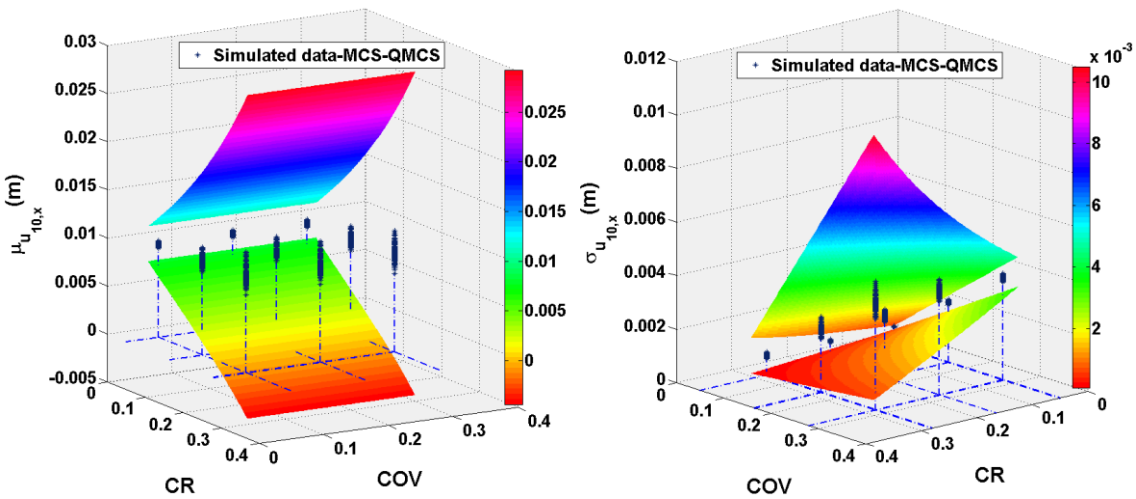

(a) (b)

Figure 3.4 Variations of upper and lower bounds of (a) mean and (b) standard deviation of $u_{10,x}$ of Case 2 of truss bridge against alternations of degree of uncertainty

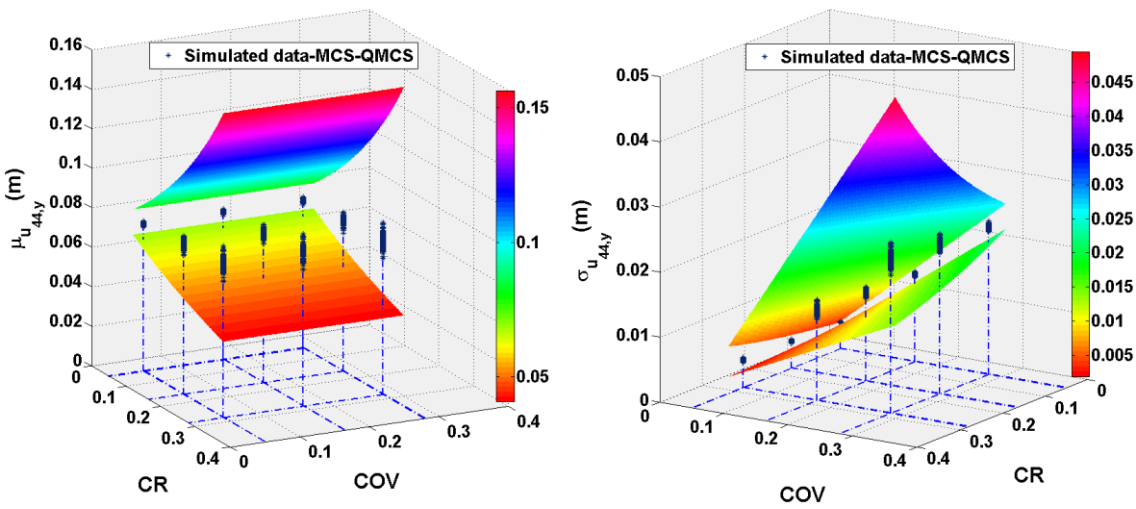

(a) (b)

Figure 3.5 Variations of upper and lower bounds of (a) mean and (b) standard deviation of $u_{44,y}$ of Case 2 of truss bridge against alternations of degree of uncertainty

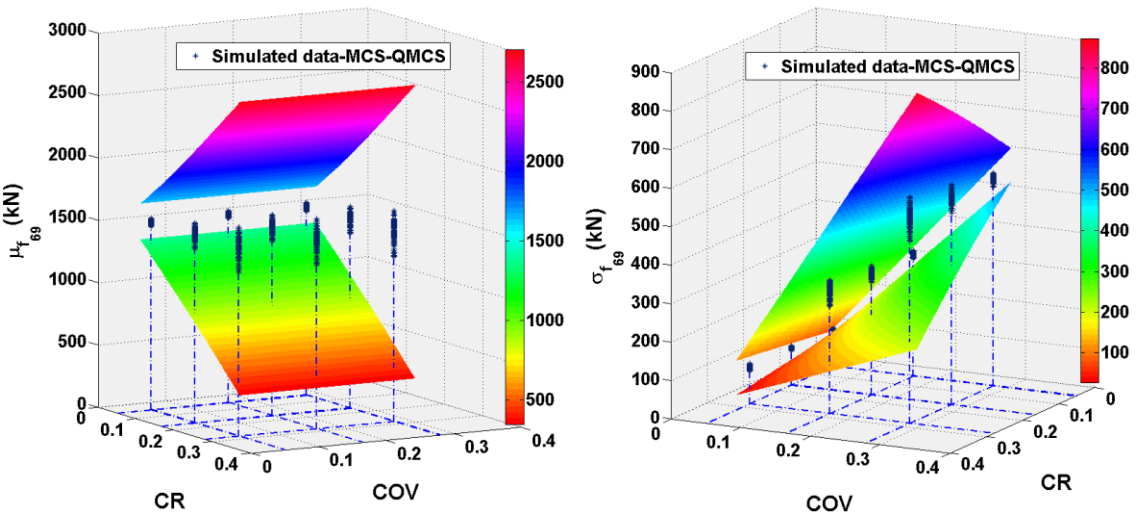

(a) (b)

Figure 3.6 Variations of upper and lower bounds of (a) mean and (b) standard deviation of f_{69} of Case 2 of truss bridge against alternations of degree of uncertainty

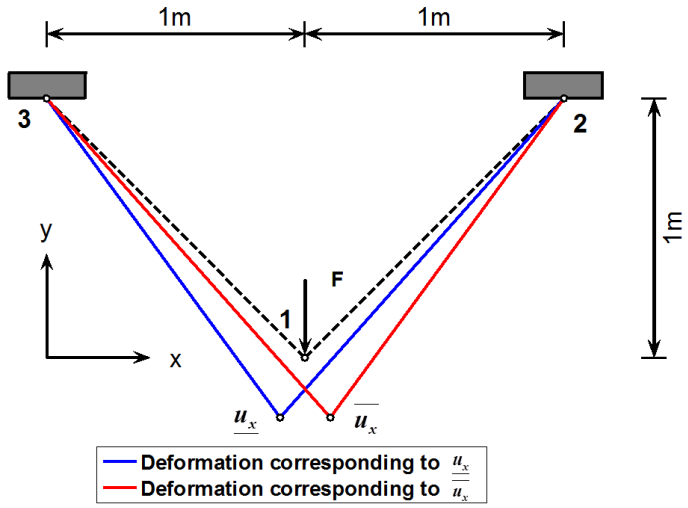

Figure 3.7 Symmetric two-bar truss with interval uncertain Young's modulus and cross-sectional area

For Case 2, the response surfaces of the upper and lower bounds of the stochastic characteristics of $u_{10,x}$, $u_{44,y}$ and f_{69} against the variations of the random forces, interval Young's modulus and cross-sectional areas are constructed by the proposed UPMP approach and shown as the 3-D plots through Figures 3.4 to 3.6. Additionally, the MCS-QMCS method with 100 interval samples and 5000 random samples against selected combinations of change ratio (CR, which equals to the interval width divided by the midpoint) of an interval variable and coefficient of variation (COV, which equals to the standard deviation divided by the mean value) of a random variable are also implemented. Thus, for each combination of CR and COV, 100 samples of mean and standard deviation are obtained and shown in the 3-D plots. Once again, the results provided by the UPMP approach enclose all the results obtained from the dual sampling method. Comparing with Case 1, the relative difference between the results obtained by both approaches are relatively large. The reason for such noticeable difference is because of the implementation of insufficient amount of sample for situations involving relatively large number of interval variables. The quality of results obtained from the QMCS-MCS

approach can be improved if more sampling points are explored. However, the increasing of the sample size would also burden the computational cost of such analysis. By further examining Figures 3.4 - 3.6, several additional interesting yet important points can be noticed which includes:

1. When the COV of random variables varies and CR of interval variables remains constant, both the upper and lower bounds of mean of the selected structural responses remain unchanged. On the other hand, the bounds of the standard deviations of the selected structural responses vary monotonically with the change of COV.
2. Under the circumstance that the COV is constant, a monotonic increase of the upper bounds and a monotonic decrease of the lower bounds of means and standard deviations of the selected structural responses can be observed when the CRs of Young's modulus and cross-sectional areas increases. Additionally, nonlinear relationship between the variations of the bounds of statistical characteristics and the changes of CRs are observed from Figures 3.4 and 3.5. Therefore, it can be concluded from Case 2 that the influence on the bounds of the stochastic characteristics of structural responses due to the variations of the interval Young's modulus and cross-sectional areas cannot be predicted by simple linear scaling. Moreover, it can be observed from Figure 3.5 that the increase of $\overline{\mu_{u_{44,y}}}$ is relatively faster in comparison with the decrease of $\underline{\mu_{u_{44,y}}}$.
3. By examining Figure 3.4(a), the $\underline{\mu_{u_{10,x}}}$ obtained by the proposed UPMP approach decreases from positive to negative when the CRs of Young's modulus and cross-sectional area increase, while the simulated samples from MCS-QMCS remain positive. The physical plausibility of such phenomenon can be demonstrated

based on a symmetric two-bar truss structure, as shown in Figure 3.7, (element 1 is between nodes 1 and 2, and element 2 is between nodes 1 and 3) with interval Young's modulus (E_1 and E_2) and cross-sectional area (A_1 and A_2) of both elements subjected to vertical load applied at node 1. The bounds of Young's modulus and cross-sectional area are:

$$\mathbf{E}^I \in \tilde{\mathbf{\Omega}} := \{\mathbf{E} \in \Re^2 \mid \underline{E} \le E_{i_E} \le \overline{E}, \text{ for } i_E = 1,2\} \tag{3.62}$$

$$\mathbf{A}^I \in \tilde{\mathbf{\Omega}} := \{\mathbf{A} \in \Re^2 \mid \underline{A} \le A_{i_A} \le \overline{A}, \text{ for } i_A = 1,2\} \tag{3.63}$$

By simply applying the interval arithmetic with structural analysis, a positive $\overline{u_x}$ can be easily obtained when $E_1 = \overline{E}$, $A_1 = \overline{A}$, $E_2 = \underline{E}$ and $A_2 = \underline{A}$ while the $\underline{u_x}$ is negative when $E_2 = \overline{E}$, $A_2 = \overline{A}$, $E_1 = \underline{E}$ and $A_1 = \underline{A}$. Thus, if the externally applied load is a random variable, the mean of u_x will varies from negative to positive. Therefore, the proposed UPMP approach has the superior advantage for situations involving the positive-to-negative variations of bounds of mean of the structural responses.

By implementing the UPMP approach, the random interval behaviors of the structural responses of the three-span truss bridge have been investigated against two different cases with various uncertain conditions. The accuracy and computational efficiency of the proposed method has been clearly illustrated in the study of Example 3.4.2. Additionally, the effects of varying interval Young's modulus and cross-sectional area and random externally applied loads on the structural responses have been investigated. From this investigation, it is necessary for engineering application to

explicitly analyze the influence of the fluctuation of random and interval uncertain system parameters acting upon the structural responses of structures.

3.4.3 Multi-bay multi-storey frame

To further investigate the performance of the proposed UPMP approach, a practical-sized multi-bay multi-storey frame subjected to diverse vertical and horizontal loadings at various locations is considered in the last numerical investigation. In this particular example, the applicability, accuracy and computational efficiency of the UPMP approach are thoroughly demonstrated through three distinctive investigations which are including a probabilistic analysis, an interval analysis, and a hybrid random and interval analysis of structural responses. The general layout and loading regime of the frame is illustrated in Figure 3.8. The plane frame model consists of 753 degrees-of-freedom and 376 elements. The considered uncertain parameters are the Young's modulus (E, unit: GPa), cross-sectional areas of beams (A_B, unit: m^2) and columns (A_C, unit: m^2), and externally applied loads (F_1, F_2 and F_3, units: kN) at reference configurations. For this frame structure, 310UC118 has been used for all columns and 310UB32 has been employed for all beams [160]. In order to maintain the compatibility between cross-sectional area and the corresponding second moment of area for both column and beam, the following compatibility functions are introduced such that the second moment of area of each element is expressed as a function of cross-sectional area. For each 310UC118 column the compatibility function is expressed as Eq. (3.64), whereas the compatibility function of each 310UB32 beam is expressed as Eq. (3.65).

$$I_C^s(A_C) = 0.5238A_C^2 + 0.0114A_C - 3\times10^{-5} \tag{3.64}$$

$$I_B^s(A_B) = -0.8876A_B^2 + 0.0288A_B - 4\times10^{-5} \tag{3.65}$$

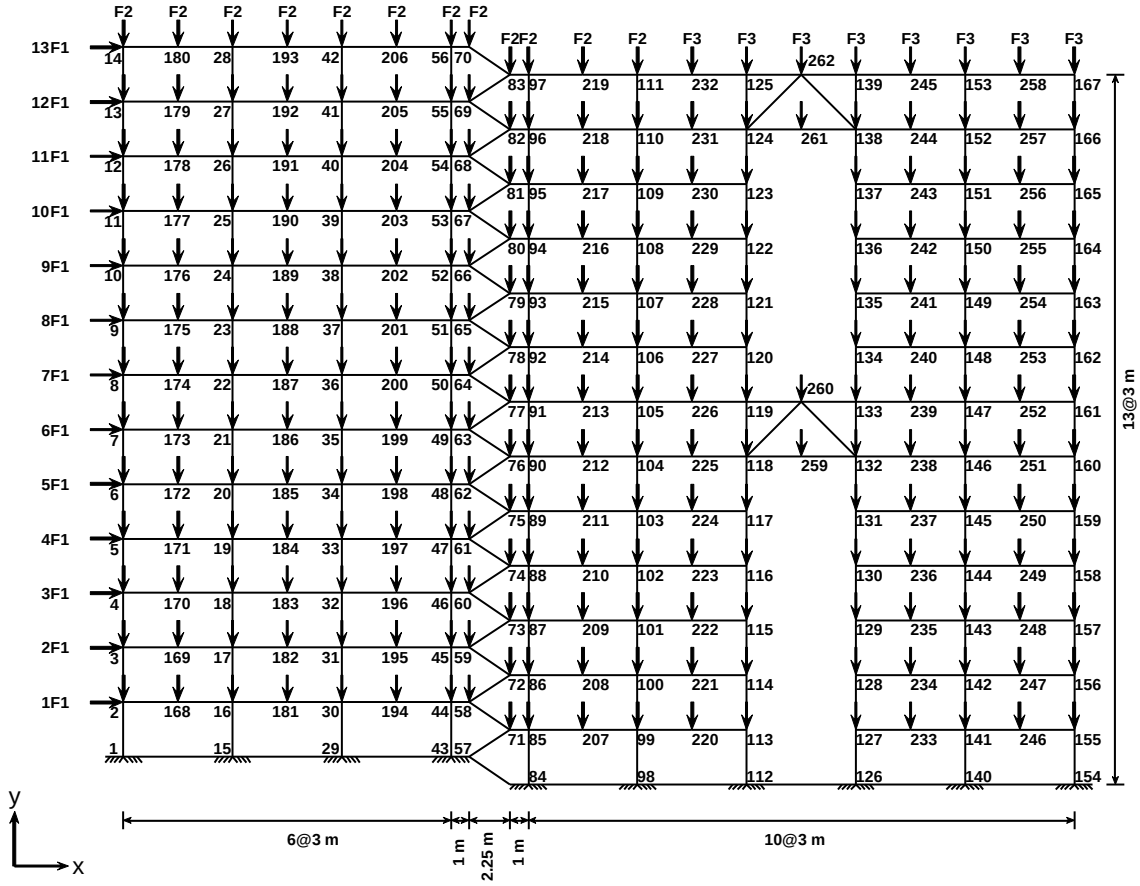

Figure 3.8 The multi-bay multi-storey frame

Table 3.5 Statistical information of all random variables considered in Case 1

Parameter	Distribution	Mean	COV
E (GPa)	lognormal	200	0.06
A_B (m^2)	normal	40.8×10^{-4}	0.05
A_C (m^2)	normal	150×10^{-4}	0.05
F_1 (kN)	normal	5.5	0.1
F_2 (kN)	normal	60	0.1
F_3 (kN)	normal	80	0.1

For this particular example, three cases with various uncertain scenarios are investigated. The details of the three distinct investigations are outlined as follows:

Case 1: All system parameters are considered as random variables whose statistical information is collectively summarized in Table 5 [161, 162].

Case 2: The Young's modulus, cross-sectional areas of each beam and column, as well as all the applied loads at reference configuration are considered as interval uncertain parameters. The detailed information regarding all considered interval parameters is summarized through Eqs. (3.66) - (3.71).

$$\mathbf{E}^I \in \tilde{\mathbf{\Omega}} := \{\mathbf{E} \in \Re^{281} \,|\, 180 \le E_{i_E} \le 220, \quad \text{for } i_E = 1,...,281\} \tag{3.66}$$

$$\mathbf{A}_B^I \in \tilde{\mathbf{\Omega}} := \{\mathbf{A}_B \in \Re^{151} \,|\, 36.72\times10^{-4} \le A_{B,i_{A_B}} \le 44.88\times10^{-4}, \quad \text{for } i_{A_B} = 1,...,151\} \tag{3.67}$$

$$\mathbf{A}_C^I \in \tilde{\mathbf{\Omega}} := \{\mathbf{A}_C \in \Re^{130} \,|\, 135\times10^{-4} \le A_{C,i_{A_C}} \le 165\times10^{-4}, \quad \text{for } i_{A_C} = 1,...,130\} \tag{3.68}$$

$$\mathbf{F}_1^I \in \tilde{\mathbf{\Omega}} := \{\mathbf{F}_1 \in \Re^{8} \,|\, 4.95 \le F_{1,i_{F_1}} \le 6.05, \quad \text{for } i_{F_1} = 1,...,13\} \tag{3.69}$$

$$\mathbf{F}_2^I \in \tilde{\mathbf{\Omega}} := \{\mathbf{F}_2 \in \Re^{156} \,|\, 54 \le F_{2,i_{F_2}} \le 66, \quad \text{for } i_{F_2} = 1,...,156\} \tag{3.70}$$

$$\mathbf{F}_3^I \in \tilde{\mathbf{\Omega}} := \{\mathbf{F}_3 \in \Re^{95} \,|\, 72 \le F_{3,i_{F_3}} \le 88, \quad \text{for } i_{F_3} = 1,...,95\} \tag{3.71}$$

Case 3: Two scenarios are thoroughly investigated to demonstrate the performance of the proposed UPMP approach in hybrid random and interval analysis. For both scenarios, the interval cross-sectional areas of beams and columns are expressed as Eqs. (68) and (69), and the details of random uncertain parameters are listed in Table 3.6.

$$\mathbf{A}_B^I \in \tilde{\mathbf{\Omega}} := \{\mathbf{A}_B \in \Re^{151} \,|\, 38.352\times10^{-4} \le A_{B,i_{A_B}} \le 43.248\times10^{-4}, \quad \text{for } i_{A_B} = 1,...,151\} \tag{3.72}$$

$$\mathbf{A}_C^I \in \tilde{\mathbf{\Omega}} := \{\mathbf{A}_C \in \Re^{130} \,|\, 141\times10^{-4} \le A_{C,i_{A_B}} \le 159\times10^{-4}, \quad \text{for } i_{A_B} = 1,...,130\} \tag{3.73}$$

Table 3.6 Random uncertain parameters of frame structure

Parameter	Distribution	Mean	COV

	Scenario 1	*Scenario 2*		
E (GPa)	lognormal	lognormal	200	0.045
F_1 (kN)	normal	gumbel	5.5	0.1
F_2 (kN)	lognormal	lognormal	60	0.1
F_3 (kN)	normal	normal	80	0.1

Table 3.7 The statistical characteristics of frame structure of Case 1

	UPMP	MCS 10,000	MCS 100,000	RR_1 (%)	RR_2 (%)
$\mu_{u_{167,x}}$ (m)	9.194×10^{-2}	9.263×10^{-2}	9.260×10^{-2}	-0.748	-0.714
$\sigma_{u_{167,x}}$ (m)	1.190×10^{-2}	1.194×10^{-2}	1.205×10^{-2}	-0.339	-1.208
$\mu_{u_{70,y}}$ (m)	1.689×10^{-2}	1.700×10^{-2}	1.699×10^{-2}	-0.628	-0.616
$\sigma_{u_{70,y}}$ (m)	1.931×10^{-3}	1.953×10^{-3}	1.946×10^{-3}	-1.111	-0.793
μ_{M_1} (kNm)	92.652	92.757	92.790	-0.113	-0.148
σ_{M_1} (kNm)	9.655	9.613	9.685	0.440	-0.311
t_{com} (s)	71.765	9.470×10^{2}	1.767×10^{4}	N/A	N/A

For Case 1 of Example 3, both UPMP and Monte-Carlo Simulation (MCS) method are implemented to investigate the random behaviour of the structural responses of this complex frame. For the MCS approach, two simulations with 10,000 and 100,000 samples have been adopted to verify the results obtained by the proposed method. The means and standard deviations of the horizontal displacement at node 167 ($u_{167,x}$), vertical displacement at node 70 ($u_{70,y}$), and the bending moment at node 1 (M_1) calculated by both approaches are outlined in Table 3.7, where R_1 and R_2 denote the relative differences between the results obtained by UPMP approach and MCS method with 10,000 and 100,000 samples, respectively. The relative difference in this case is defined as:

$$RR = \frac{UPMP - MCS}{MCS} \% \tag{3.74}$$

It is indicated in Table 3.7 that the results calculated by the UPMP approach agree well with the statistical information obtained from the MCS approach with various sample sizes, but of course in a much more computational friendly manner. Therefore, the applicability, accuracy and computational efficiency of the proposed UPMP approach for pure stochastic analysis have been rigorously justified through this investigation.

For Case 2, interval analyses of the displacement and force responses of the frame structure have been conducted by both UPMP and Quasi-Monte-Carlo Simulation (QMCS) approaches with various sample sizes. The reason for adopting QMCS in this investigation is due to the advantage of QMCS approach in generating more uniform samples than the MCS method, which could potentially enhance the effectiveness of the QMCS method. For this particular case, 100, 1000, 10,000 and 100,000 simulations have been implemented through the QMCS scheme. For the demonstration purpose, the upper and lower bounds of $u_{70,y}$ and M_1 obtained by both approaches are shown in Figure 3.9, where the colour scale in the plots indicates the computational time consumed by the QMCS approach. It can be easily observed that the UPMP approach surpasses the capability of the QMCS method by providing a larger upper bound and smaller lower bound within 20 seconds. Indeed, limited improvements of results obtained from the QMCS approach can be observed by exponentially increasing the sample size, but the possibility of engineering application for such global search based computational approach is quite challengeable due to the inevitably substantial consumption of computational effort.

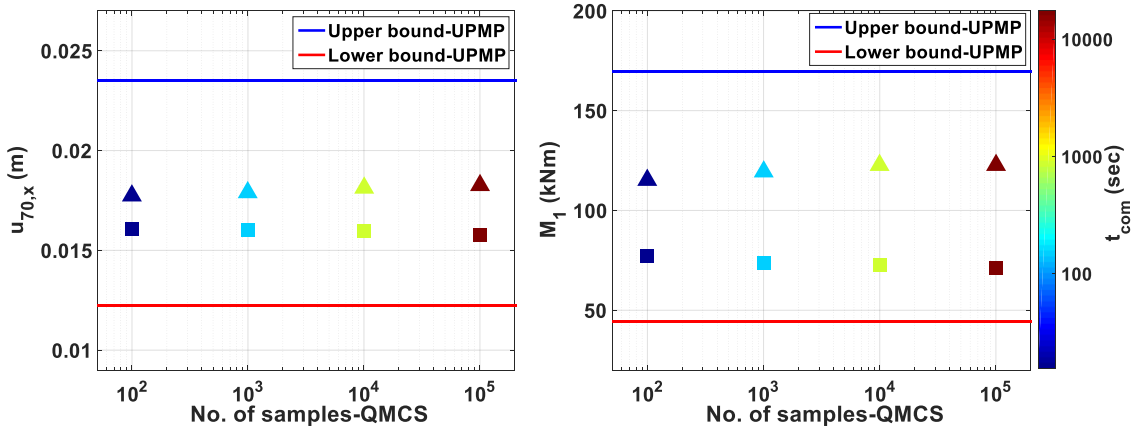

(a) (b)

Figure 3.9 Bounds of (a) $u_{70,x}$ and (b) M_1 of frame structure of Case 2

For Case 3, the uncertain-but-bounded statistical characteristic of selected displacement and force responses obtained by both approaches are listed in Table 3.8. For the MCS-QMCS method, 100 simulations have been implemented for generating realizations for interval variables through the QMCS scheme, and subsequently, 10,000 simulations have been conducted at each interval realization for the stochastic analysis. By inspecting the results reported in Table 3.8, the upper and lower bounds of statistical information regarding concerned structural responses obtained by MCS-QMCS method are enclosed by the results determined from the UPMP approach for both *Scenarios 1* and *2*. Since that the proposed approach simply requires the mean and standard deviations of the random variables, it leads to the same UPMP formulations and subsequently the results for the structural responses for both *Scenarios 1* and *2*. Comparing with the adopted sampling method, the proposed UPMP approach is capable of offering sharper bounds on the means and standard deviations of all the considered structural responses with dramatically less computational cost. Therefore, the accuracy and computational efficiency of the proposed approach in hybrid uncertainty analysis have been evidently demonstrated.

Table 3.8 The bounds of statistical characteristics of the frame structure in Case 3

	UPMP	MCS-QMCS	
		Scenario 1	*Scenario 2*
$\overline{\mu_{u_{167,x}}}$ (m)	1.016×10^{-1}	9.351×10^{-2}	9.351×10^{-2}
$\overline{\sigma_{u_{167,x}}}$ (m)	1.127×10^{-2}	1.041×10^{-2}	1.048×10^{-2}
$\underline{\mu_{u_{167,x}}}$ (m)	8.350×10^{-2}	9.105×10^{-2}	9.105×10^{-2}
$\underline{\sigma_{u_{167,x}}}$ (m)	9.640×10^{-3}	1.019×10^{-2}	1.027×10^{-2}
$\overline{\mu_{u_{70,y}}}$ (m)	1.815×10^{-2}	1.734×10^{-2}	1.734×10^{-2}
$\overline{\sigma_{u_{70,y}}}$ (m)	1.764×10^{-3}	1.691×10^{-3}	1.702×10^{-3}
$\underline{\mu_{u_{70,y}}}$ (m)	1.578×10^{-2}	1.654×10^{-2}	1.654×10^{-2}
$\underline{\sigma_{u_{70,y}}}$ (m)	1.550×10^{-3}	1.616×10^{-3}	1.627×10^{-3}
$\overline{\mu_{M_1}}$ (kNm)	110.832	101.412	101.416
$\overline{\sigma_{M_1}}$ (kNm)	10.568	9.581	9.657
$\underline{\mu_{M_1}}$ (kNm)	76.804	85.679	85.682
$\underline{\sigma_{M_1}}$ (kNm)	7.140	7.919	7.983
t_{com} (s)	2.031×10^{3}	6.399×10^{4}	6.366×10^{4}

Table 3.9 Probability distribution types identified by statistical inference analyses in Case 3

	Probability Distribution	
	Scenario 1	*Scenario 2*
$u_{167,x}$	Normal	Gumbel
$u_{70,y}$	Lognormal	Lognormal
M_1	Normal	Gumbel

Table 3.10 Parametric and non-parametric test statistics for $u_{167,x}$ for *Scenario 1* of Case 3

Scenario 1-$u_{167,x}$	
Parametric Method	Non-parametric Method

Distribution	Log Likelihood $\times 10^4$	AIC $\times 10^4$	BIC $\times 10^4$	AD Test	KS Test
Normal	***3.0879***	***-6.1755***	***-6.1740***	***0.9730***	***0.0114***
Gamma	3.0862	-6.1720	-6.1706	3.1464	0.0135
Lognormal	3.0821	-6.1638	-6.1624	8.3085	0.0191
Gumbel	3.0195	-6.0386	-6.0372	97.6199	0.0581
Logistic	3.0769	-6.1533	-6.1519	10.4052	0.0225
Log logistic	3.0742	-6.1480	-6.1465	13.6244	0.0229
Weibull	3.0461	-6.0918	-6.0903	59.0456	0.0428
Rayleigh	1.9963	-3.9925	-3.9918	2.8050×10^3	0.4340

In addition to the illustration on the applicability and effectiveness of the proposed UPMP approach, both parametric and non-parametric statistical inference analyse methods which are widely adopted [163–166] in structural engineering for identifying the probability distributions of random variables are selected to construct the probability density functions (PDFs) and cumulative distribution functions (CDFs) of the bounds of the concerned structural responses demonstrated in Table 3.8. The selected parametric methods include log-likelihood test, Akaike information criterion (AIC) test and Bayesian information criterion (BIC) test. The non-parametric analyses adopted involve Kolmogorov–Smirnov (KS) test and Anderson–Darling (AD) test. These methods are implemented on the simulated results of $u_{167,x}$, $u_{10,y}$ and M_1 at each realisation of interval parameters from MCS-QMCS for both *Scenarios 1* and *2*. According to the test statistics, the types of probability distribution which are closest fit for describing the selected structural responses are summarised in Table 3.9. For demonstration purpose, the test statistics for the samples corresponding to the 50th realisation of interval parameters for *Scenarios 1* and 2 are respectively summarised as in Table 3.10 and 3.11. The maximum test statistics obtained by the log likelihood approach indicates the best

fitted probability distribution for the given samples, while the distribution with minimum test statistics obtained by other methods is inferred as the most suitable.

Table 3.11 Parametric and non-parametric test statistics for $u_{167,x}$ for *Scenario 2* of Case 3

Case 2-$u_{167,x}$					
Parametric Method				Non-parametric Method	
Distribution	Log Likelihood $\times 10^4$	AIC $\times 10^4$	BIC $\times 10^4$	AD Test	KS Test
Normal	3.1477	-6.2949	-6.2935	83.7019	0.0623
Gamma	3.1754	-6.3503	-6.3489	46.1837	0.0475
Lognormal	3.1859	-6.3714	-6.3700	31.6121	0.0399
Gumbel	***3.2039***	***-6.4074***	***-6.4060***	***4.8649***	***0.0157***
Logistic	3.1645	-6.3286	-6.3272	48.6919	0.0381
Log logistic	3.1866	-6.3727	-6.3713	22.4190	0.0243
Weibull	3.0184	-6.0363	-6.0349	296.2260	0.1078
Rayleigh	2.0533	-4.1064	-4.1057	2.8695×10^3	0.4648

Subsequently, the probability density functions (PDFs) and cumulative distribution functions (CDFs) of the demonstrated displacement and force responses of *Scenarios 1* and *2* are shown in Figures 3.10 and 3.11, respectively. It can be observed from Figures 3.10 and 3.11 that the PDFs of the MCS-QMCS results are bounded by the upper bound of PDF (PDF-UB) and lower bound of PDF (PDF-LB) constructed based on the results of UPMP approach. Moreover, the upper bound of CDF (CDF-UB) and lower bound of CDF (CDF-LB) of the selected nodal displacement and elemental force are rigorously enclosing all CDFs constructed basing on the results of the MCS-QMCS approach.

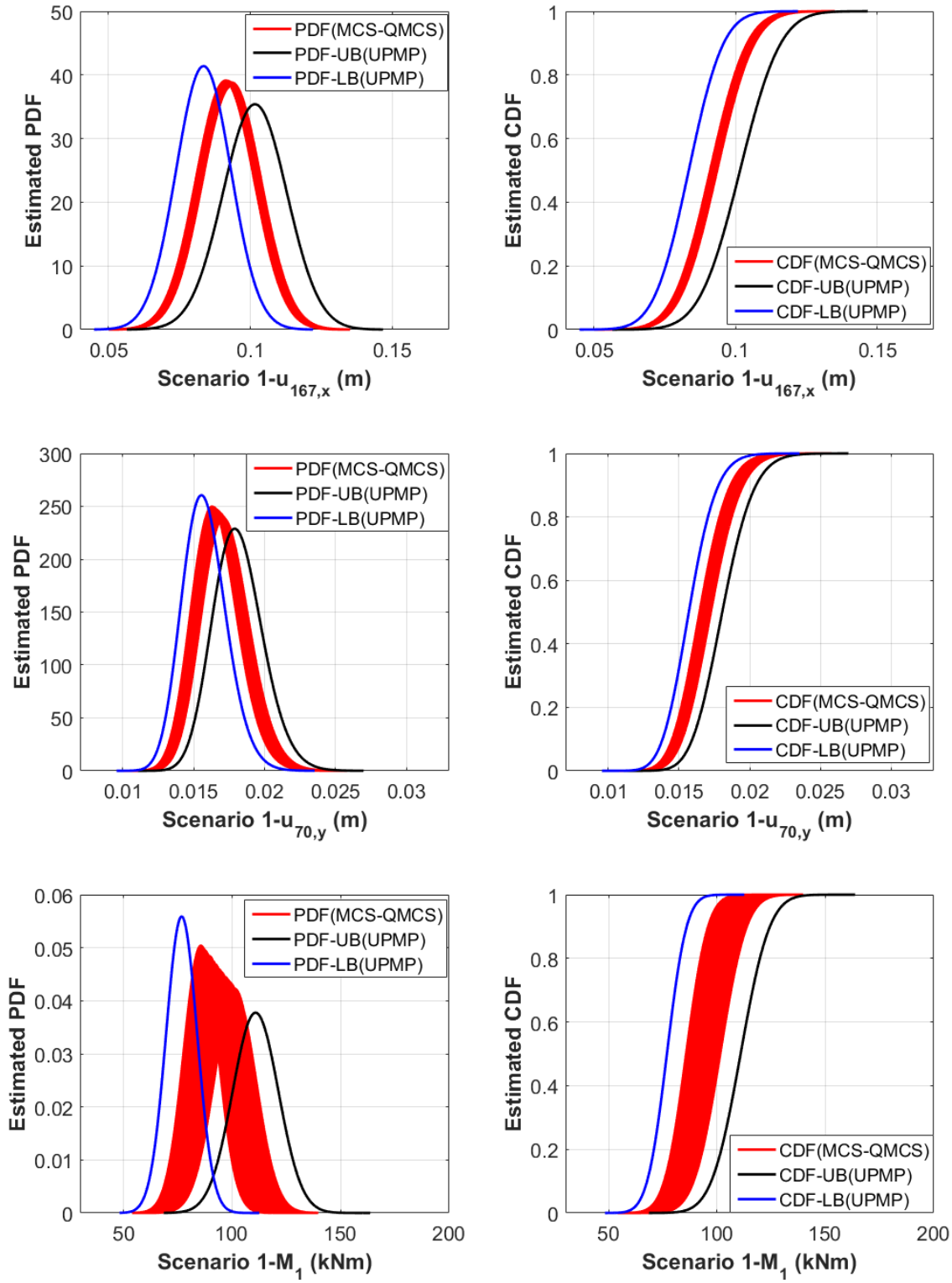

Figure 3.10 PDFs and CDFs of selected structural responses of Scenario 1 of Case 3 of the frame structure

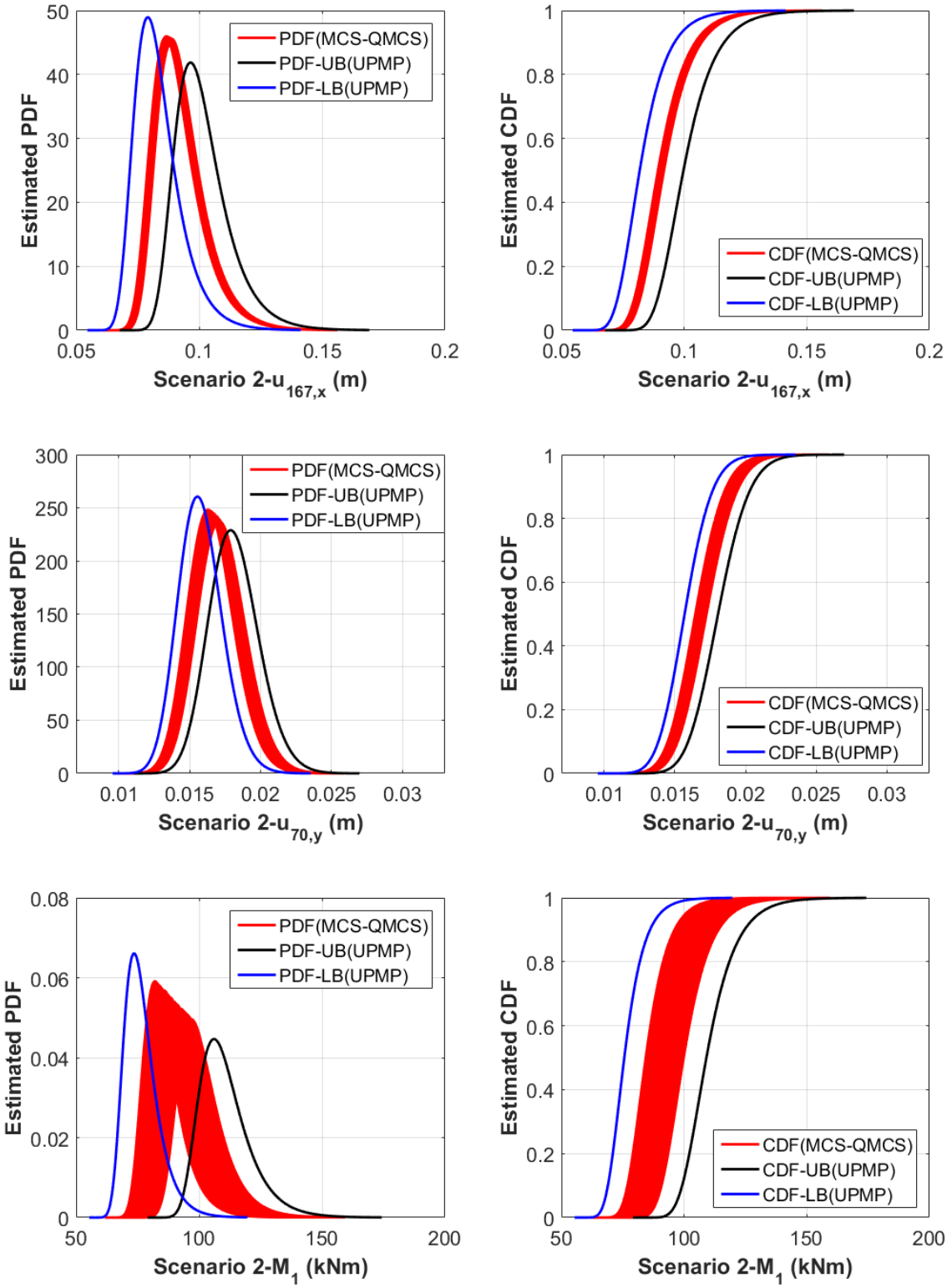

Figure 3.11 PDFs and CDFs of selected structural responses of Scenario 2 of Case 3 of the frame structure

3.5 Conclusion

This paper presents a computational scheme named as *unified perturbation mathematical programming* (UPMP) approach for structural analysis involving random and interval parameters. The proposed approach offers a potent non-sampling strategy for investigating the static response for various engineering structures. The integration of matrix perturbation with mathematical programming within the proposed computational approach transforms the intricate hybrid random interval analysis into a series of NLP problems. By treating interval parameters as inequality constraints in the mathematical programming, the interval dependency is eliminated from the algorithm.

The applicability of the proposed UPMP approach is critically validated by investigating various types of engineering structures through numbers of uncertain circumstances. By comparing with analytical solution and results obtained from sampling method, the accuracy and computational efficiency of the proposed uncertainty analysis scheme are evidently illuminated. Additionally, hypothesis test is implemented in this study for identifying the probability distribution of the structural responses.

From the computational benefits associated with the proposed UPMP approach, it is possible to further extend the proposed computational scheme for other types of engineering analyses, such as hybrid uncertain linear and nonlinear buckling analysis, dynamic analysis of structures involving random and interval uncertainties, etc. Furthermore, the concept of the proposed approach can be also extended to other areas of study where the effects of uncertainties must be evaluated.

Chapter 4 . Uncertain structural free vibration analysis with non-probabilistic spatially varying parameters

4.0 Summary

The uncertain free vibration analysis of engineering structure with the consideration of non-stochastic spatially dependent uncertain parameters is investigated. The novel concept of interval field is implemented to model the intrinsic spatial dependency of the uncertain-but-bounded system parameters. By employing the appropriate discretisation scheme, evaluations on natural frequencies for engineering structures involving interval fields can be executed within the framework of finite element method (FEM). Furthermore, a robust, yet efficient, computational strategy is freshly proposed such that, the extreme bounds of natural frequencies of the structure involving interval fields can be rigorously captured by performing two independent eigen-analyses. Within the proposed computational analysis framework, the traditional interval arithmetic is not employed so the undesirable effect of the interval overestimation can be completed eliminated. Consequently, both sharpness and physical feasibility of the results can be secured into certain extent for any particularly discretised interval fields. The plausibility of the new interval field model, as well as the feasibility of the proposed computational scheme, are evidently demonstrated by investigating both academic sized and practically motivated engineering structures.

The remainder of this chapter is organised as follows. The Section 4.1 offers a brief background of free vibration analysis of structures with uncertain variables. In Section 4.2, the detailed description of the concept of interval field and the particularly

adopted field discretisation method are introduced. Subsequently, the problem statement on uncertain free vibration analysis with interval fields and the proposed computational scheme are formally presented in Section 4.3. Furthermore, both academic sized and practically motivated numerical examples are thoroughly investigated in Section 4.4 for the purpose of illustrating the applicability and accuracy of the proposed computational scheme. Finally, some concluding remarks are drawn in Section 4.5.

The research work developed in this chapter has produced one journal paper which has been published in *ASCE-ASME Journal of Risk and Uncertainty in Engineering Systems, Part B: Mechanical Engineering*. The detail of the publication is: Feng, J., Li, Q., Sofi, A., Li, G., Wu, D., & Gao, W. (2018). Uncertain structural free vibration analysis with non-probabilistic spatially varying parameters. *ASCE-ASME Journal of Risk and Uncertainty in Engineering Systems, Part B: Mechanical Engineering*. https://doi.org/10.1115/1.4041501

4.1 Introduction

For practical engineering applications, the natural frequencies and the corresponding mode shapes are critical for analysing vibrational behaviours of structural systems. While deterministic analysis is widely adopted, the nondeterministic features or so-called uncertainties, which inherently exist within the structural systems and modelling process, could affect the credibility of the prediction of dynamic behaviours of the structures [1, 5, 8]. Therefore, it is indispensable to develop uncertain free vibration analyses for critically evaluating mercurial effects of uncertainties on the dynamic performance of engineering structures [94, 167, 168].

Conventionally, probabilistic/stochastic approaches, which are established on the solid theoretical foundation of probability and statistics, are frequently implemented for

uncertain natural frequency analysis [15, 139]. The incorporation of the probabilistic framework with FEM leads to the stochastic finite element method (SFEM), which has been extensively adopted in solving random eigenvalue problems in structural engineering [169]. The sampling approaches, such as the direct Monte-Carlo simulation method, are recognised as the most robust SFEM strategy for the probabilistic analysis of natural frequencies [28, 170]. In addition, numerous non-simulative computational strategies [171–175] have been developed which offer the alternatives to the sampling approaches by providing the numerical approximations on statistical characteristics (i.e., mean and standard deviation) of the random eigenvalues. Furthermore, the effects of spatial variabilities of the uncertain structural parameters are advantageously addressed by the introduction of spectral stochastic finite element method (SSFEM) [33–35, 176]. Despite the prevalent implementation of probabilistic methodologies for uncertain eigenvalue analysis in practical engineering applications, the creditability of such approaches strongly depends on the availability of information regarding the considered uncertain variables [154, 177].

In practical engineering applications, the prerequisites for implementing the probabilistic approaches cannot be always guaranteed due to the phenomenon of the information deficiency of uncertain system parameters. Under such circumstances, non-probabilistic methods including convex models, fuzzy sets and interval models offer the supplementary solutions for uncertainty analysis of structures [12, 13, 69, 178–180]. Among these methods, interval approaches are widely adopted in the natural frequency analysis of vibration systems with uncertainties, which lead to the interval eigenvalue problems within the framework of FEM [123].

By thoroughly examining on literatures regarding the non-stochastic uncertain eigenvalue problems, the spatial variations of uncertain-but-non-random parameters have not been systematically addressed in the free vibration analysis of engineering structures. Among all reported works regarding interval free vibration analysis, the bounded structural system parameters are either considered spatially independent, or simplified into single representation per category throughout entire structural system (i.e., the Young's moduli of all structural components are considered as a single interval variable). It has been clearly demonstrated by previous studies [115, 116] that the realistic uncertain-but-non-random fluctuations of system variables may not be precisely described by these two assumptions. Therefore, the interval eigenvalue problems of structures are necessarily to be extended to incorporate the intrinsic spatially variant characteristics of these uncertain parameters.

In order to achieve a more realistic and efficient uncertainty analysis framework, the uncertain free vibration analysis with interval fields is investigated in this study for the first time. Unlike traditional interval analysis framework, both uncertain Young's modulus and density of structural material are modelled as spatially dependent uncertain parameters. By adopting such novel uncertainty modelling technique, the uncertain system parameters can be more realistically modelled by incorporating the interaction between degree of uncertainty and variation of physical location. Consequently, the benefit of such integration is that the results of the uncertainty analysis are meaningful in both theoretical and practical aspects. Furthermore, a novel computational scheme is proposed for capturing the extreme bounds of the natural frequencies of engineering structures involving diverse interval fields. By adopting appropriate discretization techniques, the extreme bounds of natural frequencies of engineering structures can be

rigorously calculated by two independent eigen-analyses. Within the proposed computational framework, the undesirable effects of interval overestimation associated with the inappropriate practice of the interval arithmetic can be fully eliminated and also, both sharpness and physical feasibility of the computational bounds on the natural frequency of the structure can be well preserved for any particularly discretised interval fields. Consequently, both computational effectiveness and efficiency of the proposed method for uncertain free vibration analysis with interval fields can be promised into certain extent.

4.2 Concept of interval field

Conventionally, the spatial variabilities of structural system parameters are modelled by adopting the theory of random field. Benefiting from the solid theoretical background, the random field has been extensively implemented across many modern engineering applications [32, 33]. The combination of such theory with FEM leads to a powerful uncertainty analysis framework, namely the spectral stochastic finite element method (SSFEM) [34, 35]. As it is constructed based on the theory of probability, the utilisation of random field requires the classification of the type of random field as well as the determination of the spatial correlation through the establishment of the covariance function. The satisfaction of these two prerequisites becomes possible if sufficient amount of samples are available, but such optimism are generally disappointed in real life engineering due to a variety of reasons [85, 96, 115, 116]. Therefore, an alternative non-probabilistic approach is essentially needed for situations where random field model is prohibited by information deficiency.

4.2.1 Introduction of the interval field

In the motivation of offering a preliminary non-probabilistic approach to model the spatially varying uncertain parameters, the concept of interval field was initially introduced in [115] including both explicit and implicit formulations. In contrast to the random field models, the interval field has the superior competence in performing valid uncertainty analysis for engineering systems based on whatever information available for the spatially dependent uncertain parameters. For the purpose of presenting the concept of interval field in a more appropriate fashion, several essential definitions regarding such novel concept are introduced as follows [120].

Definition 1. *An interval field* $I(\chi)$ *is a collection of interval variables indexed by a continuous parameter* $\chi \in \mathbf{\Theta}$ *, where* $\mathbf{\Theta}$ *is an open set of* $\Re^{n}$.

From **Definition 1**, the realization of the interval field, denoted as $I_r(\chi)$, is a sample function of the interval field $I(\chi)$.

Definition 2. *The upper bound function of the interval field, denoted as* $\bar{I}(\chi): \Re^n \to \Re$ *, such that* $\forall \chi_p \in \mathbf{\Theta}$, $I(\chi_p) \le \bar{I}(\chi_p)$.

Definition 3. *The lower bound function of the interval field, denoted as* $\underline{I}(\chi): \Re^n \to \Re$ *, such that* $\forall \chi_p \in \mathbf{\Theta}$, $\underline{I}(\chi_p) \le I(\chi_p)$.

From **Definitions 2** and **3**, the upper and lower bound functions are essentially providing a finite envelope which is strictly bounding the interval field within. Furthermore, at any specified location χ_p, $I(\chi_p)$ becomes an interval variable of $I(\Re)$, where $\mathbf{I}(\Re)$ denotes the closed set for all real intervals, such that $I(\chi_p) = I_p := [\underline{I}(\chi_p), \bar{I}(\chi_p)] = \{I \in \Re \mid \underline{I_p} \le I \le \overline{I_p}\}$ with $\underline{I}(\chi_p) = \underline{I_p}$ and $\bar{I}(\chi_p) = \overline{I_p}$.

Definition 4. *The mid-point function of the interval field, denoted as* $I^{C}(\chi):\Re^{n}\rightarrow\Re$, *such that*

$$I^{C}(\chi):=\frac{\bar{I}(\chi)+\underline{I}(\chi)}{2},\ \forall\chi\in\boldsymbol{\Theta} \tag{4.1}$$

Definition 5. *The half-width function of the interval field, denoted as* $I^{W}(\chi):\Re^{n}\rightarrow\Re$, *such that*

$$I^{W}(\chi):=\frac{\bar{I}(\chi)-\underline{I}(\chi)}{2},\ \forall\chi\in\boldsymbol{\Theta} \tag{4.2}$$

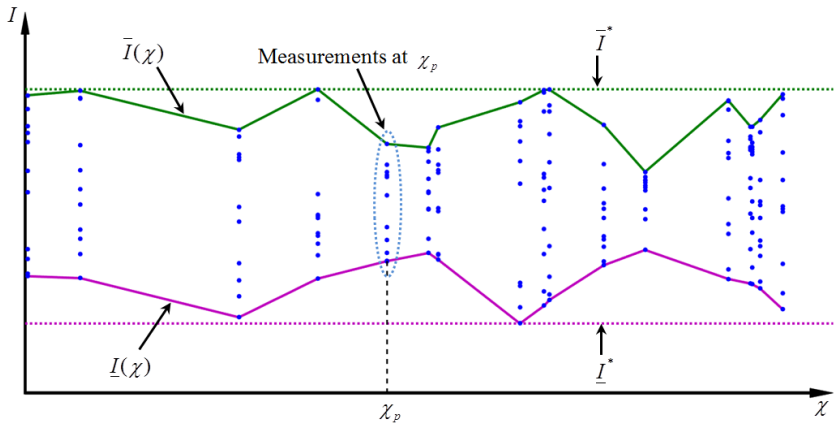

Figure 4.1 Example of 1D interval field

Definition 6. *A constant interval field is defined such that the lower and upper bound functions are constants for all* $\chi\in\boldsymbol{\Theta}$. *That is,* $\underline{I}(\chi)=\underline{I}^{*}$ *and* $\bar{I}(\chi)=\bar{I}^{*}$, *where* $\underline{I}^{*}\leq\bar{I}^{*}\in\Re$.

From **Definition 6**, a conventional interval parameter can be alternatively considered as a constant interval field. In order to illustrate the concept of interval field, a simple 1D interval field is presented in Figure 4.1. Let $\chi\in\Re_{+}:=\{\chi_{p}\,|\,0\leq\chi_{p}\leq\infty\}$ denotes a physical coordinate.

It is indicated in Figure 4.1 that sets of data have been collected at various measuring points along the $\chi-$axis. However, due to diverse reasons including cost issues, technological issues, and accessibility issues etc., the amount of collected data at each measuring point is insufficient for constructing a precise statistical profile for the considered structural system parameter. Consequently, the implementation of random field approach becomes a challenging task since that the distribution type as well as the correlation of the considered spatially varying uncertain parameter cannot be appropriately confirmed. In this context, the interval field model can be implemented which describes the considered spatial-variant uncertainty based on all the available information. From the collected data, the upper and lower bound functions of the considered uncertain variable can be simply established by collecting the upper and lower bounds of the data at each measuring point. Subsequently, the spatial variability of the considered uncertain parameter is feasibly confined by the envelope offered by the two extreme bound functions. It is emphasized that the upper and lower bound functions are defined based on the currently available information. These functions can be accordingly refined if additional information is provided. Furthermore, once sufficient amount of data has been collected, that is the precise probability profile can be constructed, the random field model can be certainly adopted to model the spatially dependent uncertain parameters instead of the interval field model.

In addition to the upper and lower bound functions, the conventional interval variable, which is also defined as a constant interval field, is also illustrated in Figure 4.1 for demonstrating the difference between two distinctive models. It can be noticed by visually comparing the two models that, the conventional interval variable simply provide an overconservative hull by taking the global maximum and minimum across the entire

measured data. Despite that all the observed realisations of the uncertain parameters are absolutely confined in this envelope, the spatial coherence of the uncertain parameter is completely neglected in the conventional interval approach. Consequently, more conservative results may be obtained from the subsequent analysis basing on such overprotective model. Therefore, it is evidently illustrated that the correlation between the physical location and the degree of variation of the uncertain parameter can be meticulously reflected within the formation of upper and lower bound functions in comparison to the traditionally adopted interval variable models.

4.2.2 Discretisation of the interval field

An interval field discretising scheme, or simply referred as the discretisation, is an approximation of the interval field $I(\chi)$ by $\hat{I}(\chi)$ defined by means of a finite set of interval variables $\{\zeta_j, j = 1,...,m^I\}$ with m^I denotes the total number of structural elements, collected by an interval vector denoted by $\mathbf{I}$, that is:

$$I(\chi) \approx \hat{I}(\chi) = \Gamma(\chi, \mathbf{I}) \tag{4.3}$$

For the purpose of this study, the adopted discretising technique is the spatial average method which was proposed by Vanmarcke and Grigoriu [121] for discretising the random field. Within the adopted discretising scheme which is constructed based on the available meshing information of the structure, the interval field is approximated as a constant within each structural element, which is calculated as the average of the original interval field over the domain of the element. If there are q ($q \geq 1$) interval fields involved in the analysis, for the $\hat{i}$ th ($\hat{i} = 1,...,q$) interval field, the implemented spatial average method can be interpreted as:

$$\hat{I}_{\hat{i},i_e}(\chi) := \frac{\int_{\mathbf{\Psi}_{i_e}} I_{\hat{i},i_e}(\chi) d\mathbf{\Psi}_{i_e}}{\left|\mathbf{\Psi}_{i_e}\right|} = \hat{I}_{\hat{i},i_e}, \chi \in \mathbf{\Psi}_{i_e}, \hat{i} = 1,...,q, i_e = 1,...,n_s \tag{4.4}$$

where $\mathbf{\Psi}_{i_e}$ denotes the domain of the i_eth structural element; $\left|\mathbf{\Psi}_{i_e}\right|$ denotes the area of the concerned element. The interval vector $\hat{\mathbf{I}}_{\hat{i}}$ corresponding to an approximation of the θth interval field can be defined as the collection of these interval variables such that $\hat{\mathbf{I}}_{\hat{i}} = [\hat{I}_{\hat{i},1}, ..., \hat{I}_{\hat{i},n_s}]^T$.

Consequently, the lower and upper bound functions can be respectively discretised into two vectors $\underline{\hat{\mathbf{I}}_{\hat{i}}} = [\underline{\hat{I}_{\hat{i},1}}, ..., \underline{\hat{I}_{\hat{i},n_s}}]^T$ and $\overline{\hat{\mathbf{I}}_{\hat{i}}} = [\overline{\hat{I}_{\hat{i},1}}, ..., \overline{\hat{I}_{\hat{i},n_s}}]^T$ in a similar fashion such that:

$$\hat{\mathbf{I}}_{\hat{i}} \in \mathbf{\Omega} := \{\hat{\mathbf{I}}_{\hat{i}} \in \Re^{n_s} \mid \underline{\hat{I}_{\hat{i},i_e}} \le \hat{I}_{\hat{i},i_e} \le \overline{\hat{I}_{\hat{i},i_e}}, i_e = 1,...,n_s\} \tag{4.5}$$

where $\overline{\hat{I}_{\hat{i},i_e}}$ and $\underline{\hat{I}_{\hat{i},i_e}}$ denote the upper and lower bounds of $\hat{I}_{\hat{i},i_e}$, respectively. Moreover, a mid-point vector $\hat{\mathbf{I}}_{\hat{i}}^C$ associated with $\hat{\mathbf{I}}_{\hat{i}}$ can be defined as:

$$\hat{\mathbf{I}}_{\hat{i}}^C \in \mathbf{\Omega} := \{\hat{\mathbf{I}}_{\hat{i}}^C \in \Re^{n_s} \mid \hat{I}_{\hat{i},i_e}^C = \frac{\overline{\hat{I}_{\hat{i},i_e}} + \underline{\hat{I}_{\hat{i},i_e}}}{2}, i_e = 1,...,n_s\} \tag{4.6}$$

and the half-width vector $\hat{\mathbf{I}}_{\hat{i}}^H$ associated with $\hat{\mathbf{I}}_{\hat{i}}$ can be additionally defined as:

$$\hat{\mathbf{I}}_{\hat{i}}^H \in \mathbf{\Omega} := \{\hat{\mathbf{I}}_{\hat{i}}^H \in \Re^{n_s} \mid \hat{I}_{\hat{i},i_e}^H = \frac{\overline{\hat{I}_{\hat{i},i_e}} - \underline{\hat{I}_{\hat{i},i_e}}}{2}, i_e = 1,...,n_s\} \tag{4.7}$$

Therefore, the original interval fields are transformed into standard interval vectors with known upper and lower bound information. This has brought substantive computational benefit for implementing such analysis in the framework of FEM.

4.3 Uncertain free vibration analysis of structures with interval fields

4.3.1 Interval eigenvalue problem with spatially dependent uncertain parameters

Within the framework of FEM, the free vibration analysis of linear undamped engineering structures with spatially dependent interval uncertainties is conducted by solving the generalised interval eigenvalue problems. For a structure with d degrees-of-freedom, the governing equation of the generalised eigenvalue problem involving interval fields is explicitly formulated as:

$$\mathbf{K}_s(\boldsymbol{\eta})\boldsymbol{\Phi}_v = \omega_v^2 \mathbf{M}_s(\boldsymbol{\eta})\boldsymbol{\Phi}_v \tag{4.8a}$$

such that:

$$\boldsymbol{\eta} \in \boldsymbol{\Omega} := \{\boldsymbol{\eta} \in \Re^q \mid \eta_{\hat{i}} \in I_{\eta_{\hat{i}}}(\boldsymbol{\chi}), \hat{i} = 1,...,q\},\ \boldsymbol{\chi} \in \boldsymbol{\Psi} \tag{4.8b}$$

where $\mathbf{K}_s(\boldsymbol{\eta}) \in \Re^{d_s \times d_s}$ denotes the stiffness matrix of the structure; $\mathbf{M}_s(\boldsymbol{\eta}) \in \Re^{d_s \times d_s}$ denotes the mass matrix of the structure; ω_v is the vth ($v = 1,...,d_s$) natural frequency and $\boldsymbol{\Phi}_v \in \Re^{d_s}$ is the associated eigenvector. $\boldsymbol{\eta}$ denotes the concerned spatially uncertain system parameters. $I_{\eta_\theta}(\boldsymbol{\chi})$ denotes the interval field associated to the θth spatially variant uncertainty; and $\boldsymbol{\Psi}$ denotes the domain of the entire structural system.

Unlike traditional uncertain eigenvalue problem associated with conventional interval variables, Eq. (4.8) is actually defines an uncertain eigenvalue problem involving spatially dependent uncertain parameters. Consequently, Eq. (4.8) is at least as challenging as the conventional interval eigenvalue problem due to fact that the intrinsic correlation between degree of uncertainty and physical location of the uncertain parameter is additionally considered. The misery of adequately conquering such difficulty is that the sharpness of the bounded eigenvalues has to be rigorously promised at the same

time, various physical feasibilities, which are including the symmetry of stiffness and mass matrices of the structural system, and the intrinsic spatial dependency of the concerned uncertain parameters have to be rigorously maintained throughout the entire calculation process. However, according to the authors' limited knowledge regarding interval eigenvalue problem involving spatial dependency, there are not any mature theoretical instructions on solving such intricate problems have been developed yet.

Even though there is a lack of theoretical support on tackling such challenges, some adequate strategies are urgently needed to overcome these hurdles in real life engineering applications. In the light of achieving a more appropriate uncertainty analysis, a new, yet robust, computational approach is proposed in this study, which serves as the first attempt on tackling the intricate problem of the uncertain structural free vibration analysis with interval fields.

4.3.2 Uncertain free vibration analysis of structures involving interval fields

The proposed computational procedure firstly integrates the concept of interval field into the framework of the finite element method (FEM). By adopting the field discretisation scheme expressed as Eq. (4.4), each interval field is approximated by a finite set of interval variables which are respectively associated to all the structural elements. For the generalised eigen-analysis with multiple spatially dependent uncertainties illustrated as Eq. (4.8), each element is assigned q interval variables by the discretisation of the interval fields. In such way, the compatibility between the spatial variation of the uncertain parameters and the implementation of FEM is thoroughly maintained by the proposed computational strategy.

Without loss of generality, for the vth element of the structural system, an elemental interval vector $\mathbf{I}_{i_e}^{e} \in \Re^{q}$ can be defined as the collection of all the q interval

variables resulted from the interval field discretisation associated with this element such that $\hat{\mathbf{I}}_{i_e}^{e} = [\hat{I}_{1,i_e}, ..., \hat{I}_{q,i_e}]^T$. The corresponding upper and lower bound vectors associated with the element can be respectively defined as $\overline{\hat{\mathbf{I}}_{i_e}^{e}} = [\overline{\hat{I}_{1,i_e}}, ..., \overline{\hat{I}_{q,i_e}}]^T$ and $\underline{\hat{\mathbf{I}}_{i_e}^{e}} = [\underline{\hat{I}_{1,i_e}}, ..., \underline{\hat{I}_{q,i_e}}]^T$, where the entries of the vectors are defined as Eq. (4.5). Subsequently, the elemental stiffness matrix $\mathbf{K}_{i_e}^{e}(\hat{\mathbf{I}}_{i_e}^{e}) \in \Re^{d_s \times d_s}$ and mass matrix $\mathbf{M}_{i_e}^{e}(\hat{\mathbf{I}}_{i_e}^{e}) \in \Re^{d_s \times d_s}$ can respectively expressed as the functions of the element interval vector. Subsequently, the spatially uncertain stiffness and mass matrices of the structural system can be explicitly approximated as Eqs. (4.9) and (4.10):

$$\mathbf{K}_s(\boldsymbol{\eta}) \approx \mathbf{K}_s(\hat{\mathbf{I}}_1, ..., \hat{\mathbf{I}}_q) = \sum_{i_e=1}^{n_s} \mathbf{K}_{i_e}^{e}(\hat{\mathbf{I}}_{i_e}^{e}) \tag{4.9}$$

$$\mathbf{M}_s(\boldsymbol{\eta}) \approx \mathbf{M}_s(\hat{\mathbf{I}}_1, ..., \hat{\mathbf{I}}_q) = \sum_{i_e=1}^{n_s} \mathbf{M}_{i_e}^{e}(\hat{\mathbf{I}}_{i_e}^{e}) \tag{4.10}$$

where $\mathbf{K}_s(\hat{\mathbf{I}}_1, ..., \hat{\mathbf{I}}_q) \in \Re^{d_s \times d_s}$ and $\mathbf{M}_s(\hat{\mathbf{I}}_1, ..., \hat{\mathbf{I}}_q) \in \Re^{d_s \times d_s}$ denote the uncertain-but-bounded global stiffness and mass matrices of the structural system. Thus, the spatial dependencies of interval uncertain parameters are thoroughly enclosed into the interval eigenvalue problem expressed as:

$$\mathbf{K}_s(\hat{\mathbf{I}}_1, ..., \hat{\mathbf{I}}_q)\hat{\boldsymbol{\Phi}}_v = \hat{\omega}_v^2 \mathbf{M}_s(\hat{\mathbf{I}}_1, ..., \hat{\mathbf{I}}_q)\hat{\boldsymbol{\Phi}}_v \tag{4.11}$$

where $\hat{\omega}_v$ denotes the approximation of ω_v of the linear structural system with spatially variant uncertainties such that $\{\hat{\omega}_v \in \Re \mid \underline{\hat{\omega}_v} \le \hat{\omega}_v \le \overline{\hat{\omega}_v},\ \text{for } v = 1, ..., d_s\}$, $\overline{\hat{\omega}_v}$ and $\underline{\hat{\omega}_v}$ denote to the upper and lower bounds of $\hat{\omega}_v$, respectively; $\hat{\boldsymbol{\Phi}}_v \in \Re^{d_s}$ denotes the eigenvector associated with $\hat{\omega}_v$. Subsequently, the uncertain eigenvalue analysis with

interval field is equivalently transformed into a format which can be processed within the framework of FEM.

By adopting the proposed interval field model, the uncertain Young's modulus and density can be respectively expressed as $I_E(\chi)$ and $I_\rho(\chi)$, with the associated upper and lower bound functions are $\overline{I_E}(\chi)$, $\underline{I_E}(\chi)$, $\overline{I_\rho}(\chi)$ and $\underline{I_\rho}(\chi)$. By implementing the spatial average approach, the uncertain-but-bounded spatial-variant Young's modulus and density are respectively discretised into the interval vectors $\hat{\mathbf{I}}_E = [\hat{I}_{E,1}, ..., \hat{I}_{E,n_s}]^T$ and $\hat{\mathbf{I}}_\rho = [\hat{I}_{\rho,1}, ..., \hat{I}_{\rho,n_s}]^T$ with n denotes the total number of structural elements. Moreover, the upper and lower bound functions are respectively discretised into the vectors $\overline{\hat{\mathbf{I}}_E} = [\overline{\hat{I}_{E,1}}, ..., \overline{\hat{I}_{E,n_s}}]^T$, $\underline{\hat{\mathbf{I}}_E} = [\underline{\hat{I}_{E,1}}, ..., \underline{\hat{I}_{E,n_s}}]^T$, $\overline{\hat{\mathbf{I}}_\rho} = [\overline{\hat{I}_{\rho,1}}, ..., \overline{\hat{I}_{\rho,n_s}}]^T$ and $\underline{\hat{\mathbf{I}}_\rho} = [\underline{\hat{I}_{\rho,1}}, ..., \underline{\hat{I}_{\rho,n_s}}]^T$ such that:

$$I_E(\chi) \approx \hat{\mathbf{I}}_E := \{\hat{\mathbf{I}}_E \in \Re^{n_s} \mid \underline{\hat{I}_{E,i_e}} \le \hat{I}_{E,i_e} \le \overline{\hat{I}_{E,i_e}}, i_e = 1,...,n_s\} \tag{4.12}$$

$$I_\rho(\chi) \approx \hat{\mathbf{I}}_\rho := \{\hat{\mathbf{I}}_\rho \in \Re^{n_s} \mid \underline{\hat{I}_{\rho,i_e}} \le \hat{I}_{\rho,i_e} \le \overline{\hat{I}_{\rho,i_e}}, i_e = 1,...,n_s\} \tag{4.13}$$

where $\overline{\hat{I}_{E,i_e}}$ and $\underline{\hat{I}_{E,i_e}}$ denote to the upper and lower bounds of $\hat{I}_{E,i_e}$, respectively; $\overline{\hat{I}_{\rho,i_e}}$ and $\underline{\hat{I}_{\rho,i_e}}$ denote the upper and lower bounds of $\hat{I}_{\rho,i_e}$, respectively. Thus, the spatially dependent uncertain stiffness and mass matrices can be respectively approximated as:

$$\mathbf{K}(I_E(\chi)) \approx \mathbf{K}(\hat{\mathbf{I}}_E) = \sum_{i_e=1}^{n_s} \mathbf{K}_{i_e}^e(\hat{I}_{E,i_e}) \tag{4.14}$$

$$\mathbf{M}(I_\rho(\chi)) \approx \mathbf{M}(\hat{\mathbf{I}}_\rho) = \sum_{i_e=1}^{n_s} \mathbf{M}_{i_e}^e(\hat{I}_{\rho,i_e}) \tag{4.15}$$

For the purpose of this study, only non-deficient structures are considered. Consequently, both stiffness and mass matrices are symmetric and positive-definite. By adopting the proposed computational approach, the upper and lower bounds of the eigenvalues can be respectively achieved by two independent eigen-analyses expressed as Eqs. (4.16) and (4.17):

$$[\mathbf{K}(\overline{\hat{\mathbf{I}}_E}) - \overline{\hat{\omega}_v^2}\mathbf{M}(\underline{\hat{\mathbf{I}}_\rho})]\overline{\hat{\mathbf{\Phi}}_v} = 0 \tag{4.16}$$

$$[\mathbf{K}(\underline{\hat{\mathbf{I}}_E}) - \underline{\hat{\omega}_v^2}\mathbf{M}(\overline{\hat{\mathbf{I}}_\rho})]\underline{\hat{\mathbf{\Phi}}_v} = 0 \tag{4.17}$$

where $\overline{\hat{\omega}_v}$ and $\underline{\hat{\omega}_v}$ denote the upper and lower bounds of $\hat{\omega}_v$, respectively; $\overline{\hat{\mathbf{\Phi}}_v}$ and $\underline{\hat{\mathbf{\Phi}}_v}$ respectively denote the eigenvectors (mode shapes) associated with $\overline{\hat{\omega}_v}$ and $\underline{\hat{\omega}_v}$, respectively. The validity of Eqs. (4.16) and (4.17) is demonstrated by the proof as follows.

Proof:

The computation for the *j*th eigenvalue ($\hat{\lambda}_v = \hat{\omega}_v^2$) of the structural system with discretised spatially dependent uncertain Young's modulus and density can be expressed as the Rayleigh's quotient:

$$\hat{\lambda}_v = \frac{\hat{\mathbf{\Phi}}_v{}^T\mathbf{K}_s(\hat{\mathbf{I}}_E)\hat{\mathbf{\Phi}}_v}{\hat{\mathbf{\Phi}}_v{}^T\mathbf{M}_s(\hat{\mathbf{I}}_\rho)\hat{\mathbf{\Phi}}_v} = \frac{\hat{\mathbf{\Phi}}_v{}^T\left[\sum_{v=1}^{n_s}\mathbf{K}_{i_e}^e(\hat{I}_{E,i_e})\right]\hat{\mathbf{\Phi}}_v}{\hat{\mathbf{\Phi}}_v{}^T\left[\sum_{i_e=1}^{n_s}\mathbf{M}_{i_e}^e(\hat{I}_{\rho,i_e})\right]\hat{\mathbf{\Phi}}_v} = \frac{a_v}{b_v} \tag{4.18}$$

Since both stiffness and mass matrices are positive-definite, the properties $a_v > 0$ and $b_v > 0$ are guaranteed. If there exists the upper and lower bounds of $\hat{\lambda}_v$ and the associated

eigenvectors within the specified variation ranges of the uncertain variables $\hat{\mathbf{I}}_E$ and $\hat{\mathbf{I}}_\rho$, then the bounds of $\hat{\lambda}_v$ can be calculated by the simple interval arithmetic expressed as Eqs. (4.19) and (4.20). In this context, the Young's modulus and density varies independently with each other.

$$\overline{\hat{\lambda}_v} = \frac{\max\left(\overline{\hat{\mathbf{\Phi}}_v}^T \mathbf{K}_s(\hat{\mathbf{I}}_E)\overline{\hat{\mathbf{\Phi}}_v}\right)}{\min\left(\overline{\hat{\mathbf{\Phi}}_v}^T \mathbf{M}_s(\hat{\mathbf{I}}_\rho)\overline{\hat{\mathbf{\Phi}}_v}\right)} = \frac{\overline{a_{1,v}}}{\underline{b_{1,v}}} \tag{4.19}$$

$$\underline{\hat{\lambda}_v} = \frac{\min\left(\underline{\hat{\mathbf{\Phi}}_v}^T \mathbf{K}_s(\hat{\mathbf{I}}_E)\underline{\hat{\mathbf{\Phi}}_v}\right)}{\max\left(\underline{\hat{\mathbf{\Phi}}_v}^T \mathbf{M}_s(\hat{\mathbf{I}}_\rho)\underline{\hat{\mathbf{\Phi}}_v}\right)} = \frac{\underline{a_{2,v}}}{\overline{b_{2,v}}} \tag{4.20}$$

where $a_{1,v} = \overline{\hat{\mathbf{\Phi}}_v}^T \mathbf{K}_s(\hat{\mathbf{I}}_E)\overline{\hat{\mathbf{\Phi}}_v}$ with its upper bound $\overline{a_{1,v}}$; $b_{1,v} = \overline{\hat{\mathbf{\Phi}}_v}^T \mathbf{M}_s(\hat{\mathbf{I}}_\rho)\overline{\hat{\mathbf{\Phi}}_v}$ with its lower bound $\underline{b_{1,v}}$; $a_{2,v} = \underline{\hat{\mathbf{\Phi}}_v}^T \mathbf{K}_s(\hat{\mathbf{I}}_E)\underline{\hat{\mathbf{\Phi}}_v}$ with its lower bound $\underline{a_{2,v}}$, and $b_{2,v} = \underline{\hat{\mathbf{\Phi}}_v}^T \mathbf{M}_s(\hat{\mathbf{I}}_\rho)\underline{\hat{\mathbf{\Phi}}_v}$ with its upper bound $\overline{b_{2,v}}$. In this context, $a_{1,v}$, $a_{2,v}$, $b_{1,v}$ and $b_{2,v}$ are real and positive. Subsequently, the computation of extremities of $\hat{\lambda}_v$ can be equivalently implemented by seeking the values of $\hat{\mathbf{I}}_E$ and $\hat{\mathbf{I}}_\rho$ which lead to $\overline{a_{1,v}}$, $\underline{a_{2,v}}$, $\underline{b_{1,v}}$ and $\overline{b_{2,v}}$.

For a real-valued function $f:\Re^{n_s} \to \Re$ which is differentiable at $\mathbf{x} \in \Re^{n_s}$, the rate of change of the function can be measured by the directional derivative of f with respect to a unit vector $\hat{\mathbf{u}} \in \Re^{n_s}$ ($|\hat{\mathbf{u}}| = 1$) defined [181] as Eq. (4.21):

$$\frac{\partial f}{\partial \hat{\mathbf{u}}}(\mathbf{x}) = \lim_{\tau \to 0} \frac{f(\mathbf{x} + \tau\hat{\mathbf{u}}) - f(\mathbf{x})}{\tau} = \nabla f(\mathbf{x}) \bullet \hat{\mathbf{u}} \tag{4.21}$$

where "$\bullet$" denote the dot product; $\hat{\mathbf{u}}$ indicates the direction of variation of $\mathbf{x}$; $\nabla f(\mathbf{x})$ denote the gradient of f at $\mathbf{x}$ which is defined as:

$$\nabla f(\mathbf{x}) = \left[\frac{\partial f}{\partial x_1}(\mathbf{x}), \ldots, \frac{\partial f}{\partial x_{n_s}}(\mathbf{x}) \right]^T \tag{4.22}$$

In this study, the increase of the discretised spatially variant Young's modulus and density from the corresponding lower bounds ($\underline{\hat{\mathbf{I}}_E}$ and $\underline{\hat{\mathbf{I}}_\rho}$) to the upper bounds ($\overline{\hat{\mathbf{I}}_E}$ and $\overline{\hat{\mathbf{I}}_\rho}$) can be respectively represented by two non-negative incremental vectors $\Delta\hat{\mathbf{I}}_E = \delta_E \hat{\mathbf{u}}_{\hat{\mathbf{I}}_E} = [\delta_E \hat{u}_{\hat{I}_{E,1}}, \ldots, \delta_E \hat{u}_{\hat{I}_{E,n_s}}]^T$ and $\Delta\hat{\mathbf{I}}_\rho = \delta_\rho \hat{\mathbf{u}}_{\hat{\mathbf{I}}_\rho} = [\delta_\rho u_{\hat{I}_{\rho,1}}, \ldots, \delta_\rho u_{\hat{I}_{\rho,n_s}}]^T$ such that:

$$\Delta\hat{\mathbf{I}}_E \in \mathbf{\Omega}_{\Delta\hat{\mathbf{I}}_E} := \{\Delta\hat{\mathbf{I}}_E \in \Re^{n_s} \mid 0 \le \delta_E \hat{u}_{\hat{I}_{E,i_e}} \le \overline{\hat{I}_{E,i_e}} - \underline{\hat{I}_{E,i_e}}, i_e = 1, \ldots, n_s\} \tag{4.23}$$

$$\Delta\hat{\mathbf{I}}_\rho \in \mathbf{\Omega}_{\Delta\hat{\mathbf{I}}_\rho} := \{\Delta\hat{\mathbf{I}}_\rho \in \Re^{n_s} \mid 0 \le \delta_\rho \hat{u}_{\hat{I}_{\rho,i_e}} \le \overline{\hat{I}_{\rho,i_e}} - \underline{\hat{I}_{\rho,i_e}}, v = 1, \ldots, n_s\} \tag{4.24}$$

where δ_E and δ_ρ denote the positive scalers which indicate the magnitude of the increase of $\hat{\mathbf{I}}_E$ and $\hat{\mathbf{I}}_\rho$, respectively; $\hat{\mathbf{u}}_{\hat{\mathbf{I}}_E} \in \Re^{n_s}$ and $\hat{\mathbf{u}}_{\hat{\mathbf{I}}_\rho} \in \Re^{n_s}$ are the arbitrary non-negative unit vectors, such that $\left|\hat{\mathbf{u}}_{\hat{\mathbf{I}}_E}\right| = 1$ and $\left|\hat{\mathbf{u}}_{\hat{\mathbf{I}}_\rho}\right| = 1$, which respectively represent the directions of $\Delta\hat{\mathbf{I}}_E$ and $\Delta\hat{\mathbf{I}}_\rho$.

Subsequently, the effect of the variation of $\hat{\mathbf{I}}_E$ on $a_{1,v}$ and $a_{2,v}$ can be evaluated by the directional derivatives of $a_{1,v}$ and $a_{2,v}$ with respect to an arbitrary increase of Young's modulus $\Delta\hat{\mathbf{I}}_E \in \Re^{n_s}$ from $\underline{\hat{\mathbf{I}}_E}$; and the effect of variation of $\hat{\mathbf{I}}_\rho$ on $b_{1,v}$ and $b_{2,v}$ can be evaluated by the directional derivatives of $b_{1,v}$ and $b_{2,v}$ with respect to an arbitrary

increase of density $\Delta\hat{\mathbf{I}}_{\rho} \in \Re^{n_s}$ from $\underline{\hat{\mathbf{I}}_{\rho}}$. The directional derivatives are illustrated as Eqs. (4.25) - (4.28) which are expressed as vector fields.

$$\nabla a_{1,v}(\underline{\hat{\mathbf{I}}_E}) \bullet \hat{\mathbf{u}}_{\hat{\mathbf{I}}_E} = \left[\frac{\partial a_{1,v}}{\partial \hat{I}_{E,1}}(\underline{\hat{\mathbf{I}}_E})\right]\hat{u}_{\hat{I}_{E,1}} + \ldots + \left[\frac{\partial a_{1,v}}{\partial \hat{I}_{E,n_s}}(\underline{\hat{\mathbf{I}}_E})\right]\hat{u}_{\hat{I}_{E,n_s}} \tag{4.25}$$

$$\nabla b_{1,v}(\underline{\hat{\mathbf{I}}_{\rho}}) \bullet \hat{\mathbf{u}}_{\hat{\mathbf{I}}_{\rho}} = \left[\frac{\partial b_{1,v}}{\partial \hat{I}_{\rho,1}}(\underline{\hat{\mathbf{I}}_{\rho}})\right]\hat{u}_{\hat{I}_{\rho,1}} + \ldots + \left[\frac{\partial b_{1,v}}{\partial \hat{I}_{\rho,n_s}}(\underline{\hat{\mathbf{I}}_{\rho}})\right]\hat{u}_{\hat{I}_{\rho,n_s}} \tag{4.26}$$

$$\nabla a_{2,v}(\underline{\hat{\mathbf{I}}_E}) \bullet \hat{\mathbf{u}}_{\hat{\mathbf{I}}_E} = \left[\frac{\partial a_{2,v}}{\partial \hat{I}_{E,1}}(\underline{\hat{\mathbf{I}}_E})\right]\hat{u}_{\hat{I}_{E,1}} + \ldots + \left[\frac{\partial a_{2,v}}{\partial \hat{I}_{E,n_s}}(\underline{\hat{\mathbf{I}}_E})\right]\hat{u}_{\hat{I}_{E,n_s}} \tag{4.27}$$

$$\nabla b_{2,v}(\underline{\hat{\mathbf{I}}_{\rho}}) \bullet \hat{\mathbf{u}}_{\hat{\mathbf{I}}_{\rho}} = \left[\frac{\partial b_{2,v}}{\partial \hat{I}_{\rho,1}}(\underline{\hat{\mathbf{I}}_{\rho}})\right]\hat{u}_{\hat{I}_{\rho,1}} + \ldots + \left[\frac{\partial b_{2,v}}{\partial \hat{I}_{\rho,n_s}}(\underline{\hat{\mathbf{I}}_{\rho}})\right]\hat{u}_{\hat{I}_{\rho,n_s}} \tag{4.28}$$

where the components of the gradients in Eqs. (4.25) - (4.28) can be respectively expressed as:

$$\frac{\partial a_{1,v}}{\partial \hat{I}_{E,i_e}}(\underline{\hat{\mathbf{I}}_E}) = \overline{\hat{\mathbf{\Phi}}_v}^T \left.\frac{\partial \mathbf{K}_s(\hat{\mathbf{I}}_E)}{\partial \hat{I}_{E,i_e}}\right|_{\hat{\mathbf{I}}_E = \underline{\hat{\mathbf{I}}_E}} \overline{\hat{\mathbf{\Phi}}_v} = \overline{\hat{\mathbf{\Phi}}_v}^T \mathbf{K}_{\underline{\hat{I}_{E,i_e}}} \overline{\hat{\mathbf{\Phi}}_j} \tag{4.29}$$

$$\frac{\partial b_{1,v}}{\partial \hat{I}_{\rho,i_e}}(\underline{\hat{\mathbf{I}}_{\rho}}) = \overline{\hat{\mathbf{\Phi}}_v}^T \left.\frac{\partial \mathbf{M}_s(\hat{\mathbf{I}}_{\rho})}{\partial \hat{I}_{\rho,i_e}}\right|_{\hat{\mathbf{I}}_{\rho} = \underline{\hat{\mathbf{I}}_{\rho}}} \overline{\hat{\mathbf{\Phi}}_v} = \overline{\hat{\mathbf{\Phi}}_v}^T \mathbf{M}_{\underline{\hat{I}_{\rho,i_e}}} \overline{\hat{\mathbf{\Phi}}_v} \tag{4.30}$$

$$\frac{\partial a_{2,v}}{\partial \hat{I}_{E,i_e}}(\underline{\hat{\mathbf{I}}_E}) = \underline{\hat{\mathbf{\Phi}}_v}^T \left.\frac{\partial \mathbf{K}_s(\hat{\mathbf{I}}_E)}{\partial \hat{I}_{E,i_e}}\right|_{\hat{\mathbf{I}}_E = \underline{\hat{\mathbf{I}}_E}} \underline{\hat{\mathbf{\Phi}}_v} = \underline{\hat{\mathbf{\Phi}}_v}^T \mathbf{K}_{\underline{\hat{I}_{E,i_e}}} \underline{\hat{\mathbf{\Phi}}_v} \tag{4.31}$$

$$\frac{\partial b_{2,v}}{\partial \hat{I}_{\rho,i_e}}(\underline{\hat{\mathbf{I}}_{\rho}}) = \underline{\hat{\mathbf{\Phi}}_v}^T \left.\frac{\partial \mathbf{M}_s(\hat{\mathbf{I}}_{\rho})}{\partial \hat{I}_{\rho,i_e}}\right|_{\hat{\mathbf{I}}_{\rho} = \underline{\hat{\mathbf{I}}_{\rho}}} \underline{\hat{\mathbf{\Phi}}_v} = \underline{\hat{\mathbf{\Phi}}_v}^T \mathbf{M}_{\underline{\hat{I}_{\rho,i_e}}} \underline{\hat{\mathbf{\Phi}}_v} \tag{4.32}$$

It has been demonstrated that the matrices $\mathbf{K}_{\underline{\hat{I}_{E,i_e}}}$ and $\mathbf{M}_{\underline{\hat{I}_{\rho,i_e}}}$ of linear structural systems are semi-positive definite [113]. Therefore, each component of the gradients expressed as Eqs. (4.29) - (4.32) are promised to be non-negative. Such property indicates that directional derivatives expressed as Eqs. (4.25) - (4.28) are also non-negative. Hence, $a_{1,v}$, and $a_{2,v}$ have monotonically increasing relationship with $\hat{\mathbf{I}}_E$ from $\underline{\hat{\mathbf{I}}_E}$ to $\overline{\hat{\mathbf{I}}_E}$, and $b_{1,v}$ and $b_{2,v}$ also monotonically increase with the increase of $\hat{\mathbf{I}}_\rho$ from the associated lower bound to the upper bound. Subsequently, the upper bounds of $a_{1,v}$ and $b_{2,v}$, and lower bounds of $a_{2,v}$ and $b_{1,v}$ can be respectively calculated as:

$$\overline{a_{1,v}} = \overline{\hat{\mathbf{\Phi}}_v}^T \left[\sum_{i_e=1}^{n_s} \mathbf{K}_{i_e}^e (\overline{\hat{I}_{E,i_e}}) \right] \overline{\hat{\mathbf{\Phi}}_v} = \overline{\hat{\mathbf{\Phi}}_v}^T \mathbf{K}_s (\overline{\hat{\mathbf{I}}_E}) \overline{\hat{\mathbf{\Phi}}_v} \tag{4.33}$$

$$\underline{b_{1,v}} = \overline{\hat{\mathbf{\Phi}}_v}^T \left[\sum_{i_e=1}^{n_s} \mathbf{M}_{i_e}^e (\underline{\hat{I}_{\rho,i_e}}) \right] \overline{\hat{\mathbf{\Phi}}_v} = \overline{\hat{\mathbf{\Phi}}_v}^T \mathbf{M}_s (\underline{\hat{\mathbf{I}}_\rho}) \overline{\hat{\mathbf{\Phi}}_v} \tag{4.34}$$

$$\underline{a_{2,v}} = \underline{\hat{\mathbf{\Phi}}_v}^T \left[\sum_{i_e=1}^{n_s} \mathbf{K}_{i_e}^e (\underline{\hat{I}_{E,i_e}}) \right] \underline{\hat{\mathbf{\Phi}}_v} = \underline{\hat{\mathbf{\Phi}}_v}^T \mathbf{K}_s (\underline{\hat{\mathbf{I}}_E}) \underline{\hat{\mathbf{\Phi}}_v} \tag{4.35}$$

$$\overline{b_{2,v}} = \underline{\hat{\mathbf{\Phi}}_v}^T \left[\sum_{i_e=1}^{n_s} \mathbf{M}_{i_e}^e (\overline{\hat{I}_{\rho,i_e}}) \right] \underline{\hat{\mathbf{\Phi}}_v} = \underline{\hat{\mathbf{\Phi}}_v}^T \mathbf{M}_s (\overline{\hat{\mathbf{I}}_\rho}) \underline{\hat{\mathbf{\Phi}}_v} \tag{4.36}$$

Subsequently, the upper bounds of all natural frequencies can be obtained with the combination of $\overline{\hat{\mathbf{I}}_E}$ and $\underline{\hat{\mathbf{I}}_\rho}$ as expressed as Eq. (4.37), and the lower bounds of all the natural frequencies are resulted from the combination of $\underline{\hat{\mathbf{I}}_E}$ and $\overline{\hat{\mathbf{I}}_\rho}$ as expressed as Eq. (4.38).

$$\overline{\hat{\lambda}_v} = \frac{\overline{\hat{\mathbf{\Phi}}_v}^T \mathbf{K}_s(\overline{\hat{\mathbf{I}}_E})\overline{\hat{\mathbf{\Phi}}_v}}{\overline{\hat{\mathbf{\Phi}}_v}^T \mathbf{M}_s(\underline{\hat{\mathbf{I}}_\rho})\overline{\hat{\mathbf{\Phi}}_v}} = \frac{\overline{\hat{\mathbf{\Phi}}_v}^T \left[\sum_{i_e=1}^{n_s} \mathbf{K}_{i_e}^e(\overline{\hat{I}_{E,i_e}})\right]\overline{\hat{\mathbf{\Phi}}_v}}{\overline{\hat{\mathbf{\Phi}}_j}^T \left[\sum_{i_e=1}^{n_s} \mathbf{M}_{i_e}^e(\underline{\hat{I}_{\rho,i_e}})\right]\overline{\hat{\mathbf{\Phi}}_v}} \tag{4.37}$$

$$\underline{\hat{\lambda}_v} = \frac{\underline{\hat{\mathbf{\Phi}}_v}^T \mathbf{K}_s(\underline{\hat{\mathbf{I}}_E})\underline{\hat{\mathbf{\Phi}}_v}}{\underline{\hat{\mathbf{\Phi}}_v}^T \mathbf{M}_s(\overline{\hat{\mathbf{I}}_\rho})\underline{\hat{\mathbf{\Phi}}_v}} = \frac{\underline{\hat{\mathbf{\Phi}}_v}^T \left[\sum_{i_e=1}^{n_s} \mathbf{K}_{i_e}^e(\underline{\hat{I}_{E,i_e}})\right]\underline{\hat{\mathbf{\Phi}}_v}}{\underline{\hat{\mathbf{\Phi}}_v}^T \left[\sum_{i_e=1}^{n_s} \mathbf{M}_{i_e}^e(\overline{\hat{I}_{\rho,i_e}})\right]\underline{\hat{\mathbf{\Phi}}_v}} \tag{4.38}$$

The Eq. (4.37) is equivalent to Eq. (4.16), and the Eq. (4.38) is equivalent to Eq. (4.17).

This concludes the proof of the proposition. □

4.4 Numerical examples

In this section, the applicability and effectiveness of the proposed computational scheme are critically verified through investigations on both academic sized and practically motivated engineering structures. Due to the unavailability of experiment data, the upper and lower bound functions are constructed based on assumption in order to demonstrate the concept and applicability of interval field. For the purpose of validation, the upper and lower bounds of natural frequencies obtained by the proposed method are compared with the results provided by the Latin Hypercube Sampling method [182]. The advantage of the adopted simulation approach is that it is capable of offering more uniformly distributed samples within the bounded domain than the conventional Monte-Carlo simulation. The presented numerical results are obtained by using a workstation with CPU of Intel Core i7-4770, 32 GB of memory, and 1 TB of hard drive.

4.4.1 I-section cantilever beam

The first investigation considers an I-section cantilever Euler-Bernoulli beam with the geometrical properties depicted in Figure 4.2. The Young's modulus and density of the cantilever beam are considered as interval fields such that the upper and lower bounds vary continuously along the span of the beam (x-axis). The upper and lower bound functions of Young's modulus (E , unit: GPa) and density (ρ , unit: kg/m^3) are demonstrated in Figures 4.3 and 4,4. $\overline{I_E}(x)$ and $\underline{I_E}(x)$ respectively denote the upper and lower bound functions of Young's modulus which are expressed in Eqs. (4.39) and (4.40); $\overline{I_\rho}(x)$ and $\underline{I_\rho}(x)$ respectively denote the upper and lower bound functions of density which are expressed in Eqs. (4.41) and (4.42).

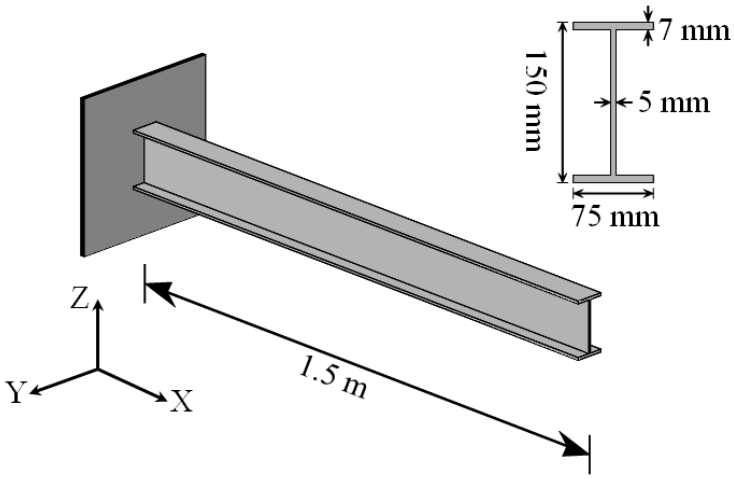

Figure 4.2 I-section cantilever beam

$$\overline{I_E}(x) = 205 - 1.5e^{(-2\sin(\pi x/0.25)-2.4)} + 2e^{(-3\sin(\pi x/0.22)-3.6)} \tag{4.39}$$

$$\underline{I_E}(x) = 195 + 1.2e^{(-3\sin(\pi x/0.22)-3.6)} - 2e^{(-1.5\sin(\pi x/0.28)-1.8)} \tag{4.40}$$

$$\overline{I_\rho}(x) = 7800 + 400e^{(-1.5\cos(\pi(x+0.5)/0.23)-1.8)} + 300e^{(-2.5\sin(\pi(x+0.5)/0.24)-3)} \tag{4.41}$$

$$\underline{I}_{\rho}(x) = 7800 - 400e^{(-1.5\cos(\pi(x+1.5)/0.24)-1.8)} - 300e^{(-3.5\sin(\pi(x+0.5)/0.23)-4.2)} \tag{4.42}$$

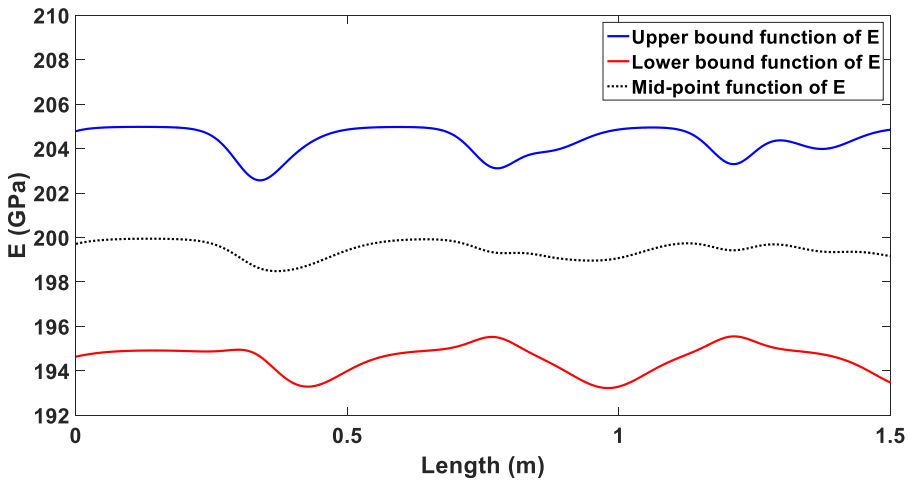

Figure 4.3 Upper bound, lower bound and mid-point functions of E

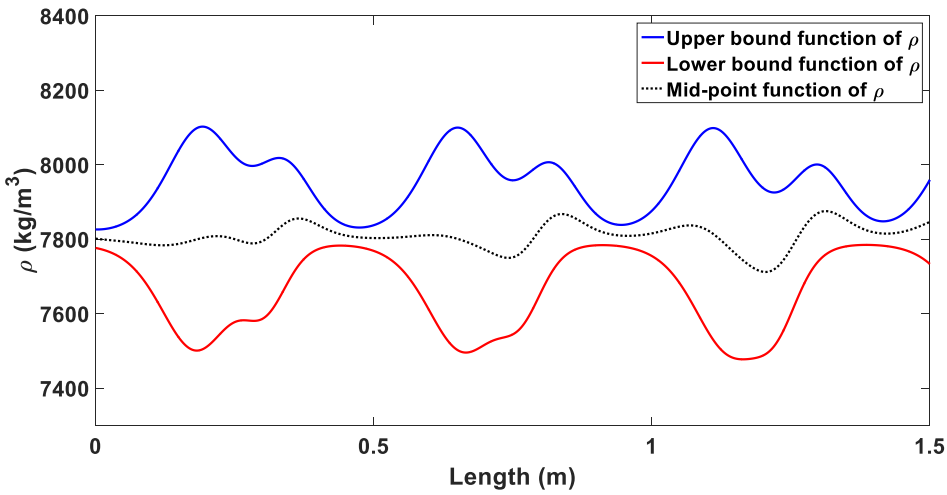

Figure 4.4 Upper bound, lower bound and mid-point functions of ρ

The numerical investigation on the cantilever beam is firstly conducted with three different discretization sizes for the interval fields, and consequently, the structure can be respectively divided into 20, 100 and 1,000 beam elements. The adopted three distinctive discretisation sizes for $\overline{I}_E(x)$, $\underline{I}_E(x)$, $\overline{I}_{\rho}(x)$ and $\underline{I}_{\rho}(x)$ are shown in Figures 4.5 and 4.6. It can be observed from Figures 4.5 and 4.6 that, with the increase of element number,

the smoothness of the transition between the discretised values of both upper and lower bound functions of adjacent elements is improved.

The upper and lower bounds of the natural frequencies of the cantilever beam with regarding to the discretisations are computed by adopting the proposed computational scheme. As indicated in Section 4.3.2, the relation between eigenvalues and Young's modulus is monotonic increasing, while it is a monotonic decreasing relationship between the eigenvalues and the density. Therefore, the upper bounds of natural frequencies are effectively calculated with the combination of upper bounds of Young's modulus and lower bounds of density at each discretisation, whereas the lower bounds of the natural frequencies are resulted from the lower bounds of Young's modulus combined with the upper bounds of density.

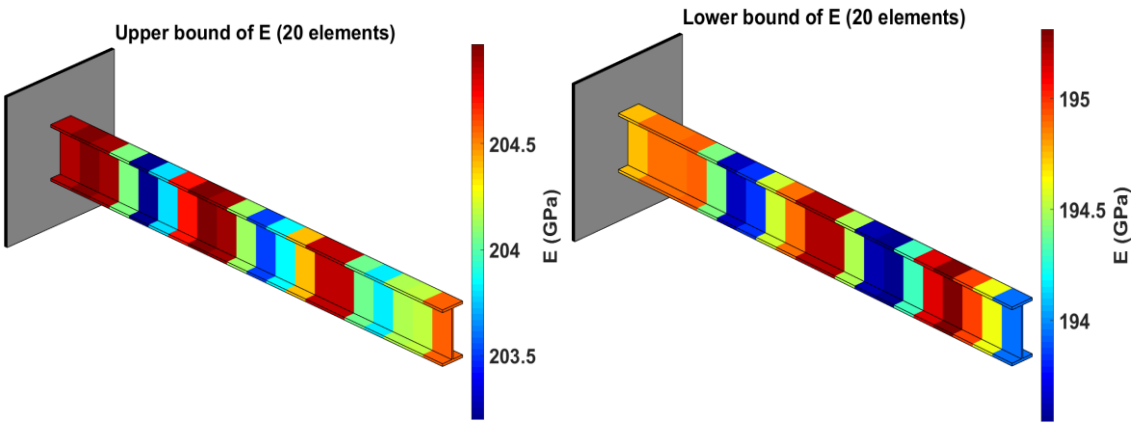

(a)

(b)

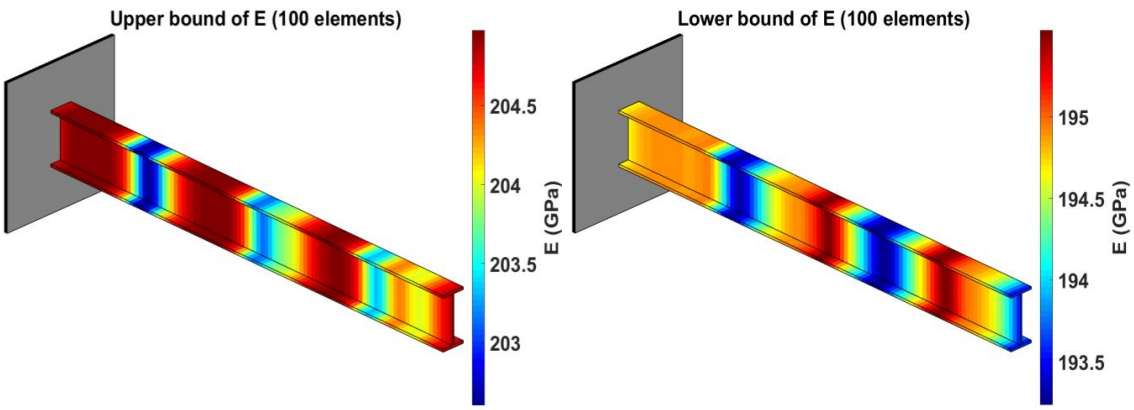

(c) (d)

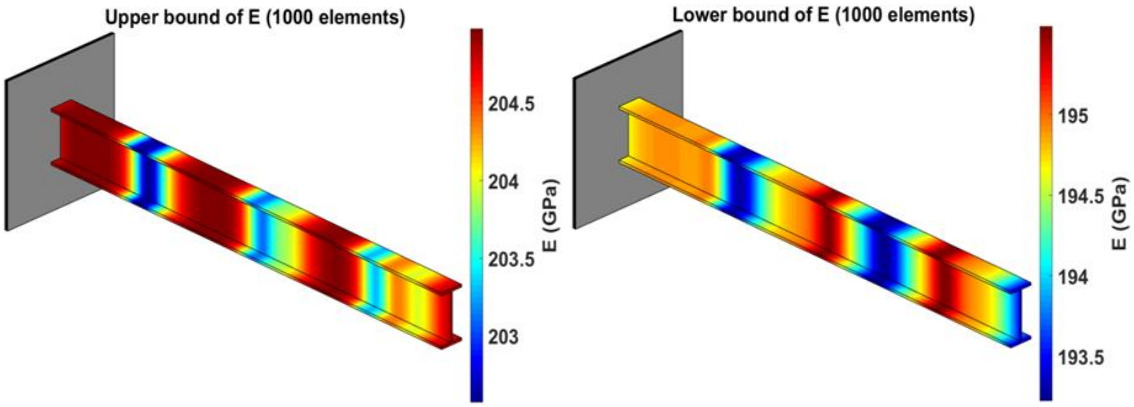

(e) (f)

Figure 4.5 Discretisation of $\overline{I_E}(x)$ and $\underline{I_E}(x)$ with 20 (a and b), 100 (c and d) and 1,000 (e and f) elements

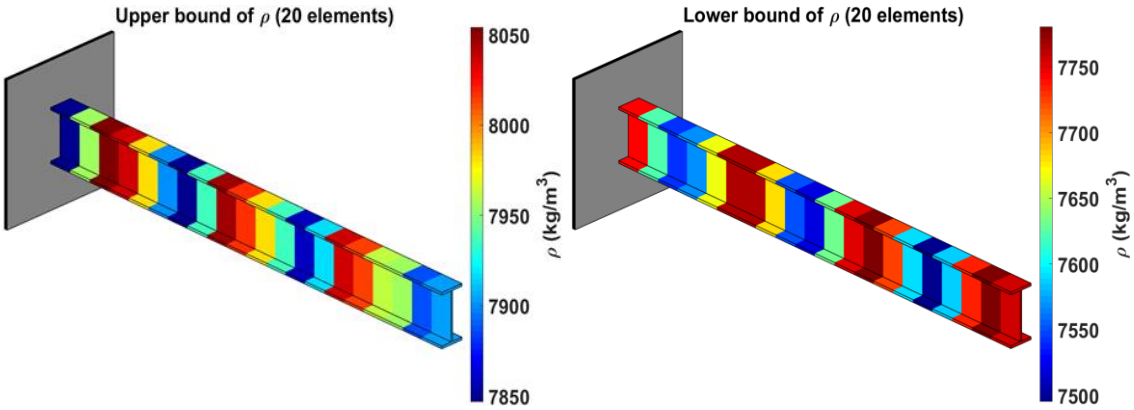

(a) (b)

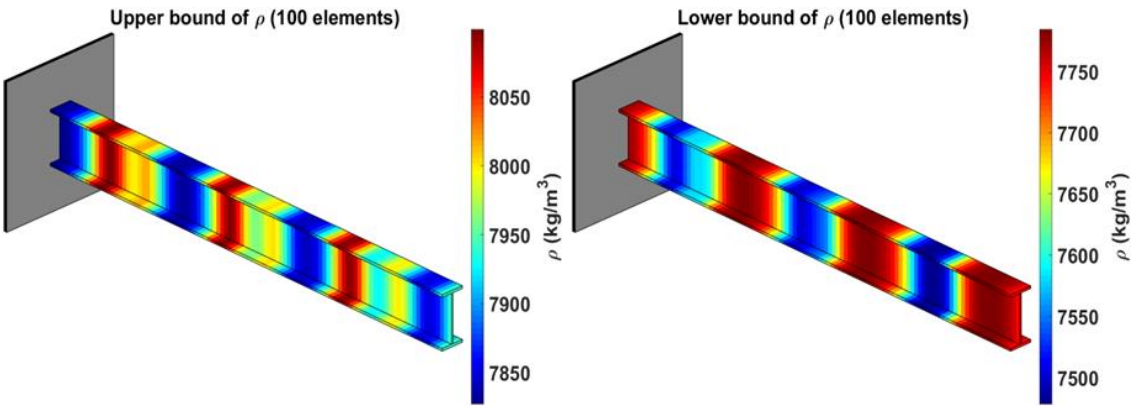

(c) (d)

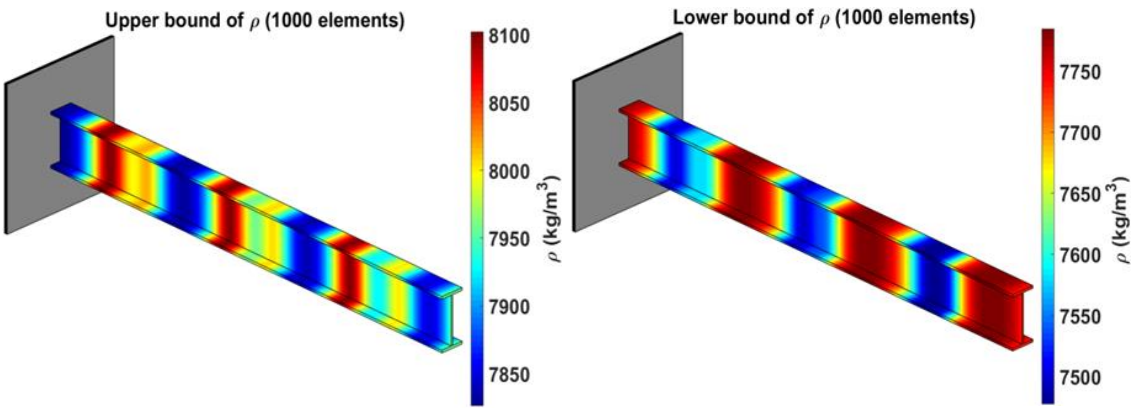

(e) (f)

Figure 4.6 Discretisation of $\overline{I_\rho}(x)$ and $\underline{I_\rho}(x)$ with 20 (a and b), 100 (c and d) and 1,000 (e and f) elements

Table 4.1 Bounds of first two natural frequencies of the cantilever beam

	Number of elements				
	20	50	100	500	1000
$\overline{\omega_1}$ (Hz)	248.119	248.101	248.098	248.052	247.457
$\underline{\omega_1}$ (Hz)	238.159	238.205	238.211	238.123	237.119
$\overline{\omega_2}$ (Hz)	1554.913	1554.744	1554.722	1554.710	1554.640
$\underline{\omega_2}$ (Hz)	1492.359	1492.613	1492.649	1492.661	1492.539

In addition to the previously adopted discretisation sizes shown in Figures 4.5 and 4.6, the beam is once again meshed into 50 and 500 elements for the evaluation of the bounds of the natural frequencies. The extreme bounds of the first two natural frequencies obtained by the proposed approach are summarised in Table 4.1. It is revealed from the data that the upper bounds of the investigated natural frequencies gradually reduce with the increase of number of structural elements, while the lower bounds fluctuate with

different number of elements. Such observed phenomenon is actually attributed to the insufficient approximation on the interval field with coarse discretisation.

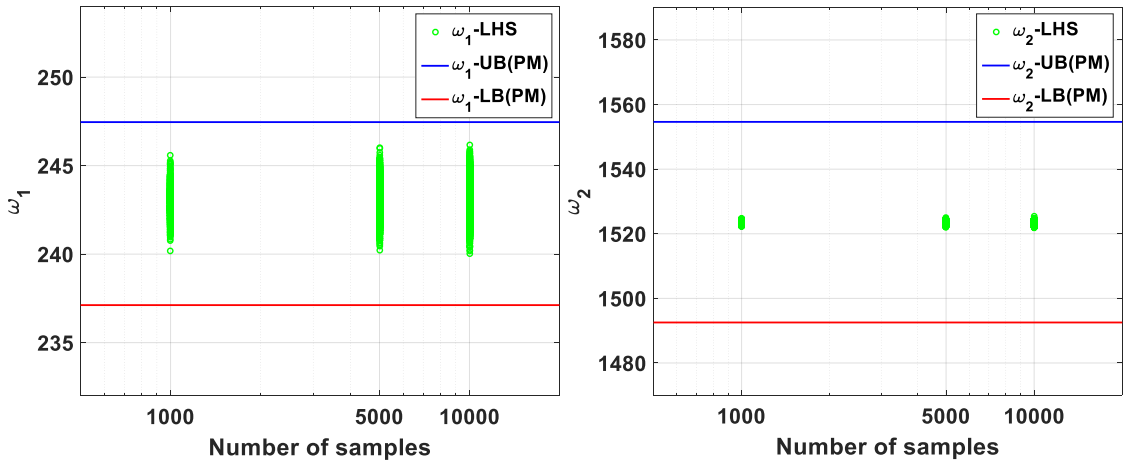

(a) (b)

Figure 4.7 Extreme bounds of ω_1 (a) and ω_2 (b)

The accuracy of the proposed method (PM) is verified by comparing with the results obtained by the Latin Hypercube Sampling (LHS) approach. In this comparison study, the discretization with 1,000 elements is adopted for both approaches. For the sampling method, simulations with 1,000, 5,000 and 10,000 samples are respectively conducted. The results for the first two natural frequencies are presented in the Figure 4.7. It is indicated by Figure 4.7(a) and (b) that all simulative results are completely enclosed by the upper bounds (UB) and lower bounds (LB) obtained by the proposed computational approach. Marginal improvement can be observed for the sampling approach by significantly increasing the number of samples, but the computational cost is also exponentially increased as well. Thus, the applicability of the introduced concept of interval field and the effectiveness of the proposed computational method has been evidently justified.

4.4.2 L-shape simply supported plate

In the second example, the interval natural frequency analysis of an L-shape thin plate with out-of-plane vibration is investigated. The general layout of the structure with boundary conditions at reference configuration is shown in Figure 4.8(a). The plate is discretised into 341 nodes with 300 rectangular Kirchhoff plate elements as shown in Figure 4.8(b). The nodes 1 - 5 of the plate are simply supported. This investigation concerns that the Young's modulus (E, unit: GPa) and density (ρ, unit: kg/m^3) are spatially variant uncertainties which are described as interval fields, while the Poisson's ratio (ν) is considered as deterministic. The corresponding upper and lower bound functions are respectively expressed as Eqs. (4.43) - (4.46). In order to enhance the visualization on the 2D interval fields, the spatially dependent fluctuation of E and ρ are demonstrated in Figures 4.9 and 4.10.

$$\overline{I_E}(x,y) = 74.084 + 1.5\sin(2.083\pi(x+y)) + 1.5\cos(0.766\pi(x-y)) \tag{4.43}$$

$$\underline{I_E}(x,y) = 72.084 + 1.5\sin(2.083\pi(x+y)) - 1.5\cos(0.766\pi(x-y) \tag{4.44}$$

$$\overline{I_\rho}(x,y) = 2880 + 15\sin(8.267\pi(x-y) + 15\cos(0.766\pi(x+y)) \tag{4.45}$$

$$\underline{I_\rho}(x,y) = 2720 + 15\sin(-8.267\pi(x-y)) - 15\cos(0.766\pi(x+y)) \tag{4.46}$$

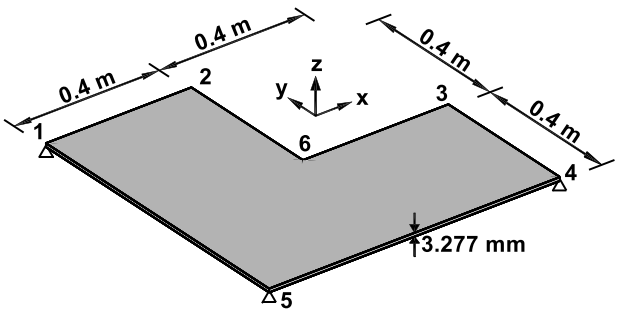

(a)

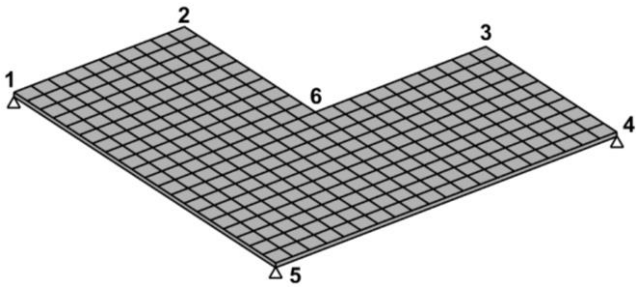

(b)

Figure 4.8 L-shape simply supported thin plate: (a) general layout and (b) FEM mesh

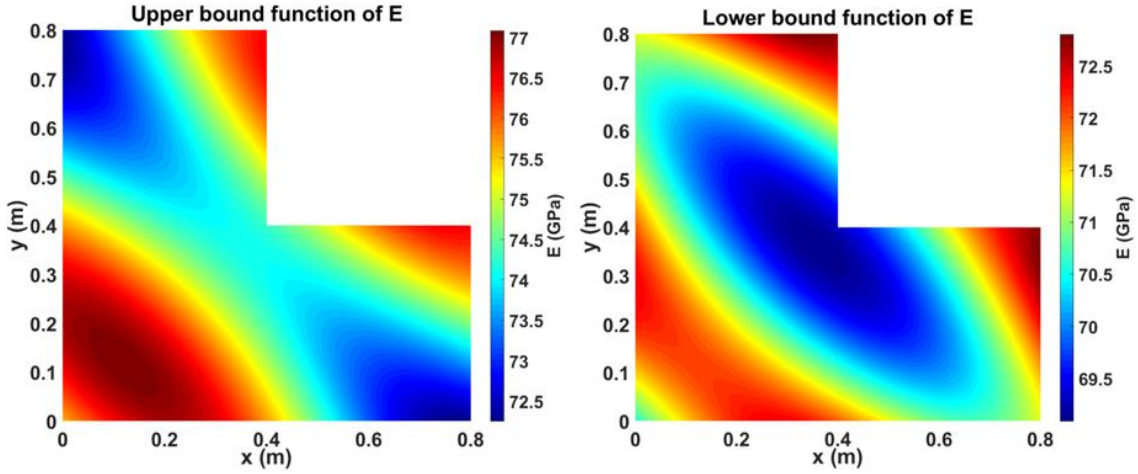

(a) (b)

Figure 4.9 The (a) upper and (b) lower bound functions of the Young's modulus

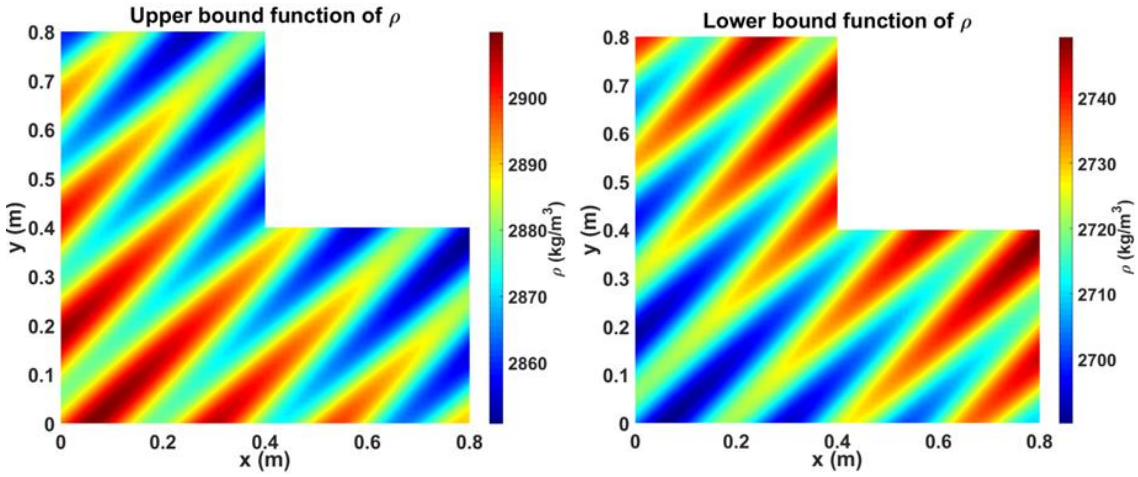

(a) (b)

Figure 4.10 The (a) upper and (b) lower bound functions of the density

The extreme bounds of the natural frequencies of the structure are calculated by adopting the proposed method (PM) which are subsequently compared with the results obtained by the Latin Hypercube Sampling (LHS) approach with 10,000 samples. The results of the first six uncertain-but-bounded natural frequencies are summarised in Table 4.2 with the relative difference that has been defined in Eq. (4.47). It is evidently illustrated in Table 4.2 that the results obtained by the proposed approach rigorously enclose the computational results obtained from the sampling approach for all six considered natural frequencies.

Table 4.2 Extreme bounds of ω_1 - ω_6 of the L-shape plate

	PM (Hz)	LHS (Hz)	RR (%)
$\overline{\omega}_1$	34.834	33.925	2.608
$\underline{\omega}_1$	32.836	33.710	-2.662
$\overline{\omega}_2$	66.473	64.921	2.335
$\underline{\omega}_2$	62.958	64.461	-2.388
$\overline{\omega}_3$	121.211	118.211	2.475
$\underline{\omega}_3$	114.393	117.328	-2.565
$\overline{\omega}_4$	161.942	158.113	2.364
$\underline{\omega}_4$	153.421	157.120	-2.411
$\overline{\omega}_5$	165.310	161.588	2.252
$\underline{\omega}_5$	156.995	160.595	-2.293
$\overline{\omega}_6$	240.649	235.173	2.276
$\underline{\omega}_6$	228.147	233.469	-2.333

where

$$RR = \frac{PM - LHS}{PM}\% \tag{4.47}$$

Mode shape - $\overline{\omega}_1$

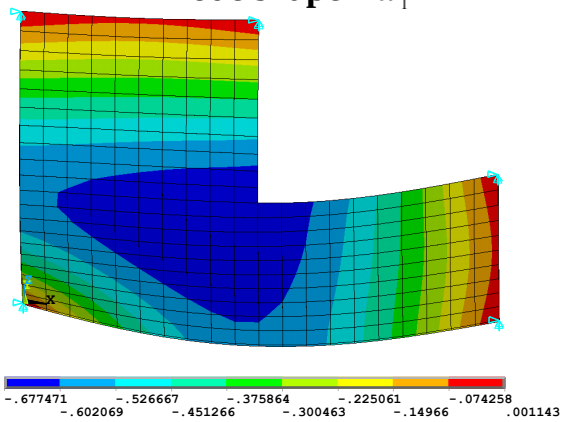

(a)

Mode shape - $\underline{\omega}_1$

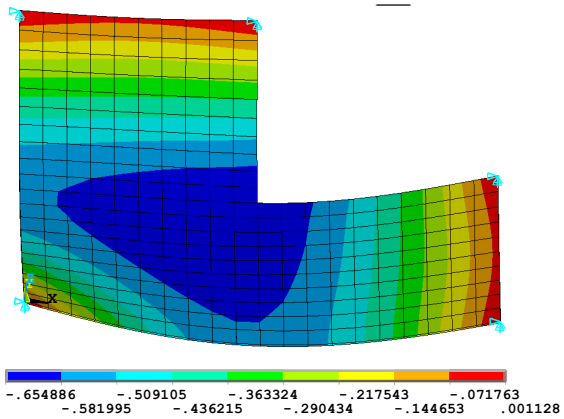

(b)

Mode shape - $\overline{\omega}_2$

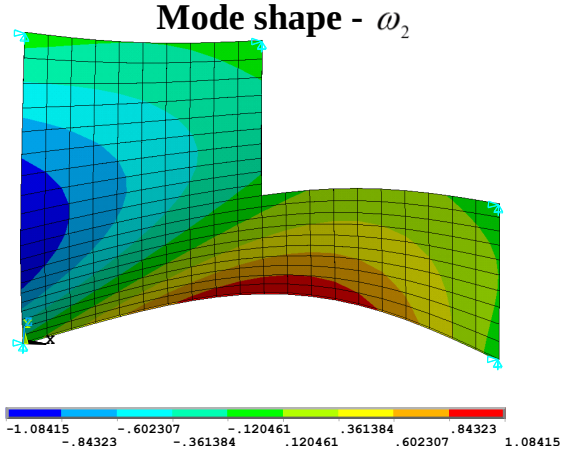

(c)

Mode shape - $\underline{\omega}_2$

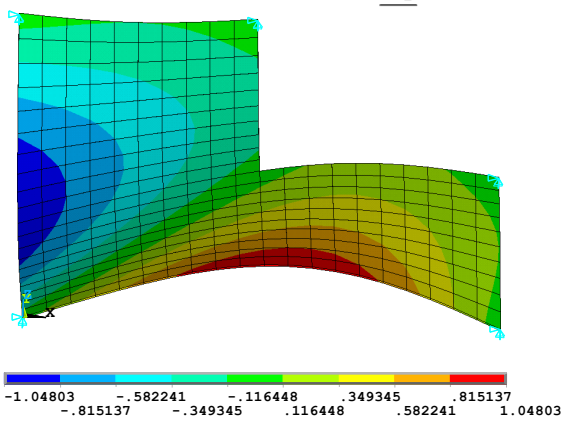

(d)

Mode shape - $\overline{\omega}_3$

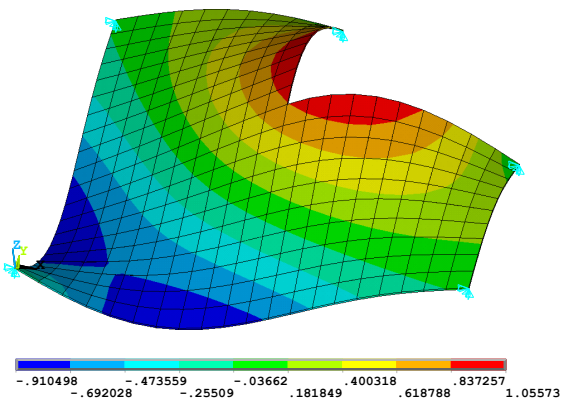

(e)

Mode shape - $\underline{\omega}_3$

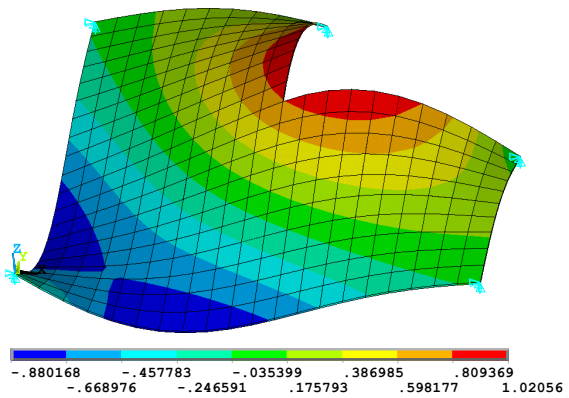

(f)

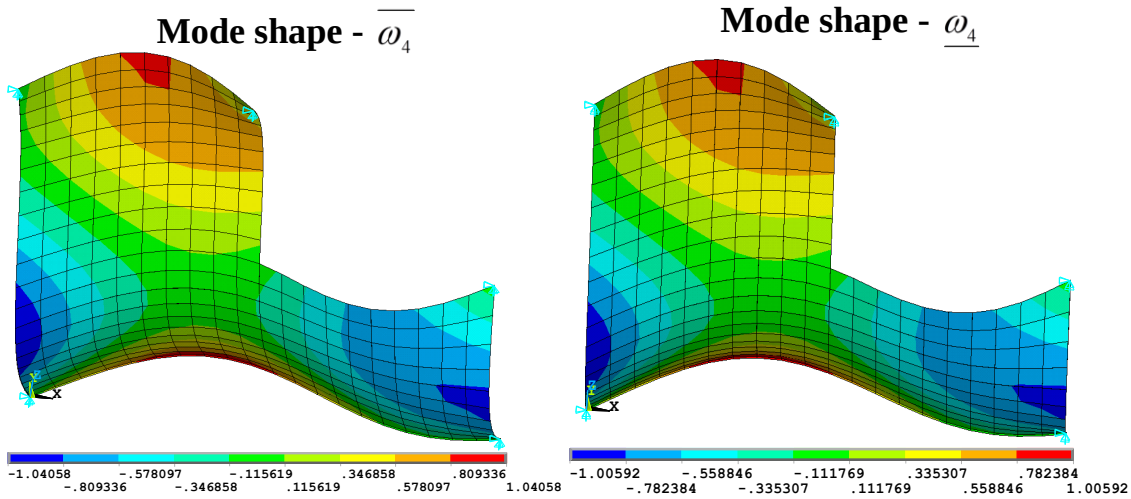

(g) (h)

Figure 4.11 Mode shapes associated with the upper and lower bounds of ω_1 - ω_4

In addition to the natural frequencies, the mode shapes (normalised with respect to mass matrices corresponding to the extreme bounds of natural frequencies) associated with the upper and lower bounds of ω_1 - ω_4 are obtained from ANSYS [183]. By comparing the mode shapes listed in Figure 4.11, an interesting observation can be made which is that the general shape of the mode shape of the plate associated with the upper bound of natural frequency is same as the one corresponding to the lower bound.

Thus, the applicability of the proposed interval field concept and the accuracy of the computational approach are evidently illustrated. One highlight should be mentioned here is that the proposed uncertainty model, as well as the computational scheme can be directly integrated into the commercial FEM software.

4.4.3 Cantilever plate

To further investigate the effectiveness of the proposed computational approach, a practical-sized cantilever plate is considered in the final numerical investigation by adopting the Kirchhoff plate theory. The general layout of the structure is shown in Figure

4.12. In this example, the material properties such as Young's modulus (E , unit: GPa) and density (ρ , unit: kg/m^3) are respectively considered as 2D spatially dependent interval uncertain parameters. For this example, two cases of different upper and lower bound functions are considered which are respectively expressed in Eqs. (4.48) - (4.51) and Eqs. (4.52) - (4.55). The Poisson's ratio of the plate is considered as $\nu = 0.3$. For the purpose of providing deep insight of the spatial variations of the considered uncertain parameters, the upper and lower bound functions and the associated discretisation under the adopted mesh are illustrated in Figures 4.13 – 4.14.

Case 1:

$$\overline{I_{E,1}}(x,y) = 75 + 2e^{-3.5\sin(\pi x/5+\pi y/4)-4.2} + 2e^{-1.5\sin(\pi x/2+\pi y/1.53)-1.8} \tag{4.48}$$

$$\underline{I_{E,1}}(x,y) = 71.5 - 2e^{-3.5\sin(\pi x/2+\pi y/3.9)-4.2} + 2e^{-1.5\sin(\pi x/1.8+\pi y/4.2)-1.8} \tag{4.49}$$

$$\overline{I_{\rho,1}}(x,y) = 2800 + 100e^{-1.5\cos(\pi(x-y)/5.64)-1.8} + 100e^{-2.5\cos(\pi(x+y)/6.83)-3} \tag{4.50}$$

$$\underline{I_{\rho,1}}(x,y) = 2700 + 100e^{-1.5\cos(\pi(x-y)/3.64)-1.8} - 100e^{-3.5\cos(\pi(x+y)/5.83)-4.2} \tag{4.51}$$

Case 2:

$$\overline{I_{E,2}}(x,y) = 74 + \sin(x/12 + 0.6\pi) + \cos(y/4.5 + 1.2) - \sin(xy/6.5 + 0.1) \tag{4.52}$$

$$\underline{I_{E,2}}(x,y) = 72.5 - \cos(x/12 + y/1.7) + \sin(y/21 - x/2.3) - \cos(xy/47) \tag{4.53}$$

$$\overline{I_{\rho,2}}(x,y) = 2800 + 60\cos((x^2 - y^2 + 1.2)/56) - 100\sin((x^2 + y^2)/68) \tag{4.54}$$

$$\underline{I_{\rho,2}}(x,y) = 2700 + 40\sin((x-y)^2/34) - 100\cos((x+y)^2/53 + 0.1) \tag{4.55}$$

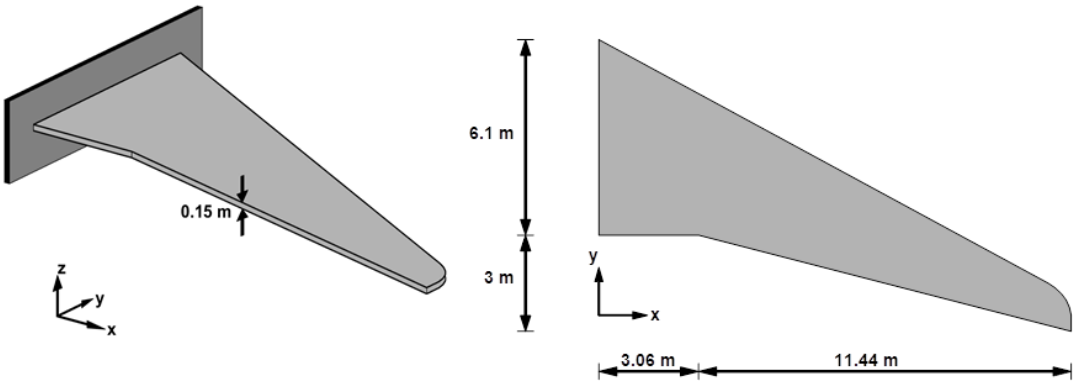

Figure 4.12 General layout of the cantilever plate

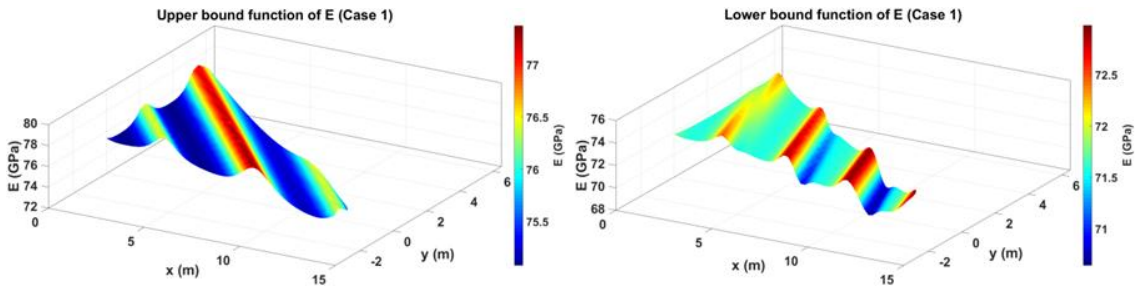

(a) (b)

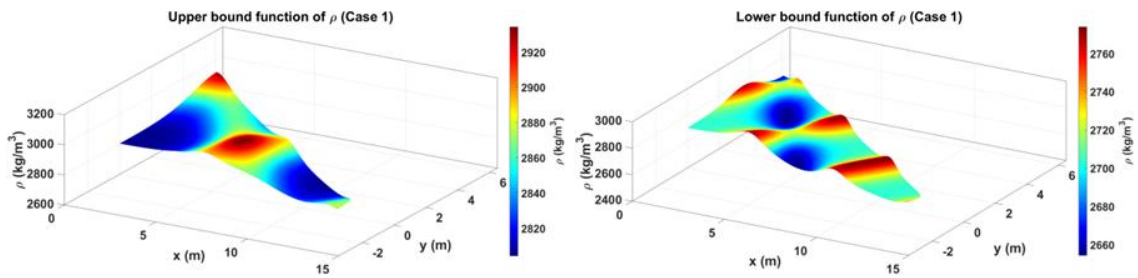

(c) (d)

Figure 4.13 Upper and lower bound functions of E and ρ of Case 1

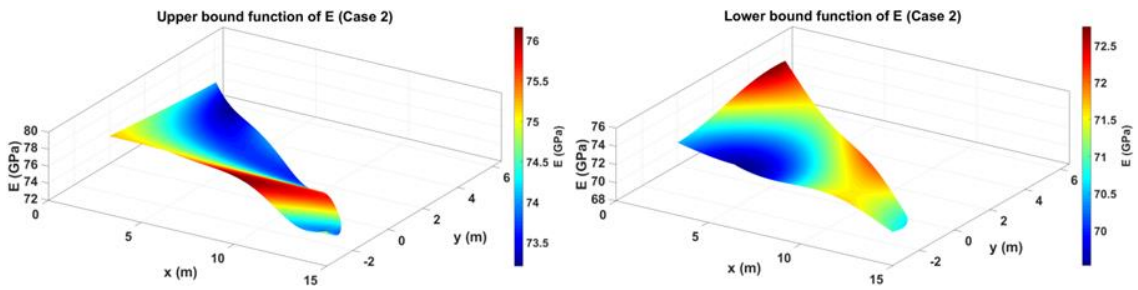

(a) (b)

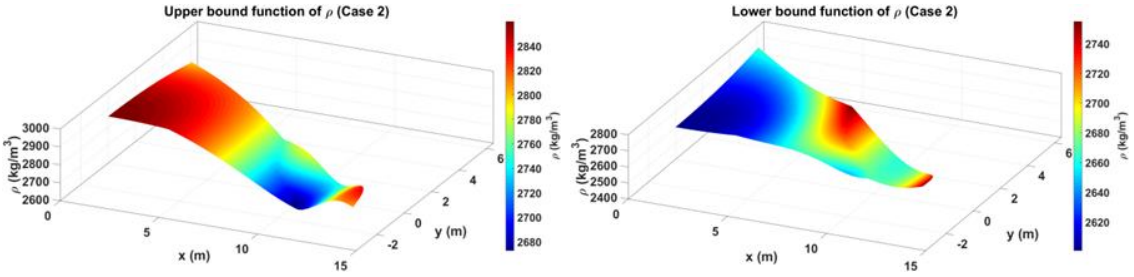

(c) (d)

Figure 4.14 Upper and lower bound functions of E and ρ of Case 2

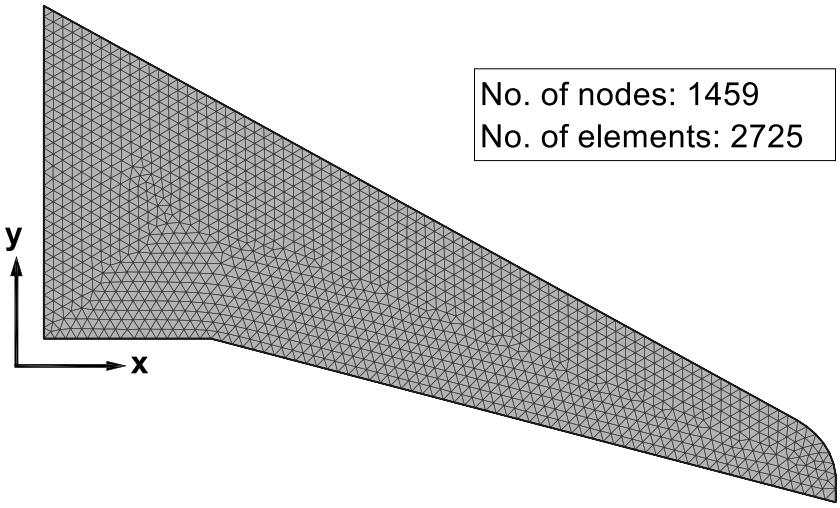

Figure 4.15 Adopted FEM mesh for comparing results of PM with LHS

For evaluating the upper and lower bounds of the natural frequencies of the structure, both the proposed method (PM) and Latin Hypercube Sampling (LHS) method are implemented in this numerical investigation by adopting an unstructured triangular mesh with 2,725 elements and 1,459 nodes. Such unstructured mesh is generated by employing a Delaunay mesh-generator [184] which is proved to be capable in generating high-quality triangular mesh. For the LHS approach, 5,000 samples have been adopted for the purpose of result verification. By adopting the proposed computational approach, the upper and lower bounds of the first four natural frequencies are obtained by conducting two independent eigen-analyses and the results are summarised in Table 4.3. In addition, the results produced by the LHS approach are also reported in Table 4.3,

where RR denote the relative difference between the results from PM and LHS as defined in Eq. (4.47). It is evidently demonstrated in Table 4.3 that the results obtained by the proposed approach are completely enclosing the ones obtained from the LHS method. In addition to the superior computational effectiveness, the computational time (t_{com}, unit: sec) of the proposed approach is much less than the adopted sampling method. Once again, the applicability, accuracy as well as the efficiency of the proposed method is fully illustrated through the investigation on practically motivated engineering structure.

Additionally, convergence studies are conducted for both Cases 1 and 2 in order to investigate the effect of mesh size on the results of proposed method. Thus, totally 11 unstructured meshes (including the mesh shown in Figure 4.15) with the number of elements ranging from 453 to 17,169 are considered. In addition to the two cases with uncertainties, a deterministic case with $E = 73GPa$, $\rho = 2800kg/m^3$ and $\nu = 0.3$ is involved in such numerical test such that the convergence of FEM analysis can be demonstrated simultaneously. By employing the proposed method, the upper (UB) and lower (LB) bounds of the first (ω_1) and second (ω_2) natural frequencies of Cases 1 and 2 are shown in Figures 4.16 - 4.17 together with the results obtained from deterministic analysis. By thoroughly examining the Figures 4.16 - 4.17, there are two observations can be drawn: (1) refining the mesh from coarse to fine can gradually lead to the convergence of the calculation of both uncertain and deterministic natural frequencies; (2) the extreme bounds of natural frequencies converge in the same trend as the results from deterministic FEM analysis. Subsequently, it can be concluded that the convergence of the proposed uncertain free vibration analysis of structures with interval field is promised in the context of the convergence of FEM analysis for such vibration problem of bending plate.

Table 4.3 Extreme bounds of ω_1 - ω_4 of the cantilever plate of Cases 1 and 2

	Case 1 (unit: Hz)			Case 2 (unit: Hz)		
	PM	LHS	RR (%)	PM	LHS	RR (%)
$\overline{\omega_1}$	0.8703	0.8507	2.252	0.8665	0.8520	1.673
$\underline{\omega_1}$	0.8289	0.8473	-2.220	0.8350	0.8489	-1.665
$\overline{\omega_2}$	4.0682	3.9614	2.625	4.0499	3.9696	1.983
$\underline{\omega_2}$	3.8473	3.9422	-2.467	3.8834	3.9559	-1.867
$\overline{\omega_3}$	9.0418	8.8145	2.514	9.0090	8.8329	1.955
$\underline{\omega_3}$	8.5677	8.7759	-2.430	8.6445	8.8010	-1.810
$\overline{\omega_4}$	10.6454	10.3975	2.329	10.6654	10.4259	2.246
$\underline{\omega_4}$	10.1277	10.3563	-2.257	10.1664	10.3843	-2.143
t_{com}	168.831	1.273×10^4	N/A	164.539	1.173×10^4	N/A

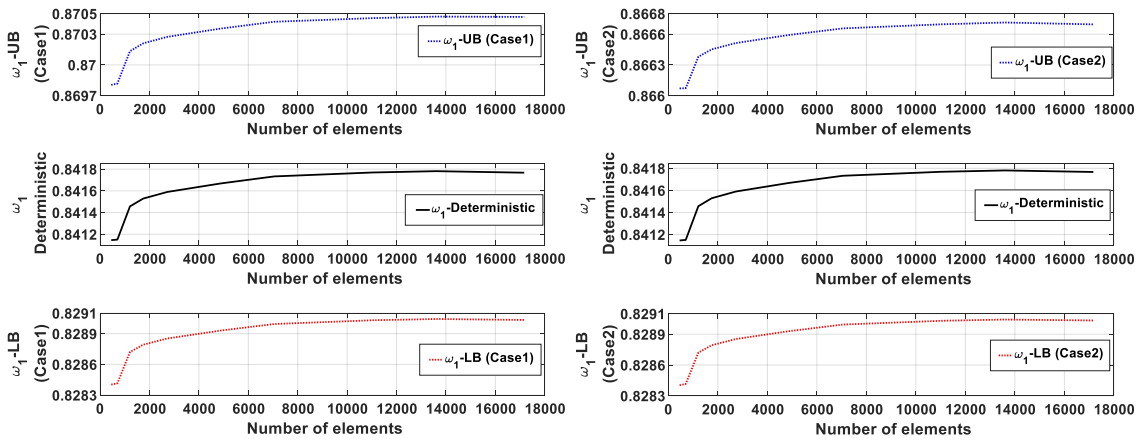

(a) (b)

Figure 4.16 Convergence study of $\overline{\omega_1}$ and $\underline{\omega_1}$ of (a) Cases 1 and (b) Case 2 with comparison to the deterministic analysis

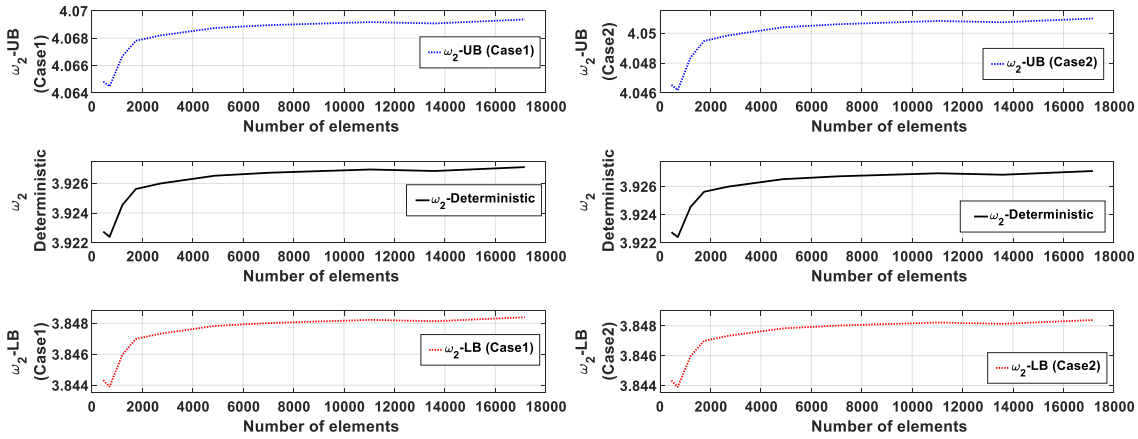

(a) (b)

Figure 4.17 Convergence study of $\overline{\omega_2}$ and $\underline{\omega_2}$ of (a) Cases 1 and (b) Case 2 with comparison to the deterministic analysis

4.5 Conclusion

In this study, the free vibration of engineering structures with non-probabilistic spatially dependent uncertain parameters is thoroughly investigated for the first time. In order to model the spatial variations of system variables with insufficient information, a new concept of interval field is proposed which simply requires the upper and lower bound functions to describe the non-stochastic uncertainties. Additionally, the spatial average approach is adopted to discretise the interval field into a finite set of interval variables such that the extremities of eigenvalues can be calculated within the framework of finite element method.

Furthermore, an efficient computational approach is proposed to obtain the bounds of natural frequencies, which excludes either numerical estimation of bounds of eigenvalues or combinatory approaches. Accordingly, the upper and lower bounds of natural frequencies can be achieved by performing two independent eigen-analyses. The applicability of the interval field model and the accuracy of the proposed approach for

calculating the bounds of natural frequencies are evidently testified through investigations on academic and practical-sized structures.

Chapter 5 . Uncertain natural frequency analysis for structures with hybrid spatially variant stochastic and interval parameters

5.0 Summary

This chapter presents a robust non-deterministic free vibration analysis for engineering structures involving hybrid, yet spatially dependent, uncertain system parameters. Distinguished from the conventional hybrid uncertain eigenvalue problem, the concept of interval field is enclosed with random field model such that, both the stochastic and non-stochastic representations of the spatial dependency of the uncertainties are simultaneously incorporated within a unified non-deterministic free vibration analysis for the first time. In order to determine the probabilistic characteristics (i.e., means and standard deviations) of the extremities of structural natural frequencies, an extended unified interval stochastic sampling (X-UISS) method is implemented for the purpose of effective hybrid uncertain free vibration analysis. By meticulously blending sharpness-promised interval eigenvalue analysis with stochastic sampling techniques, the stochastic profiles (i.e., probability density functions (PDFs) and the cumulative distribution functions (CDFs)) of the extreme bounds of the structural natural frequencies can be rigorously established by utilizing the adequate statistical inference methods. The applicability and effectiveness of the proposed computational framework are evidently demonstrated through the numerical investigations on various practically motivated engineering structures.

The remainder of the Chapter 5 is organized as follows. In Sections 5.2, a brief summary of the concept of random field and the adopted discretization scheme are

provided. The details of the adopted interval field concept have been demonstrated in Chapter 4 and it is omitted in this chapter. Then, the extended hybrid uncertain eigenvalue problem which encloses both the random and interval fields as well as the proposed computational framework for analyzing the hybrid uncertain natural frequencies of structures are comprehensively introduced in Section 5.3. Furthermore, two practically motivated numerical examples are investigated by the proposed approach and then critically compared with computational exhausted simulation approach in Section 5.4. Finally, some concluding remarks are drawn in the Section 5.5. The research work developed in this chapter has produced one journal paper which has been published in *Computer Methods in Applied Mechanics and Engineering*. The detail of the publication is: Feng, J., Wu, D., Gao, W., & Li, G. (2018). Hybrid uncertain natural frequency analysis for structures with random and interval fields. *Computer Methods in Applied Mechanics and Engineering*, *328*, 365-389. https://doi.org/10.1016/j.cma.2017.09.004

5.1 Introduction

The natural frequency, as a key indicator for the vibrational performance of engineering structural systems, has been extensively studied in the past decades. With the aid of finite element method (FEM), such essential dynamic characteristic of engineering structures can be adequately obtained by solving the generalized eigenvalue problems. The existence of uncertainties potentially affects the credibility of the analyzing results of the dynamic behaviours of the structural systems, which leads to the indispensability of developing an uncertain free vibration analysis framework for a more effective and meaningful prediction on the structural natural frequencies as well as other dynamic characteristics [145, 169, 176].

Conventionally, the uncertain free vibration analysis is initialized by implementing probabilistic/stochastic approaches, which are established on the solid theoretical foundation of probability or statistics. In structural engineering, the random eigenvalue problem is adequately addressed by the stochastic finite element method (SFEM) by incorporating the probabilistic strategies within the FEM [148, 168, 185, 186]. Accordingly, the concerned uncertainties of the structural system parameters are modelled as stochastic parameters with the pre-defined statistical information such as mean and standard deviations. Admitting the universal application of SFEM, it is worthy to pointing out that the creditability of such stochastic procedures is conditional to the availability of the statistical information of the concerned uncertainties in practical engineering applications [124, 139, 188].

For the circumstance where the prerequisites of the probabilistic approaches are not satisfied, the non-stochastic procedures are extensively developed so the implementation of uncertainty analysis is not restrained by the insufficiency of the information of system parameters. Profiting from the conceptual simplicity, the interval approaches have been widely adopted into the FEM for the free vibration analysis involving uncertain-but-non-random variables. Numerous computational procedures have been developed in the light of pursuing a more accurate estimation of the exact extreme bounds of natural frequencies [99, 100, 112, 113]. Unlike the extensive adoption of the theoretically well-established random field models in SFEM, the exploration of inclosing the spatial dependency of uncertainties in non-stochastic analysis just started recently in statics analysis where various interval field models have been introduced with different solution algorithms [85, 115, 116, 120].

In modern engineering problems, both random and interval uncertain variables can exist simultaneously. Therefore, the approaches which can enclose both types of uncertainties are necessary for obtaining a more realistic analysis in engineering application. However, based on the thorough literature review, there is still a blank to fill in the free vibration analysis of structures with spatially dependent uncertain system parameters, specifically with the spatial representation of non-stochastic uncertainties.

Thus, the aim of this chapter is to provide an adequate insight of the eigenvalue problem with mixed type of spatially dependent uncertainties for the first time. In this study, the conventional hybrid uncertain eigenvalue problem is extended into a generalized form such that the theory random field and the concept of interval field proposed by [133] are enclosed simultaneously. Since that such generalized spatial uncertain eigenvalue problem has not been systematically addressed, a feasible computational framework is necessarily to be introduced for the investigation of the hybrid uncertain natural frequencies. Therefore, a new computational strategy, namely the extended unified interval stochastic sampling (X-UISS) approach, is adopted for the hybrid uncertain eigenvalue analysis with diverse uncertainties. As a modification of the computational validated UISS approach [133], the X-UISS method can be effectively applied in uncertain free vibration analysis of structural systems with either spatially dependent or independent hybrid random and interval parameters. In the proposed investigation, the Poisson's ratio is considered by the random field model while the Young's modulus and density of materials are modelled as either random or interval field. By utilizing the semi-sampling X-UISS strategy, the upper and lower bounds of all the natural frequencies are firstly calculated by two independent eigen-analyses. Within the framework of FEM, it can be proved that sharpness and feasibility of the achieved

extremities of eigenvalues of the structures can be preserved in the context of discretised interval fields. Subsequently, the statistical profiles (i.e. means, standard deviations, PDFs and CDFs) of each of the eigenvalues can be robustly established based on the collected samples. Since the interval arithmetic is excluded from the X-UISS approach, the associated cacoethic effect of the potential overestimation (so-called dependency issue) [113, 116] is eliminated from the computational scheme. Additionally, the adopted computational framework is applicable with multiple types of random fields such as Gaussian and lognormal distributed fields. Therefore, the X-UISS approach provides an effective and feasible computational framework for the uncertain free vibration analysis of structures with hybrid spatially dependent uncertain system parameters.

5.2 Stochastic approach for modelling spatially dependent uncertainties

5.2.1 The concept of random field

Given a probability space $(\mathbf{\Omega},\ \tilde{F},\ \mathrm{P})$, a random field $H(\boldsymbol{\chi},\theta)$ is defined as a collection of random variables indexed by a continuous parameter $\boldsymbol{\chi} \in \Re^n$ which is the description of the system geometry, where $\theta \in \mathbf{\Omega}$ denote an arbitrary sampling point in the sample space $\mathbf{\Omega}$, $\tilde{F}$ denote the $\sigma-$algebra, and the probability measure is denoted by P which is a function on $\tilde{F}$ such that $P:\tilde{F} \rightarrow [0,\ 1]$. At an arbitrary point $\boldsymbol{\chi}_p$ within the domain of the system, $H(\boldsymbol{\chi}_p,\theta)$ denotes a random variable such that $\forall \boldsymbol{\chi}_p \in \Re^n,\ H(\boldsymbol{\chi}_p,\theta) \sim f_{H(\boldsymbol{\chi}_p,\theta)}(x)$, where $f_{(\bullet)}(x)$ denotes the PDF of the random variable $(\bullet)$. For a specified outcome θ_p, $H(\boldsymbol{\chi},\theta_p)$ can be considered as a realization of the random field.

Practically, the Gaussian random field, benefiting from its conceptual simplicity, has been prevalently adopted in a wide range of engineering applications [5, 131, 189,

190]. Therefore, such type of random field is implemented in the proposed hybrid vibration analysis as a probabilistic representation of spatially variant uncertain parameters. Additionally, some structural system variables, such as material properties, considered in the engineering practices are commonly positive. Hence, non-negative random field, typically the lognormal random field, is adopted to model the spatially coherent material properties. Among all the available covariance functions, the exponential covariance function is frequently employed within the random field and here adopted in this investigation as well. The incorporated exponential covariance functions have generalized forms as:

$$C_H(x,\hat{x}) = \begin{cases} \sigma_H^2 \exp\left(-\dfrac{|x-\hat{x}|}{L_x}\right) & \text{for 1D fields} \\ \sigma_H^2 \exp\left(-\dfrac{|x-\hat{x}|}{L_x} - -\dfrac{|y-\hat{y}|}{L_y}\right) & \text{for 2D fields} \end{cases} \tag{5.1}$$

where $\sigma_H \in \Re$ denotes the standard deviation of the random field; L_x, $L_y \in \Re$ denote the correlation lengths in *x*- and *y*-direction respectively.

5.2.2 The Karhunen-Loève expansion

As a special case of the orthogonal series expansion methods, the Karhunen-Loève (KL) expansion is which has been successfully implemented for simulating the random field [189, 191]. By employing the KL expansion, the random field $H(\chi,\theta)$ over any outcome ω can be expanded as:

$$H(\chi,\theta) = w(\chi) + \sum_{k=1}^{\infty} \sqrt{\lambda_k}\psi_k(\theta)\varphi_k(\chi) \tag{5.2}$$

where $w(\chi)$ is the mean function of the random field; $\{\psi_k(\theta), k = 1,\ 2,...\}$ are mutually uncorrelated random variables; λ_k and $\varphi_k(\chi)$ respectively denote the *k*th eigenvalue and

eigenfunction of the covariance function $C_H(\chi,\hat{\chi})$ which can be spectrally decomposed as:

$$C_H(\chi,\hat{\chi}) = \sum_{k=1}^{\infty} \lambda_k \varphi_k(\chi)\,\varphi_k(\hat{\chi}) \tag{5.3}$$

As indicated by the theory, the ciance function is bounded, symmetrical, as well as positive definite. The eigen-pairs presented in Eq. (5.3) form the solutions to the Fredholm integral equation, such that:

$$\int_{\Psi} C_H(\chi,\hat{\chi})\varphi_k(\chi)\,\mathrm{d}\chi = \lambda_k\,\varphi_k(\hat{\chi}) \tag{5.4}$$

with the eigenfunction satisfying the orthogonal property as:

$$\int_{\Psi} \varphi_k(\chi)\varphi_l(\chi)\,\mathrm{d}x = \delta_{kl} \tag{5.5}$$

where Ψ denotes the spatial domain that the considered random field is defined within; δ_{kl} denotes the Kronecker delta. Based on the orthogonal characteristic of the eigenfunction, the *k*th component of $\{\psi_k(\theta),\ k=1,\ 2,..\}$ can be analytically achieved as [190]:

$$\psi_k(\theta) = \frac{1}{\sqrt{\lambda_k}} \int_{\Psi} \left[H(\chi,\theta) - \mu(\chi)\right] \varphi_k(\chi)\, d\Psi \tag{5.6}$$

In the context that Gaussian random field is implemented, the entire set $\{\psi_k(\theta),\ k=1,\ 2,..\}$ is a collection of independent standard normal variables. Considering the computational efficiency issue in practice, the KL expansion of the random field expressed in Eq. (5.2) is replaced by the *d*th order (i.e., $d >> 1$) series expansion which is expressed as:

$$H(\chi,\theta) \approx \hat{H}^d(\chi,\theta) = \mu(\chi) + \sum_{k=1}^{d} \sigma(\chi)\sqrt{\lambda_k}\psi_k(\theta)\varphi_k(\chi) \tag{5.7}$$

where $\hat{H}^d(\chi,\theta)$ denotes dth order approximation of the random field; $\mu(\chi)$ and $\sigma(\chi)$ respectively denote the mean and standard deviation of the Gaussian random field. If the lognormal random field is adopted, the random field can be formulated as the exponential of a Gaussian random field [50]:

$$H(\chi,\theta) \approx \hat{H}^d(\chi,\theta) = \exp\left[\mu(\chi) + \sum_{k=1}^{d} \sigma(\chi)\sqrt{\lambda_k}\psi_k(\theta)\varphi_k(\chi)\right] \tag{5.8}$$

where the mean $\mu(\chi)$ and standard deviation $\sigma(\chi)$ of the enclosed Gaussian random field are calculated based on the mean $\mu_{\log}(\chi)$ and standard deviation $\sigma_{\log}(\chi)$ of the considered lognormal field as

$$\sigma(\chi) = \sqrt{\ln\left(1 + \sigma_{\log}^2(\chi) / \mu_{\log}^2(\chi)\right)} \tag{5.9}$$

$$\mu(\chi) = \ln \mu_{\log}(\chi) - \frac{1}{2}\sigma(\chi) \tag{5.10}$$

5.3 Hybrid uncertain free vibration analysis of structures with spatial-variant random and interval uncertainties

5.3.1 Generalized spatially uncertain eigenvalue problem

As an extension of the conventional eigenvalue problem with uncertain variables, the free vibration analysis of linear undamped engineering structures with spatially dependent stochastic and non-stochastic uncertainties is investigated in this study. The two types of uncertain system variables are considered as mutually independent. Such extension, here namely as the generalized spatially uncertain eigenvalue problem, thoroughly involved the theories of both random and interval fields into a unified framework of free vibration

analysis of structural system for the first time. For a structure with d_s degrees-of-freedom, the governing equation of the generalized spatially uncertain eigenvalue problem is explicitly formulated as:

$$\mathbf{K}_s(\boldsymbol{\psi},\boldsymbol{\eta})\boldsymbol{\Phi}_v = \lambda_v \mathbf{M}_s(\boldsymbol{\psi},\boldsymbol{\eta})\boldsymbol{\Phi}_v \tag{5.11a}$$

such that:

$$\boldsymbol{\psi} \in \boldsymbol{\Omega} := \{\boldsymbol{\psi} \in \Re^m \mid \psi_i \in H_{\psi_i}(\boldsymbol{\chi},\theta), i = 1,...,m\},\ \boldsymbol{\chi} \in \boldsymbol{\Psi} \tag{5.11b}$$

$$\boldsymbol{\eta} \in \boldsymbol{\Omega} := \{\boldsymbol{\eta} \in \Re^q \mid \eta_{\hat{i}} \in I_{\eta_{\hat{i}}}(\boldsymbol{\chi}), \hat{i} = 1,...,q\},\ \boldsymbol{\chi} \in \boldsymbol{\Psi} \tag{5.11c}$$

where $\mathbf{K}_s(\boldsymbol{\psi},\boldsymbol{\eta}) \in \Re^{d_s \times d_s}$ denotes the hybrid uncertain stiffness matrix of the structure; $\mathbf{M}_s(\boldsymbol{\psi},\boldsymbol{\eta}) \in \Re^{d_s \times d_s}$ denotes the hybrid uncertain mass matrix of the structure; λ_v is the *v*th ($v = 1,...,d_s$) eigenvalue and $\boldsymbol{\Phi}_v \in \Re^{d_s}$ is the associated eigenvector. $\boldsymbol{\psi}$ denotes the concerned spatial-variant stochastic uncertainties of the structural system, $\boldsymbol{\eta}$ denotes the concerned spatially uncertain system parameters with non-stochastic characteristics. $H_{\psi_i}(\boldsymbol{\chi},\theta)$ denotes the random field adopted for describing the *a*th random variable ψ_i; $I_{\eta_{\hat{i}}}(\boldsymbol{\chi})$ denotes the interval field associated to the $\hat{i}$ th non-probabilistic yet spatially variant uncertainty, and $\boldsymbol{\Psi}$ denotes the domain of the entire structural system. Within the defined eigenvalue problem, both the stiffness and mass matrices are functions of the spatially dependent random and interval uncertain parameters. Moreover, it is necessary to emphasize here that, for non-defective engineering structures which are considered in the proposed study, the stiffness and mass matrices are consistently symmetric and positive-definite [191] despite of the fluctuation of the considered uncertain variables.

A mixture of both random and interval fields is enclosed in the proposed uncertain eigenvalue problem, the outcomes, which are the natural frequencies investigated in this study, consist both probabilistic and interval characteristics. Comparing with the conventional non-deterministic eigenvalue problem with single type of uncertainty (either stochastic or non-stochastic), the complexities for solving the hybrid spatially uncertain free vibration are including:

1. There are infinite combinations for the possible realizations of random and interval fields such that infinite number of outcomes can be obtained, which will result the hybrid uncertain structural free vibration analysis to be computationally intractable.
2. Despite of the well-established theoretical support for either random or interval analysis, a unified theory for the hybrid uncertain structural free vibration analysis of structures with both random and interval fields is not systematically established.

Due to the above mentioned barriers, the currently available approaches for uncertain free vibration analysis are incapable of being directly implemented in solving the eigenvalue problem with a mixture of random and interval fields. Therefore, some adequate computational strategies must be developed to address such intricate free vibration analysis with the capability of overcoming the aforementioned complexities.

5.3.2 Extended unified interval stochastic sampling (X-UISS) approach

In the light of providing an adequate computational strategy for solving the uncertain eigenvalue problem with spatially dependent uncertain variables, a general semi-sampling uncertainty analysis approach, namely the extended unified interval stochastic sampling (X-UISS) method is adopted. For the generalized spatially uncertain eigenvalue

problem investigated in this study, the Young's modulus (E) and mass density (ρ) are considered as interval fields while the Poisson's ratio (ν) is represented by random field. Additionally, the random and interval variables are considered as mutually independent.

Considering the aforementioned intricacies of the hybrid uncertain eigenvalue problem, the aim of the proposed computational strategy is to offer a generalized description of the non-deterministic natural frequencies which contain both random and interval characteristics. Due to the existence of interval fields, the natural frequencies corresponding to a specific realization of random fields may vary within a range instead of being a deterministic value. Inspired by the concept of statistics, the samples of upper and lower bounds can be collected in the context of the given observations of random fields and then the means and standard deviations of the samples of extreme bounds of natural frequencies are respectively obtained. Subsequently, the governing equation of the adopted procedure can be formulated as:

Find $\mu_{\overline{\omega_v}}$, $\sigma_{\overline{\omega_v}}$, $\mu_{\underline{\omega_v}}$ and $\sigma_{\underline{\omega_v}}$

$$\mathbf{K}_s(E,\nu)\mathbf{\Phi}_v = \omega_v^2 \mathbf{M}_s(\rho)\mathbf{\Phi}_v \tag{5.12a}$$

such that:

$$E \in I_E(\boldsymbol{\chi}) \vee H(\boldsymbol{\chi},\theta_E) \tag{5.12b}$$

$$\nu \in H(\boldsymbol{\chi},\theta_\nu) \tag{5.12c}$$

$$\rho \in I_\rho(\boldsymbol{\chi}) \vee H(\boldsymbol{\chi},\theta_\rho) \tag{5.12d}$$

where $\overline{\omega_v}$ and $\underline{\omega_v}$ respectively denote the upper and lower bounds of the *v*th natural frequency ω_v ; $\mu_{(\bullet)}$ and $\sigma_{(\bullet)}$ respectively denote the mean and standard deviation of

variable $(\bullet)$; $H(\boldsymbol{\chi},\theta_\nu)$ denote the random field corresponding to Poisson's ratio; $I_E(\boldsymbol{\chi})$ and $I_\rho(\boldsymbol{\chi})$ denote the interval fields for the spatially dependent uncertain Young's modulus and mass density, respectively.

Within the framework of X-UISS, the spatially dependent uncertain system parameters are firstly transformed into either random or interval vectors by employing the aforementioned field discretization techniques. Thus, the spatially dependent uncertain free vibration is equivalently investigated by analyzing a non-deterministic structural free vibration analysis with spatially independent uncertainties. Subsequently, the random field for Poisson's ratio to the *d*th order can be formulated as:

$$H(\boldsymbol{\chi},\theta_\nu) \approx \hat{H}^d(\boldsymbol{\chi},\theta_\nu) = w(\boldsymbol{\chi}) + \sum_{i=1}^{d} \sqrt{\lambda_i}\psi_i(\theta)\varphi_i(\boldsymbol{\chi}) \tag{5.13}$$

Then the interval fields of Young's modulus and density are respectively discretized as:

$$I_E(\boldsymbol{\chi}) \approx \hat{\mathbf{I}}_E := \{\hat{\mathbf{I}}_E \in \Re^{n_s} \mid \underline{\hat{I}_{E,i_e}} \le \hat{I}_{E,i_e} \le \overline{\hat{I}_{E,i_e}}, i_e = 1,\ldots,n_s\} \tag{5.14}$$

$$I_\rho(\boldsymbol{\chi}) \approx \hat{\mathbf{I}}_\rho := \{\hat{\mathbf{I}}_\rho \in \Re^{n_s} \mid \underline{\hat{I}_{\rho,i_e}} \le \hat{I}_{\rho,i_e} \le \overline{\hat{I}_{\rho,i_e}}, i_e = 1,\ldots,n_s\} \tag{5.15}$$

The X-UISS method is initialized by arbitrarily generating a total number of m_{MCS} sampling points for the discretized random field of Poisson's ratio such that:

$$\boldsymbol{\Omega}_{\hat{\gamma}^R} := \{\hat{\boldsymbol{\gamma}}^R \in \Re^{m_{MCS}} \mid \hat{\boldsymbol{\gamma}}^R_{i_s} = \hat{H}^d(\boldsymbol{\chi},\theta_\nu),\ for\ i_s = 1,\ldots,m_{MCS}, \boldsymbol{\chi} \in \boldsymbol{\psi}\} \tag{5.16}$$

where $\boldsymbol{\Omega}_{\hat{\gamma}^R}$ denotes the set collecting all the realizations, $\hat{\boldsymbol{\gamma}}^R_{i_s}$ denotes the $i_s th$ realization point, $\boldsymbol{\psi}$ represents the concerned domain of the non-deterministic structure. Thus, at the $i_s th$ sampling point, the hybrid spatially uncertain eigenvalue problem is transformed into:

$$\mathbf{K}_s(\hat{\mathbf{I}}_E, \hat{\boldsymbol{\gamma}}_{i_s}^R)\hat{\boldsymbol{\Phi}}_{v,i_s} = \hat{\omega}_{v,i_s}^2 \mathbf{M}_s(\hat{\mathbf{I}}_\rho)\hat{\boldsymbol{\Phi}}_{v,i_s} \tag{5.17}$$

where $\hat{\omega}_{v,i_s}$ is the approximation of the vth natural frequency ω_{v,i_s} at the $i_s th$ sampling point; $\hat{\boldsymbol{\Phi}}_{v,i_s}$ denotes the eigenvectors associated with $\hat{\omega}_{v,i_s}$. Eq. (5.17) indicates that at each sampling point, an interval eigenvalue analysis needs to be conducted such that the upper and lower bounds of natural frequencies associated with this sampling point are determined. Therefore, it is critical for the adopted method to achieve the sharp bounds of natural frequencies at each sampling point. The following proposition indicates that the sharp bounds of eigenvalues are achievable in specified conditions.

Proposition:

Consider two real matrices $\mathbf{A}$ and $\mathbf{B}$ which are defined by

$$\mathbf{A} = \left\{ \mathbf{A} \in \Re^{d_s \times d_s} \middle| \mathbf{A} = \sum_{i_e=1}^{n_s} \hat{\zeta}_{i_e} \cdot \mathbf{a}_{i_e},\ \underline{\hat{\zeta}_i} \le \hat{\zeta}_{i_e} \le \overline{\hat{\zeta}_{i_e}},\ \hat{\zeta} \in \Re^{n_s}, \mathbf{a}_{i_e} \succeq 0, \mathbf{a}_{i_e} \in \Re^{d_s \times d_s} \right\} \tag{5.18}$$

$$\mathbf{B} = \left\{ \mathbf{B} \in \Re^{d_s \times d_s} \middle| \mathbf{B} = \sum_{i_e=1}^{n_s} \zeta_{i_e} \cdot \mathbf{b}_{i_e},\ \underline{\zeta_{i_e}} \le \zeta_{i_e} \le \overline{\zeta_{i_e}},\ \zeta \in \Re^{n_s}, \mathbf{b}_{i_e} \succeq 0, \mathbf{b}_{i_e} \in \Re^{d_s \times d_s} \right\} \tag{5.19}$$

where $\mathbf{a}_{i_e}$ and $\mathbf{b}_{i_e}$ are constant positive-semidefinite matrices. For the eigenvalue problem $\mathbf{A}\mathbf{Y}_v = \lambda_v \mathbf{B}\mathbf{Y}_v$, if the conditions $\mathbf{A} \succ 0$, $\mathbf{B} \succ 0$ and $\hat{\zeta} \cap \zeta = \varnothing$ hold, then:

$$\max_{\hat{\zeta},\zeta}\{\lambda_v\} = \frac{\overline{\mathbf{Y}_v^T}\,\overline{\mathbf{A}}\,\overline{\mathbf{Y}_v}}{\overline{\mathbf{Y}_v^T}\,\underline{\mathbf{B}}\,\overline{\mathbf{Y}_v}} \tag{5.20}$$

$$\min_{\hat{\zeta},\zeta}\{\lambda_v\} = \frac{\underline{\mathbf{Y}_v^T}\,\underline{\mathbf{A}}\,\underline{\mathbf{Y}_v}}{\underline{\mathbf{Y}_v^T}\,\overline{\mathbf{B}}\,\underline{\mathbf{Y}_v}} \tag{5.21}$$

where $\overline{\mathbf{A}} = \sum_{i_e=1}^{n_s} \overline{\hat{\zeta}_{i_e}} \cdot \mathbf{a}_{i_e}$, $\underline{\mathbf{A}} = \sum_{i_e=1}^{n_s} \underline{\hat{\zeta}_{i_e}} \cdot \mathbf{a}_{i_e}$, $\overline{\mathbf{B}} = \sum_{i_e=1}^{n_s} \overline{\zeta_{i_e}} \cdot \mathbf{b}_i$ and $\underline{\mathbf{B}} = \sum_{i_e=1}^{n_s} \underline{\zeta_{i_e}} \cdot \mathbf{b}_{i_e}$; $\overline{\mathbf{Y}_v} \in \Re^{d_s}$ and $\underline{\mathbf{Y}_v} \in \Re^{d_s}$ denote the eigenvectors associated with $\max_{\hat{\zeta},\zeta}\{\lambda_v\}$ and $\min_{\hat{\zeta},\zeta}\{\lambda_v\}$, respectively.

Proof:

By Rayleigh quotient, the *v*th eigenvalue of generalized eigenvalue problem can be calculated as:

$$\lambda_v = \frac{\mathbf{Y}_v^T \mathbf{A} \mathbf{Y}_v}{\mathbf{Y}_v^T \mathbf{B} \mathbf{Y}_v}, \text{ for } v = 1, ..., d_s \tag{5.22}$$

Since $\mathbf{A} \succ 0$, $\mathbf{B} \succ 0$, and $\hat{\boldsymbol{\zeta}} \cap \boldsymbol{\zeta} = \varnothing$, that is:

$$\begin{cases} \mathbf{A} \succ 0 \Rightarrow \mathbf{Y}_v^T \mathbf{A} \mathbf{Y}_v \in \Re \text{ and } \mathbf{Y}_v^T \mathbf{A} \mathbf{Y}_v > 0 \\ \mathbf{B} \succ 0 \Rightarrow \mathbf{Y}_v^T \mathbf{B} \mathbf{Y}_v \in \Re \text{ and } \mathbf{Y}_v^T \mathbf{B} \mathbf{Y}_v > 0 \end{cases} \tag{5.23}$$

Therefore the extreme bounds of eigenvalues can be calculated by:

$$\max_{\hat{\zeta},\zeta}\{\lambda_v\} = \frac{\max_{\hat{\zeta}}\{\overline{\mathbf{Y}_v^T} \mathbf{A} \overline{\mathbf{Y}_v}\}}{\min_{\zeta}\{\overline{\mathbf{Y}_v^T} \mathbf{B} \overline{\mathbf{Y}_v}\}} = \frac{\max_{\hat{\zeta}}\{\hat{a}_1\}}{\min_{\zeta}\{\hat{b}_1\}} \tag{5.24a}$$

$$\min_{\hat{\zeta},\zeta}\{\lambda_v\} = \frac{\min_{\hat{\zeta}}\{\underline{\mathbf{Y}_v^T} \mathbf{A} \underline{\mathbf{Y}_v}\}}{\max_{\zeta}\{\underline{\mathbf{Y}_v^T} \mathbf{B} \underline{\mathbf{Y}_v}\}} = \frac{\min_{\hat{\zeta}}\{\hat{a}_2\}}{\max_{\zeta}\{\hat{b}_2\}} \tag{5.24b}$$

The partial derivatives of $\hat{a}_1$, $\hat{a}_2$, $\hat{b}_1$ and $\hat{b}_2$ with respect to associated uncertain variables satisfy

$$\begin{cases} \dfrac{\partial \hat{a}_1}{\partial \hat{\zeta}_{i_e}} = \overline{\mathbf{Y}_v^T} \mathbf{a}_{i_e} \overline{\mathbf{Y}_v} \geq 0 \\ \dfrac{\partial \hat{a}_2}{\partial \hat{\zeta}_{i_e}} = \underline{\mathbf{Y}_v^T} \mathbf{a}_{i_e} \underline{\mathbf{Y}_v} \geq 0 \\ \dfrac{\partial \hat{b}_1}{\partial \zeta_{i_e}} = \overline{\mathbf{Y}_v^T} \mathbf{b}_{i_e} \overline{\mathbf{Y}_v} \geq 0 \\ \dfrac{\partial \hat{b}_2}{\partial \zeta_{i_e}} = \underline{\mathbf{Y}_v^T} \mathbf{b}_{i_e} \underline{\mathbf{Y}_v} \geq 0 \end{cases}, \quad \forall i_e = 1,...,n_s, \forall v = 1,...,d_s \tag{5.25}$$

From Eq. (5.26), it is concluded that $\hat{a}_1$ and $\hat{a}_2$ are monotonically increasing functions of $\hat{\zeta}_{i_e}$, $\hat{b}_1$ and $\hat{b}_2$ are monotonically increasing functions of ζ_{i_e}. Therefore, the upper bounds of $\hat{a}_1$ and $\hat{b}_2$, and the lower bounds of $\hat{a}_2$ and $\hat{b}_1$ are obtained as following

$$\begin{cases} \max\limits_{\hat{\zeta}}\{\hat{a}_1\} = \overline{\mathbf{Y}_v^T} \overline{\mathbf{A}} \overline{\mathbf{Y}_v} \\ \min\limits_{\hat{\zeta}}\{\hat{a}_2\} = \underline{\mathbf{Y}_v^T} \underline{\mathbf{A}} \underline{\mathbf{Y}_v} \\ \min\limits_{\zeta}\{\hat{b}_1\} = \overline{\mathbf{Y}_v^T} \underline{\mathbf{B}} \overline{\mathbf{Y}_v} \\ \max\limits_{\zeta}\{\hat{b}_2\} = \underline{\mathbf{Y}_v^T} \overline{\mathbf{B}} \underline{\mathbf{Y}_v} \end{cases} \tag{5.26}$$

which is equivalent to Eq. (5.24).

This concludes the proof. □

For linear, elastic and non-deficient structures with adequate boundary conditions, the stiffness and mass matrices are proved to be positive definite [67] regardless of the realizations of $\hat{\mathbf{I}}_E$ and $\hat{\mathbf{I}}_\rho$. Therefore, for any realization of $\hat{\mathbf{I}}_E$ and $\hat{\mathbf{I}}_\rho$, if $\hat{\mathbf{\Phi}}_{v,i_s} \neq \mathbf{0}$ then the following property holds:

$$\mathbf{K}_s(\hat{\mathbf{I}}_E, \hat{\boldsymbol{\gamma}}_{i_s}^R) \succ 0 \Rightarrow \hat{\mathbf{\Phi}}_{v,i_s}^T \mathbf{K}(\hat{\mathbf{I}}_E, \hat{\boldsymbol{\gamma}}_{i_s}^R) \hat{\mathbf{\Phi}}_{v,i_e} > 0 \tag{5.27}$$

$$\mathbf{M}_s(\hat{\mathbf{I}}_\rho) \succ 0 \Rightarrow \hat{\mathbf{\Phi}}_{v,i_s}^T \mathbf{M}(\hat{\mathbf{I}}_\rho) \hat{\mathbf{\Phi}}_{v,i_s} > 0 \tag{5.28}$$

Moreover, considering the discretization of interval field, the uncertain stiffness and mass matrices of the structural system can be alternatively expressed as:

$$\mathbf{K}_s(\hat{\mathbf{I}}_E, \hat{\boldsymbol{\gamma}}_{i_s}^R) = \sum_{i_e=1}^{n_s} \hat{I}_{E,i_e} \cdot \tilde{\mathbf{K}}_{i_e} \tag{5.29}$$

$$\mathbf{M}_s(\hat{\mathbf{I}}_\rho) = \sum_{i_e=1}^{n_s} \hat{I}_{\rho,i_e} \cdot \tilde{\mathbf{M}}_{i_e} \tag{5.30}$$

where $\{\hat{I}_{E,i_e} \cdot \tilde{\mathbf{K}}_{i_e}\} \in \Re^{d_s \times d_s}$ denotes the uncertain elemental stiffness matrix; and $\{\hat{I}_{\rho,i_e} \cdot \tilde{\mathbf{M}}_{i_e}\} \in \Re^{d_s \times d_s}$ denotes the uncertain elemental mass matrix. Considering the linear elastic structure, within the framework of FEM, the total strain energy (U) and kinetic energy (T) of the structural system are respectively expressed as:

$$U = \frac{1}{2}\mathbf{u}_s{}^T \mathbf{K}_s(\hat{\mathbf{I}}_E, \hat{\boldsymbol{\gamma}}_{i_s}^R)\mathbf{u}_s = \sum_{i_e=1}^{n_s} U_{i_e} = \frac{1}{2}\sum_{i_e=1}^{n_s} \hat{I}_{E,i_e} \cdot \mathbf{u}_s{}^T \tilde{\mathbf{K}}_{i_e} \mathbf{u}_s \tag{5.31}$$

$$T = \frac{1}{2}\dot{\mathbf{u}}_s^T \mathbf{M}_s(\hat{\mathbf{I}}_\rho)\dot{\mathbf{u}}_s = \sum_{i_e=1}^{n_s} T_{i_e} = \frac{1}{2}\sum_{i_e=1}^{n_s} \hat{I}_{\rho,i_e} \cdot \dot{\mathbf{u}}_s^T \tilde{\mathbf{M}}_{i_e} \dot{\mathbf{u}}_s \tag{5.32}$$

where $\mathbf{u}_s \in \Re^{d_s}$ denotes the structure displacement vector; $\dot{\mathbf{u}}_s \in \Re^{d_s}$ denotes the structure velocity vector. By definition, if the structure is adequately restrained, the total strain energy and kinetic energy must be positive. Meanwhile, the elemental strain energy (U_i) and kinetic energy (T_i) must be non-negative. Such phenomenon is self-explained since that the elemental stiffness matrix $\{\hat{I}_{E,i_e} \cdot \tilde{\mathbf{K}}_{i_e}\} \in \Re^{d_s \times d_s}$ and mass matrix $\{\hat{I}_{\rho,i_e} \cdot \tilde{\mathbf{M}}_{i_e}\} \in \Re^{d_s \times d_s}$ can be considered as the global stiffness and mass matrices of a deficient structural system where the rigid body motion is not prevented. Additionally,

both $\hat{\mathbf{I}}_E$ and $\hat{\mathbf{I}}_\rho$ are positive vectors by definition. Therefore, the following relationships are valid:

$$U = \sum_{i_e=1}^{n_s} U_{i_e} > 0 \Rightarrow U_{i_e} = \frac{1}{2}\hat{I}_{E,i_e} \cdot \mathbf{u}_s^T \tilde{\mathbf{K}}_{i_e} \mathbf{u} \geq 0 \Rightarrow \mathbf{u}_s^T \tilde{\mathbf{K}}_{i_e} \mathbf{u} \geq 0 \tag{5.33}$$

$$T = \sum_{i_e=1}^{n_s} T_{i_e} > 0 \Rightarrow T_{i_e} = \frac{1}{2}\hat{I}_{\rho,i_e} \cdot \dot{\mathbf{u}}_s^T \tilde{\mathbf{M}}_{i_e} \dot{\mathbf{u}}_s \geq 0 \Rightarrow \dot{\mathbf{u}}_s^T \tilde{\mathbf{M}}_{i_e} \dot{\mathbf{u}}_s \geq 0 \tag{5.34}$$

Hence, the matrices $\tilde{\mathbf{K}}_{i_e}$ and $\tilde{\mathbf{M}}_{i_e}$ are both positive semi-definite for the considered structural system in this study. Subsequently, the upper and lower bounds of $\hat{\lambda}_{v,i_s}$ can be rigorously determined from two independent eigen-analyses with the interval input as expressed in Eqs. (5.35) and (5.36):

$$\overline{\hat{\lambda}_{v,i_s}} = \overline{\hat{\omega}_{v,i_s}}^{\,2} = \frac{\overline{\hat{\mathbf{\Phi}}_{v,i_s}}^{\,T} \mathbf{K}_s(\overline{\hat{\mathbf{I}}_E}, \hat{\boldsymbol{\gamma}}_{i_s}^R)\overline{\hat{\mathbf{\Phi}}_{v,i_s}}}{\overline{\hat{\mathbf{\Phi}}_{v,i_s}}^{\,T} \mathbf{M}_s(\underline{\hat{\mathbf{I}}_\rho})\overline{\hat{\mathbf{\Phi}}_{v,i_s}}} \tag{5.35}$$

$$\underline{\hat{\lambda}_{v,i_s}} = \underline{\hat{\omega}_{v,i_s}}^{\,2} = \frac{\underline{\hat{\mathbf{\Phi}}_{v,i_s}}^{\,T} \mathbf{K}_s(\underline{\hat{\mathbf{I}}_E}, \hat{\boldsymbol{\gamma}}_{i_s}^R)\underline{\hat{\mathbf{\Phi}}_{v,i_s}}}{\underline{\hat{\mathbf{\Phi}}_{v,i_s}}^{\,T} \mathbf{M}_s(\overline{\hat{\mathbf{I}}_\rho})\underline{\hat{\mathbf{\Phi}}_{v,i_s}}} \tag{5.36}$$

where $\overline{\hat{\mathbf{I}}_E}$ and $\underline{\hat{\mathbf{I}}_E}$ respectively denote the upper and lower bounds of $\hat{\mathbf{I}}_E$; $\overline{\hat{\mathbf{I}}_\rho}$ and $\underline{\hat{\mathbf{I}}_\rho}$ respectively denote the upper and lower bounds of $\hat{\mathbf{I}}_\rho$. Therefore, the extreme bounds of the natural frequencies calculated by the X-UISS in the context of $\hat{\mathbf{I}}_E$ and $\hat{\mathbf{I}}_\rho$ (the discretization of $I_E(\boldsymbol{\chi})$ and $I_\rho(\boldsymbol{\chi})$) at each sampling point of $\hat{H}^d(\boldsymbol{\chi}, \theta_v)$ are promised to be exact. □

Then, for both upper and lower bounds of the vth ($v = 1,...,d_s$) eigenvalue, a collection of r samples are provided after implementing the interval analysis at all the sampling points. Benefiting from the offered samples, the sample means and standard deviations of the upper and lower bounds of natural frequencies can be respectively determined as:

$$\hat{\mu}_{\overline{\hat{\omega}_v}} = \frac{1}{m_{MCS}} \sum_{i_s=1}^{m_{MCS}} \overline{\hat{\omega}_{v,i_s}} \tag{5.37}$$

$$\hat{\mu}_{\underline{\hat{\omega}_v}} = \frac{1}{m_{MCS}} \sum_{i_s=1}^{m_{MCS}} \underline{\hat{\omega}_{v,i_s}} \tag{5.38}$$

$$\hat{\sigma}^2_{\overline{\hat{\omega}_v}} = \frac{1}{m_{MCS}-1} \sum_{i_s=1}^{m_{MCS}} (\overline{\hat{\omega}_{v,i_s}} - \mu_{\overline{\hat{\omega}_v}})^2 \tag{5.39}$$

$$\hat{\sigma}^2_{\underline{\hat{\omega}_v}} = \frac{1}{m_{MCS}-1} \sum_{i_s=1}^{m_{MCS}} (\underline{\hat{\omega}_{v,i_s}} - \mu_{\underline{\hat{\omega}_v}})^2 \tag{5.40}$$

where $\hat{\mu}_{(\bullet)}$ and $\hat{\sigma}_{(\bullet)}$ denote the sample mean and standard deviation of the concerned extreme bound of $\hat{\omega}_v$, respectively. If $\mu_{\overline{\hat{\omega}_v}}$ and $\mu_{\underline{\hat{\omega}_v}}$ respectively denote the true mean of upper and lower bounds of $\hat{\omega}_v$, then based on the linearity of expected value, that is:

$$\mathrm{E}[\hat{\mu}_{\overline{\hat{\omega}_v}}] = \mathrm{E}\left[\frac{1}{m_{MCS}} \sum_{i_s=1}^{m_{MCS}} \overline{\hat{\omega}_{v,i_s}}\right] = \frac{1}{m_{MCS}} \sum_{i_s=1}^{m_{MCS}} \mathrm{E}[\overline{\hat{\omega}_{v,i_s}}] = \frac{1}{m_{MCS}} \cdot m_{MCS} \cdot \mu_{\overline{\hat{\omega}_v}} = \mu_{\overline{\hat{\omega}_v}} \tag{5.41}$$

$$\mathrm{E}[\hat{\mu}_{\underline{\hat{\omega}_v}}] = \mathrm{E}\left[\frac{1}{m_{MCS}} \sum_{i_s=1}^{m_{MCS}} \underline{\hat{\omega}_{v,i_s}}\right] = \frac{1}{m_{MCS}} \sum_{i_s=1}^{m_{MCS}} \mathrm{E}[\underline{\hat{\omega}_{v,i_s}}] = \frac{1}{m_{MCS}} \cdot m_{MCS} \cdot \mu_{\underline{\hat{\omega}_v}} = \mu_{\underline{\hat{\omega}_v}} \tag{5.42}$$

where $\mathrm{E}[\bullet]$ denotes the expectation operator for $[\bullet]$. Furthermore, the variance of the variance estimators illustrated in Eqs. (5.43) – (5.44) are approaching to zero as r (number of samples) increases to infinity, which can be demonstrated as:

$$\begin{aligned}\mathrm{Var}[\hat{\mu}_{\overline{\hat{\omega}_v}}] &= \mathrm{Var}\left[\frac{1}{m_{MCS}}\sum_{i_s=1}^{m_{MCS}}\overline{\hat{\omega}_{v,i_s}}\right] = \frac{1}{m_{MCS}^{\ 2}}\sum_{i_s=1}^{m_{MCS}}\mathrm{Var}[\overline{\hat{\omega}_{v,i_s}}] \\ &= \frac{1}{m_{MCS}^{\ 2}}\cdot m_{MCS}\cdot\sigma^2_{\overline{\hat{\omega}_v}} = \frac{\sigma^2_{\overline{\hat{\omega}_v}}}{m_{MCS}}\end{aligned} \tag{5.43}$$

$$\begin{aligned}\mathrm{Var}[\hat{\mu}_{\underline{\hat{\omega}_v}}] &= \mathrm{Var}\left[\frac{1}{m_{MCS}}\sum_{i_s=1}^{m_{MCS}}\underline{\hat{\omega}_{v,i_s}}\right] = \frac{1}{m_{MCS}^{\ 2}}\sum_{i_s=1}^{m_{MCS}}\mathrm{Var}[\underline{\hat{\omega}_{v,i_s}}] \\ &= \frac{1}{m_{MCS}^{\ 2}}\cdot m_{MCS}\cdot\sigma^2_{\underline{\hat{\omega}_v}} = \frac{\sigma^2_{\underline{\hat{\omega}_v}}}{m_{MCS}}\end{aligned} \tag{5.44}$$

where $\mathrm{Var}[\bullet]$ denotes the variance operator for $[\bullet]$, and $\sigma^2_{\overline{\hat{\omega}_v}}$ and $\sigma^2_{\underline{\hat{\omega}_v}}$ respectively denote the true variance of upper and lower bounds of $\hat{\omega}_v$. Subsequently, according to the Kolmogorov's Strong Law of Large Numbers, if the size of sample tends to infinity, the sample mean of the extreme bounds of the *j*th natural frequency converge almost surely to the corresponding true expected values. Therefore, the estimators in Eqs. (5.43) - (5.44) are consistent as well. Moreover, the point estimation for the variance of extreme bounds of *v*th natural frequency can be proved to be unbiased, and converge almost surely to the true variances by adopting the same theoretical support for the estimators of mean [137]. In this context, the robust point estimations of mean and standard deviations of the upper and lower bounds of any concerned natural frequency can be achieved by implementing the X-UISS scheme.

Additionally, the probability distribution of the extreme bounds can be conveniently identified by employing adequate statistical inference methods (i.e. parametric and non-parametric analysis). Subsequently, the probability density functions (PDFs) and cumulative distribution functions (CDFs) can be established as:

$$f^{PDF}_{\overline{\omega_{i_s}}}(\overline{\omega_{i_s}}) \approx \tilde{f}^{PDF}_{\overline{\omega_{i_s}}}(\overline{\hat{\omega}_{i_s}}) = \tilde{f}^{PDF}(\mu_{\overline{\omega_v}}, \sigma^2_{\overline{\omega_v}}, \overline{\hat{\omega}_{v,i_s}}), \quad \text{for } i_s = 1,\ldots,m_{MCS} \tag{5.45}$$

$$f_{\underline{\omega_{i_s}}}^{PDF}(\underline{\omega_{i_s}}) \approx \tilde{f}_{\underline{\omega_{i_s}}}^{PDF}(\underline{\hat{\omega}_{i_s}}) = \tilde{f}^{PDF}(\mu_{\underline{\omega_v}}, \sigma_{\underline{\omega_v}}^2, \underline{\hat{\omega}_{v,i_s}}), \quad \text{for } i_s = 1,...,m_{MCS} \tag{5.46}$$

$$f_{\overline{\omega_{i_s}}}^{CDF}(\overline{\omega_{i_s}}) \approx \tilde{f}_{\overline{\omega_{i_s}}}^{CDF}(\overline{\hat{\omega}_{i_s}}) = \int_{-\infty}^{\infty} \tilde{f}_{\overline{\hat{\omega}_{i_s}}}(\overline{\hat{\omega}_{i_s}}) d\overline{\hat{\omega}_i} \tag{5.47}$$

$$f_{\underline{\omega_{i_s}}}^{CDF}(\underline{\omega_{i_s}}) \approx \tilde{f}_{\underline{\omega_{i_s}}}^{CDF}(\underline{\hat{\omega}_{i_s}}) = \int_{-\infty}^{\infty} \tilde{F}_{\underline{\hat{\omega}_{i_s}}}(\underline{\hat{\omega}_{i_s}}) d\underline{\hat{\omega}_{i_s}} \tag{5.48}$$

where $f_{(\bullet)}^{PDF}$ and $\tilde{f}_{(\bullet)}^{PDF}$ denote the true and estimated PDFs of the random variable $(\bullet)$, respectively; $f_{(\bullet)}^{CDF}$ and $\tilde{f}_{(\bullet)}^{CDF}$ denote the true and estimated CDFs of the random variable $(\bullet)$, respectively. Furthermore, if ω_v^* denotes the constraint of the *v*th natural frequency, then the upper and lower bounds of the structural reliability against such constraint can be respectively estimated as:

$$\overline{P_r} = \Pr\{\overline{\hat{\omega}_v} \le \omega_v^*\} = \int_{-\infty}^{\omega_v^*} \tilde{f}_{\overline{\hat{\omega}_v}}(x) dx \tag{5.49}$$

$$\underline{P_r} = \Pr\{\underline{\hat{\omega}_v} \le \omega_v^*\} = \int_{-\infty}^{\omega_v^*} \tilde{f}_{\underline{\hat{\omega}_v}}(x) dx \tag{5.50}$$

The solution algorithm of X-UISS for the uncertain free vibration analysis with spatially dependent random Poisson's ratio, and interval Young's modulus and density are demonstrated in the flowchart as Figure 5.1.

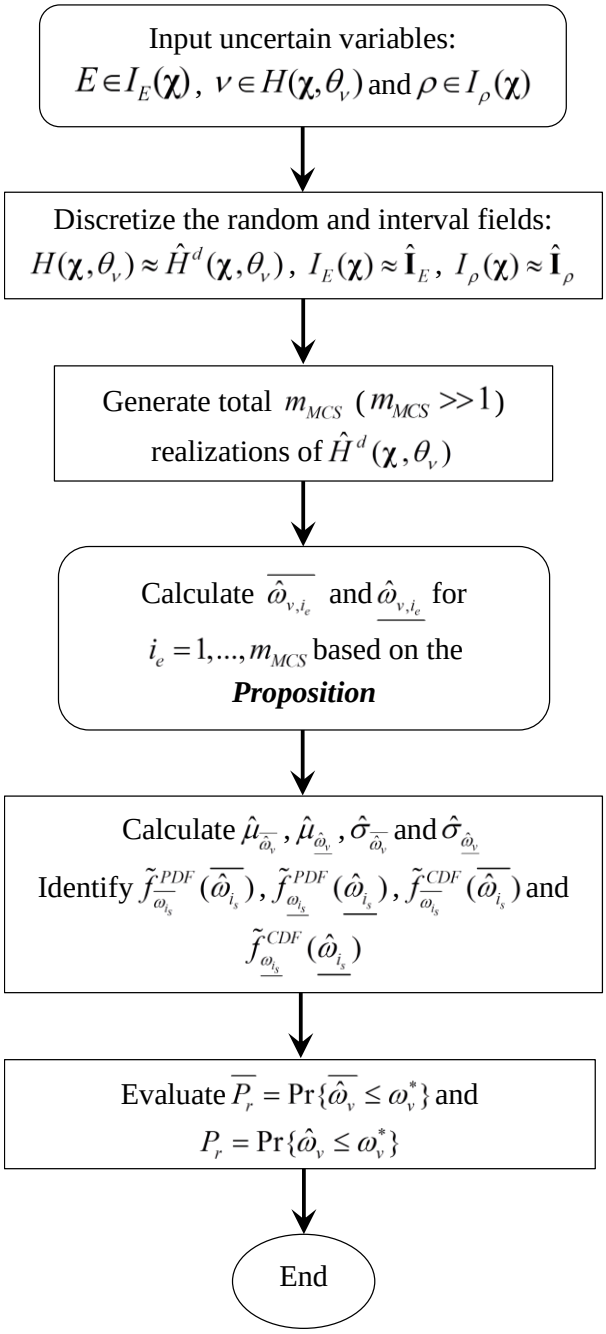

Figure 5.1 Solution algorithm of X-UISS method

The X-UISS approach offers a robust, effective and rational strategy for the hybrid uncertain free vibration analysis for engineering structures with spatially dependent and mutually independent random and interval uncertainties. The implemented computational framework transfers the generalized spatially uncertain eigenvalue problem into a stochastic interval analysis which provides valid and robust estimations on the statistical

characteristics of the extreme bounds of the natural frequencies. Since the independency between random and interval uncertainties is assumed, the physical feasibility of the investigated eigenvalue problem is not affected by respectively discretizing the two types of spatial-variant uncertain parameters. Subsequently, the X-UISS method converts the spatially dependent eigenvalue analysis into a spatially independent one by adopting appropriate discretizing methods.

Benefiting from the calculated samples of upper and lower bounds of the natural frequencies, the PDFs and CDFs of the extremities of all concerned natural frequencies can be obtained by implementing either parametric or non-parametric statistical inference methods in addition to the statistical characteristics (i.e. mean and standard deviations). Evidently supported by the proposition, the sharpness of each interval analysis enclosed in the X-UISS method is promised. Therefore, for any concerned natural frequency, the accordingly constructed PDFs of upper and lower bounds offer a solution hull for the variation of such natural frequency at any specific probability. Moreover, the robustly bounded reliability as indicated in Eqs. (5.49) - (5.50) are rationally obtained by the CDFs of upper and lower bounds of the concerned natural frequency. As a semi-sampling computational strategy, the X-UISS is not only applicable where normally distributed random variables exist but also extendable to the spatially uncertain free vibration problem involving random fields with other types of distribution (e.g. lognormal distribution). Thus, the X-UISS approach offers a robust and effective computational framework for analyzing the uncertain free vibration problem with hybrid random and interval fields.

5.4 Numerical examples

The applicability and effectiveness of the proposed computational scheme are critically verified through investigations on the practically motivated engineering structures in this section. According to the previous studies on the stochastic finite element method, the KL expansion for some typical covariance functions can be truncated at relatively small numbers of orders ($d \leq 20$) [192] while the convergence is maintained acceptable. In order to a though the convergence, the dependent KL expansion is truncated at the order of 40 for all random fields considered in this investigation. Due to the limitation of authors in the access to experimental data, the adopted upper and lower bound functions of interval field are based on assumption. For validation purposes, the statistical characteristics of the extreme bounds of natural frequencies obtained by the X-UISS method are contrasted by comparing with results provided by a hybrid sampling method (LHS-MCS) which combines the Latin Hypercube Sampling (LHS) approach [193] with the Monte Carlo simulation (MCS). Within the hybrid sampling approach, the LHS is utilized for generating sampling points for interval fields, while the MCS is implemented for generating samples of random fields. Subsequently, a stochastic MCS is conducted at each interval sampling point such that the collection of means and standard deviations of natural frequencies can be obtained. Then, the variations of the statistical characteristics of natural frequencies can be revealed. The presented numerical results are obtained by using a workstation with CPU of Intel Core i7-4770, 32 GB of memory, and 1 TB of hard drive.

5.4.1 Cantilever plate

The first investigation considers a cantilever plate, which is the same structure used in Section 4.4.3, with spatially dependent uncertain material properties. The general layout

of the structure with geometrical properties is depicted in Figure 4.12. Moreover, 3-node triangular element based on Kirchhoff plate theory is implemented for the uncertain free vibration analysis of the structure.

For this example, both Young's modulus (E , unit: GPa) and Poisson's ratio (ν) are considered as random fields with Gaussian distribution [30], with $\mu_E = 73.084\ GPa$, $\sigma_E = 7.3084\ GPa$, and $\mu_\nu = 0.03$, $\sigma_\nu = 0.003$. The exponential covariance function with correlation length of $L_x = 7.5m$ and $L_y = 3m$ are adopted for both the random fields of both E and ν . The mass density of the cantilever plate is considered as an interval field such that the upper and lower bounds vary continuously along the x and y axes. The upper and lower bound functions of density (ρ , unit: kg/m^3) are expressed in Eqs. (5.51) - (5.52). In order to visibly demonstrate the spatial variance of the uncertain Young's modulus and Poison's ratio, some selected realizations of the random fields are shown in Figures 5.2 and 5.3. Moreover, the extreme bound functions of ρ can be visualized as Figure 5.4

$$\begin{aligned}\overline{\rho}(x,y) &= 2800 + 60\sin\left(\frac{x}{12} + 0.6\pi\right) \\ &\quad + 100\cos\left(\frac{y}{4.5} + 1.2\right) - 50\sin\left(\frac{xy + 4x}{6.5} + 0.1\right)\end{aligned} \tag{5.51}$$

$$\begin{aligned}\underline{\rho}(x,y) &= 2730 + 70\cos\left(\frac{x}{2\pi} + \frac{y}{1.8}\right) \\ &\quad - 100\sin\left(\frac{y}{2.5} - \frac{x}{4.3}\right) - 40\cos\left(\frac{\pi}{45}(y - 2x)\right)\end{aligned} \tag{5.52}$$

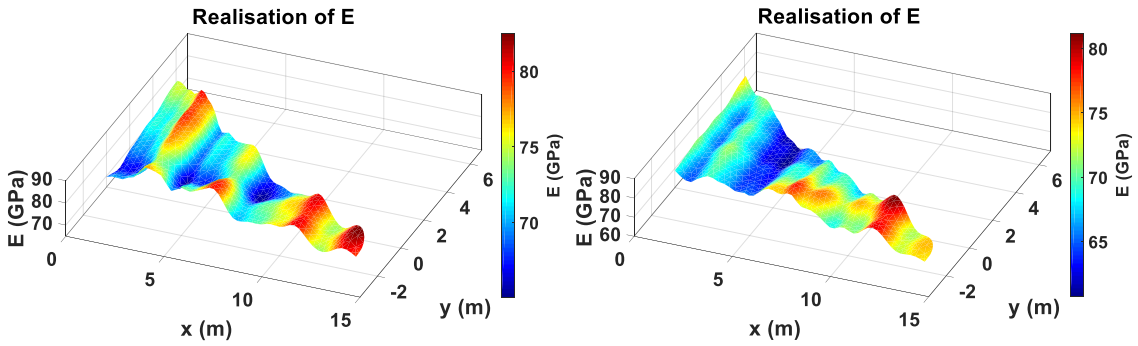

Figure 5.2 Selected realizations of the random fields of E

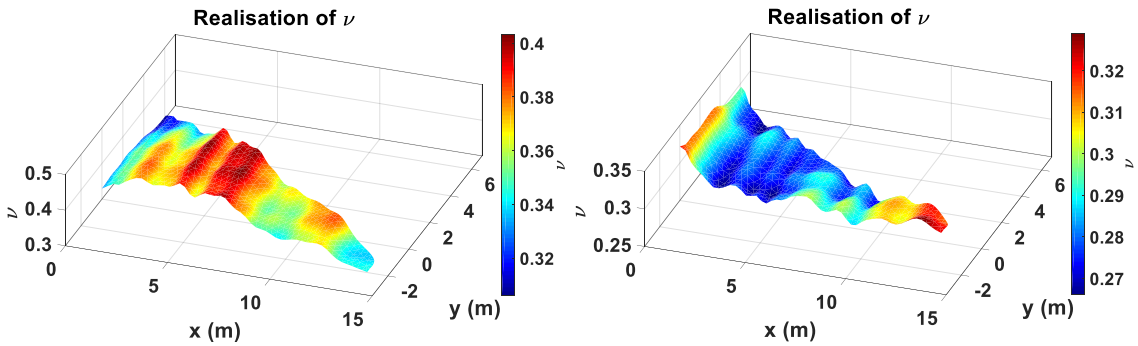

Figure 5.3 Selected realizations of the random fields of ν

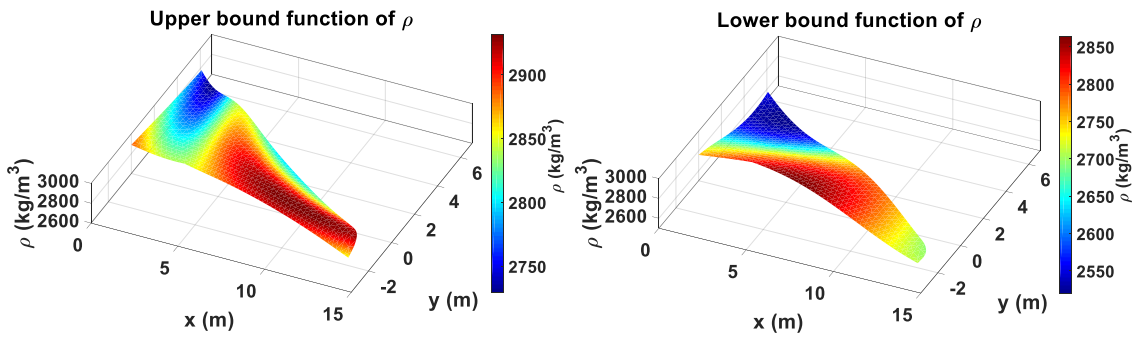

(a) (b)

Figure 5.4 Upper (a) and lower (b) bound functions of ρ

Table 5.1 Different meshes adopted for Example 5.4.1

Mesh	1	2	3	4	5	6
Number Of nodes	1,167	1,459	1,908	2,568	3,680	5,708
Number of elements	2,161	2,725	3,594	4,873	7,048	11,030

To investigate the effect of mesh size on the computational output, total 6 unstructured triangular meshes are adopted for the computation of the X-UISS approach. The details of the different FEM discretization are summarized in Table 5.1, which indicates that the number of elements and nodes increases from Mesh 1 to Mesh 6. Such unstructured mesh is generated by employing a Delaunay mesh-generator [184] which is proved to be capable in generating high-quality triangular mesh. Subsequently, by utilizing the spatial average discretization on the interval fields, the discretized upper and lower bound functions of the uncertain mass density are respectively represented by two upper and lower bound vectors. The discretized upper and lower bound functions resulted from Mesh 1, 3 and 5 are shown in Figure 5.5 which offers an intuitional expression of the interval field discretization.

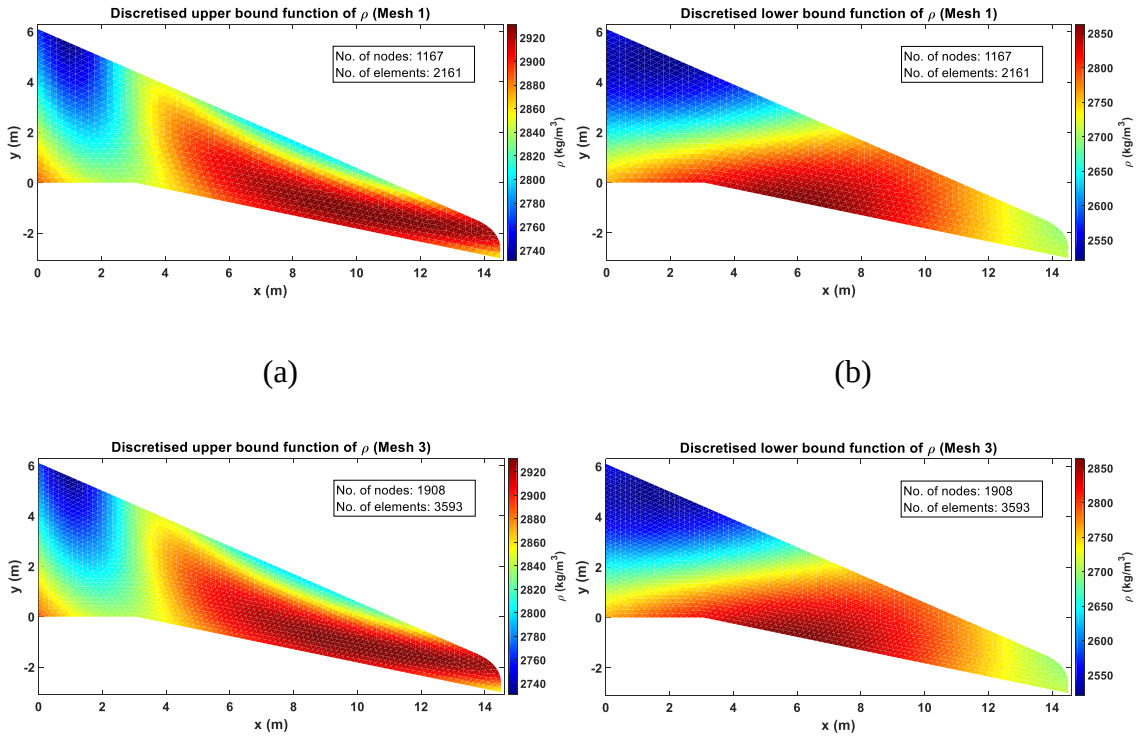

(a) (b)

(c) (d)

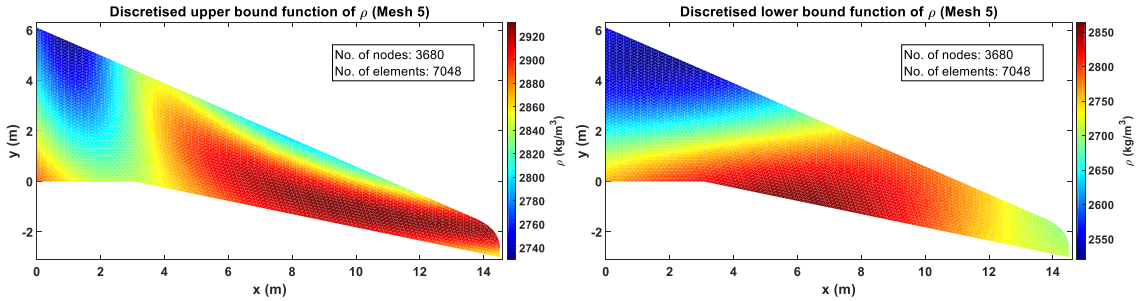

(e) (f)

Figure 5.5 Discretized upper and lower bound functions of ρ corresponding to Mesh 1 (a and b), 3 (c and d) and 5 (e and f)

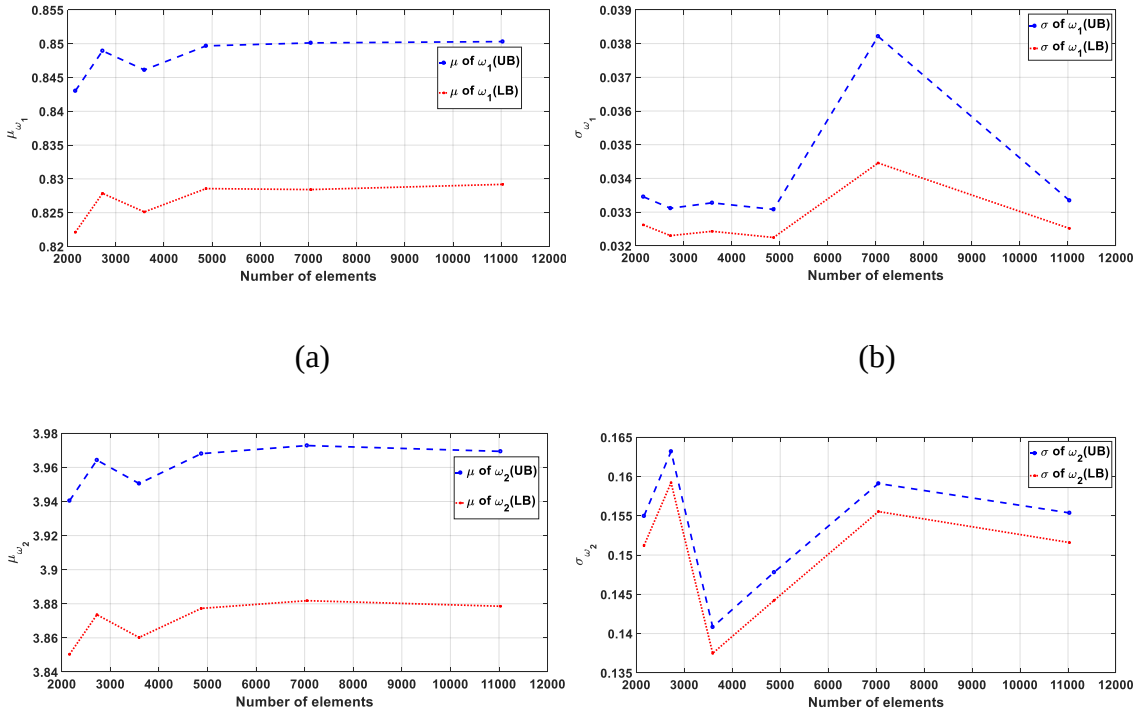

(a) (b)

(c) (d)

Figure 5.6 Mean (μ) and standard deviation (σ) of the upper bound (UB) and lower bound (LB) of ω_1 and ω_2 with respect to different meshes

By implementing the X-UISS method with 1,000 sampling points on all the different meshes, the mean and standard deviations of the extreme bounds of the natural frequencies are calculated. For the purpose of demonstration, the results of the first two natural frequencies obtained by the X-UISS method are summarized in Figure 5.6. The

presented results indicate that the means of the upper and lower bounds of natural frequencies gradually converge with the increase of total element number of the FEM discretization. In contrast, the standard deviations fluctuate at different element sizes.

In order to verify the results achieved by the X-UISS approach, the LHS-MCS method with total 100,000 simulations (1,000 samples for random fields and 100 samples for interval field) is conducted on Mesh 2 and the computational results are also illustrated in Table 5.2. It is revealed that the results calculated by LHS-MCS method are enclosed by the results of the X-UISS approach. Furthermore, the computational time of the X-UISS method is 1.206×10^{4} second which is much less than the simulation time (6.211×10^{5} second) of the LHS-MCS approach. Thus, it is evidently demonstrated that the X-UISS approach offers the high-quality results with competitive computational efficiency.

Table 5.2 The statistical characteristics of bounds of ω_1 and ω_2 of Example 5.4.1 obtained by X-UISS and LHS-MCS with Mesh 2

	X-UISS (1000)	LHS-MCS(100×1000)
$\mu_{\overline{\omega_1}}$ (Hz)	0.8489	0.8365
$\sigma_{\overline{\omega_1}}$ (Hz)	0.0331	0.0326
$\mu_{\underline{\omega_1}}$ (Hz)	0.8279	0.8345
$\sigma_{\underline{\omega_1}}$ (Hz)	0.0323	0.0325
$\mu_{\overline{\omega_2}}$ (Hz)	3.9643	3.9128
$\sigma_{\overline{\omega_2}}$ (Hz)	0.1632	0.1557
$\mu_{\underline{\omega_2}}$ (Hz)	3.8736	3.9058
$\sigma_{\underline{\omega_2}}$ (Hz)	0.1592	0.1545

Furthermore, the effect of sample size on the results of X-UISS method is preliminarily addressed based on Mesh 2. In addition to the 1,000 sampling points as aforementioned, the X-UISS method is implemented with 5,000, 10,000, 25,000 and 50,000 sample sizes. The statistical characteristics of the extreme bounds of ω_1 and ω_2 are demonstrated in Figure 5.7. As indicated by Figure 5.7, limited variation of the mean of extreme bounds of the concerned natural frequencies appears with the increasing of sample size, while the standard deviations gradually converge and then fluctuate when the sample size is increased to more than 10,000. Thus, as a trade-off of computational efficiency and accuracy, 10,000 sampling points is capable in offering the results with reasonable quality in this context.

Overall, it can be revealed from the results presented in Table 5.2 and Figure 5.7 that the X-UISS approach offers an effective computational strategy for solving the spatially uncertain free vibration problem with hybrid random and interval fields.

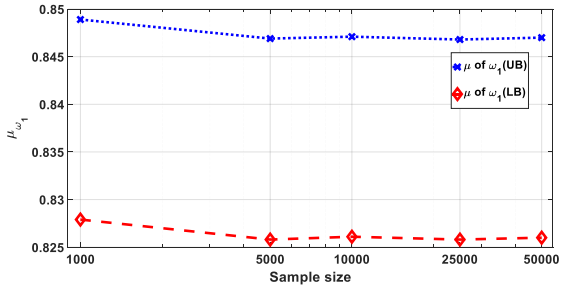

(a)

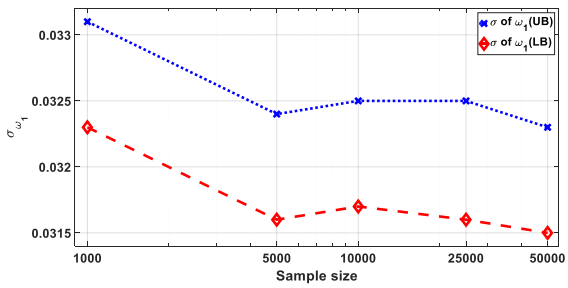

(b)

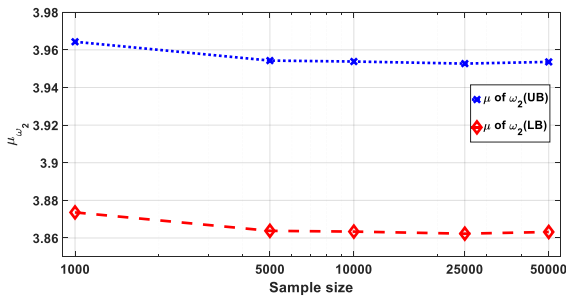

(c)

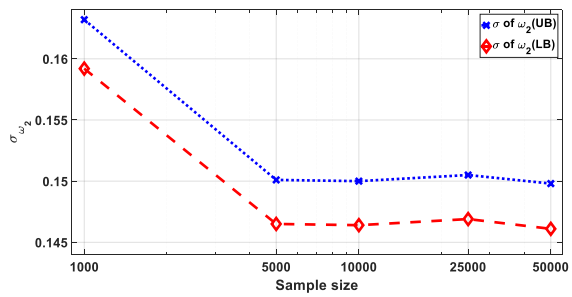

(d)

Figure 5.7 Mean (μ) and standard deviation (σ) of the upper bound (UB) and lower bound (LB) of ω_1 and ω_2 with respect to different sampling points

5.4.2 Steel arch bridge

To further investigate the uncertain free vibration of structures with spatially dependent uncertain parameters as well as the performance of the X-UISS method, a practical-sized 3-D steel bridge consisting four arches is considered in the second example. The general layout and dimensions of the steel arch bridge are demonstrated in Figure 5.8. Additionally, the details of the cross-sections of the four arches and the bracing members of the bridge are presented in Figure 5.9. As indicated by Figure 5.8, each arch is discretized into 100 3-D beam elements and each bracing member is modelled as one 3-D beam element.

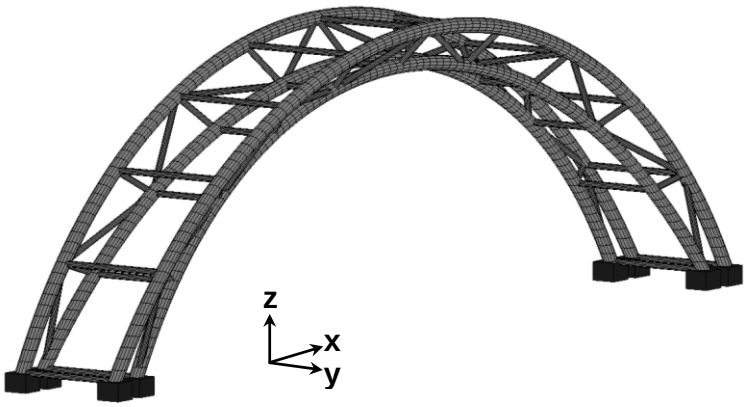

(a)

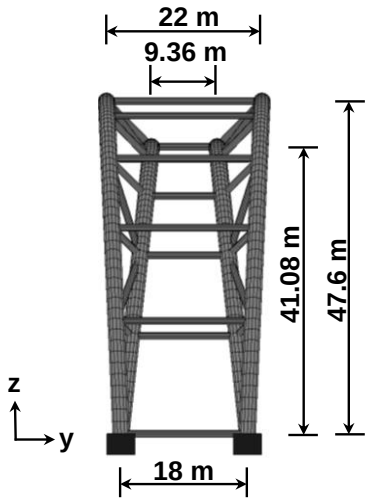

(b)

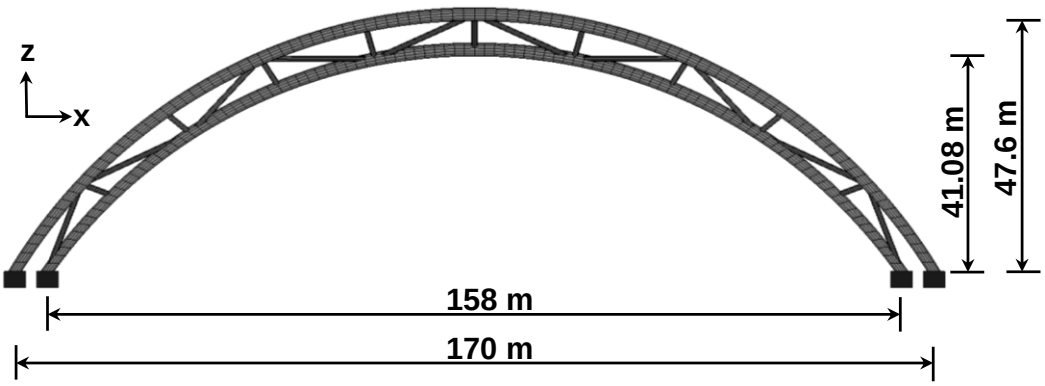

(c)

Figure 5.8 The general layout (a) and the dimensions (b and c) of the steel arch bridge

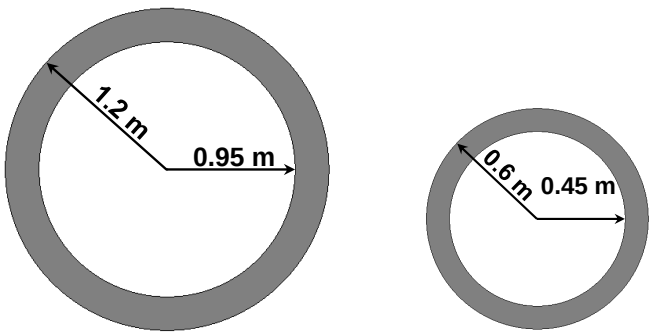

(a) (b)

Figure 5.9 Cross-sections of arch (a) and bracing (b) members

For this particular investigation, the Young's modulus, density and Poisson's ratio of the main arches of the bridge are considered as spatially dependent uncertain parameters which vary along the x-axis, while the material properties of the bracing elements are remained deterministic. The density (ρ) of each arch is modelled as lognormal random field with $\mu_\rho = 7{,}850\ kg/m^3$ and $\sigma_\rho = 785\ kg/m^3$, and an exponential covariance function with correlation length $L_{\rho,x} = 40\ m$. The Poisson's ratio (ν) is considered as Gaussian random field [194] with $\mu_\nu = 0.303$ and $\sigma_\nu = 0.0303$, and an exponential covariance function with correlation length $L_{\nu,x} = 50\ m$. The Young's modulus (E) of main arches are modelled as interval fields with the upper and lower bound functions expressed as Eqs. (5.53) - (5.60). The arches with span $158\ m$ (inner span) are labelled as 1 and 2, and the other two arches (outer span) are labelled as 3 and 4 in this example. The deterministic Young's modulus, density and Poisson's ration of bracing members are: $E_b = 200\ GPa$, $\rho_b = 7{,}850\ kg/m^3$ and $\nu_b = 0.303$. Moreover, selected examples of realizations of spatially dependent and randomly distributed density and Poisson's ratio are demonstrated in Figure 5.10 and the visualization of the extreme bound functions of Young's modulus is presented in Figure 5.11 to offer a more intuitionistic illustration.

$$\overline{I_{E,1}}(x) = 205 + 2.48\sin\left(\frac{8(100-5x)}{L_1}\right) + 0.81\cos\left(\frac{15\pi x}{L_1}\right) \tag{5.53}$$

$$\underline{I_{E,1}}(x) = 195 - 2.48\cos\left(\frac{8(100-3x)}{L_1}\right) + 0.81\sin\left(\frac{25\pi x}{L_1}\right) \tag{5.54}$$

$$\overline{I_{E,2}}(x) = 202 + 0.9\exp\left(-2\cos\left(\frac{3x}{L_1} + 2.3\right) + 0.9\left(\sin\left(\frac{2\pi x}{22}\right) + 1.2\right)\right) \tag{5.55}$$

$$\underline{I_{E,2}}(x) = 200 - 0.5\exp\left(-3\sin\left(\frac{2x}{L_1} + 3.2\right) + 0.6\left(\cos\left(\frac{3\pi x}{28}\right) + 1.2\right)\right) \tag{5.56}$$

$$\overline{I_{E,3}}(x) = 202 + 1.6\left(\sin\left(\frac{\pi x}{54}\right) + 3.2\right) - 0.7\exp\left(-3\left(\cos\left(L_2 - \frac{\pi x}{L_2}\right) + 1.2\right)\right) \tag{5.57}$$

$$\underline{I_{E,3}}(x) = 195 + 0.8\exp\left(\sin\left(L_2 + \frac{\pi x}{L_2} + 3.2\right) + 1.2\right) - \exp\left(0.9\cos\left(\frac{\pi x}{62} + 4.2\right)\right) \tag{5.58}$$

$$\overline{I_{E,4}}(x) = 205 + 3.5\cos\left(\frac{2.5x}{L_2}\right) + 1.5\sin\left(\frac{\pi x}{12}\right) - 2.5\cos\left(\frac{\pi x}{22}\right) \tag{5.59}$$

$$\underline{I_{E,4}}(x) = 195 + 1.5\sin\left(\frac{1.5\pi x}{34}\right) - 2.5\cos\left(\frac{\pi x}{22}\right) - 0.9\sin\left(\frac{\pi x}{L_2}\right) \tag{5.60}$$

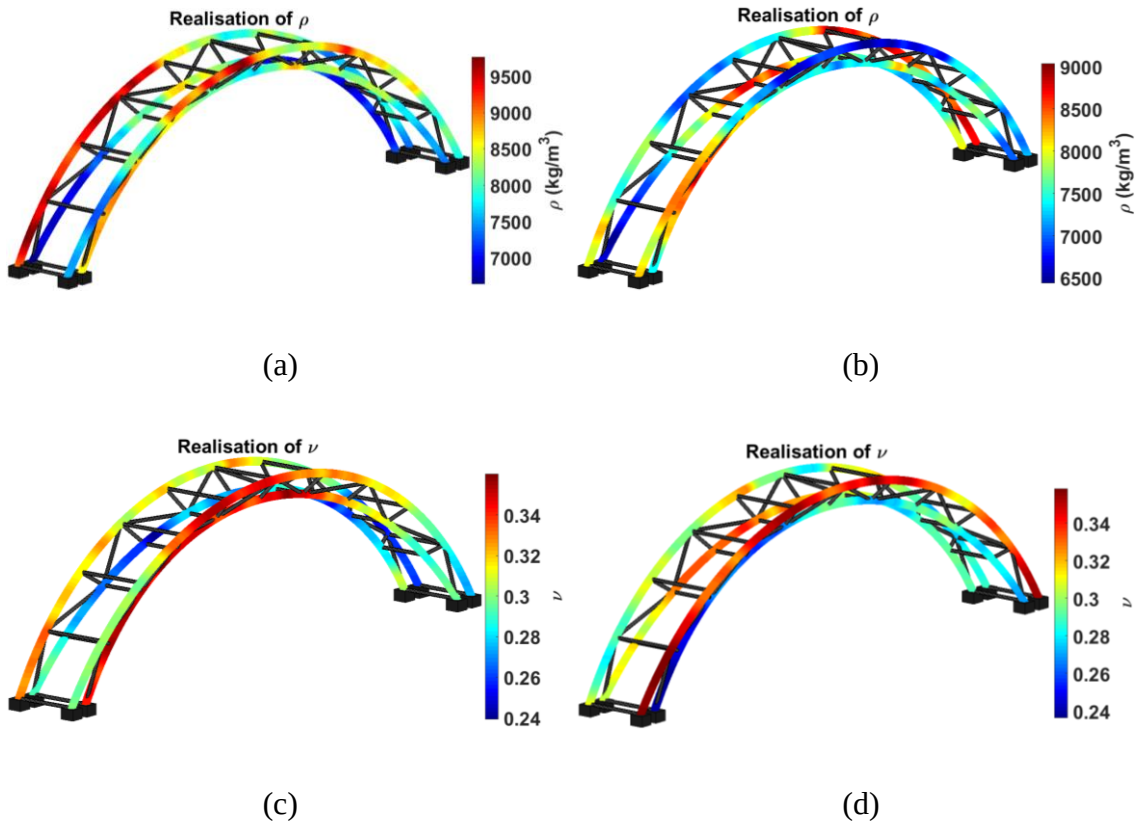

Figure 5.10 Selected realizations of random fields of Example 5.4.2: density (a and b) and Poisson's ratio (c and d)

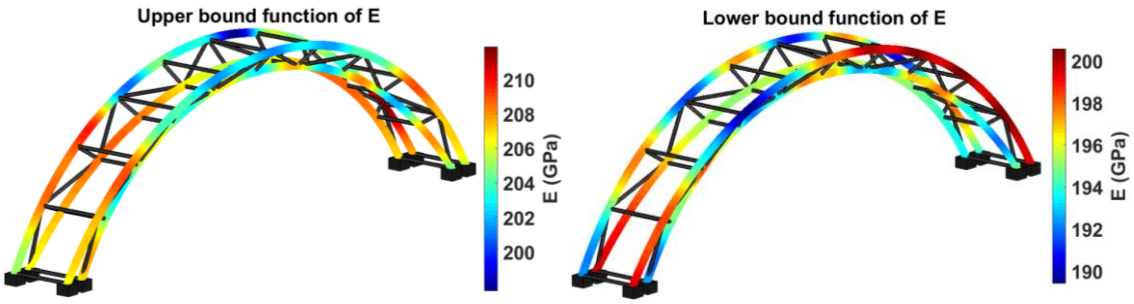

(a) (b)

Figure 5.11 Upper (a) and lower (b) bound functions of the interval fields of Example 5.4.2

Within this numerical investigation, the X-UISS method is utilized with 1,000, 5,000, 10,000 and 50,000 sampling points such that the statistical information of the extreme bounds of natural frequencies is achieved. For demonstrating the applicability of the X-UISS approach for the spatially uncertain free vibration analysis, the first three natural frequencies (ω_1 - ω_3) are selected as observation reference and the simulation results are summarized in Table 5.3. It can be observed from the results in Table 5.3 that reasonable convergence is achieved for X-UISS approach with 10,000 simulations for this example.

Table 5.3 The statistical characteristics of bounds of ω_1 - ω_3 of Example 5.4.2 with respect to different sample sizes

	X-UISS (1000)	X-UISS (5,000)	X-UISS (10,000)	X-UISS (50,000)	LHS-MCS (100×1000)
$\mu_{\overline{\omega_1}}$ (Hz)	0.7079	0.7078	0.7079	0.7080	0.7034
$\sigma_{\overline{\omega_1}}$ (Hz)	0.0109	0.0113	0.0111	0.0111	0.0113
$\mu_{\underline{\omega_1}}$ (Hz)	0.6982	0.6981	0.6982	0.6983	0.7023
$\sigma_{\underline{\omega_1}}$ (Hz)	0.0108	0.0111	0.0110	0.0110	0.0113
$\mu_{\overline{\omega_2}}$ (Hz)	1.3351	1.3351	1.3353	1.3353	1.3233
$\sigma_{\overline{\omega_2}}$ (Hz)	0.0205	0.0212	0.0210	0.0210	0.0211
$\mu_{\underline{\omega_2}}$ (Hz)	1.3091	1.3091	1.3093	1.3094	1.3207

$\sigma_{\underline{\omega_2}}$ (Hz)	0.0201	0.0208	0.0206	0.0206	0.0211
$\mu_{\overline{\omega_3}}$ (Hz)	1.7757	1.7754	1.7757	1.7758	1.7645
$\sigma_{\overline{\omega_3}}$ (Hz)	0.0255	0.0262	0.0257	0.0258	0.0262
$\mu_{\underline{\omega_3}}$ (Hz)	1.7516	1.7513	1.7516	1.7518	1.7623
$\sigma_{\underline{\omega_3}}$ (Hz)	0.0252	0.0259	0.0254	0.0254	0.0261

Additionally, the computationally expensive dual sampling LHS-MCS approach with total 100,000 simulations (i.e. 100 samples for interval field and 1,000 samples for random field) is implemented and the mean and standard deviations of ω_1 - ω_3 are reported in Table 5.3 for the partial result verification purpose. By comparing the simulation results of both methods, the mean obtained by dual sampling approach are enclosed by the results calculated by X-UISS approach, while minor differences in standard deviations are indicated.

Furthermore, the probability plots of the results obtained by X-UISS approach with 50,000 samples are implemented to identify the distributions of the extreme bounds of the concerned natural frequencies. The probability plots of upper and lower bound samples of ω_1 - ω_3 against wildly adopted distributions are illustrated in Fig. 5.12. The construction of the PDFs of various distributions can be conveniently implemented by using statistical analysis toolbox integrated in Matlab [158]. Additionally, the kernel density estimation (KDE) which is a non-parametric approach to represent the PDFs of random variables based on the available samples is adopted and accordingly constructed PDFs are demonstrated in Figure 5.12. By reviewing all the probability plots in Figures 5.12(a) and 5.12(b), both the Gaussian and lognormal distributions are overlapped with the PDF generated by KDE for ω_1. Additionally, same observation can be obtained for

ω_2 and ω_3 from Figures 5.12(c) - 5.12(f) since both normal and lognormal PDFs fit the histogram of the samples. Thus, it is potential that the concerned system outputs follow either normal or lognormal distribution despite that the input variables contain both Gaussian and lognormal random fields.

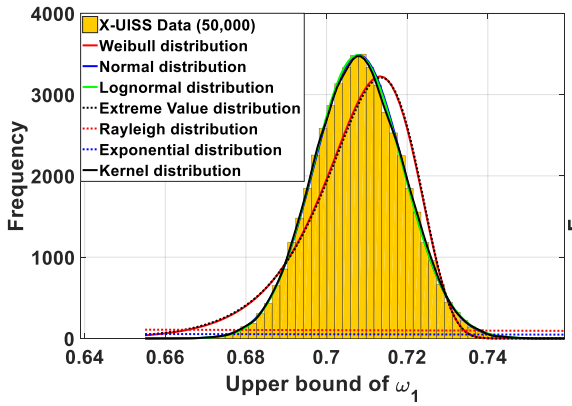

(a)

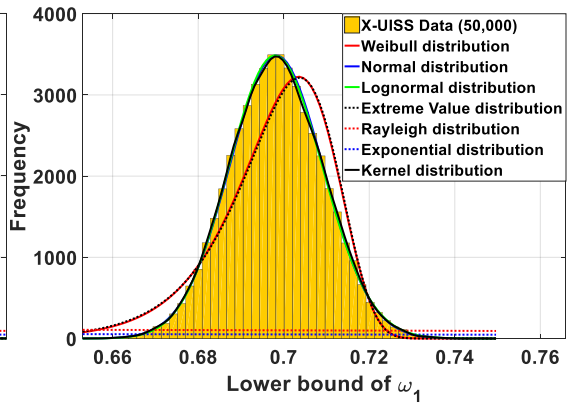

(b)

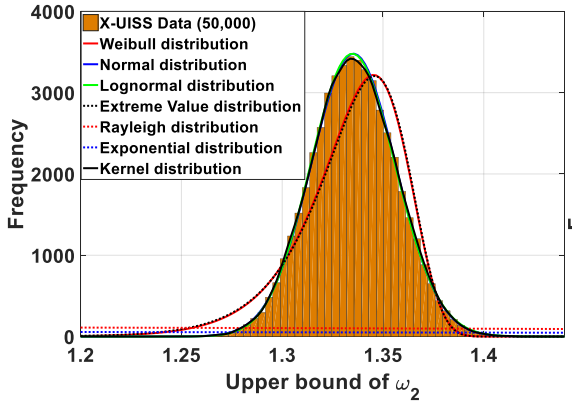

(c)

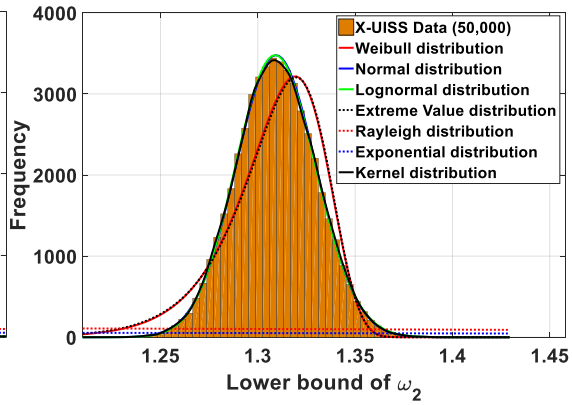

(d)

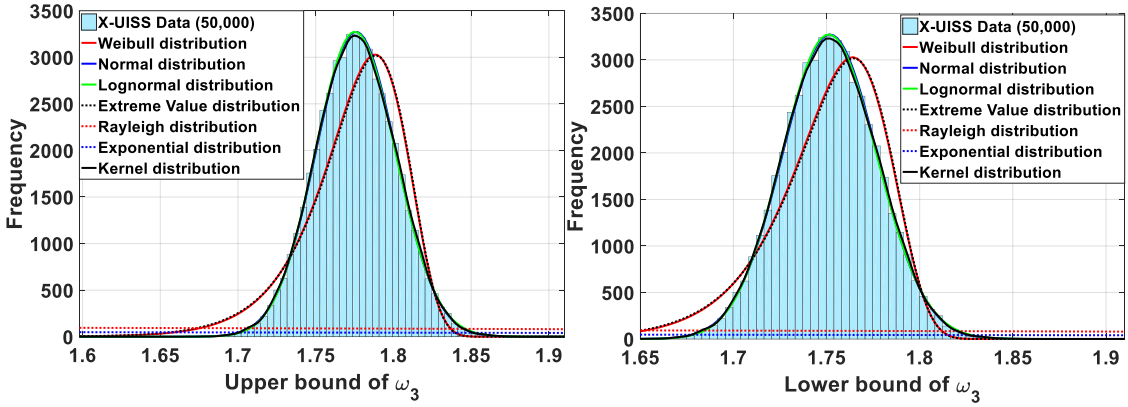

(e) (f)

Figure 5.12 Probability plots for the upper and lower bounds of ω_1 - ω_3 of Example 5.4.2

To ensure the consistency of the numerical study, the KDE is implemented in all the results obtained by X-UISS approach such that the PDFs and CDFs against different samples are constructed and shown in Figure 5.13. Additionally, the estimated PDFs and CDFs based on the output samples from LHS-MCS are also demonstrated for comparison purpose. It is noticeable that the PDFs and CDFs resulted from the dual sampling simulation are completely enclosed by the ones constructed by the X-UISS approach. Such large variation ranges between the PDFs and CDFs of extreme bounds calculated by X-UISS method is due to the fact that the sharpness of the results computed by the interval analysis at each sampling point of random field can be promised explicitly. Moreover, by increasing the sample size of X-UISS method, smoother PDFs, which are estimated by the adopted non-parametric statistical analysis, can be achieved, while limited effect on the variations of CDFs are observed in this investigation. Accordingly, the X-UISS approach offers a robust estimation of the probability profile of the extreme bounds of the natural frequencies of structures with hybrid random and interval fields.

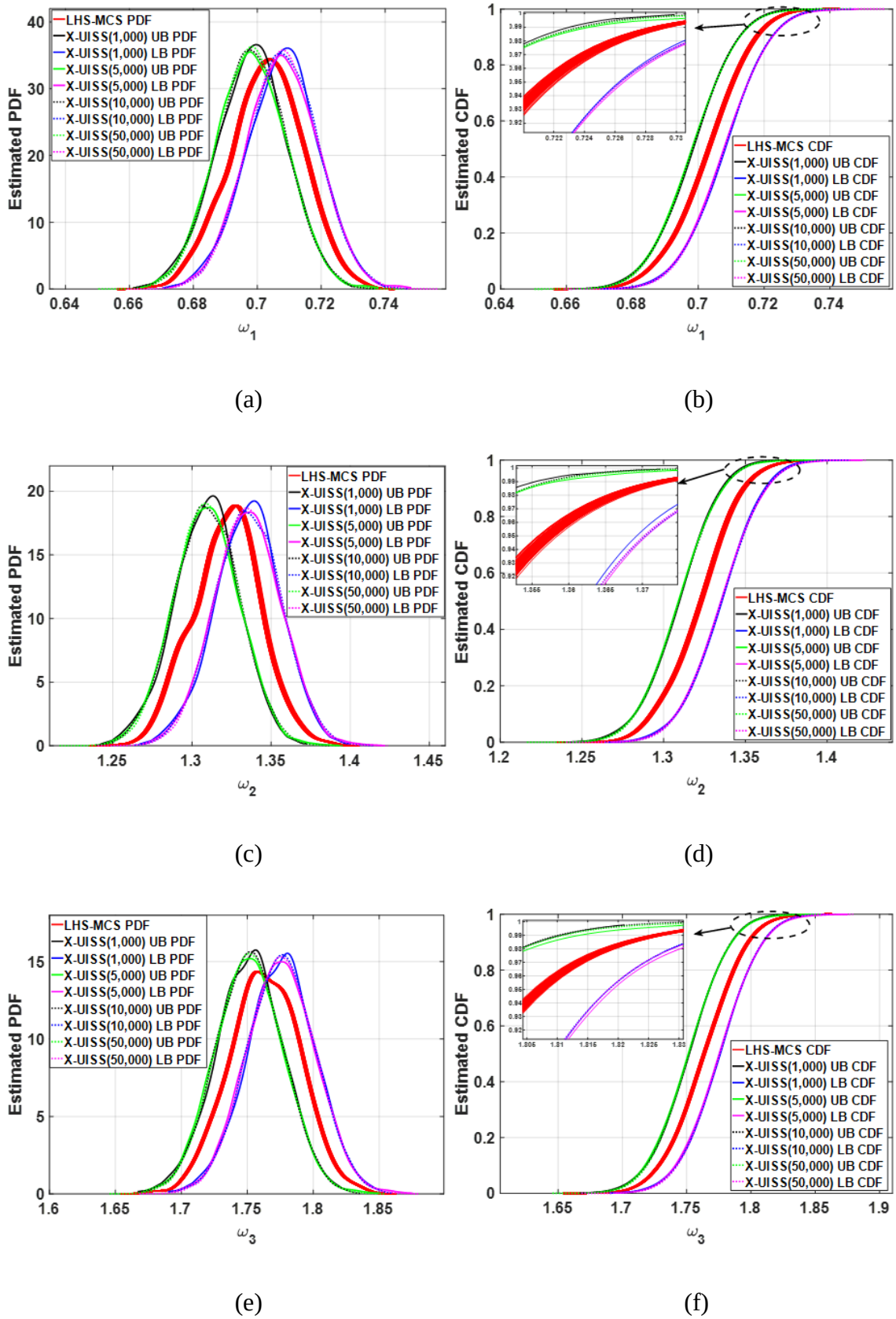

Figure 5.13 Estimated PDFs and CDFs of the upper and lower bounds of ω_1 - ω_3 of Example 5.4.2

5.5 Conclusion

This chapter presents an investigation of the non-deterministic free vibration problem of engineering structures considering the material uncertainties. As a novel extension of the conventional uncertain eigenvalue problem, the non-stochastic yet spatially dependent uncertain parameters and the random field theory are combined into a unified numerical analysis framework for the first time. In this study, the innovative concept of interval field is adopted as the representation of spatial-variant uncertainties which cannot be modelled precisely by random field.

A semi-sampling approach, namely the extended unified interval stochastic sampling (X-UISS) method, is adopted for robustly investigating the spatially uncertain free vibration problem. Within the computational framework, the extreme bounds of natural frequencies at each realization of random field are calculated by two independent eigen-analyses. The sharpness of the enclosed interval analysis is evidently promised in the context that Young's modulus and mass density are considered as interval fields. Benefitting from the generation of samples, the random field is not limited to be Gaussian distributed but applicable for other types of distribution. Various types of engineering structure have been investigated such that the applicability and effectiveness the X-UISS method as well as the robustness of the resultant PDFs and CDFs are systematically demonstrated.

Chapter 6 . Dynamic reliability analysis using the extended support vector regression (X-SVR)

6.0 Summary

In this chapter, a new machine learning based metamodel, namely the extended support vector regression (X-SVR) is proposed for the structural dynamic reliability analysis using the first-passage theory. Furthermore, a new kernel function constructed based on the vectorized Gegenbauer polynomial is introduced to enhance the capability of X-SVR in approximating complex engineering analyses. Through the proposed approach, the relationship between the extremum of the structural dynamic response and input uncertain parameters is approximated by training the X-SVR model such that the probability of failure can be efficiently predicted without further finite element analysis. The performance of the proposed surrogate model and its application in structural dynamic reliability analysis is investigated by comparing with the conventional ε-insensitive support vector regression (ε-SVR) with Gaussian kernel and Monte Carlo simulation (MSC). Four numerical examples are adopted such that the effectiveness and efficiency of the proposed X-SVR method is evidently demonstrated.

The rest of the chapter is organized as following. In Section 6.1, the background and available methods for dynamic reliability analysis is briefly introduced. The Section 6.2 will give a brief review on the theoretical background of structural dynamic reliability analysis using the first-passage probability. Then in Section 6.3, the detailed formulation of the proposed extended support vector machine and the generalized Gegenbauer kernel (GGK) function is demonstrated. The procedures for applying the proposed X-SVR on structural dynamic reliability analysis are illustrated in Section 6.4. The capability of X-

SVR with GGK is tested by applying it to two benchmark problems and two reliability analysis problems in Section 6.5. Then, some concluding remarks are summarized in Section 6.6.

The work presented in Chapter 6 has produced one journal paper which has been submitted to *Mechanical Systems and Signal Processing*. The detail of the publication is: Feng, J., Liu, L., Wu D., Li, G., Gao, W., & Beer M. (2019). Dynamic reliability analysis using the extended support vector regression (X-SVR). *Mechanical Systems and Signal Processing*, *126*, 368-391. https://doi.org/10.1016/j.ymssp.2019.02.027

6.1 Introduction

The dynamic reliability of engineering systems is essential and important to be investigated so that the effects of the uncertain variables can be thoroughly evaluated in the analyses and designs [151, 154, 195, 196]. As a matter of fact, the corresponding stochastic response in dynamics is time-dependent and should therefore be represented by a stochastic process, which increases the computational cost in comparison with the static reliability analysis.

In the past decades, there are numerous methods that have been developed for estimating the dynamic reliability of engineering systems, which focus on estimating the first-passage probability by evaluating the mean out-crossing rate [197]. The integration of the out-crossing rate is usually based on considering the out-crossing events either individually (Poisson model) or in a group (Markov model) [198]. In addition to the stochastic approaches, a non-probabilistic alternative convex process model is introduced in [118] to solve the first-passage reliability analysis. The most efficient stochastic approaches in this regard are based on approximately determining the probability density function (PDF) of the extreme system performance, which allows for a direct evaluation

and estimation of the failure probability. The extreme system performance is quantified with an extreme value distribution (EVD) for the first-passage reliability computation [198, 199]. In the EVD approach, the time-dependent reliability analysis is beneficially converted into the time-independent reliability evaluation. For the problems with small variations of coefficients, an envelope function method was introduced with the first-order approximation of the motion error function [200]. Concepts of stochastic averaging/linearization [201], of dimension reduction [202], and of numerical path integral solutions [203] provide currently the most efficient pathways to solve the first passage problem. Nevertheless, the derivation of a closed-form equation for the extreme values is technically difficult for generalized dynamic responses [204]. Despite of the comprehensively established theory, the first-passage probability of failure can be analytically obtained only in limited cases and is mostly restricted to single degree of freedom (SDOF) problems [205]. The consideration of nonlinearities and the expansion to several degrees of freedom are topics of current research [206].

As an alternative pathway, the probability distribution of extreme system performance can be obtained via sampling-based approaches. Within the framework of EVD, the probability density evolution method [207] and the equivalent extreme value approach [208] are developed for estimating the probability density function of the extreme values in the responses of the dynamic systems numerically. However, the numerical integration for evaluation of the PDF using these approaches still requires a large number of deterministic dynamic analyses with respect to selected representative points of input random variables. To increase the computational efficiency, the numerical integration can be replaced by using the first-order reliability method (FORM) in association with some specific adjustments such as PHI2 method [209] or discretized

stochastic processes [198]. Although useful for small practical cases, FORM is associated with its known limitations (only weak nonlinearities, small dimensionality etc.). Also, the advanced sampling schemes have been proven powerful in enhancing the efficiency of the generally applicable Monte Carlo simulation techniques [210].

In this chapter, a novel surrogate model, namely the extended support vector regression (X-SVR) is proposed for the dynamic reliability analysis. The underpinned analysis framework is based on the first-passage failure theorem. Comparing with the classical SVM approach, the satisfaction of the Mercer's condition is not prerequisite for the kernel functions employed in the nonlinear X-SVR. To further enhance the capability of the kernelized X-SVR in approximating complex functions, a new orthogonal polynomial kernel function, namely the generalized Gegenbauer kernel (GGK), is proposed. The introduced GGK is an admissible Mercer kernel, and it can be applied to other kernel learning methods which strictly require the satisfaction of the Mercer's condition. As a mixed kernel function, the proposed GGK consists of both orthogonal polynomial and Gaussian kernel function. Therefore, the advantages of both global and local kernels are included. Instead of using the conventional grid search technique, the hyperparameters of the X-SVR model are efficiently selected by the Bayesian optimization algorithm. After the establishment of the X-SVR surrogate model with GGK, the limit state function based on the first-passage principle can be explicitly approximated from the obtained X-SVR regression function. Subsequently, the probability of failure can be evaluated by Monte-Carlo Simulation (MCS) method with the constructed metamodel instead of using the actual computationally expensive numerical models (e.g., finite element analysis) with high-fidelity. This leads to a tremendous reduction of the computational cost.

6.2 A brief review of dynamic reliability analysis of structures

6.2.1 Stochastic dynamics of structure

The global equations of motion for a linear engineering structure with multi-degrees of freedom (MDOF) can be expressed as:

$$\mathbf{M}_s\ddot{\mathbf{u}}(t)+\mathbf{C}_s\dot{\mathbf{u}}(t)+\mathbf{K}_s\mathbf{u}(t)=\mathbf{F}(t) \tag{6.1}$$

where $\mathbf{M}_s$, $\mathbf{C}_s$ and $\mathbf{K}_s$ are the mass, damping and stiffness matrices of the structure, respectively; $\mathbf{F}(t)$ denotes the external excitation vector which is time-dependent; $\ddot{\mathbf{u}}(t)$, $\dot{\mathbf{u}}(t)$ and $\mathbf{u}(t)$ are the time dependent acceleration, velocity and displacement vectors, respectively. Due to the existence of uncertain parameters, the mass, damping, stiffness matrices and the external excitation are non-deterministic [19, 211, 212]. In this study, the uncertainties are considered as independent random variables and $\mathbf{M}_s$, $\mathbf{C}_s$ and $\mathbf{K}_s$ can be expressed as functions of the random parameters. Without loss of generality, the random vector $\mathbf{x}\in\Re^n$ is adopted as the collection of uncertainties included in both parameters in the dynamic system and the external excitation. Thus, the non-deterministic dynamic responses can be calculated by the following global equation:

$$\mathbf{M}_s(\mathbf{x})\ddot{\mathbf{u}}(t)+\mathbf{C}_s(\mathbf{x})\dot{\mathbf{u}}(t)+\mathbf{K}_s(\mathbf{x})\mathbf{u}(t)=\mathbf{F}(\mathbf{x},t) \tag{6.2}$$

Given a time interval $[0,T]$, the initial condition is considered as deterministic as Eq. (6.3):

$$\mathbf{u}(0)=\mathbf{u}_0,\ \dot{\mathbf{u}}(0)=\dot{\mathbf{u}}_0 \tag{6.3}$$

The stochastic dynamic response for a non-defect system is a stochastic process which is dependent on the random vector $\mathbf{x}$. Thus, the solution of Eq. (6.2) can be conveniently expressed as:

$$\mathbf{u}(t) = \mathbf{H}(\mathbf{x}, t) \tag{6.4}$$

where $\mathbf{H}$ denotes a deterministic operator. Despite of the existence of Eq. (6.4), the explicit formulation of $\mathbf{H}(\mathbf{x}, t)$ is usually available for some special cases rather than practical engineering problems with MDOF [197, 207]. Subsequently, the determination of an explicit tractable expression for the joint probability density function (PDF) of $\mathbf{u}(t)$ becomes computationally infeasible. Among the numerical approaches developed for approximately evaluating the statistical characteristics of stochastic dynamic response of structures, the Monte Carlo method is considered as the versatile strategy and widely adopted due to the straightforward implementation process [133, 180].

6.2.2 The first-passage failure theorem

The reliability of a system is typically evaluated by calculating the probability of failure which is commonly measured by the responses, such as the stresses, strains or displacements of the specified critical element or control point in structural dynamics. The systems are considered as unsafe if the concerned responses exceed the safety threshold for the first time. Mathematically, the computation of the probability of failure (p_f) is expressed as:

$$p_f = \Pr\{g(\mathbf{x}) \le 0\} = \int_{g(\mathbf{x}) \le 0} f_{\mathbf{x}}^{PDF}(\mathbf{x}) d\mathbf{x} = \int_{\Re^n} \mathrm{I}[g(\mathbf{x}) \le 0] f_{\mathbf{x}}^{PDF}(\mathbf{x}) d\mathbf{x} \tag{6.5}$$

where $\Pr\{\bullet\}$ denotes the probability; $\mathbf{x} \in \Re^n$ is the input random vector; $\mathrm{I}[\bullet]$ is the indicator function which equals to 1 if $[\bullet]$ is "true" and 0 when $[\bullet]$ is false"; $f_{\mathbf{x}}^{PDF}(\mathbf{x})$ denotes the joint PDF for $\mathbf{x}$ and $g(\mathbf{x})$ represents the limit state function, which defines a structural failure when $g(\mathbf{x}) \le 0$. Within the context of structural dynamic reliability, the structural outputs including displacement and stress become time-variant

uncertainties. Thus, the limit state function can be explicitly expressed as a function of random variable $\mathbf{x}$ and time t. For a given time interval $[0,T]$, the probability of failure can be described as:

$$p_f = \Pr\{\exists t \in [0,T], g(\mathbf{x},t) \le 0\} \tag{6.6}$$

Thus, an efficient and accurate evaluation of p_f is the key task in the structural dynamic reliability analysis.

Conventionally, for structural dynamic reliability, the probability of failure is widely computed by adopting the first-passage theory which is developed based on stochastic process [213]. In general, the security margin for the first passage theory can be categorized into single-sided barrier, two-sided barrier and enveloping barrier [214, 215]. Among them, the single-sided barrier can be regarded as a special case of the two-sided barrier problems. In this work, the two-sided barrier circumstance is studied for demonstrating the capability of the proposed X-SVR meta-model. The safe domain for two-sided barrier problem in a given time interval $[0,T]$, as shown in Figure 6.1, is defined as $\tilde{b}_2 < u(\mathbf{x},t) < \tilde{b}_1$ which is equivalent to $g(\mathbf{x},t) > 0$, where $u(\mathbf{x},t)$ is the stochastic structural dynamic response; $\tilde{b}_1$ and $\tilde{b}_2$ are the upper and lower threshold, respectively.

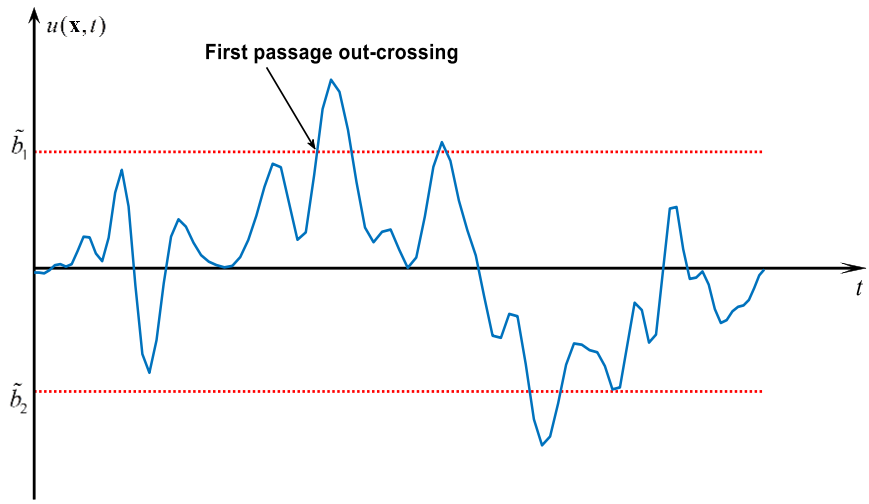

Figure 6.1 The first-passage failure model for dynamic response of structure

For a structural system with input uncertain variable $\mathbf{x}$, the probability of failure based on the first-passage theory is obtained by evaluating the probability of the first occurrence of an excursion of the performance function (stress or displacement) exceeds the safe domain. In this context, probability of failure in time interval $[0,T]$ can be expressed as:

$$p_f = \Pr\{\exists t \in [0,T], \max u(\mathbf{x},t) \geq \tilde{b}_1 \cup \min u(\mathbf{x},t) \leq \tilde{b}_2\} \tag{6.7}$$

For the two-sided barrier where $\tilde{b}_1 = -\tilde{b}_2 = \tilde{b}$ within the time interval $[0,T]$, the limit state function can be defined with the extreme of the dynamic response as $g(\mathbf{x}) = \tilde{b} - \max(|u(\mathbf{x},t)|)$. Thus, the p_f expressed in Eq. (6.7) can be simplified as Eq. (6.8):

$$p_f = \Pr\{\exists t \in [0,T], \tilde{b} - \max(|u(\mathbf{x},t)|) \leq 0\} \tag{6.8}$$

By implementing the out-crossing rate-based approach, the first-passage failure probability is approximated according to the out-crossing rate $v^+(t)$ which is defined in Eq. (6.9):

$$v^{+}(t) = \lim_{\Delta t \to 0, \Delta t > 0} \frac{\Pr\{g(\mathbf{x},t) > 0 \cap g(\mathbf{x},t+\Delta t) < 0\}}{\Delta t} \tag{6.9}$$

Among the existing hypothetical models for computing the cumulative probability of failure based on the out-crossing rate, the Poisson and Markov models are the two widely adopted [198]. The Poisson model assumes that the out-crossing events are mutually independent and the occurrence follows Poisson distribution. The Markov approach adopts an alternative path by assuming that the out-crossing events tend to occur in independent groups. Accordingly, the probability of failure in a given time interval $[0,T]$ evaluated by the Poisson and Markov models can be expressed in Eqs. (6.10) and (6.11), respectively:

$$p_f = 1 - \exp\left[-\int_0^T v^{+}(t)dt \right] \tag{6.10}$$

$$p_f = 1 - \exp\left[-\int_0^T \frac{v^{+}(t)}{1 - p_{f,ins}(t)} dt \right] \tag{6.11}$$

where $p_{f,ins}(t) = \Pr\{g(\mathbf{x},t) \le 0\}$ denotes the instantaneous probability of failure at time t. It can be observed from Eqs. (6.10) and (6.11) that both approaches require the integration of the out-crossing rate which is difficult to be obtained for the general stochastic process [205]. Thus, the closed-form solutions for Eqs. (6.6) - (6.8) are usually available for rather simple and special problems.

In this context, the Monte Carlo simulation (MCS) is commonly employed for computing the estimated probability of failure $\hat{p}_f$ by generating a large number of samples [118, 180]. Given m samples $\mathbf{x}_i$ ($i = 1, 2, ..., m$) for input variables, the probability of failure can be approximated by Eq. (6.12):

$$p_f \approx \hat{p}_f = \frac{1}{m}\sum_{i=1}^{m} \mathrm{I}[g(\mathbf{x}_i) \le 0] = \frac{m_f}{m} \tag{6.12}$$

where m_f is the number of samples that result in the failure of the structure. In Eq. (6.8), the limit state function can represent either internal force or structural deformation, which leads the first-passage failure mode to either the strength failure or deformation failure criterion [118]. Despite the fact that the first-passage theorem is conceptually simple through the MCS approach, the determination of the first-passage probability requires the computation of the whole dynamic response in the given time interval $[0, T]$ recursively. Thus, the majority of the computational cost is spent on repeatedly evaluating the limit state functions not to mention that the finite element analysis for complex structures in each simulative cycle can be computationally intensive [133, 216]. Alternatively, the meta-modelling techniques are introduced to approximate the relationship between inputs and outputs by an explicit function (i.e. polynomial). The meta-models are generally much less complicated than the original structural models, and it is expected that the computing effort will be reduced by approximating the limit state function by using surrogate models.

6.3 The extended support vector regression (X-SVR) with generalized Gegenbauer kernel (GGK)

In this section, a new surrogate model, namely the *extended support vector regression* (X-SVR), is proposed for reducing the computational cost of the conventional MCS approach. Furthermore, a new orthogonal polynomial kernel based on the Gegenbauer polynomial is introduced and adopted in the kernelized X-SVR. Firstly, the theory of the classic support vector regression will be reviewed in Section 6.3.1. As a statistical learning method, the X-SVR model is developed as an extension of the doubly regularized

support vector machine (DrSVM) which will be briefly described in Section 6.3.2. Then, the detailed formulation of the X-SVR and proposed orthogonal polynomial kernel will be presented in the remaining sections.

6.3.1 Classic support vector regression

The Support Vector Machines is a supervised learning algorithm introduced by Vapnik [217] for binary classification problem and later on extended to regression analysis [218] and multiclass classification problems [219]. The aim of the SVM is to find a hyperplane which has the maximum distance to the closest data points located on each side. Given the training dataset with input $\mathbf{x}_{train} = [\mathbf{x}_1, \mathbf{x}_2, ..., \mathbf{x}_i, ..., \mathbf{x}_m]^T \in \Re^{m \times n}$ ($\mathbf{x}_i \in \Re^n, i = 1, 2, ..., m$) and output $\mathbf{y}_{train} \in \Re^m$, the hyperplane that separating the two classes is then given as Eq. (6.13),

$$\hat{f}(\mathbf{x}) = \mathbf{w}^T \mathbf{x} - \gamma \tag{6.13}$$

where m is the number of training samples; n denotes the number of input variables; $\mathbf{w} \in \Re^n$ denotes the normal to the hyperplane and $\gamma \in \Re$ denotes the bias. In the case of applying the Support Vector theory to regression estimation, namely Support Vector Regression (SVR), Eq. (6.13) is the regression function to be obtained and $y^i_{train} \in \Re$ is the output of the true function $f(\mathbf{x}_i)$. Instead of using the empirical risk minimization (ERM) principle, the Support Vector method utilizes the structural risk minimization (SRM) principle which minimizes the upper bound on the structural risk $R(\hat{f})$. For the support vector machine, the structural risk aims at ensuring the training data is well classified while maximising the margin. In general, the relationship between the empirical risk $R_{emp}(\hat{f})$ and the structural risk $R(\hat{f})$ [217] can be expressed as Eq. (6.14):

$$
\begin{aligned}
R(\hat{f}) &\le R_{emp}(\hat{f}) + J(m/h) \\
&= \frac{1}{m}\sum_{i=1}^{m} l(y_{train}^{i} - \hat{f}(\mathbf{x}_i)) + \lambda \|\mathbf{w}\|_2^2
\end{aligned}
\tag{6.14}
$$

where $l(y_{train}^{i} - \hat{f}(\mathbf{x}_i))$ denotes the loss function measuring the empirical risk of the training samples; h is Vapnik Chervonenkis (VC) dimension and J is the confidence interval named as "VC confidence". The commonly employed loss function for SVR is the ε-insensitive loss function $l^{\varepsilon}(y_{train}^{i} - \hat{f}(\mathbf{x}_i))$ [220], which is defined in Eq. (6.15), is incorporated into the developed regression model as the tolerance of the deviation between the true output $\mathbf{y}_{train}$ and the model prediction $\hat{f}(\mathbf{x}_{train})$ for the training dataset.

$$
l^{\varepsilon}(y_{train}^{i} - \hat{f}(\mathbf{x}_i)) = \max(0, \left| y_{train}^{i} - \hat{f}(\mathbf{x}_i) \right| - \varepsilon), i = 1, \ldots m \tag{6.15}
$$

where ε denotes the tolerable deviation between y_{train}^{i} and $\hat{f}(\mathbf{x}_i)$. Such error tolerance can be demonstrated in Figure 6.2 by using a one-dimensional linear SVR model. In Figure 6.2, the slack variables ξ and $\hat{\xi}$ are introduced for respectively allowing some excess positive and negative deviations for the prediction function $\hat{f}(x)$.

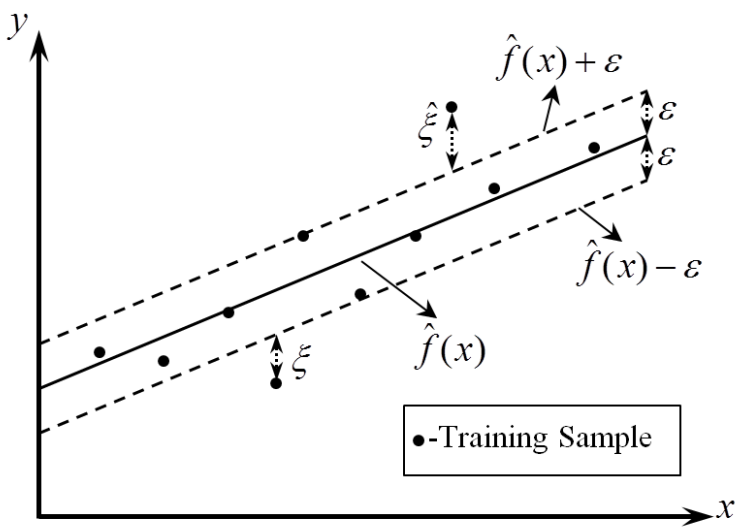

Figure 6.2 The ε-insensitive band for a one-dimension linear SVR

Thus, by including the ε-insensitive loss function, the regression function for linear SVR can be obtained by solving the optimization problem illustrated in Eq. (6.16). Due to the employment of the ε-insensitive loss function, the regression method expressed by Eq. (6.16) is commonly referred as ε-SVR.

$$\min_{\mathbf{w},\gamma,\xi,\hat{\xi}} : \frac{1}{2}\|\mathbf{w}\|_2^2 + c\sum_{i=1}^{m}(\xi_i + \hat{\xi}_i) \tag{6.16a}$$

$$s.t. \quad \begin{cases} y_{train}^i - (\mathbf{w}^T\mathbf{x}_i - \gamma) \le \varepsilon + \xi_i \\ (\mathbf{w}^T\mathbf{x}_i - \gamma) - y_{train}^i \le \varepsilon + \hat{\xi}_i \\ \xi_i, \hat{\xi}_i \ge 0, i = 1, 2, ..., m \end{cases} \tag{6.16b}$$

where $c > 0$ is the penalty constant which is defined for maintaining a proper balance between the flatness of $\hat{f}(\mathbf{x})$ and the empirical error; $\|\bullet\|_2$ represents the l_2 norm. It can be verified that Eq. (6.16) is a convex problem. By using the Lagrange multiplier method with Karush-Kuhn-Tucker (KKT) conditions for convex problem, the minimization problem defined by Eq. (6.16) can be equivalently solved by the following dual problem expressed in Eq. (6.17):

$$\max_{\boldsymbol{\alpha},\hat{\boldsymbol{\alpha}}} : -\frac{1}{2}\sum_{j=1}^{m}\sum_{i=1}^{m}(\hat{\alpha}_i - \alpha_i)(\hat{\alpha}_j - \alpha_j)\mathbf{x}_i^T\mathbf{x}_j - \varepsilon\sum_{i=1}^{m}(\hat{\alpha}_i + \alpha_i) + \sum_{i=1}^{m} y_i(\hat{\alpha}_i - \alpha_i) \tag{6.17a}$$

$$s.t. \quad \begin{cases} \sum_{i=1}^{m}(\hat{\alpha}_i - \alpha_i) = 0 \\ 0 \le \alpha_i, \hat{\alpha}_i \le c, i = 1, 2, ..., m \end{cases} \tag{6.17b}$$

where α_i and $\hat{\alpha}_i$ are the Lagrange multipliers. Then, by solving the dual optimization problem, $\mathbf{w}$ and γ can be obtained as Eqs. (6.18) - (6.20):

$$\mathbf{w} = \sum_{i=1}^{m} (\hat{\alpha}_i - \alpha_i)\mathbf{x}_i \tag{6.18}$$

$$\gamma = \mathbf{w}^T \mathbf{x}_i + \varepsilon - y_{train}^i, \; for \;\; \hat{\alpha}_i \in (0, c) \tag{6.19}$$

or

$$\gamma = \mathbf{w}^T \mathbf{x}_i - \varepsilon - y_{train}^i, \; for \;\; \alpha_i \in (0, c) \tag{6.20}$$

Subsequently, the regression function $\hat{f}(\mathbf{x})$ obtained by the linear ε-SVR is expressed as Eq. (6.21):

$$\hat{f}(\mathbf{x}) = \mathbf{w}^T \mathbf{x} - \gamma = \sum_{i=1}^{m} (\hat{\alpha}_i - \alpha_i)\mathbf{x}_i^T \mathbf{x} - \gamma \tag{6.21}$$

The above mentioned linear ε-SVR can be extended to nonlinear regression analysis by implicitly mapping the input data $\mathbf{x}_i$ from the low-dimension origin space $\Re^n$ into a higher-dimensional Euclidian space or even infinite dimensional Hilbert feature space F^* by using an appropriate mapping function $\mathbf{\Phi}(\mathbf{x}_i)$. Then, the linear support vector regression model can be constructed in the feature space. Subsequently, the nonlinear ε-SVR can be written by replacing the product $\mathbf{x}_i^T \mathbf{x}_j$ in Eq. (6.17a) with $\mathbf{\Phi}(\mathbf{x}_i)^T \mathbf{\Phi}(\mathbf{x}_j)$. Due to the existence of inner product of the mapping functions, the kernel method [221] is adopted in the support vector machine theory such that $\mathbf{\Phi}(\mathbf{x}_i)^T \mathbf{\Phi}(\mathbf{x}_j)$ can be directly calculated as a function of the original input data. The kernel function $\mathrm{K}(\mathbf{x}_i, \mathbf{x}_j)$ is defined as Eq. (6.22).

$$\mathrm{K}(\mathbf{x}_i, \mathbf{x}_j) = \mathbf{\Phi}(\mathbf{x}_i)^T \mathbf{\Phi}(\mathbf{x}_j) \tag{6.22}$$

The introduction of the kernel function leads to that an explicit definition or formulation of $\mathbf{\Phi}(\mathbf{x}_i)$ is not necessary, which avoid dealing directly with the high-dimensional feature space. Additionally, the employment of kernel function defined in Eq. (6.22) results in that $\mathbf{\Phi}(\mathbf{x}_i)$ is only determined by the kernel function and independent to the training samples. Thus, the feature space F^* is also named as *intrinsic vector space* [221] and the mapping can be illustrated as:

$$\mathbf{x}_i = [x_{i,1}, x_{i,2}, ..., x_{i,n}] \mapsto \mathbf{\Phi}(\mathbf{x}_i) = [\phi^1(\mathbf{x}_i), \phi^2(\mathbf{x}_i), ..., \phi^{\tilde{\Gamma}}(\mathbf{x}_i)]^T \tag{6.23}$$

where the dimension $\tilde{\Gamma}$ is referred as the *intrinsic degree*, which can be either finite or infinite. Subsequently, the nonlinear ε-SVR can be obtained by solving the optimization problem expressed in Eq. (6.24).

$$\max_{\boldsymbol{\alpha},\hat{\boldsymbol{\alpha}}} : -\frac{1}{2}\sum_{j=1}^{m}\sum_{i=1}^{m}(\hat{\alpha}_i - \alpha_i)(\hat{\alpha}_j - \alpha_j)\mathrm{K}(\mathbf{x}_i, \mathbf{x}_j) - \varepsilon\sum_{i=1}^{m}(\hat{\alpha}_i + \alpha_i) + \sum_{i=1}^{m} y_{train}^{i}(\hat{\alpha}_i - \alpha_i) \tag{6.24a}$$

$$s.t. \quad \begin{cases} \sum_{i=1}^{m}(\hat{\alpha}_i - \alpha_i) = 0 \\ 0 \le \alpha_i, \hat{\alpha}_i \le c, i = 1, 2, ..., m \end{cases} \tag{6.24b}$$

Then, the regression function in Eq. (6.21) is now expressed as Eq. (6.25):

$$\hat{f}(\mathbf{x}) = \sum_{i=1}^{m}(\hat{\alpha}_i - \alpha_i)\mathrm{K}(\mathbf{x}_i, \mathbf{x}) - \gamma \tag{6.25}$$

The kernel functions used for support vector machine/ regression should satisfy the Mercer's theorem which requires $\mathrm{K}(\mathbf{x}_i, \mathbf{x}_j)$ to be positive semi-definite [222]. This property is also a guarantee that the optimization problem expressed by Eq. (6.24) is a convex quadratic programming problem. The commonly used kernel functions are

Gaussian and polynomial kernel functions which are formulated as Eqs (6.26) and (6.27), respectively.

$$\mathrm{K}(\mathbf{x}_i, \mathbf{x}_j) = \exp(-\sigma_{\mathrm{K}} \left\| \mathbf{x}_i - \mathbf{x}_j \right\|_2^2) \tag{6.26}$$

$$\mathrm{K}(\mathbf{x}_i, \mathbf{x}_j) = (\sigma_{\mathrm{K}} \mathbf{x}_i^T \mathbf{x}_j + 1)^d \tag{6.27}$$

where $\sigma \in \Re^+$ is the kernel scale and $d \in \mathbb{Z}^+$ denotes the order of the polynomial. The kernel parameters, together with the penalty parameter c and insensitive tube ε, are referred as the hyper-parameters which strongly affect the prediction performance of the ε-SVR.

6.3.2 The doubly regularized support vector machine (DrSVM)

As an extension of the theory of support vector machine (SVM), the doubly regularised support vector machine (DrSVM) was proposed by [223] such that the classification and feature selection can be conducted simultaneously. Theoretically, the DrSVM is a combination of elastic net penalty which contains both l_1 norm and l_2 norm penalty [224] with the hinge loss function for reducing the effect of noise and outliers in the training dataset [225]. Accordingly, the DrSVM can be expressed as follows:

$$\min_{\mathbf{w},\gamma} : \frac{\lambda_a}{2} \left\| \mathbf{w} \right\|_2^2 + \lambda_b \left\| \mathbf{w} \right\|_1 + \sum_{i=1}^{m} [1 - y_{train}^i f(\mathbf{x}_i)]_+ \tag{6.28}$$

where the tunning parameters $\lambda_a, \lambda_b > 0$ control the balance between the classification performance and feature selection; $\left\| \bullet \right\|_1$ represents the l_1 norm; $[1 - y_{train}^i f(\mathbf{x}_i)]_+$ denotes the hinge loss function which is defined as Eq. (6.29):

$$[1 - y_{train}^i f(\mathbf{x}_i)]_+ = \begin{cases} 0, & 1 - y_{train}^i f(\mathbf{x}_i) \le 0 \\ 1 - y_{train}^i f(\mathbf{x}_i), & 1 - y_{train}^i f(\mathbf{x}_i) > 0 \end{cases} \tag{6.29}$$

Due to the additional capability in feature selection, the DrSVM is attracting increasing attention since its introduction. It has been pointed out by [224] that the hinge loss function is not differentiable everywhere. To address such deficiency, a Hybrid Huberised SVM is proposed by [226] who replace the hinge loss function by the huberised loss function.

Recently, a new doubly regularised SVM, namely the *pq*-SVM was proposed by [227] as an alternative approach for solving the optimization problem defined in Eq. (6.28). In the *pq*-SVM model, two non-negative variables $\mathbf{p},\mathbf{q} \in \Re^n$ are introduced such that $\mathbf{w} = \mathbf{p} - \mathbf{q}$. The variables $\mathfrak{p}$ and $\mathfrak{q}$ are defined as in Eq. (6.30):

$$p_j := \begin{cases} 0, & w_j \le 0 \\ w_j, & w_j > 0 \end{cases} \text{ and } q_j := \begin{cases} -w_j, & w_j < 0 \\ 0, & w_j \ge 0 \end{cases} \tag{6.30}$$

It is indicated by the definition in Eq. (6.30) that $p_j q_j = 0$ is promised $\forall j$. Thus, the $\|\mathbf{w}\|_1$ and $\|\mathbf{w}\|_2^2$ can be alternatively expressed as Eqs (6.31) and (6.32):

$$\begin{aligned} \|\mathbf{w}\|_1 &= |w_1| + |w_2| + \ldots + |w_n| \\ &= p_1 + q_1 + p_2 + q_2 + \ldots + p_n + q_n \\ &= \mathbf{e}_n^T(\mathbf{p} + \mathbf{q}) \end{aligned} \tag{6.31}$$

$$\begin{aligned} \|\mathbf{w}\|_2^2 &= \|\mathbf{p} - \mathbf{q}\|_2^2 \\ &= \|\mathbf{p}\|_2^2 + \|\mathbf{q}\|_2^2 - 2\mathbf{p}^T\mathbf{q} \\ &= \|\mathbf{p}\|_2^2 + \|\mathbf{q}\|_2^2 \end{aligned} \tag{6.32}$$

where $\mathbf{e}_n = [1,1,\ldots,1]^T \in \Re^n$. Such decomposition is proved as an effective approach by the implementation in nonlinear optimization [228] and l_1 norm support vector regression [220]. In this context, the decision function (Eq. (6.13)) can be reformulated as:

$$f(\mathbf{x}) = \mathbf{x}^T(\mathbf{p}-\mathbf{q}) - \gamma \tag{6.33}$$

Moreover, the non-smooth huberised loss function is replaced by a linear constraint to consider the noise and outliers in the training dataset. Similar as the soft margin SVM, a non-negative slack variable $\boldsymbol{\xi} \in \Re^m$ is introduced into the optimization to control the marginal error. Therefore, the *pq*-SVM can be expressed as:

$$\min_{\mathbf{p},\mathbf{q},\gamma,\boldsymbol{\xi}} : \frac{\lambda_a}{2}(\|\mathbf{p}\|_2^2 + \|\mathbf{q}\|_2^2) + \lambda_b \mathbf{e}_n^T(\mathbf{p}+\mathbf{q}) + \mathbf{e}_m^T\boldsymbol{\xi} \tag{6.34a}$$

$$s.t. \quad \begin{cases} \mathbf{D}\left[\mathbf{x}_{train}(\mathbf{p}-\mathbf{q}) - \gamma\mathbf{e}_m\right] + \boldsymbol{\xi} \geq \mathbf{e}_m \\ \mathbf{p},\mathbf{q} \geq \mathbf{0}_n ; \boldsymbol{\xi} \geq \mathbf{0}_m \end{cases} \tag{6.34b}$$

where $\mathbf{0}_m = [0,0,...,0]^T \in \Re^m$ and $\mathbf{D}_{pq} \in \Re^{m\times m}$, as expressed in Eq. (6.35), is a diagonal matrix which contains all labels associated with training dataset

$$\mathbf{D}_{pq} = \begin{bmatrix} y_{train}^1 & & \\ & \ddots & \\ & & y_{train}^m \end{bmatrix} \tag{6.35}$$

By using the Lagrange method, the *pq*-SVM can be reformulated into a quadratic programming problem, which indicates the advantage of the introduction of variables $\mathbf{p}$ and $\mathbf{q}$ for decomposing $\|\mathbf{w}\|_1$. In addition to the conventional classification problem, the *pq*-SVM is modified as knowledge-based SVM by incorporating the prior knowledge in the form of uncertain linear constraints [229]. Despite of the successful implementation of DrSVM and *pq*-SVM in classification problem, according to the authors' best knowledge, a doubly regularised support vector regression model has not yet been developed.

6.3.3 The proposed extended support vector regression (X-SVR)

Inspired by the success of *pq*-SVM in classification, a new support vector regression (SVR) model, namely the *extended support vector regression* (X-SVR) is developed by adopting the concept of DrSVM and extended from binary classification to the regression estimation. In the proposed regression model, the decomposition method applied in the *pq*-SVM is adopted such that the l_1 norm computation $\|\mathbf{w}\|_1$ is eliminated. Additionally, instead of using the widely adopted linear ε-insensitive loss function expressed in Eq. (6.16), the proposed X-SVR incorporated the quadratic ε-insensitive loss function which is defined in Eq. (6.36).

$$l_2^{\varepsilon}(y_{train}^i - \hat{f}(\mathbf{x}_i)) = \left| y_{train}^i - \hat{f}(\mathbf{x}_i) \right|^2, i = 1,...m \tag{6.36}$$

By using the non-negative slack variables $\xi, \hat{\xi} \in \Re^m$, the X-SVR can be derived by solving the constrained optimization problem formulated as Eq. (6.37):

$$\min_{\mathbf{p},\mathbf{q},\gamma,\xi,\hat{\xi}} : \frac{\lambda_a}{2}(\|\mathbf{p}\|_2^2 + \|\mathbf{q}\|_2^2) + \lambda_b \mathbf{e}_n^T(\mathbf{p}+\mathbf{q}) + \frac{c}{2}(\xi^T\xi + \hat{\xi}^T\hat{\xi}) \tag{6.37a}$$

$$s.t. \quad \begin{cases} \mathbf{x}_{train}(\mathbf{p}-\mathbf{q}) - \gamma\mathbf{e}_m - \mathbf{y}_{train} \le \varepsilon\mathbf{e}_m + \xi \\ \mathbf{y}_{train} - (\mathbf{x}_{train}(\mathbf{p}-\mathbf{q}) - \gamma\mathbf{e}_m) \le \varepsilon\mathbf{e}_m + \hat{\xi} \\ \mathbf{p},\mathbf{q} \ge \mathbf{0}_n; \xi, \hat{\xi} \ge \mathbf{0}_m \end{cases} \tag{6.37b}$$

where $c > 0$ is the penalty constant which controls the emphasis on the error minimization. As pointed out in [222, 230], the introduction of quadratic ε-insensitive loss function leads to the redundancy of the non-negative constraint for the slack variables ξ and $\hat{\xi}$. Furthermore, γ^2 (the square of bias parameter) is added to the objective function, which enables the simultaneous optimizing the orientation and location of the

regression model [227, 231]. For the sake of simplicity, Eq. (6.37) can be further modified as the following optimization problem:

$$\min_{\mathbf{z},\gamma} : \frac{1}{2}(\mathbf{z}^T \hat{\mathbf{C}} \mathbf{z} + \gamma^2) + \lambda_b \mathbf{b}^T \mathbf{z} \tag{6.38a}$$

$$s.t. \quad (\hat{\mathbf{A}} + \mathbf{I}_{(2m+2n)\times(2m+2n)})\mathbf{z} + (\varepsilon \mathbf{I}_{(2m+2n)\times(2m+2n)} + \gamma \hat{\mathbf{G}})\hat{\mathbf{e}} + \hat{\mathbf{d}} \geq \mathbf{0}_{2m+2n} \tag{6.38b}$$

where $\mathbf{I}_{(2m+2n)\times(2m+2n)} \in \Re^{(2m+2n)\times(2m+2n)}$ denotes the identity matrix and $\mathbf{0}_{2m+2n} \in \Re^{2m+2n}$ denotes the zero vector. The matrices $\hat{\mathbf{C}}$, $\hat{\mathbf{G}}$ and $\hat{\mathbf{A}}$ are defined as:

$$\hat{\mathbf{C}} = \begin{bmatrix} \lambda_a \mathbf{I}_{n\times n} & & & \\ & \lambda_a \mathbf{I}_{n\times n} & & \\ & & c\mathbf{I}_{m\times m} & \\ & & & c\mathbf{I}_{m\times m} \end{bmatrix} \tag{6.39a}$$

$$\hat{\mathbf{G}} = \begin{bmatrix} \mathbf{0}_{2n\times 2n} & \mathbf{0}_{2n\times m} & \mathbf{0}_{2n\times m} \\ \mathbf{0}_{m\times 2n} & \mathbf{I}_{m\times m} & \mathbf{0}_{m\times m} \\ \mathbf{0}_{m\times 2n} & \mathbf{0}_{m\times m} & -\mathbf{I}_{m\times m} \end{bmatrix} \tag{6.39b}$$

$$\hat{\mathbf{A}} = \begin{bmatrix} \mathbf{0}_{2n\times n} & \mathbf{0}_{2n\times n} & \mathbf{0}_{2n\times 2m} \\ -\mathbf{x}_{train} & \mathbf{x}_{train} & \mathbf{0}_{m\times 2m} \\ \mathbf{x}_{train} & -\mathbf{x}_{train} & \mathbf{0}_{m\times 2m} \end{bmatrix} \tag{6.38c}$$

and the vectors $\mathbf{b}$, $\hat{\mathbf{e}}$, $\hat{\mathbf{d}}$ and $\mathbf{z}$ are defined as:

$$\mathbf{b} = \begin{bmatrix} \mathbf{e}_n \\ \mathbf{e}_n \\ \mathbf{0}_{2m} \end{bmatrix}, \ \hat{\mathbf{e}} = \begin{bmatrix} \mathbf{0}_{2n} \\ \mathbf{e}_m \\ \mathbf{e}_m \end{bmatrix}, \ \hat{\mathbf{d}} = \begin{bmatrix} \mathbf{0}_{2n} \\ \mathbf{y}_{train} \\ -\mathbf{y}_{train} \end{bmatrix}, \ \mathbf{z} = \begin{bmatrix} \mathbf{p} \\ \mathbf{q} \\ \boldsymbol{\xi} \\ \hat{\boldsymbol{\xi}} \end{bmatrix} \tag{6.40}$$

The non-negative constraint on the variables $\mathbf{p}$ and $\mathbf{q}$ has been included in Eq. (6.38b). It can be observed from matric $\hat{\mathbf{C}}$ that there would be zero elements along the diagonal

if the linear ε-insensitive loss function is utilised. Thus, the adoption of quadratic ε-insensitive loss function can enhance the numerical stability in solving optimization problem.

The optimization problem expressed in Eq. (6.38) can be equivalently solved in the dual formulation. Thus, the Lagrange function $L(\mathbf{z},\gamma,\mathbf{u})$ is shown as Eq. (6.41):

$$\begin{aligned} L(\mathbf{z},\gamma,\mathbf{u}) = \frac{1}{2}(\mathbf{z}^T\hat{\mathbf{C}}\mathbf{z}+\gamma^2)+\lambda_b\mathbf{b}^T\mathbf{z}-[(\hat{\mathbf{A}}+\mathbf{I}_{(2m+2n)\times(2m+2n)})\mathbf{z} \\ +(\varepsilon\mathbf{I}_{(2m+2n)\times(2m+2n)}+\gamma\hat{\mathbf{G}})\hat{\mathbf{e}}+\hat{\mathbf{d}}]^T\mathbf{u} \end{aligned} \tag{6.41}$$

where $\mathbf{u}\in\Re^{2m+2n}$ denotes the vector contains all Lagrange multipliers. Then, the Karush-Kuhn-Tucker (KKT) conditions for the dual problem are:

$$\frac{\partial L(\mathbf{z},\gamma,\mathbf{u})}{\partial\mathbf{z}} = \hat{\mathbf{C}}\mathbf{z}+\lambda_2\mathbf{b}-(\hat{\mathbf{A}}+\mathbf{I}_{(2m+2n)\times(2m+2n)})^T\mathbf{u}=\mathbf{0}_{2m+2n} \tag{6.42a}$$

$$\frac{\partial L(\mathbf{z},\gamma,\mathbf{u})}{\partial\gamma} = \gamma-\hat{\mathbf{e}}^T\hat{\mathbf{G}}\mathbf{u}=0 \tag{6.42b}$$

$$\mathbf{u}\geq\mathbf{0}_{2m+2n} \tag{6.42c}$$

By substituting the Eqs. (6.42a) and (6.42b) into Eq. (6.41), the Lagrange function can be then written as:

$$\begin{aligned} L(\mathbf{u}) &= -\frac{1}{2}\mathbf{u}^T(\hat{\mathbf{A}}+\mathbf{I}_{(2m+2n)\times(2m+2n)})\hat{\mathbf{C}}^{-1}(\hat{\mathbf{A}}+\mathbf{I}_{(2m+2n)\times(2m+2n)})^T\mathbf{u}-\frac{1}{2}\lambda_b^2\mathbf{b}^T\hat{\mathbf{C}}^{-1}\mathbf{b} \\ &\quad -\frac{1}{2}\mathbf{u}^T\hat{\mathbf{G}}\hat{\mathbf{e}}\hat{\mathbf{e}}^T\hat{\mathbf{G}}\mathbf{u}+[\lambda_b\mathbf{b}^T\hat{\mathbf{C}}^{-1}(\hat{\mathbf{A}}+\mathbf{I}_{(2m+2n)\times(2m+2n)})^T-\varepsilon\hat{\mathbf{e}}^T-\hat{\mathbf{d}}^T]\mathbf{u} \\ &= -\frac{1}{2}\mathbf{u}^T[(\hat{\mathbf{A}}+\mathbf{I}_{(2m+2n)\times(2m+2n)})\hat{\mathbf{C}}^{-1}(\hat{\mathbf{A}}+\mathbf{I}_{(2m+2n)\times(2m+2n)})^T+\hat{\mathbf{G}}\hat{\mathbf{e}}\hat{\mathbf{e}}^T\hat{\mathbf{G}}]\mathbf{u} \\ &\quad +[\lambda_b\mathbf{b}^T\hat{\mathbf{C}}^{-1}(\hat{\mathbf{A}}+\mathbf{I}_{(2m+2n)\times(2m+2n)})^T-\varepsilon\hat{\mathbf{e}}^T-\hat{\mathbf{d}}^T]\mathbf{u}-\frac{1}{2}\lambda_b^2\mathbf{b}^T\hat{\mathbf{C}}^{-1}\mathbf{b} \end{aligned} \tag{6.43}$$

Since $\lambda_b^2\mathbf{b}^T\hat{\mathbf{C}}^{-1}\mathbf{b}$ is a real constant, the dual problem can be then formulated as:

$$\min_{\mathbf{u}} : \frac{1}{2}\mathbf{u}^T\mathbf{Q}\mathbf{u} - \mathbf{m}^T\mathbf{u} \tag{6.44a}$$

$$s.t. \quad \mathbf{u} \geq \mathbf{0}_{2m+2n} \tag{6.44b}$$

where $\mathbf{Q} \in \Re^{(2m+2n)\times(2m+2n)}$ and $\mathbf{m} \in \Re^{2m+2n}$ are defined by:

$$\mathbf{Q} = (\hat{\mathbf{A}} + \mathbf{I}_{(2m+2n)\times(2m+2n)})\hat{\mathbf{C}}^{-1}(\hat{\mathbf{A}} + \mathbf{I}_{(2m+2n)\times(2m+2n)})^T + \hat{\mathbf{G}}\hat{\mathbf{e}}\hat{\mathbf{e}}^T\hat{\mathbf{G}} \tag{6.44a}$$

$$\mathbf{m} = \lambda_b(\hat{\mathbf{A}} + \mathbf{I}_{(2m+2n)\times(2m+2n)})\hat{\mathbf{C}}^{-1}\mathbf{b} - \varepsilon\hat{\mathbf{e}} - \hat{\mathbf{d}} \tag{6.44b}$$

By using the dual formulation, the number of variables in the optimization problem is reduced from $2m+2n+1$ in Eq. (6.38) to $2m+2n$ in Eq (6.44). Moreover, the constraint in the dual problem is much less complex than that in the primary problem. In order to demonstrate that proposed X-SVR has the global minimum solution, we can equivalently prove that the dual problem is a convex optimization problem as the following *Proposition 1*.

Proposition 1:

Given the training dataset with input $\mathbf{x}_{train} \in \Re^{m\times n}$ and output $\mathbf{y}_{train} \in \Re^{m}$, with pre-defining the positive tunning parameters for X-SVR as $\lambda_1, \lambda_2, c, \varepsilon \in \Re^{+}$, the optimization problem defined in Eq. (6.44) is a convex quadratic programming problem.

Proof:

For quadratic programming expressed in Eq. (6.44), the proof of convexity is equivalent to proving that $\mathbf{Q} \succeq 0$. Moreover, considering that $\hat{\mathbf{C}}$ is a positive and diagonal matrix by definition, then $\hat{\mathbf{C}} \succ 0$ and also $\hat{\mathbf{C}}^{-1} \succ 0$. Let $\mathbf{v} \in \Re^{2m+2n}$ be a non-zero column vector, then:

$$\begin{aligned}\mathbf{v}^T\mathbf{Q}\mathbf{v} &= \mathbf{v}^T\left[(\hat{\mathbf{A}}+\mathbf{I}_{(2m+2n)\times(2m+2n)})\hat{\mathbf{C}}^{-1}(\hat{\mathbf{A}}+\mathbf{I}_{(2m+2n)\times(2m+2n)})^T+\hat{\mathbf{G}}\hat{\mathbf{e}}\hat{\mathbf{e}}^T\hat{\mathbf{G}}\right]\mathbf{v} \\ &= \left[(\hat{\mathbf{A}}+\mathbf{I}_{(2m+2n)\times(2m+2n)})^T\mathbf{v}\right]\hat{\mathbf{C}}^{-1}\left[(\hat{\mathbf{A}}+\mathbf{I}_{(2m+2n)\times(2m+2n)})^T\mathbf{v}\right]+(\hat{\mathbf{e}}^T\hat{\mathbf{G}}\mathbf{v})^2 \\ &\geq 0\end{aligned} \tag{6.45}$$

Therefore, the dual problem defined in Eq. (6.44) is a convex quadratic programming problem.

This concludes the proof. □

Subsequently, the global optimum solution for the proposed X-SVR can be obtained by solving the associated dual problem by either gradient based method or available quadratic programming solvers. Let $\mathbf{u}^* \in \Re^{2m+2n}$ be the obtained solution for the X-SVR, then the variables $\mathbf{z}$ and γ can be respectively computed as:

$$\mathbf{z} = \hat{\mathbf{C}}^{-1}\left[(\hat{\mathbf{A}}+\mathbf{I}_{(2m+2n)\times(2m+2n)})^T\mathbf{u}^* - \lambda_b\mathbf{b}\right] \tag{6.46}$$

$$\gamma = \hat{\mathbf{e}}^T\hat{\mathbf{G}}\mathbf{u}^* \tag{6.47}$$

Then, the coefficient $\mathbf{w}$ can be obtained as:

$$\mathbf{w} = \mathbf{p}-\mathbf{q} = \mathbf{z}(1:n)-\mathbf{z}(n+1:2n) \tag{6.48}$$

Thus, the regression function obtained by the proposed by the proposed X-SVR is expressed as:

$$\hat{f}(\mathbf{x}) = (\mathbf{p}-\mathbf{q})^T\mathbf{x} - \hat{\mathbf{e}}^T\hat{\mathbf{G}}\mathbf{u}^* \tag{6.49}$$

Similar as the classic support vector regression, the proposed X-SVR can be further modified into a nonlinear regression method such that the introduced approach can be applied on the more complex problems. Despite of the convenience of the kernel method used in the ε-SVR, mapping to the intrinsic vector space can only applied as a

replacement of $\mathbf{x}_i^T\mathbf{x}_j$ for avoiding the explicit calculation of $\mathbf{\Phi}(\mathbf{x}_i)$ and $\mathbf{\Phi}(\mathbf{x}_j)$. In the proposed X-SVR, such implicit kernel map approach is not applicable since that the linear combinations of $\mathbf{x}_i$ ($i = 1, 2, ..., m$), in addition to the inner product $\mathbf{x}_i^T\mathbf{x}_j$ are included in the dual formulation expressed as Eq. (6.44). To extend the linear X-SVR to a kernelized learning method, an alternative approach, namely the *empirical kernel map* [221, 232], is utilized in the proposed surrogate model. The adopted empirical kernelization can be expressed in Eq. (6.50):

$$\mathbf{x}_i = [x_{i,1}, x_{i,2}, ..., x_{i,n}]^T \mapsto \boldsymbol{\kappa}(\mathbf{x}_i) = \begin{bmatrix} \mathbf{\Phi}(\mathbf{x}_1)^T\mathbf{\Phi}(\mathbf{x}_i) \\ \mathbf{\Phi}(\mathbf{x}_2)^T\mathbf{\Phi}(\mathbf{x}_i) \\ \vdots \\ \mathbf{\Phi}(\mathbf{x}_m)^T\mathbf{\Phi}(\mathbf{x}_i) \end{bmatrix} = \begin{bmatrix} \mathrm{K}(\mathbf{x}_1, \mathbf{x}_i) \\ \mathrm{K}(\mathbf{x}_2, \mathbf{x}_i) \\ \vdots \\ \mathrm{K}(\mathbf{x}_m, \mathbf{x}_i) \end{bmatrix} \tag{6.50}$$

where the kernel-induced vector $\boldsymbol{\kappa}(\mathbf{x}_i)$ is known as the *empirical feature vector* with the *empirical degree* m defined as the number of training samples [221]. Such m-dimensional vector space is named as the *empirical feature space* [233]. Then, the empirical feature vector $\boldsymbol{\kappa}(\mathbf{x}_i)$ is regarded as the training sample for constructing the learning model. Comparing with the implicit kernel map approach used in ε-SVR, the empirical feature space is finite-dimensional and jointly defined by the employed kernel function and training samples. Such kernel map approach has also been effectively applied on the other kernelized learning method, including kernelized LASSO (Least Absolute Selection and Shrinkage Operator) [234], kernelized elastic net [235], linear programming SVR [80] and multiple empirical kernel learning machine [236]. The architecture of the nonlinear X-SVR is shown in Figure 6.3.

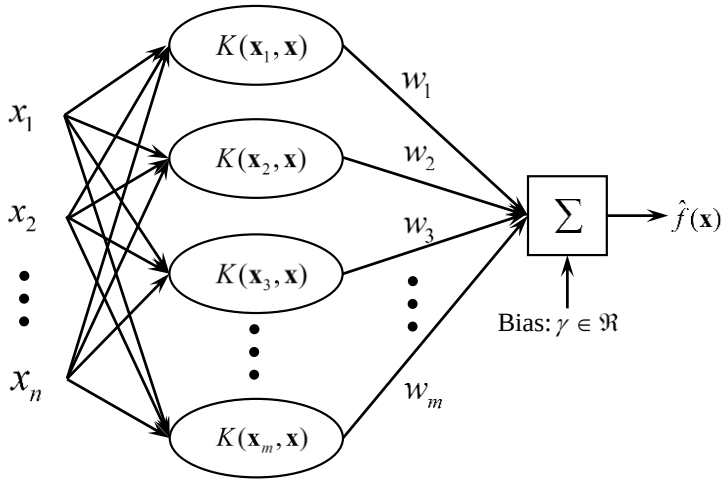

Figure 6.3 The architecture of the X-SVR

Thus, given the training dataset $\mathbf{x}_{train}$ and a specific kernel function $\mathrm{K}(\mathbf{x}_i,\mathbf{x}_j)$, the original training samples are transferred into the kernel matrix $\mathbf{K}_{train} \in \Re^{m\times m}$ which is expressed as Eq. (6.51):

$$\mathbf{K}_{train} = \begin{bmatrix} \mathrm{K}(\mathbf{x}_1,\mathbf{x}_1) & \mathrm{K}(\mathbf{x}_1,\mathbf{x}_2) & \cdots & \mathrm{K}(\mathbf{x}_1,\mathbf{x}_m) \\ \mathrm{K}(\mathbf{x}_2,\mathbf{x}_1) & \mathrm{K}(\mathbf{x}_2,\mathbf{x}_2) & \cdots & \mathrm{K}(\mathbf{x}_2,\mathbf{x}_m) \\ \vdots & \vdots & \cdots & \vdots \\ \mathrm{K}(\mathbf{x}_m,\mathbf{x}_1) & \mathrm{K}(\mathbf{x}_m,\mathbf{x}_2) & \cdots & \mathrm{K}(\mathbf{x}_m,\mathbf{x}_m) \end{bmatrix} \tag{6.51}$$

Then, the kernel matrix $\mathbf{K}_{train}$ is used as the training dataset and the nonlinear X-SVR problem is now formulated as Eq. (6.52):

$$\min_{\mathbf{p}_k,\mathbf{q}_k,\gamma,\xi,\hat{\xi}} : \frac{\lambda_a}{2}(\|\mathbf{p}_k\|_2^2 + \|\mathbf{q}_k\|_2^2) + \lambda_b \mathbf{e}_m^T(\mathbf{p}_k + \mathbf{q}_k) + \frac{c}{2}(\xi^T\xi + \hat{\xi}^T\hat{\xi}) \tag{6.52a}$$

$$s.t. \quad \begin{cases} \mathbf{K}_{train}(\mathbf{p}_k - \mathbf{q}_k) - \gamma\mathbf{e}_m - \mathbf{y}_{train} \le \varepsilon\mathbf{e}_m + \xi \\ \mathbf{y}_{train} - (\mathbf{K}_{train}(\mathbf{p}_k - \mathbf{q}_k) - \gamma\mathbf{e}_m) \le \varepsilon\mathbf{e}_m + \hat{\xi} \\ \mathbf{p}_k, \mathbf{q}_k, \xi, \hat{\xi} \ge \mathbf{0}_m \end{cases} \tag{6.52b}$$

where $\mathbf{p}_k, \mathbf{q}_k \in \Re^m$ and have the same function as $\mathbf{p}$ and $\mathbf{q}$ for linear X-SVR; the subscript k is for indicating that this is a kernelized learning model. Then, by adopting

the same concept as expressed in Eq. (6.38) for the proposed linear X-SVR, the kernelized X-SVR shown in Eq. (6.52) can be further modified into:

$$\min_{\mathbf{z}_k,\gamma} : \frac{1}{2}(\mathbf{z}_k^T \hat{\mathbf{C}} \mathbf{z}_k + \gamma^2) + \lambda_b \mathbf{b}_k^T \mathbf{z}_k \tag{6.53a}$$

$$s.t. \quad (\hat{\mathbf{A}}_k + \mathbf{I}_{4m\times 4m})\mathbf{z}_k + (\varepsilon \mathbf{I}_{4m\times 4m} + \gamma \hat{\mathbf{G}}_k)\hat{\mathbf{e}}_k + \hat{\mathbf{d}}_k \geq \mathbf{0}_{4m} \tag{6.53b}$$

where $\mathbf{I}_{4m\times 4m} \in \Re^{4m\times 4m}$ denotes the identity matrix and $\mathbf{0}_{4m} \in \Re^{4m}$ denotes the zero matrix. The matrices $\hat{\mathbf{C}}_k$, $\hat{\mathbf{G}}_k$ and $\hat{\mathbf{A}}_k$ are defined as:

$$\hat{\mathbf{C}}_k = \begin{bmatrix} \lambda_a \mathbf{I}_{m\times m} & & & \\ & \lambda_a \mathbf{I}_{m\times m} & & \\ & & c\mathbf{I}_{m\times m} & \\ & & & c\mathbf{I}_{m\times m} \end{bmatrix} \tag{6.54a}$$

$$\hat{\mathbf{G}}_k = \begin{bmatrix} \mathbf{0}_{2m\times 2m} & \mathbf{0}_{2m\times m} & \mathbf{0}_{2m\times m} \\ \mathbf{0}_{m\times 2m} & \mathbf{I}_{m\times m} & \mathbf{0}_{m\times m} \\ \mathbf{0}_{m\times 2m} & \mathbf{0}_{m\times m} & -\mathbf{I}_{m\times m} \end{bmatrix} \tag{6.54b}$$

$$\hat{\mathbf{A}}_k = \begin{bmatrix} \mathbf{0}_{2m\times m} & \mathbf{0}_{2m\times m} & \mathbf{0}_{2m\times 2m} \\ -\mathbf{K}_{train} & \mathbf{K}_{train} & \mathbf{0}_{m\times 2m} \\ \mathbf{K}_{train} & -\mathbf{K}_{train} & \mathbf{0}_{m\times 2m} \end{bmatrix} \tag{6.54c}$$

and the vectors $\mathbf{b}_k$, $\hat{\mathbf{e}}_k$, $\hat{\mathbf{d}}_k$ and $\mathbf{z}_k$ are defined as:

$$\mathbf{b}_k = \begin{bmatrix} \mathbf{e}_m \\ \mathbf{e}_m \\ \mathbf{0}_{2m} \end{bmatrix}, \ \hat{\mathbf{e}}_k = \begin{bmatrix} \mathbf{0}_{2m} \\ \mathbf{e}_m \\ \mathbf{e}_m \end{bmatrix}, \ \hat{\mathbf{d}}_k = \begin{bmatrix} \mathbf{0}_{2m} \\ \mathbf{y}_{train} \\ -\mathbf{y}_{train} \end{bmatrix}, \ \mathbf{z}_k = \begin{bmatrix} \mathbf{p}_k \\ \mathbf{q}_k \\ \boldsymbol{\xi} \\ \hat{\boldsymbol{\xi}} \end{bmatrix} \tag{6.55}$$

Similar as the linear X-SVR, the optimization problem demonstrated in Eq. (6.53) can be equivalently solved in its dual formulation by using Lagrange method with KKT

conditions. Thus, by introducing the non-negative Lagrange multiplier $\mathbf{u}_k \in \Re^{4m}$, the proposed kernelized X-SVR can be solved as the quadratic programming problem shown in Eq. (6.56):

$$\min_{\mathbf{u}_k} : \frac{1}{2}\mathbf{u}_k^T \mathbf{Q}_k \mathbf{u}_k - \mathbf{m}_k^T \mathbf{u}_k \tag{6.56a}$$

$$s.t. \quad \mathbf{u}_k \geq \mathbf{0}_{4m} \tag{6.56b}$$

where $\mathbf{Q}_k \in \Re^{4m\times 4m}$ and $\mathbf{m}_k \in \Re^{4m}$ are defined by:

$$\mathbf{Q}_k = (\hat{\mathbf{A}}_k + \mathbf{I}_{4m\times 4m})\hat{\mathbf{C}}_k^{-1}(\hat{\mathbf{A}}_k + \mathbf{I}_{4m\times 4m})^T + \hat{\mathbf{G}}_k \hat{\mathbf{e}}_k \hat{\mathbf{e}}_k^T \hat{\mathbf{G}}_k \tag{6.56c}$$

$$\mathbf{m}_k = \lambda_b (\hat{\mathbf{A}}_k + \mathbf{I}_{4m\times 4m})\hat{\mathbf{C}}_k^{-1}\mathbf{b}_k - \varepsilon \hat{\mathbf{e}}_k - \hat{\mathbf{d}}_k \tag{6.56d}$$

Let $\mathbf{u}_k^* \in \Re^{4m}$ be the obtained solution for the optimization problem illustrated in Eq. (6.56), then the variables $\mathbf{z}_k$ and γ_k can be respectively computed as:

$$\mathbf{z}_k = \hat{\mathbf{C}}_k^{-1}\left[(\hat{\mathbf{A}}_k + \mathbf{I}_{4m\times 4m})^T \mathbf{u}_k^* - \lambda_b \mathbf{b}_k\right] \tag{6.57}$$

$$\gamma = \hat{\mathbf{e}}_k^T \hat{\mathbf{G}}_k \mathbf{u}_k^* \tag{6.58}$$

Then, the coefficient $\mathbf{w}$ can be obtained as:

$$\mathbf{w} = \mathbf{p}_k - \mathbf{q}_k = \mathbf{z}_k(1:m) - \mathbf{z}_k(m+1:2m) \tag{6.59}$$

Thus, the nonlinear regression function obtained by the proposed kernelized X-SVR is expressed as:

$$\hat{f}(\mathbf{x}) = (\mathbf{p}_k - \mathbf{q}_k)^T \boldsymbol{\kappa}(\mathbf{x}) - \hat{\mathbf{e}}_k^T \hat{\mathbf{G}}_k \mathbf{u}_k^* \tag{6.60}$$

It can be easily observed that the only difference between the linear and nonlinear X-SVR is that the input dataset is mapped into the empirical space by using specified

kernel function. Thus, the kernelized X-SVR can be regarded as a linear X-SVR with a manipulated input samples and therefore the convex property is still maintained regardless of the type of kernel function. In this context, the selected kernel function is not restricted to the category satisfying the Mercer's theorem [232].

6.3.4 Generalized Gegenbauer kernel - a new orthogonal polynomial kernel function

For both nonlinear classification and regression applications, the performance of support vector machine is significantly affected by the employed kernel functions [237]. Despite that Gaussian and polynomial kernels are commonly adopted, it is pointed out that these kernels can lead to unsatisfied results in approximating some complex function [237, 238]. Specifically, Gaussian and polynomial kernels are not complete orthonormal base, which result in that they cannot approach to the curves in quadratic continuous integral space [239]. To overcome such drawback, the wavelet kernel function is proposed and receives favourable results for both classification and regression [237, 239]. Motivated by the properties of orthogonal polynomials which have been effectively and efficiently used for functions approximation, the development of orthogonal polynomial kernels for SVM/ SVR models receives increasingly attention from researchers. An orthogonal Chebyshev polynomial kernel is introduced by [240] for single variable input then extended to vector input by various approaches including unified Chebyshev kernels [241], generalized and modified Chebyshev kernels [242]. A modified Hermite polynomial kernel is constructed by [243] as an extension to the Hermite polynomial kernel originally introduced by Vapnik [244]. By adopting the similar kernel construction approach, a Legendre polynomial kernel is proposed by [245]. A comprehensive experiment on the orthogonal polynomial kernels including the has been conducted by [246], which offers a valuable reference for researchers for kernel function selection.

Among the family of orthogonal polynomials, the Gegenbauer polynomial is also widely adopted for uncertainty quantification and function approximation by using the Gegenbauer series expansion [141, 247]. The univariate Gegenbauer polynomials, denoted by $P_d^{\tilde{\alpha}}(x)$, with degree $d \in \mathbb{Z}$ and polynomial parameter $\tilde{\alpha} > 0$ can be defined by the recurrence relations as Eq. (6.61):

$$\begin{cases} P_0^{\tilde{\alpha}}(x) = 1 \\ P_1^{\tilde{\alpha}}(x) = 2\tilde{\alpha}x \\ P_d^{\tilde{\alpha}}(x) = \dfrac{1}{d}[2x(d+\tilde{\alpha}-1)P_{d-1}^{\tilde{\alpha}}(x) - (d+2\tilde{\alpha}-2)P_{d-2}^{\tilde{\alpha}}(x)], \quad d = 2,3,4,... \end{cases} \tag{6.61}$$

For a given $\tilde{\alpha}$, the Gegenbauer polynomials are orthogonal on $x \in [-1,1]$ with respect to the weight function $\rho^{\tilde{\alpha}}(x)$, which can be expressed as:

$$\int_{-1}^{1} \rho^{\tilde{\alpha}}(x) P_l^{\tilde{\alpha}}(x) P_v^{\tilde{\alpha}}(x) dx = \begin{cases} h_l^{\tilde{\alpha}}, & l = v \\ 0, & l \neq v \end{cases} \tag{6.62}$$

where $l, v = 0,1,2,...,d$ and $\rho^{\tilde{\alpha}}(x)$ and $h_l^{\tilde{\alpha}}$ can be formulated as:

$$\rho^{\tilde{\alpha}}(x) = (1-x^2)^{\tilde{\alpha}-\frac{1}{2}} \tag{6.63a}$$

$$h_l^{\tilde{\alpha}} = \frac{\pi 2^{1-2\tilde{\alpha}} \Gamma(d+2\tilde{\alpha})}{d!(d+\tilde{\alpha})\Gamma^2(\tilde{\alpha})} \tag{6.63b}$$

In Eq. (6.63b), $\Gamma(\bullet)$ denotes the Gamma function. As the particular solutions of the Gegenbauer differential equation, such polynomial is the generalization of Chebyshev and Legendre polynomials by substituting various value for $\tilde{\alpha}$ [248].

Considering generalization ability of Gegenbauer polynomial, Padierna et al. [249] proposed a new orthogonal polynomial kernel based on the Gegenbauer polynomial and

implemented on binary classification problems. Similar as the Legendre and Hermite polynomial kernels, the Gegenbauer polynomial kernel is constructed as the tensor product of the inner product of univariate polynomials, which is conceptually identical with the method for extending one-dimensional polynomials to multi-dimensional. As pointed out by [241–243, 245], the kernel constructed by the tensor product approach may yield either an extremely small and larger value which will significantly impact the performance the corresponding kernelized learning models. Such phenomenon is avoided in the Gegenbauer polynomial kernel by multiplying weight and scaling functions to the product univariate polynomials and limiting the variation range of the polynomial parameter. However, it is point out by Ozer et al. [242] that such type of kernel construction approach may force the learning along each input variable rather than the input vectors. Thus, it is suggested that the orthogonal polynomial kernel functions should be applied directly onto the input vectors rather than each pair of input elements.

Inspired by the pioneering work by Ozer et al. [242] and Padierna et al. [249], we developed a new orthogonal polynomial kernel function for the proposed kernelized X-SVR. Deferring from the kernel function introduced by Padierna et al. [249], the proposed orthogonal polynomial kernel is constructed by using the partial sum of the inner product of generalized Gegenbauer polynomials, namely the *generalized Gegenbauer kernel* (GGK). By adopting the strategy utilized for defining the generalized Chebyshev polynomial for vector inputs [242], the generalized Gegenbauer polynomials are defined recursively as following:

$$\begin{cases} P_0^{\tilde{\alpha}}(\mathbf{x}) = 1 \\ P_1^{\tilde{\alpha}}(\mathbf{x}) = 2\tilde{\alpha}\mathbf{x}^T \\ P_d^{\tilde{\alpha}}(\mathbf{x}) = \dfrac{1}{d}[2\mathbf{x}^T(d+\tilde{\alpha}-1)P_{d-1}^{\tilde{\alpha}}(\mathbf{x}) - (d+2\tilde{\alpha}-2)P_{d-2}^{\tilde{\alpha}}(\mathbf{x})], \quad d = 2,3,4,\ldots \end{cases} \tag{6.64}$$

where $\mathbf{x} \in \Re^n$ denotes the column vector of input variables. It can be revealed from Eq. (6.64) that the generalized Gegenbauer polynomial $P_d^{\tilde{\alpha}}$ yields a scalar value when the polynomial order d is an even number, otherwise it will yield a column vector. Considering that an exponential function, such as Gaussian kernel function, has better capability in capturing local information than the originally employed square root function [242, 250], the Gaussian kernel function is adopted here as the weighting function for the proposed GGK. Thus, the proposed *d*th order generalized Gegenbauer kernel function $\mathrm{K}_{GGK}(\mathbf{x}_i, \mathbf{x}_j)$ of two arbitrary input vectors $\mathbf{x}_i$ and $\mathbf{x}_j$ is defined as Eq. (6.65):

$$K_{GGK}(\mathbf{x}_i, \mathbf{x}_j) = \frac{\sum_{l=0}^{d} P_l^{\tilde{\alpha}}(\mathbf{x}_i)^T P_l^{\tilde{\alpha}}(\mathbf{x}_j)}{\exp(\sigma_{\mathrm{K}} \left\| \mathbf{x}_i - \mathbf{x}_j \right\|_2^2)} \tag{6.65}$$

where each element of $\mathbf{x}_i$ and $\mathbf{x}_j$ is defined in $[-1,1]$. In this context, both $\tilde{\alpha}$ and σ_{K} are here considered as the kernel scales or the so-called decaying parameters of the proposed kernel function.

It is worthy to addressing that the proposed GGK satisfies the Mercer Theorem [217, 225] which is a prerequisite for implementing the kernel function in SVM/SVR. Thus, not just in the proposed X-SVR model, the generalized Gegenbauer Kernel introduced in this study can be also employed in the other kernelized learning models which require the Mercer condition to be satisfied. The property that the proposed GGK is a valid Mercer kernel can be systematically demonstrated by the *Proposition 2*. It can be observed from Eq. (6.65), the novel GGK possesses three kernel parameters: the polynomial order d and two positive kernel scale parameters $\tilde{\alpha}$ and σ_{K} .

Proposition 2:

The proposed generalized Gegenbauer kernel (GGK) expressed in Eq. (6.65) is a valid Mercer kernel.

Proof:

Firstly, the proposed GGK can be alternatively expressed as the product of two kernel functions $\mathrm{K}_1(\mathbf{x}_i,\mathbf{x}_j)=\exp(-\sigma_{\mathrm{K}}\left\|\mathbf{x}_i-\mathbf{x}_j\right\|_2^2)$ and $\mathrm{K}_2(\mathbf{x}_i,\mathbf{x}_j)=\sum_{l=0}^{d}P_l^{\tilde{\alpha}}(\mathbf{x}_i)^T P_l^{\tilde{\alpha}}(\mathbf{x}_j)$ such that:

$$\mathrm{K}_{GGK}(\mathbf{x}_i,\mathbf{x}_j)=\mathrm{K}_1(\mathbf{x}_i,\mathbf{x}_j)\mathrm{K}_2(\mathbf{x}_i,\mathbf{x}_j) \tag{6.66}$$

According to [217, 244], the multiplication of two valid Mercer kernels is also a valid kernel function. Since that $\mathrm{K}_1(\mathbf{x}_i,\mathbf{x}_j)$ is the Gaussian kernel ($\sigma_{\mathrm{K}}>0$) which satisfied the Mercer Theorem, $\mathrm{K}_{GGK}(\mathbf{x}_i,\mathbf{x}_j)$ can be proved as a valid kernel by verifying that $\mathrm{K}_2(\mathbf{x}_i,\mathbf{x}_j)$ satisfies the Mercer Theorem.

Given an arbitrary squared integrable function $\tilde{h}(\mathbf{x})$ defined as $\tilde{h}:\Re^n\rightarrow\Re$ and assuming each element in $\mathbf{x}_i$ and $\mathbf{x}_j$ is independent with each other, then

$$\begin{aligned}
&\iint \mathrm{K}_2(\mathbf{x}_i,\mathbf{x}_j)\tilde{h}(\mathbf{x}_i)\tilde{h}(\mathbf{x}_j)d\mathbf{x}_i d\mathbf{x}_j \\
&=\iint\sum_{l=1}^{d}P_l^{\tilde{\alpha}}(\mathbf{x}_i)^T P_l^{\tilde{\alpha}}(\mathbf{x}_j)\tilde{h}(\mathbf{x}_i)\tilde{h}(\mathbf{x}_j)d\mathbf{x}_i d\mathbf{x}_j \\
&=\sum_{l=0}^{d}\iint P_l^{\tilde{\alpha}}(\mathbf{x}_i)^T P_l^{\tilde{\alpha}}(\mathbf{x}_j)\tilde{h}(\mathbf{x}_i)\tilde{h}(\mathbf{x}_j)d\mathbf{x}_i d\mathbf{x}_j \\
&=\sum_{l=0}^{d}\left[\int P_l^{\tilde{\alpha}}(\mathbf{x}_i)^T\tilde{h}(\mathbf{x}_i)d\mathbf{x}_i\int P_l^{\tilde{\alpha}}(\mathbf{x}_j)\tilde{h}(\mathbf{x}_j)d\mathbf{x}_j\right] \\
&=\sum_{l=0}^{d}\left[\left(\int P_l^{\tilde{\alpha}}(\mathbf{x}_i)^T\tilde{h}(\mathbf{x}_i)d\mathbf{x}_i\right)\left(\int P_l^{\tilde{\alpha}}(\mathbf{x}_i)\tilde{h}(\mathbf{x}_i)d\mathbf{x}_i\right)\right]\geq 0
\end{aligned} \tag{6.67}$$

Thus, $\mathrm{K}_2(\mathbf{x}_i, \mathbf{x}_j)$ is a valid Mercer kernel. Therefore, the proposed GGK $\mathrm{K}_{GGK}(\mathbf{x}_i, \mathbf{x}_j)$ is an admissible Mercer kernel function.

This concludes the proof. □

It can be observed from the proof of Proposition 2 that the proposed GGK is a mixed kernel function which combines one local kernel $\mathrm{K}_1(\mathbf{x}_i, \mathbf{x}_j)$ (Gaussian kernel) and one global kernel $\mathrm{K}_2(\mathbf{x}_i, \mathbf{x}_j)$ (a generalized polynomial kernel) [251]. Subsequently, by integrating the proposed generalized Gegenbauer kernel, the nonlinear X-SVR can be also regarded as a multiple kernel learning algorithm using fixed rules approach [252].

6.3.5 Hyperparameter optimization for X-SVR with generalized Gegenbauer kernel

In the proposed X-SVR with the generalized Gegenbauer kernel (GGK), there are seven hyperparameters including the two regularization parameters λ_a and λ_b, the penalty parameter c, the insensitive tube width ε, the polynomial order d and two positive kernel scale parameters $\tilde{\alpha}$ and σ_{K}. Similar as the conventional SVR model, the prediction accuracy of the proposed X-SVR with GGK is strongly dependent on the selection of these parameters. For machine learning approaches, the k-fold cross-validation (CV) over the training samples is an effective approach to ensure the regression model has the generalized ability in accurately predicting the training dataset while checking if the selected parameters will result in overfitting [253]. Practically, k is commonly set to 5-10 as a trade-off of computational cost and prediction accuracy. In present work, the 5-fold CV error which denoted by Err_{5CV} is employed as the training error measure for X-SVR, which is formulated as following:

$$Err_{5CV} = \frac{1}{5}\sum_{i=1}^{5} err_i \tag{6.68}$$

where err_i is the mean squared error (MSE) between the predicted output $\hat{f}(\mathbf{x})$ obtained by the X-SVR model and the output of the true function $f(\mathbf{x})$ in each fold i. err_i is expressed as Eq. (6.69):

$$err_i = \frac{1}{m_i}\sum_{j=1}^{m_i}(y_{i,j} - \hat{f}(\mathbf{x}_{i,j}))^2 \tag{6.69}$$

where m_i denotes the number of training samples in the fold i; $y_{i,j}$ denotes the *j*th output in the fold *i*; $\mathbf{x}_{i,j}$ represents the *j*th inputs sample in the fold *i*.

Since that the selected hyperparameters will lead to the minimization of Err_{5CV}, the hyperparameter tuning can be considered as an optimization problem. For SVM/ SVR models, several techniques have been developed for hyperparameter selection such as grid search [220], random search [254], genetic algorithm [255], particle swarm optimization [239, 250] and other population-based optimization strategies [256]. Recently, Bayesian optimization is becoming increasingly popular in tuning learning parameters for complex machine learning algorithm such as deep neural network [257]. Typically, Bayesian optimization construct a probabilistic approximation of the objective function by using Gaussian process and then determines the next estimation point which results in the maximum of the acquisition function [258]. Instead of using the local gradient or Hessian approximations, Bayesian optimization relies on all the available information from previous evaluations of the objective function. Subsequently, the minimum of the objective function can be efficiently obtained with relative less iterations [258]. Considering that more hyperparameters are included in proposed X-SVR model

with Generalized Gegenbauer kernel in comparison with the classic nonlinear ε-SVR, Bayesian optimization method is integrated in the proposed meta-model for automatically selecting the suitable learning parameters. In the presented work, the Bayesian optimization is conducted by using the MATLAB Statistical and Machine Leaning toolbox [259]. The searching range for the hyperparameters are summarized in Table 6.1 as following:

Table 6.1 Searching range of X-SVR hyperparameters

Hyperparameter	Searching range
λ_a	$[10^{-3},10^{3}]$
λ_b	$[10^{-3},10^{3}]$
c	$[10^{-1},10^{4}]$
ε	$[10^{-5},10^{-1}]$
d	$[1,6]$
$\tilde{\alpha}$	$[10^{-3},1]$
σ_{K}	$[10^{-2},10^{2}]$

6.4 Structural dynamic reliability analysis by using X-SVR

This chapter offers a metamodel-based Monte Carlo Simulation method for structural dynamic reliability analysis by adopting the proposed X-SVR with the generalized Gegenbauer kernel. In this proposed reliability analysis strategy, the true structural limit state function is approximated by using the X-SVR metamodel to replace the precise FEM model. Then, the probability of failure is evaluated by conducting the Monte Carlo simulation based on the constructed surrogate model. Thus, the performance of the proposed method is significantly affected by the quality of the trained X-SVR model. In practice, metamodels are trained by limit number of running the original models based

on the Design of Experiments (DOEs) and expected to have good predictions over the entire domain of input variables, which is commonly achieved by employing uniform sampling techniques [260, 261]. In this study, the training samples are generated by quasi-Monte Carlo sampling method with Sobol's sequence [262]. Such low-discrepancy sampling technique can generate samples evenly distributed over the design space. Then, the X-SVR surrogate model will be trained by using the DOE and subsequently used for analyzing the probability of failure (p_f).

In the presented study, the first passage problem with equal barriers ($b_1 = -b_2 = b$) is investigated for demonstrating the capability of the proposed metamodel-based reliability analysis approach. The procedure for this reliability analysis is summarized as follows:

1. Generate m_{MCS} Monte Carlo samples $\mathbf{x}_{MCS} \in \Re^{m_{MCS} \times n}$ for input variables using the quasi-MCS scheme. The generated samples will be used as the input samples for the trained metamodel for reliability analysis using metamodel. m_{MCS} is expected to be large (i.e. $10^5 - 10^6$).

2. Define the DOE with m_{train} ($m_{train} \ll m_{MCS}$) training samples $\mathbf{x}_{train}$ and $\mathbf{y}_{train}$ using the quasi-MCS (Sobol's sequence). Here $y_{train,i} = \max\left|u(\mathbf{x}_i, t)\right|$ for $i = 1, ..., m_{train}$, which is obtained by high-fidelity numerical analysis (i.e. FEM) in this study.

3. Train the X-SVR model based on the samples $\{\mathbf{x}_{train}, \mathbf{y}_{train}\}$ obtained in step 2. The limit state function of the investigated structure can be approximately expressed as $\hat{g}(\mathbf{x})$ by employing the trained X-SVR surrogate model.

4. Input the MCS samples into the metamodel-based limit state function $\hat{g}(\mathbf{x})$ to analysis the dynamic response. Compute the number of failure samples m_f which are indicated by $\hat{g}(\mathbf{x}) \leq 0$.

5. The probability of failure for the investigated structure is approximated calculated as $\hat{p}_f = m_f / m_{MCS}$.

The flowchart of the computational procedures is shown in Figure 6.4.

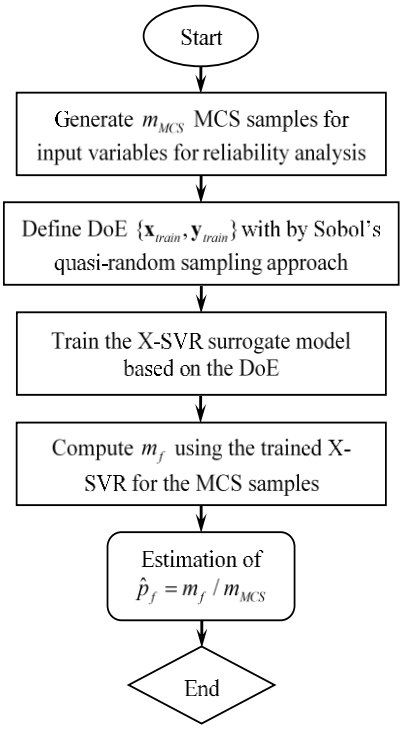

Figure 6.4 Flowchart for the X-SVR based structural dynamic reliability analysis

6.5 Numerical examples

To demonstrate the capability and accuracy of the proposed approach, four numerical examples are presented in this study. The first two analytical examples are benchmark functions which are adopted here for illustrating the performance of the proposed approach. Then, the proposed approach is further tested by one structural dynamic problem and one acoustic problem for demonstrating its reliability and versatility. The

results are compared with the classical ε - support vector regression (ε-SVR) model with widely used Gaussian kernel. Moreover, the direct Monte-Carlo simulation (MCS) is conducted for each example as a reference for comparing the accuracy of the two methods. In all the considered examples, both the proposed method and ε-SVR model are trained by samples generated by Quasi MCS with Sobol sequence [262]. In this work, the ε-SVR integrated in the MATLAB Statistical and Machine Leaning toolbox [259] is adopted. The presented numerical results are obtained by using a workstation with CPU of Intel Core i7-4770, 32 GB of memory, and 1 TB of hard drive.

6.5.1 Borehole function

The first example employed for demonstrating the performance of the proposed method is called the Borehole function which is commonly used as a benchmark example for emulation and prediction tests [263]. This function, as expressed in Eq. (6.70), was originally derived for modelling the water flow through a borehole. There are totally 8 input parameters which are all modeled as independent and uniformly distributed variables. The details of the variation range are presented in Table 6.2.

$$f(\mathbf{x}) = \frac{2\pi x_3 (x_4 - x_6)}{\ln(x_2 / x_1)(1 + \frac{2x_7 x_3}{\ln(x_2 / x_1) x_1^2 x_8} + \frac{x_3}{x_5})} \tag{6.70}$$

Table 6.2 Details of the input parameters for the Borehole function

Input parameters	Range
x_1	$[0.05, 0.15]$
x_2	$[100, 50000]$
x_3	$[63070, 115600]$
x_4	$[990, 1110]$
x_5	$[63.1, 116]$

x_6	$[700, 820]$
x_7	$[1120, 1680]$
x_8	$[9855, 12045]$

The performance of the proposed model is tested with a variety number of training samples (m_{train}). In this example, the initial design of experiment (DOE) consists 25 sampling points and then augmented to 50, 100 until 200 samples. Moreover, the classical ε-SVR model with Gaussian kernel is applied with the same DOEs for comparison purpose. The accuracy of the metamodels is assessed by evaluating two types of relative error: the root mean squared error (RMSE) and the coefficient of determination (R^2) which are described as in Table 6.3, where $f(\mathbf{x}_i)$ denotes the output of the actual model at the sampling point $\mathbf{x}_i$; $\hat{f}(\mathbf{x}_i)$ denotes the output of the constructed surrogate model at the sampling point $\mathbf{x}_i$; and μ_f denotes the estimated mean of the outputs of all the m_{MCS} sampling points for the actual model. The RMSE is scale-dependent to the magnitude of data to be predicted and a lower RMSE value indicates a higher accuracy of the surrogate model. The R^2 offers a statistical measure of the goodness of regression predictions in approximating the real data points. Surrogate models are indicated to have better capability in prediction if R^2 is closer to 1. The two validation errors are computed for each surrogate model with different numbers of training samples by using the MCS with $m_{MCS} = 5 \times 10^4$ samples in this example.

Table 6.3 The expressions of RMSE and R^2

Error metrics	Expression

Root mean square error (RMSE)	$RMSE = \sqrt{\frac{1}{m_{MCS}} \sum_{i=1}^{m_{MCS}} (f(\mathbf{x}_i) - \hat{f}(\mathbf{x}_i))^2}$
Coefficient of determination (R^2)	$R^2 = 1 - \frac{\sum_{i=1}^{m_{MCS}} (f(\mathbf{x}_i) - \hat{f}(\mathbf{x}_i))^2}{\sum_{i=1}^{m_{MCS}} (f(\mathbf{x}_i) - \mu_f)^2}$

To statistically assess the predicting performance of the surrogate models, the analysis is replicated 50 times at each DOE for both methods and boxplots of the RMSE and R^2 of predicted results are shown in Figures 6.5 and 6.6, respectively. In the figures, the median error, the quantile error values and the extreme error values of the 50 independently repeated simulations are demonstrated. As shown in Figure 6.5, the proposed X-SVR method has a better predicting performance than the conventional ε-SVR in terms of median value. It is also noticed from Figure 6.5 that, for $m_{train} = 25$, more outliers are shown in the boxplot of RMSE of the simulation results obtained by ε-SVR than the proposed approach. Additionally, both the median value and variation range for the RMSE of the X-SVR prediction decrease with the increase of training sample size. This phenomenon is not clearly demonstrated from Figure 6.5 for the ε-SVR. Similarly, it is shown in Figure 6.6 that the proposed surrogate model has the less scattered R^2 value than the conventional SVR method. Thus, it can be concluded that the proposed model has a better performance in this example.

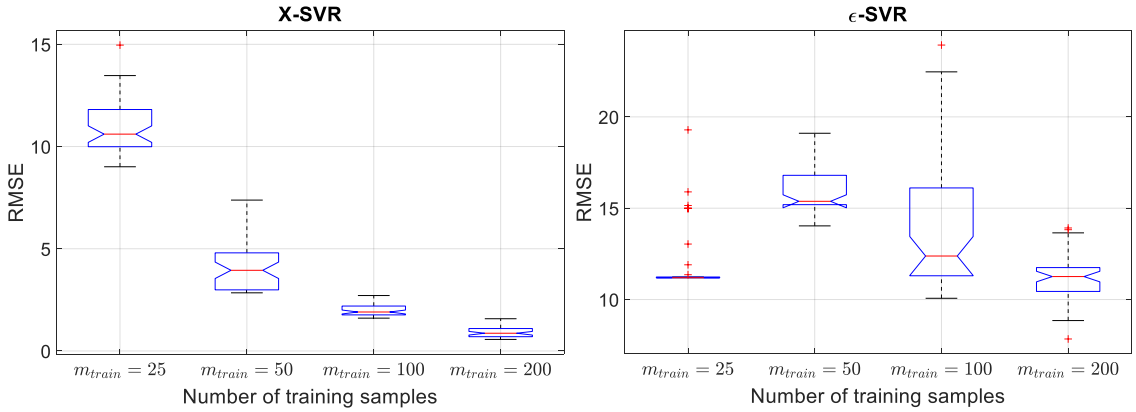

(a) (b)

Figure 6.5 The boxplots of RMSE for 50 independent simulations of (a) X-SVR and (b) ε-SVR trained by different DOEs

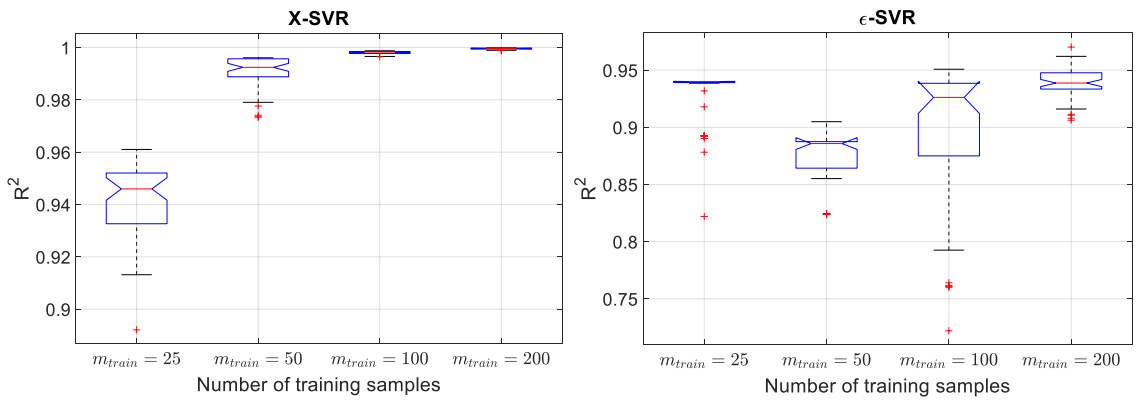

(a) (b)

Figure 6.6 The boxplots of R^2 for 50 independent simulations of (a) X-SVR and (b) ε-SVR trained by different DOEs

6.5.2 50-D function

For testing the capability of the proposed X-SVR method for high-dimensional problems, an analytical example with 50 input parameters is utilized. Such 50-D function [264] has been widely used in evaluating the performance of optimization algorithm in high dimensional space. The considered function is expressed in Eq. (6.71). In this example, the input variables are assumed to be independent and uniformly distributed within the range $[0,1]$.

$$f(\mathbf{x}) = 1 - \exp(-0.01\sum_{i=1}^{50} x_i^2); x_i \in [0,1] \tag{6.71}$$

Similar as in the Example 6.5.1, the performance of the proposed X-SVR with generalized Gegenbauer kernel is investigated by comparing the ε-SVR with widely used Gaussian kernel against various numbers of training samples (m_{train}). Considering of the relatively large number of input variables, the initial DOE is selected as 50 and increased gradually to 400. The validation errors RMSE and R^2 for both surrogate models trained with different m_{train} are computed using $m_{MCS} = 5\times10^4$ MCS samples and are plotted in Figure 6.7. It can be observed from simulation results that, the RMSE for X-SVR is less than that for ε-SVR while the R^2 for X-SVR is larger than that for ε-SVR with any adopted m_{train}, which indicates that the X-SVR with generalized Gegenbauer kernel outperforms the ε-SVR with Gaussian kernel in this example. Despite of that the validation errors reduce with the increase of m_{train} for both methods, the RMSE and R^2 for the proposed ε-SVR converge faster than that for the classic ε-SVR. Under the circumstance of small number of training samples ($m_{train} \le 150$), it is shown in Figure 6.7(a) that the X-SVR has much less RMSE than the ε-SVR.

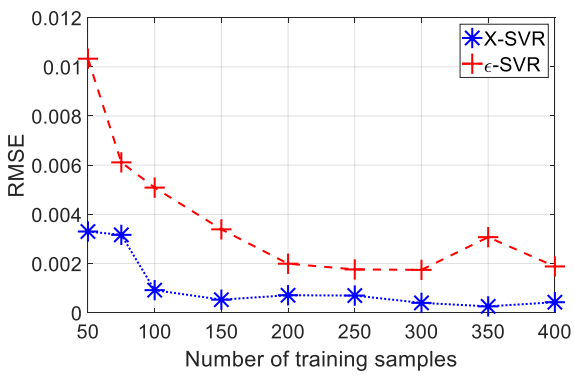

(a)

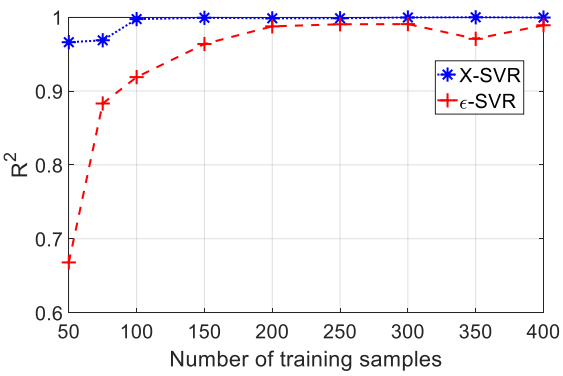

(b)

Figure 6.7 The (a) RMSE and (b) R^2 of X-SVR and ε-SVR trained with various DOEs

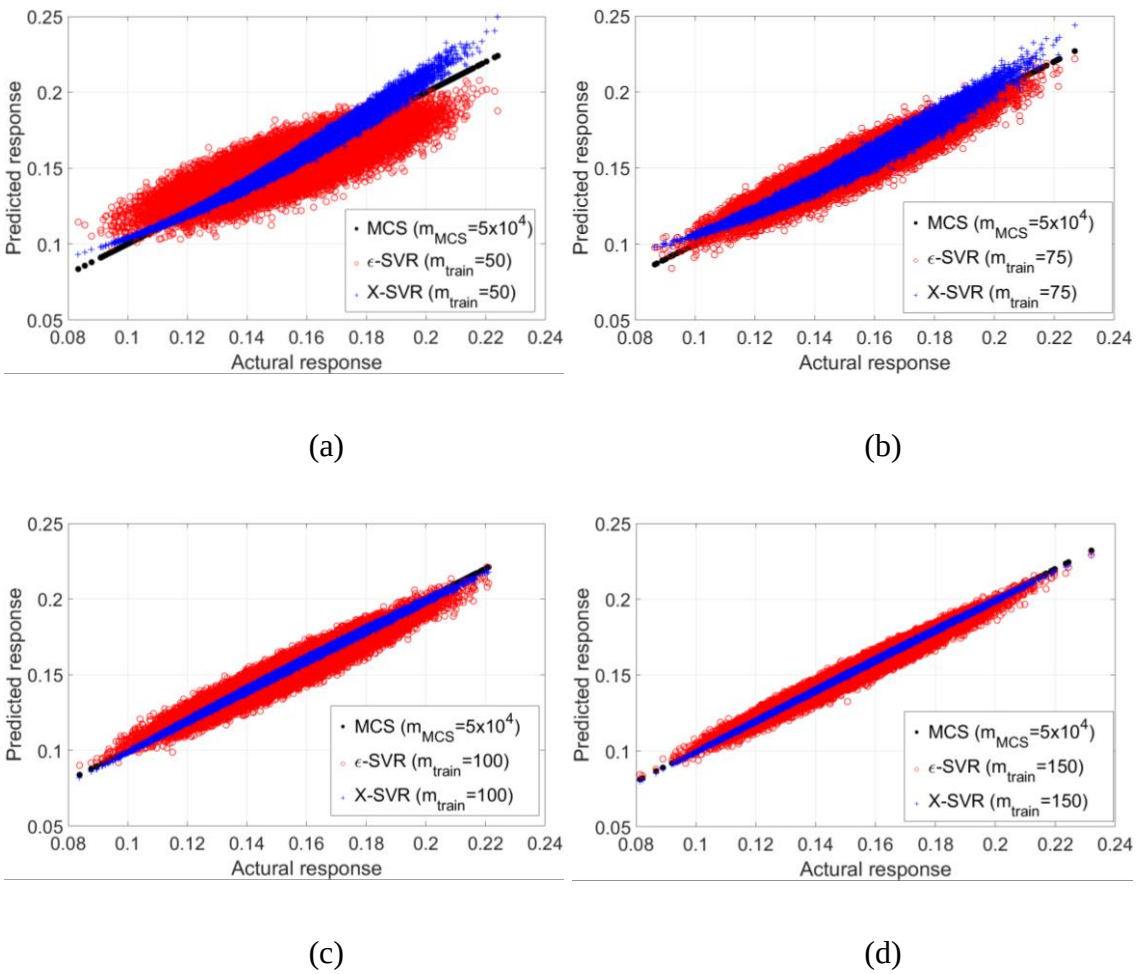

Figure 6.8 Comparative assessment of by X-SVR and ε-SVR utilizing various numbers of training samples: (a) $m_{train} = 50$, (b) $m_{train} = 75$, (c) $m_{train} = 100$ and (d) $m_{train} = 150$

In order to offer a visible demonstration, the scatter plots of prediction results (predicted response in Figure 6.8) obtained by both X-SVR and ε-SVR trained with relatively small number of DOEs are shown in Figure 6.8. It can be visualized that, with $m_{train} = 50$ and 75, the prediction obtained by X-SVR is less variant from the true value (actual response in Figure 6.8) of the 50-D function obtained by direct MCS. In the context that $m_{train} = 100$ and 150, the function value predicted by X-SVR is almost identical to the MCS results by observation. Thus, the proposed X-SVR with generalized

Gegenbauer kernel has superior capability in approximating the 50-D function than the ε-SVR with Gaussian kernel.

6.5.3 Spring-mass-damper system with three degrees of freedom

In this example, a spring-mass-damper system with three degrees of freedom (DOFs) modified from [265] is used for testing the capability of the proposed X-SVR based structural dynamic reliability analysis. The detailed configuration of the adopted vibration system is shown in Figure 6.9. The dynamic equations of this spring-mass-damper system can be expressed as Eq. (6.72):

$$\begin{cases} m_1\ddot{u}_1(t)+(c_1+c_2)\dot{u}_1(t)-c_2\dot{u}_2(t)+(k_1+k_2)u_1(t)-k_2u_2(t)=F(t) \\ m_2\ddot{u}_2(t)-c_2\dot{u}_1(t)+(c_2+c_3)\dot{u}_2(t)-c_3\dot{u}_3(t)-k_2u_1(t)+(k_2+k_3)u_2(t)-k_3u_3(t)=0 \\ m_3\ddot{u}_3(t)-c_3\dot{u}_2(t)+(c_3+c_4)\dot{u}_3(t)+(k_3+k_4)u_3(t)-k_3u_2(t)=0 \end{cases} \quad (6.72)$$

where m_1, m_2 and m_3 denote the masses of the system, respectively; k_1, k_2, k_3 and k_4 denote the stiffness of the springs in the system, respectively; c_1, c_2, c_3 and c_4 denote the dampers of the system; $u_1(t)$, $u_2(t)$ and $u_3(t)$ denote the displacements of the three lumped masses in this system. A time-dependent harmonic excitation $F(t)=F_0e^{-0.5t}\cos(4t)$ is applied to the mass m_1. The initial conditions of this system are set as $[u_1(0),u_2(0),u_3(0),\dot{u}_1(0),\dot{u}_2(0),\dot{u}_3(0)]=[0,0,0,0,0,0]$.

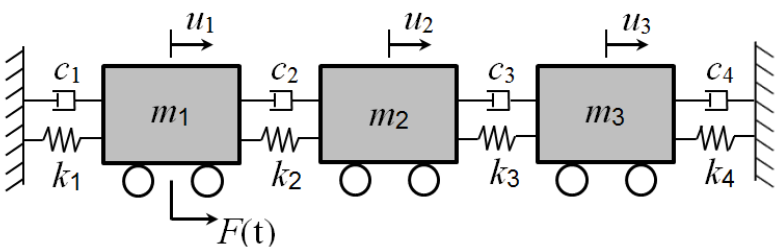

Figure 6.9 The spring-mass-damper system with three degrees of freedom (DOFs)

Table 6.4 The statistical information for uncertain parameters of Example 6.5.3

Parameter		F_0 (N)	m_1, m_2, m_3 (kg)	c_1, c_2, c_3, c_4 (N/(m/s))	k_1, k_2, k_3, k_4 (N/m)
Mean (μ)		5	3	0.475	95
Distribution (σ)		Normal	Lognormal	Lognormal	Lognormal
COV	Case 1	2.5%			
	Case 2	5%			
	Case 3	10%			

The amplitude F_0 of the harmonic excitation is considered as a random variable with normal distribution while the masses, stiffness and dampers of the system are considered as random variables with lognormal distribution. Moreover, three different coefficients of variation (COVs) ranging from 2.5% to 10% are studied in this example. The details of the statistical information of the considered 12 random variables are listed in Table 6.4. For the investigation, the displacement of m_1 is assumed to be critical for the safety of the system. According to the first-passage failure theory, the limit state function of the spring-mass-damper system is defined by

$$g(\mathbf{x}) = \overline{u_1} - \max_t(|u_1(t)|) \tag{6.73}$$

where $\mathbf{x} = [k_1, k_2, k_3, k_4, c_1, c_2, c_3, c_4, m_1, m_2, m_3, F_0]$ and $\overline{u_1}$ denotes the allowable displacement at m_1 and is set to be 8.5 cm. The COV is defined as Eq. (6.74):

$$COV = \frac{\sigma_{input}}{\mu_{input}} \tag{6.74}$$

where μ_{input} and σ_{input} denote the mean and standard deviation of the input random variable, respectively.

The "exact" probability of failure ($\tilde{p}_f$) for the considered three cases is obtained by using direct Monte Carlo simulation with $m_{MCS} = 10^6$ samplings. For demonstrating the capability of the proposed surrogate model, the X-SVR models are respectively constructed with various training samples ($m_{train} = 25, 50, 100$) and the predicted probability of failure ($\hat{p}_f$) is then calculated accordingly. Meanwhile, the conventional ε-SVR model with Gaussian kernel is trained and tested with the same datasets. The accuracy of the proposed surrogate model is measured by calculating the relative difference ε_{p_f} between $\hat{p}_f$ and $\tilde{p}_f$ as the Eq. (6.75).

$$\varepsilon_{p_f} = \frac{\left|\hat{p}_f - \tilde{p}_f\right|}{\hat{p}_f} \times 100 \tag{6.75}$$

Table 6.5 The probability of failure - Case 1, Example 6.5.3

Method	Case 1					
	$\hat{p}_f$ ($m_{train} = 25$)	ε_{p_f}	$\hat{p}_f$ ($m_{train} = 50$)	ε_{p_f}	$\hat{p}_f$ ($m_{train} = 100$)	ε_{p_f}
X-SVR	0.1006	12.25%	0.0808	9.86%	0.0861	3.90%
ε-SVR	0.1224	36.51%	0.0570	36.46%	0.1138	26.97%
MCS	$\tilde{p}_f = 0.0896$					

Table 6.6 The probability of failure - Case 2, Example 6.5.3

Method	Case 2					
	$\hat{p}_f$ ($m_{train} = 25$)	ε_{p_f}	$\hat{p}_f$ ($m_{train} = 50$)	ε_{p_f}	$\hat{p}_f$ ($m_{train} = 100$)	ε_{p_f}
X-SVR	0.3160	12.39%	0.2924	3.99%	0.2903	3.25%
ε-SVR	0.2123	24.49%	0.3017	7.29%	0.2961	5.31%

MCS	$\tilde{p}_f = 0.2812$

The simulated probability of failure by using the proposed method and ε-SVR model for Cases 1-3 are summarised in Tables 6.5 - 6.7, respectively. By reviewing the simulation results, the proposed method surpasses the classical support vector regression model by offering less relative difference in predicting the probability of failure of the investigated spring-mass-damping system under various uncertainty levels. Additionally, it is indicated by the results that the probability of failure estimated by the proposed X-SVR approaches to $\hat{p}_f$ with increasing number of samples for training, while such trend is not obvious based on the simulation results obtained from ε-SVR.

Table 6.7 The probability of failure - Case 3, Example 6.5.3

Method	Case 3					
	$\hat{p}_f$ ($m_{train} = 25$)	ε_{p_f}	$\hat{p}_f$ ($m_{train} = 50$)	ε_{p_f}	$\hat{p}_f$ ($m_{train} = 100$)	ε_{p_f}
X-SVR	0.3569	7.48%	0.3641	5.58%	0.3978	3.15%
ε-SVR	0.2458	36.28%	0.2728	29.28%	0.1827	52.62%
MCS	$\tilde{p}_f = 0.3857$					

6.5.4 Acoustic wave radiation from a 3D open structure

The effectiveness and capability of the proposed X-SVR based reliability analysis approach is further applied to acoustic problem in this section. The 3D acoustic analysis of an open structure submerged in an infinite acoustic space is investigated. As shown in Figure 6.10, the open structure is assumed to be a rigid hollow sphere with one quarter

cut-off, where r_0 and r_1 ($r_1 = 1.2r_0$)denote the inner and outer radii of the open hollow sphere, respectively. The inner surface of the open sphere is uniformly subjected to a transient acoustic flux $f_s(t)$, which is defined in a dimensionless manner in Figure 6.11. In Figure 6.11(a), the applied transient flux is normalized by its peak magnitude F_{st} and plotted against the dimensionless time $t_d = t\dfrac{\hat{c}}{r_0}$, where $\hat{c}$ denotes the nominal value of sound speed c_{sound}. The Fourier transform of the flux $f_s(t)$ is also shown in Figure 6.11(b) with the dimensionless amplitude $F_s(\omega)/F_{st}$ and the dimensionless frequency $\omega_d = \omega r_0 / \hat{c}$. The corresponding highest frequency of interest is estimated to be $\omega_{d,\max} \approx 6$.

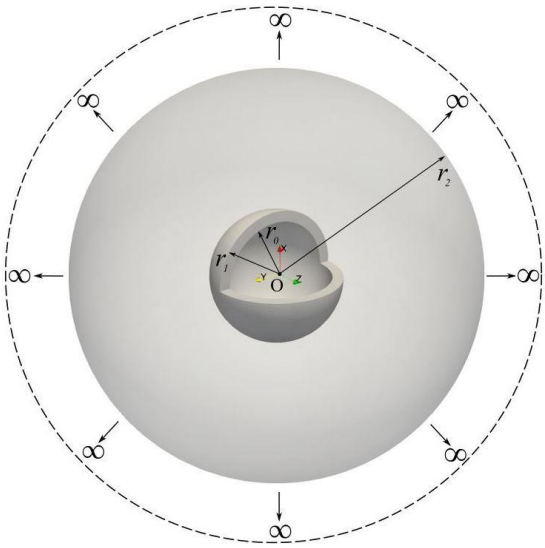

Figure 6.10 Problem setup of a 3D open-sphere structure submerged in infinite acoustic domain

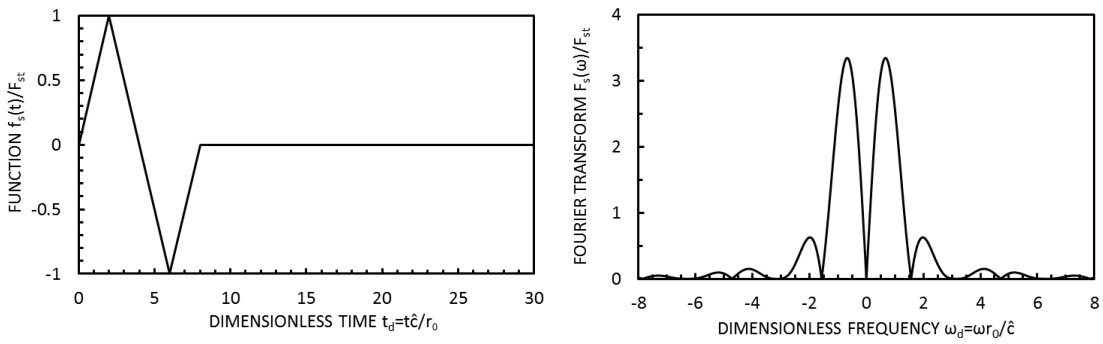

(a) (b)

Figure 6.11 Time variation of transient flux $f_s(t)$ applied on the inner spherical boundary: (a) time history and (b) Fourier transform.

In this example, the time-dependent acoustic pressure $p_O(t)$ at point $O(0,0,0)$ marked in Figure 6.10 is considered for reliability analysis. The commercial software ANSYS [183] is employed for the acoustic analysis. Due to the infinitely large acoustic field, the acoustic field is firstly truncated to a bounded and an unbounded acoustic domain by the translucent spherical shell in Figure 6.10 with the radius of r_2. In the ANSYS model, the bounded acoustic domain is modelled by FLUID30 elements (4-node tetrahedral elements). The unbounded acoustic domain is represented by the FLUID130 elements (3-node triangular elements) attached to the outer surface (spherical surface) of the bounded domain. According to Figure 6.11(b), the minimum wavelength can be calculated as $\lambda_{\min} = \frac{2\pi}{\omega_{d,\max}} r_0 \approx 1.05 r_0$. In order to guarantee the accuracy, the element edge length is set to be $0.1r_0$ in ANSYS. This can provide approximately 11 nodes per minimum wavelength. From the ANSYS manual [183], the FLUID130 element is recommended to be placed at $0.2\frac{2\pi}{\omega_0} r_0 \approx 1.88 r_0$ away from the source of excitation. Therefore, the radius if the truncated spherical boundary r_2 is set to be $3r_1$ in this model

for accuracy.The total number of elements and nodes in this acoustic model are 1566852 and 271172, respectively. The mesh of this acoustic model is also illustrated in Figure 6.12. The global equations of motion for this acoustic model can be formulated as:

$$\mathbf{M}_G^a \ddot{\mathbf{z}}_G(t) + \mathbf{C}_G^a \dot{\mathbf{z}}_G(t) + \mathbf{K}_G^a \mathbf{z}_G(t) = \mathbf{r}_G(t) \tag{6.76}$$

where $\mathbf{M}_G^a$, $\mathbf{C}_G^a$ and $\mathbf{K}_G^a$ denote the global mass, damping and stiffness matrices of acoustics, respectively; $\mathbf{z}_G(t)$ is the vector containing all nodal pressures $\mathbf{p}(t)$; and $\mathbf{r}_G(t)$ denotes the global flux vector which relates to $f_s(t)$. It should be noticed that the existence of damping matrix in Eq.(6.75) is due to the unbounded acoustic domain. The initial condition of the system is $[\mathbf{z}_G(0), \dot{\mathbf{z}}_G(0)] = [\mathbf{0}, \mathbf{0}]$.

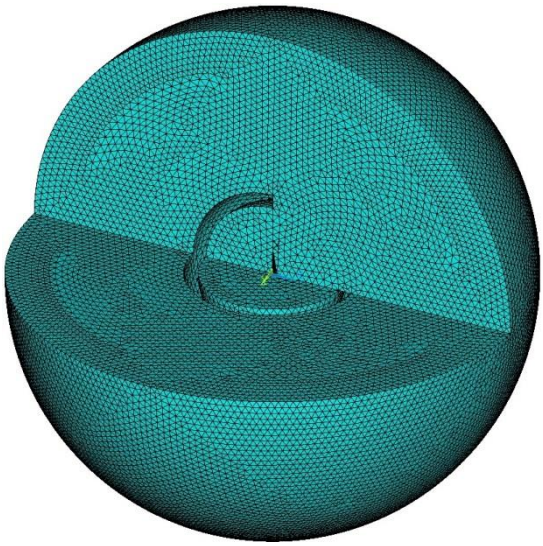

Figure 6.12 The mesh used in ANSYS for modelling the acoustic field of the 3D open-structure model

The sound speed c_{sound} and the peak flux magnitude F_{st} are considered as random variables following Gaussian distribution with $COV = 10\%$. For the purpose of demonstrating the effectiveness of the proposed method, the input parameters are considered as dimensionless [266] while $\hat{c}$ and the nominal value of F_{st} are both defined

as unitary such that $\mu_c = 1$ and $\mu_{F_{st}} = 1$. The uncertainties in c_{sound} and F_{st} results in the fluctuation in the pressure response, which can be demonstrated in Figure 6.13. The limit state of the acoustic system is defined as the dimensionless pressure $\frac{p_O(t)}{r_0 F_{st}}$ at point $O(0,0,0)$ shall not exceed the ultimate capacity which is assumed as $\overline{\hat{p}_O} = 8.5$ in this example. Thus, the limit state function for this example can be expressed as in Eq. (6.77).

$$g(c, F_{st}) = \overline{\hat{p}_O} - \max\left(\left|\frac{p_O(t)}{r_0 F_{st}}\right|\right) \tag{6.77}$$

Table 6.8 The probability of that the acoustic pressure at Point O exceeds $\overline{\hat{p}_O}$

Method	Probability of failure			
	$\hat{p}_f$ ($m_{train} = 20$)	ε_{p_f}	$\hat{p}_f$ ($m_{train} = 40$)	ε_{p_f}
X-SVR	0.1030	2.83%	0.1040	1.89%
ε-SVR	0.1140	7.55%	0.1000	5.66%
MCS	$\tilde{p}_f = 0.1060$			

The X-SVR is employed for approximating the relationship between the input variables and extremum of the dimensionless pressure at point O. The probability of failure will be computed by using the constructed X-SVR surrogate model, which requires significantly less computational efforts than using the original ANSYS model. Similar to Example 6.5.3, the results obtained by the X-SVR model are comparing with the results obtained using ε-SVR with Gaussian kernel and the conventional MCS. Due to the excessive complexity of the model, the MCS is conducted with 1000 samples ($m_{train} = 1000$), which takes approximately 1.34×10^6 seconds. The predicted probability of failure ($\hat{p}_f$) estimated by both X-SVR and ε-SVR and the 'exact' probability of failure

($\tilde{p}_f$) obtained by the MCS ($m_{train} = 1000$) are summarized in Table 6.8. For the given numbers of training samples, the $\hat{p}_f$ obtained by X-SVR has less relative difference with $\tilde{p}_f$ in comparison with the ε-SVR. Furthermore, the probability density functions (PDFs) and cumulative distribution functions (CDFs) predicted by both X-SVR and ε-SVR are shown in Figure 6.14 with the PDFs and CDFs obtained by the MCS. Similar as the predicted probability of failure, the PDFs and CDFs obtained by the proposed X-SVR have relatively less variation to the ones obtained by the MCS, which is more visible in the PDF plots in Figures 6.14(a) and 6.14(c). This study indicates that the proposed X-SVR model shows high efficiency and curacy for the reliability analysis of 3D acoustic application with unbounded domain.

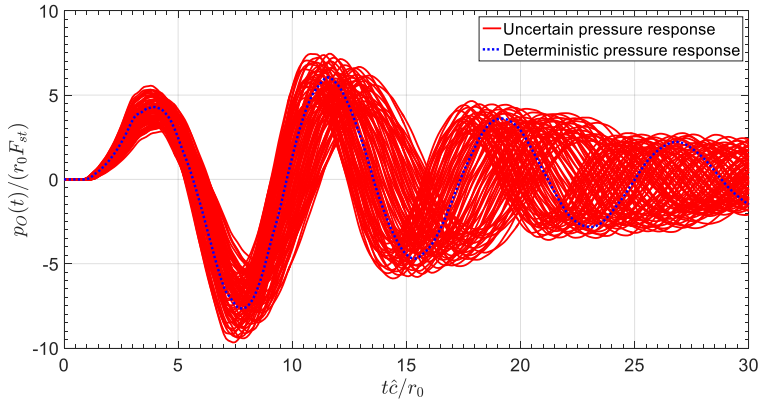

Figure 6.13 Uncertain acoustic pressure response (dimensionless) at point O of the 3D open-structure model

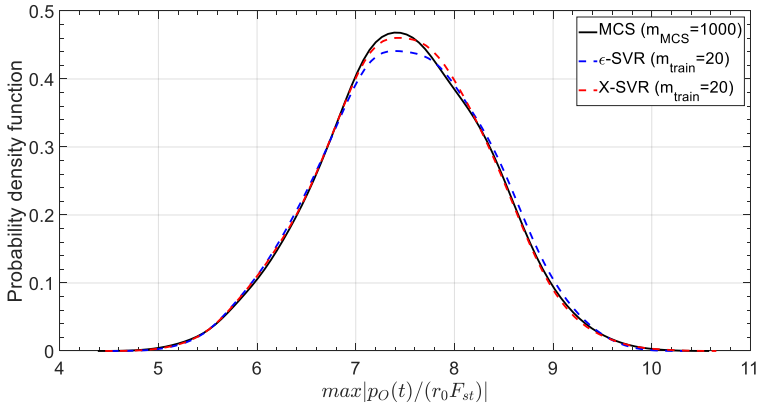

(a)

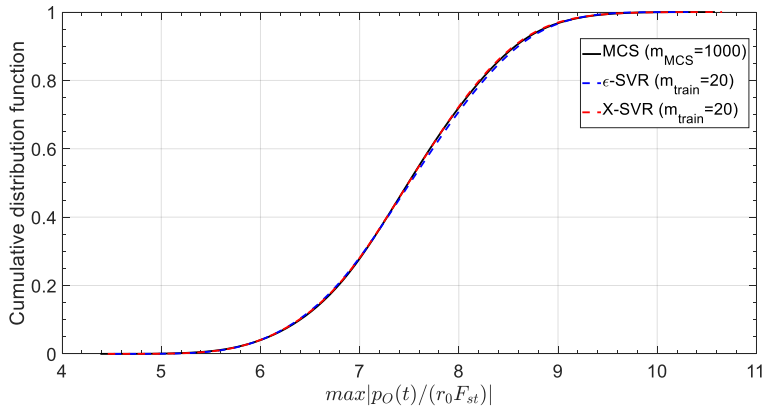
Cumulative distribution function
MCS (m_MCS=1000)
ϵ-SVR (m_train=20)
X-SVR (m_train=20)
max|p_O(t)/(r_0F_st)|

(b)

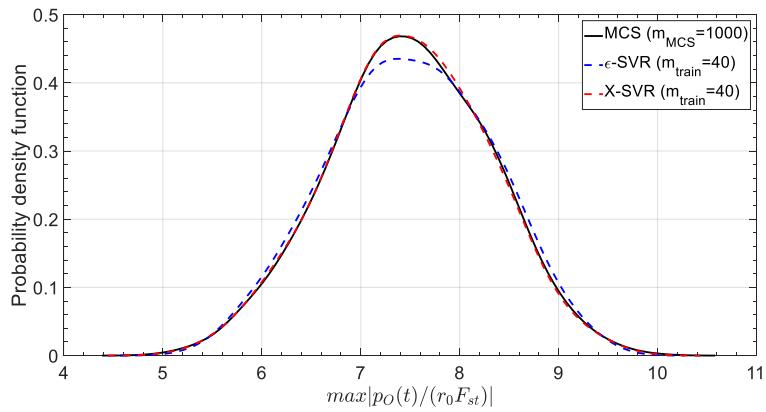
Probability density function
MCS (m_MCS=1000)
ϵ-SVR (m_train=40)
X-SVR (m_train=40)
max|p_O(t)/(r_0F_st)|

(c)

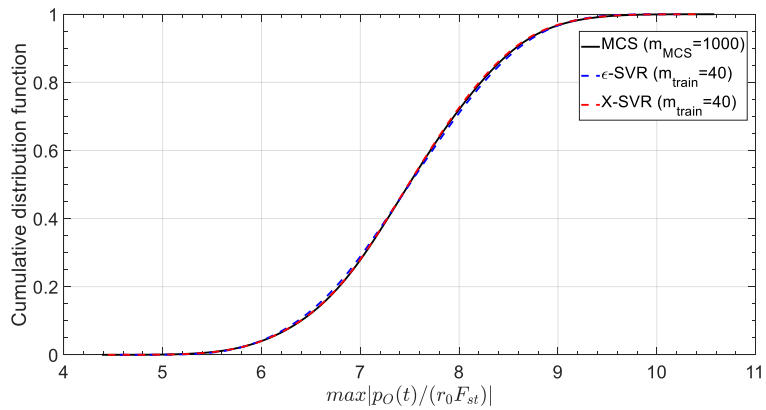
Cumulative distribution function
MCS (m_MCS=1000)
ϵ-SVR (m_train=40)
X-SVR (m_train=40)
max|p_O(t)/(r_0F_st)|

(d)

Figure 6.14 The estimated PDFs and CDFs of $\max(|p_O(t)/r_0F_{st}|)$ obtained by X-SVR and ε-SVR with different m_{train} and comparing with MCS

6.6 Conclusion

In this paper, a metamodel-based MCS strategy is proposed for the dynamic analysis with random input variables by evaluating the first-passage failure probability of systems. Within the proposed framework, the extended support vector regression (X-SVR) is introduced based on the theory of doubly regularized support vector machine. Since the proposed model can be formulated as convex quadratic programming problem, the global optimal solution for the given training dataset is promised. The suitable X-SVR parameters can be automatically selected by adopting the Bayesian optimization method. To enhance the capability of the introduced X-SVR approach, a new orthogonal polynomial kernel function satisfying the Mercer's condition is proposed by vectorizing the Gegenbauer polynomial. By implementing the proposed approach, an explicit function is constructed by training the X-SVR model to approximate the relationship between the input uncertain parameters and the extremum dynamic response of the system within a given time interval. Subsequently, the limit state function of the system can be efficiently evaluated such that the computational efficiency for obtaining the probability of failure using the MCS can be increased. The feasibility, efficiency and capability of the proposed method are systematically investigated by utilizing two benchmark examples and two engineering problems. By comparing the results obtained by proposed X-SVR model, the ε-SVR with Gaussian kernel and conventional MCS, the superior performance of the proposed method is evidently demonstrated.

Chapter 7 . Conclusion and future studies

7.1 Conclusion

The uncertainties exist in most engineering application and accurate modelling of the uncertain parameters is critical for structural analysis and design. Generally, probabilistic approaches and non-probabilistic approaches are implemented in the uncertainty analysis of structural systems. Hybrid probabilistic and interval analysis is attracting increasingly more attention from researchers due to the algorithm robustness in considering multiple types of uncertainties. The aim of this research is to propose a series of new uncertainty analysis methods which is capable to include both probabilistic and non-probabilistic uncertain parameters. The methods proposed in this thesis have the applicability to practical engineering application. The accuracy and computational efficiency are well preserved.

The Chapter 2 focuses on the uncertain static response analysis of linear structural systems with hybrid probabilistic and interval variables. In this chapter, an efficient hybrid uncertainty analysis approach, namely the *unified perturbation mathematical programming* (UPMP), is introduced as a combination of the conventional perturbation approach and mathematical programming. This method takes the advantage of the perturbation method which expresses the mean and standard deviation of the structural response as explicit functions of the interval parameters. By using an alternative finite element formulation, the upper and lower bounds of the statistical characteristics can be obtained by solving the nonlinear programming problems. Such solution algorithm excludes the interval arithmetic from the computation of upper and lower bounds, which leads to the elimination of the so-called dependency issue. The numerical examples indicate that the proposed UPMP approach has superiority in computational efficiency

comparing with the traditional sampling approach in estimating the mean and standard deviations of structural responses.

The non-deterministic analysis of natural frequencies of structures with spatially variant uncertainties is proposed in Chapter 4. Instead of using the conventional random field model, the spatial-variant uncertainties are described by adopting a recently introduced interval field concept to address the situation that only limited amount of data is available. Specifically, the Young's modulus and mass density of structures are considered as interval fields. For efficiently capturing the extreme bounds of natural frequencies, a novel computational scheme is proposed such that the upper and lower bounds can be achieved by two eigen-analyses after discretising the input interval fields. Within the proposed computational framework, it can be proved that the extremum of natural frequencies is resulted from the combination of bounds of Young's modulus and mass density. The effectiveness of the proposed computational scheme is validated by both academic-sized and practically motivated numerical examples.

Chapter 5 extends the uncertain natural frequency analysis of structures with interval fields demonstrated in Chapter 4 to the hybrid analysis. In this study, both random and interval fields are considered, which leads to the generalized spatially uncertain eigenvalue problem. Due to the simultaneous existence of random and interval uncertainties, the upper and lower bounds of structural natural frequencies are considered as random parameters rather than the conventional constant. To robustly estimate the statistical characteristics of the extremum of eigenvalues, a semi-sampling approach, namely the *extended unified stochastic sampling* (X-UISS) approach, is proposed. For each sampling point of random fields, an interval eigenvalue analysis based on Chapter 4 is implemented. Thus, for both upper and lower bounds of natural frequencies, a

collection of stochastic samples can be obtained. Subsequently, not only the sample mean and standard deviations can be computed, but also the probability profile could be constructed by using statistical inference analysis.

In Chapter 6, the dynamic reliability analysis of engineering systems is conducted based on the widely adopted first-passage failure theorem. Accordingly, the probability of failure is estimated by constructing the probability profile of the extremum of the response of engineering systems. To efficiently evaluate the probability of failure, a new machine learning based surrogate model, namely the *extended support vector machine* (X-SVR), is introduced and implemented such that only limited number of runs of the high-fidelity numerical models (i.e. FEM) are required. Additionally, a new orthogonal kernel function is proposed based on the Gegenbauer polynomial and integrated in the X-SVR, which enhances the capability of the surrogate model in approximating complex engineering problems. Both benchmark tests and engineering examples indicate that the effectiveness and efficiency of the proposed method for dynamic reliability analysis.

7.2 Future studies

The methods proposed in this research can be further developed in theory study and extended in engineering applications.

Firstly, the efficiency of the UISS method in computing the bounds of standard deviations of structural response is significantly affected by the number of random variables, which is resulted from the conventional perturbation method. With the increase in the number of random parameters, the complexity of the formulation of the NLP for the standard deviation will increase dramatically. In this context, solving the optimization problem becomes more difficult. Increasing the capability of the UISS method in considering more random uncertainties will be included in the future works. Then,

comparing with the random field theory which has been extensively studied in the past decades, the concept of interval field was just recently introduced and still under development. Despite of the agreement of that the non-probabilistic yet spatially variant uncertainties should receive attention, the necessity of interval correlation is currently under argument and there is still lack of well-established theory for the interval covariance. Thus, the correlation between the interval parameters at different location is excluded in this research and will be investigated in further research. Moreover, the study of the effect of hybrid random and interval field on other engineering applications including dynamic response and advanced materials will also be conducted in future studies.

Thirdly, further development of the X-SVR model will be included in the future works. As a non-intrusive method, the performance of surrogate models relies on the quality of training samples. Active learning approaches have been implemented in other metamodeling techniques including Kriging (Gaussian process), classic Support Vector Machine/ Regression and Polynomial Chaos expansion methods, which demonstrated the effectiveness of such method. Integrating the active learning and advanced sampling methods into the reliability analysis using X-SVR model will be the future research direction.

Reference

[1] B. Möller and M. Beer, “Engineering computation under uncertainty - Capabilities of non-traditional models,” *Comput. Struct.*, vol. 86, no. 10, pp. 1024–1041, 2008.

[2] D. Wu, W. Gao, G. Li, S. Tangaramvong, and F. Tin-Loi, “Robust assessment of collapse resistance of structures under uncertain loads based on Info-Gap model,” *Comput. Methods Appl. Mech. Eng.*, vol. 285, pp. 208–227, 2015.

[3] M. F. Pellissetti and G. I. Schueller, “The effects of uncertainties in structural analysis,” *Struct. Eng. Mech.*, vol. 25, no. 3, pp. 311–330, Feb. 2007.

[4] C. Jiang, X. Han, F. J. Guan, and Y. H. Li, “An uncertain structural optimization method based on nonlinear interval number programming and interval analysis method,” *Eng. Struct.*, vol. 29, no. 11, pp. 3168–3177, 2007.

[5] G. I. Schuëller and H. J. Pradlwarter, “Uncertainty analysis of complex structural systems,” *Int. J. Numer. Methods Eng.*, vol. 80, no. 6-7, pp. 881–913, Feb. 2009.

[6] W. Gao, D. Wu, C. Song, F. Tin-Loi, and X. Li, “Hybrid probabilistic interval analysis of bar structures with uncertainty using a mixed perturbation Monte-Carlo method,” *Finite Elem. Anal. Des.*, vol. 47, no. 7, pp. 643–652, 2011.

[7] D. Wu, W. Gao, C. Song, and S. Tangaramvong, “Probabilistic interval stability assessment for structures with mixed uncertainty,” *Struct. Saf.*, vol. 58, pp. 105–118, 2016.

[8] M. Kleiber and T. D. Hien, *The stochastic finite element method : basic perturbation technique and computer implementation*. Wiley, 1992.

[9] Y. Ben-Haim and I. Elishakoff, *Convex Models of Uncertainty in Applied*

Mechanics. Elsevier Science, 1990.

[10] B. Y. Ni, C. Jiang, and X. Han, "An improved multidimensional parallelepiped non-probabilistic model for structural uncertainty analysis," *Appl. Math. Model.*, vol. 40, no. 7–8, pp. 4727–4745, Apr. 2016.

[11] Y. C. Bai, X. Han, C. Jiang, and R. G. Bi, "A response-surface-based structural reliability analysis method by using non-probability convex model," *Appl. Math. Model.*, vol. 38, no. 15–16, pp. 3834–3847, Aug. 2014.

[12] Y. Luo, Z. Kang, Z. Luo, and A. Li, "Continuum topology optimization with non-probabilistic reliability constraints based on multi-ellipsoid convex model," *Struct. Multidiscip. Optim.*, vol. 39, no. 3, pp. 297–310, Sep. 2009.

[13] Z. Luo, L.-P. Chen, J. Yang, Y.-Q. Zhang, and K. Abdel-Malek, "Fuzzy tolerance multilevel approach for structural topology optimization," *Comput. Struct.*, vol. 84, no. 3–4, pp. 127–140, Jan. 2006.

[14] S. Dey, T. Mukhopadhyay, H. H. Khodaparast, and S. Adhikari, "Fuzzy uncertainty propagation in composites using Gram–Schmidt polynomial chaos expansion," *Appl. Math. Model.*, vol. 40, no. 7–8, pp. 4412–4428, Apr. 2016.

[15] W. Gao, C. Song, and F. Tin-Loi, "Probabilistic interval analysis for structures with uncertainty," *Struct. Saf.*, vol. 32, no. 3, pp. 191–199, 2010.

[16] B. Xia, D. Yu, and J. Liu, "Probabilistic Interval Perturbation Methods for Hybrid Uncertain Acoustic Field Prediction," *J. Vib. Acoust.*, vol. 135, no. 2, p. 021009, Feb. 2013.

[17] B. Xia, D. Yu, X. Han, and C. Jiang, "Unified response probability distribution analysis of two hybrid uncertain acoustic fields," *Comput. Methods Appl. Mech.*

Eng., vol. 276, pp. 20–34, Jul. 2014.

[18] B. Xia and D. Yu, "Change-of-variable interval stochastic perturbation method for hybrid uncertain structural-acoustic systems with random and interval variables," *J. Fluids Struct.*, vol. 50, pp. 461–478, Oct. 2014.

[19] B. Xia, D. Yu, and J. Liu, "Hybrid uncertain analysis for structural–acoustic problem with random and interval parameters," *J. Sound Vib.*, vol. 332, no. 11, pp. 2701–2720, May 2013.

[20] C. Jiang, X. Han, W. X. Li, J. Liu, and Z. Zhang, "A Hybrid Reliability Approach Based on Probability and Interval for Uncertain Structures," *J. Mech. Des.*, vol. 134, no. 3, p. 031001, 2012.

[21] Y. Luo, Z. Kang, and A. Li, "Structural reliability assessment based on probability and convex set mixed model," *Comput. Struct.*, vol. 87, no. 21–22, pp. 1408–1415, Nov. 2009.

[22] G. Stefanou and M. Papadrakakis, "Assessment of spectral representation and Karhunen–Loève expansion methods for the simulation of Gaussian stochastic fields," *Comput. Methods Appl. Mech. Eng.*, vol. 196, no. 21–24, pp. 2465–2477, Apr. 2007.

[23] M. Papadrakakis, V. Papadopoulos, and N. D. Lagaros, "Structural reliability analyis of elastic-plastic structures using neural networks and Monte Carlo simulation," *Comput. Methods Appl. Mech. Eng.*, vol. 136, no. 1–2, pp. 145–163, Sep. 1996.

[24] M. Papadrakakis and V. Papadopoulos, "Robust and efficient methods for stochastic finite element analysis using Monte Carlo simulation," *Comput.*

Methods Appl. Mech. Eng., vol. 134, no. 3–4, pp. 325–340, Aug. 1996.

[25] J. C. Helton, J. D. Johnson, W. L. Oberkampf, and C. B. Storlie, "A sampling-based computational strategy for the representation of epistemic uncertainty in model predictions with evidence theory," *Comput. Methods Appl. Mech. Eng.*, vol. 196, no. 37–40, pp. 3980–3998, Aug. 2007.

[26] E. Castillo, A. J. O'Connor, M. Nogal, and A. Calviño, "On the physical and probabilistic consistency of some engineering random models," *Struct. Saf.*, vol. 51, pp. 1–12, Nov. 2014.

[27] M. Kamiński and B. Lauke, "Uncertainty in effective elastic properties of particle filled polymers by the Monte-Carlo simulation," *Compos. Struct.*, vol. 123, pp. 374–382, May 2015.

[28] M. Shinozuka, "Monte Carlo solution of structural dynamics," *Comput. Struct.*, vol. 2, no. 5–6, pp. 855–874, 1972.

[29] H. C. Noh and T. Park, "Monte Carlo simulation-compatible stochastic field for application to expansion-based stochastic finite element method," *Comput. Struct.*, vol. 84, no. 31–32, pp. 2363–2372, 2006.

[30] G. Stefanou, D. Savvas, and M. Papadrakakis, "Stochastic finite element analysis of composite structures based on material microstructure," *Compos. Struct.*, vol. 132, pp. 384–392, 2015.

[31] J. E. Warner, M. Grigoriu, and W. Aquino, "Stochastic reduced order models for random vectors: Application to random eigenvalue problems," *Probabilistic Eng. Mech.*, vol. 31, pp. 1–11, 2013.

[32] R. G. Ghanem and P. D. Spanos, "Stochastic Finite Elements: A Spectral

Approach," in *Stochastic Finite Elements: A Spectral Approach*, New York, NY: Springer New York, 1991, pp. 1–13.

[33] E. Oja and J. Karhunen, "On stochastic approximation of the eigenvectors and eigenvalues of the expectation of a random matrix," *J. Math. Anal. Appl.*, vol. 106, no. 1, pp. 69–84, Feb. 1985.

[34] C. V. Verhoosel, M. A. Gutiérrez, and S. J. Hulshoff, "Iterative solution of the random eigenvalue problem with application to spectral stochastic finite element systems," *Int. J. Numer. Methods Eng.*, vol. 68, no. 4, pp. 401–424, Oct. 2006.

[35] R. Ghanem and D. Ghosh, "Efficient characterization of the random eigenvalue problem in a polynomial chaos decomposition," *Int. J. Numer. Methods Eng.*, vol. 72, no. 4, pp. 486–504, Oct. 2007.

[36] F. Tahmasebinia, G. Ranzi, and A. Zona, "Probabilistic three-dimensional finite element study on composite beams with steel trapezoidal decking," *J. Constr. Steel Res.*, vol. 80, pp. 394–411, Jan. 2013.

[37] A. Shaw, S. Sriramula, P. D. Gosling, and M. K. Chryssanthopoulos, "A critical reliability evaluation of fibre reinforced composite materials based on probabilistic micro and macro-mechanical analysis," *Compos. Part B Eng.*, vol. 41, no. 6, pp. 446–453, Sep. 2010.

[38] G. . Székely and G. . Schuëller, "Computational procedure for a fast calculation of eigenvectors and eigenvalues of structures with random properties," *Comput. Methods Appl. Mech. Eng.*, vol. 191, no. 8–10, pp. 799–816, Dec. 2001.

[39] H. Keitel and A. Dimmig-Osburg, "Uncertainty and sensitivity analysis of creep models for uncorrelated and correlated input parameters," *Eng. Struct.*, vol. 32, no.

11, pp. 3758–3767, Nov. 2010.

[40] M. de Angelis, “Advanced Line Sampling for efficient robust reliability analysis,” *Struct. Saf.*, vol. 52, pp. 170–182, Jan. 2015.

[41] I. Elishakoff and Y. Ren, *Finite element methods for structures with large stochastic variations*. Oxford University Press, 2003.

[42] M. M. Kamiński and P. Świta, “Generalized stochastic finite element method in elastic stability problems,” *Comput. Struct.*, vol. 89, no. 11–12, pp. 1241–1252, 2011.

[43] S. Nakagiri, T. H., and S. Tani, “Uncertain eigenvalue analysis of composite laminated plate by stochastic finite element method.,” *J. Manuf. Sci. Eng.*, vol. 109, no. 1, pp. 9–12, 1987.

[44] Ö. Çavdar, A. Bayraktar, and A. Çavdar, “Effects of random material and geometrical properties on structural safety of steel-concrete composite systems,” *Int. j. numer. method. biomed. eng.*, vol. 27, no. 9, p. n/a-n/a, Sep. 2010.

[45] X. G. Hua, Y. Q. Ni, Z. Q. Chen, and J. M. Ko, “An improved perturbation method for stochastic finite element model updating,” *Int. J. Numer. Methods Eng.*, vol. 73, no. 13, pp. 1845–1864, Mar. 2008.

[46] P. B. Nair and A. J. Keane, “An approximate solution scheme for the algebraic random eigenvalue problem,” *J. Sound Vib.*, vol. 260, no. 1, pp. 45–65, Feb. 2003.

[47] S. Adhikari and M. I. Friswell, “Random matrix eigenvalue problems in structural dynamics,” *Int. J. Numer. Methods Eng.*, vol. 69, no. 3, pp. 562–591, Jan. 2007.

[48] B. Xia, D. Yu, and J. Liu, “Transformed perturbation stochastic finite element method for static response analysis of stochastic structures,” *Finite Elem. Anal.*

Des., vol. 79, pp. 9–21, 2014.

[49] X. Y. Long, C. Jiang, X. Han, and W. Gao, "Stochastic response analysis of the scaled boundary finite element method and application to probabilistic fracture mechanics," *Comput. Struct.*, vol. 153, pp. 185–200, Jun. 2015.

[50] X. Y. Long, C. Jiang, C. Yang, X. Han, W. Gao, and J. Liu, "A stochastic scaled boundary finite element method," *Comput. Methods Appl. Mech. Eng.*, vol. 308, pp. 23–46, Aug. 2016.

[51] K. Sepahvand, S. Marburg, and H. J. Hardtke, "Stochastic free vibration of orthotropic plates using generalized polynomial chaos expansion," *J. Sound Vib.*, vol. 331, no. 1, pp. 167–179, 2012.

[52] M. Oberguggenberger, "Analysis and computation with hybrid random set stochastic models," *Struct. Saf.*, vol. 52, pp. 233–243, Jan. 2015.

[53] H. Meidani and R. Ghanem, "Spectral Power Iterations for the Random Eigenvalue Problem," *AIAA J.*, vol. 52, no. 5, pp. 912–925, May 2014.

[54] K. Li, W. Gao, D. Wu, C. Song, and T. Chen, "Spectral stochastic isogeometric analysis of linear elasticity," *Comput. Methods Appl. Mech. Eng.*, vol. 332, pp. 157–190, Apr. 2018.

[55] M. Di Paola, "Probabilistic analysis of truss structures with uncertain parameters (virtual distortion method approach)," *Probabilistic Eng. Mech.*, vol. 19, no. 4, pp. 321–329, Oct. 2004.

[56] S. E. Pryse and S. Adhikari, "Stochastic finite element response analysis using random eigenfunction expansion," *Comput. Struct.*, vol. 192, pp. 1–15, Nov. 2017.

[57] G. Su, L. Peng, and L. Hu, "A Gaussian process-based dynamic surrogate model

for complex engineering structural reliability analysis," *Struct. Saf.*, vol. 68, pp. 97–109, Sep. 2017.

[58] N. Impollonia and A. Sofi, "A response surface approach for the static analysis of stochastic structures with geometrical nonlinearities," *Comput. Methods Appl. Mech. Eng.*, vol. 192, no. 37–38, pp. 4109–4129, 2003.

[59] C. G. Bucher and U. Bourgund, "A fast and efficient response surface approach for structural reliability problems," *Struct. Saf.*, vol. 7, no. 1, pp. 57–66, Jan. 1990.

[60] L. Faravelli, "Response-Surface Approach for Reliability Analysis," *J. Eng. Mech.*, vol. 115, no. 12, pp. 2763–2781, Dec. 1989.

[61] X. Zhai, C.-W. Fei, Y.-S. Choy, and J.-J. Wang, "A stochastic model updating strategy-based improved response surface model and advanced Monte Carlo simulation," *Mech. Syst. Signal Process.*, vol. 82, pp. 323–338, Jan. 2017.

[62] Y. Jiang *et al.*, "Multiple response surfaces method with advanced classification of samples for structural failure function fitting," *Struct. Saf.*, vol. 64, pp. 87–97, Jan. 2017.

[63] B. Sudret, "Global sensitivity analysis using polynomial chaos expansions," *Reliab. Eng. Syst. Saf.*, vol. 93, no. 7, pp. 964–979, Jul. 2008.

[64] G. Blatman and B. Sudret, "An adaptive algorithm to build up sparse polynomial chaos expansions for stochastic finite element analysis," *Probabilistic Eng. Mech.*, vol. 25, no. 2, pp. 183–197, 2010.

[65] G. Blatman and B. Sudret, "Adaptive sparse polynomial chaos expansion based on least angle regression," *J. Comput. Phys.*, vol. 230, no. 6, pp. 2345–2367, 2011.

[66] D. Xiu and G. Em Karniadakis, "Modeling uncertainty in steady state diffusion

problems via generalized polynomial chaos," *Comput. Methods Appl. Mech. Eng.*, vol. 191, no. 43, pp. 4927–4948, Sep. 2002.

[67] S. Oladyshkin and W. Nowak, "Data-driven uncertainty quantification using the arbitrary polynomial chaos expansion," *Reliab. Eng. Syst. Saf.*, vol. 106, pp. 179–190, Oct. 2012.

[68] S. Yin, D. Yu, Z. Luo, and B. Xia, "Unified polynomial expansion for interval and random response analysis of uncertain structure–acoustic system with arbitrary probability distribution," *Comput. Methods Appl. Mech. Eng.*, vol. 336, pp. 260–285, Jul. 2018.

[69] J. Wu, Z. Luo, Y. Zhang, N. Zhang, and L. Chen, "Interval uncertain method for multibody mechanical systems using Chebyshev inclusion functions," *Int. J. Numer. Methods Eng.*, vol. 95, no. 7, pp. 608–630, Aug. 2013.

[70] J. Wu, Z. Luo, N. Zhang, and Y. Zhang, "A new interval uncertain optimization method for structures using Chebyshev surrogate models," *Comput. Struct.*, vol. 146, pp. 185–196, 2015.

[71] V. Dubourg, B. Sudret, and J.-M. Bourinet, "Reliability-based design optimization using kriging surrogates and subset simulation," *Struct. Multidiscip. Optim.*, vol. 44, no. 5, pp. 673–690, Nov. 2011.

[72] Y. Shi, Z. Lu, S. Chen, and L. Xu, "A reliability analysis method based on analytical expressions of the first four moments of the surrogate model of the performance function," *Mech. Syst. Signal Process.*, vol. 111, pp. 47–67, Oct. 2018.

[73] G. Xue, H. Dai, H. Zhang, and W. Wang, "A new unbiased metamodel method for efficient reliability analysis," *Struct. Saf.*, vol. 67, pp. 1–10, Jul. 2017.

[74] B. Echard, N. Gayton, and M. Lemaire, “AK-MCS: An active learning reliability method combining Kriging and Monte Carlo Simulation,” *Struct. Saf.*, vol. 33, no. 2, pp. 145–154, Mar. 2011.

[75] H. Zhao, Z. Yue, Y. Liu, Z. Gao, and Y. Zhang, “An efficient reliability method combining adaptive importance sampling and Kriging metamodel,” *Appl. Math. Model.*, vol. 39, no. 7, pp. 1853–1866, Apr. 2015.

[76] Z. Wang and P. Wang, “A Nested Extreme Response Surface Approach for Time-Dependent Reliability-Based Design Optimization,” *J. Mech. Des.*, vol. 134, no. 12, p. 121007, Nov. 2012.

[77] C. Lu, Y. W. Feng, R. P. Liem, and C. W. Fei, “Improved Kriging with extremum response surface method for structural dynamic reliability and sensitivity analyses,” *Aerosp. Sci. Technol.*, vol. 76, pp. 164–175, 2018.

[78] Z. Wang and P. Wang, “A double-loop adaptive sampling approach for sensitivity-free dynamic reliability analysis,” *Reliab. Eng. Syst. Saf.*, vol. 142, pp. 346–356, 2015.

[79] J. E. Hurtado and D. A. Alvarez, “Neural-network-based reliability analysis: a comparative study,” *Comput. Methods Appl. Mech. Eng.*, vol. 191, no. 1–2, pp. 113–132, Nov. 2001.

[80] H. Dai, B. Zhang, and W. Wang, “A multiwavelet support vector regression method for efficient reliability assessment,” *Reliab. Eng. Syst. Saf.*, vol. 136, pp. 132–139, Apr. 2015.

[81] H. Dai, G. Xue, and W. Wang, “An Adaptive Wavelet Frame Neural Network Method for Efficient Reliability Analysis,” *Comput. Civ. Infrastruct. Eng.*, vol. 29,

no. 10, pp. 801–814, Nov. 2014.

[82] L.-K. Song, J. Wen, C.-W. Fei, and G.-C. Bai, “Distributed collaborative probabilistic design of multi-failure structure with fluid-structure interaction using fuzzy neural network of regression,” *Mech. Syst. Signal Process.*, vol. 104, pp. 72–86, May 2018.

[83] J. Zheng, H. Pan, and J. Cheng, “Rolling bearing fault detection and diagnosis based on composite multiscale fuzzy entropy and ensemble support vector machines,” *Mech. Syst. Signal Process.*, vol. 85, pp. 746–759, Feb. 2017.

[84] C.-W. Fei and G.-C. Bai, “Distributed collaborative probabilistic design for turbine blade-tip radial running clearance using support vector machine of regression,” *Mech. Syst. Signal Process.*, vol. 49, no. 1–2, pp. 196–208, Dec. 2014.

[85] G. Muscolino, A. Sofi, and M. Zingales, “One-dimensional heterogeneous solids with uncertain elastic modulus in presence of long-range interactions: Interval versus stochastic analysis,” *Comput. Struct.*, vol. 122, pp. 217–229, 2013.

[86] L. A. Zadeh, “Fuzzy sets,” *Inf. Control*, vol. 8, no. 3, pp. 338–353, Jun. 1965.

[87] L. Farkas, D. Moens, D. Vandepitte, and W. Desmet, “Fuzzy finite element analysis based on reanalysis technique,” *Struct. Saf.*, vol. 32, no. 6, pp. 442–448, Nov. 2010.

[88] M. Hanss, *Applied fuzzy arithmetic : an introduction with engineering applications*. Springer-Verlag, 2005.

[89] D. Wu, W. Gao, C. Wang, S. Tangaramvong, and F. Tin-Loi, “Robust fuzzy structural safety assessment using mathematical programming approach,” *Fuzzy Sets Syst.*, vol. 293, pp. 30–49, Jun. 2016.

[90] G. Li, Z. Lu, and J. Xu, “A fuzzy reliability approach for structures based on the probability perspective,” *Struct. Saf.*, vol. 54, pp. 10–18, May 2015.

[91] S. Adhikari and H. H. Khodaparast, “A spectral approach for fuzzy uncertainty propagation in finite element analysis,” *Fuzzy Sets Syst.*, vol. 243, pp. 1–24, May 2014.

[92] Y. Ben-Haim, “A non-probabilistic concept of reliability,” *Struct. Saf.*, vol. 14, no. 4, pp. 227–245, 1994.

[93] C. Jiang, X. Han, G. Y. Lu, J. Liu, Z. Zhang, and Y. C. Bai, “Correlation analysis of non-probabilistic convex model and corresponding structural reliability technique,” *Comput. Methods Appl. Mech. Eng.*, vol. 200, no. 33–36, pp. 2528–2546, Aug. 2011.

[94] C. Jiang, Q. F. Zhang, X. Han, J. Liu, and D. A. Hu, “Multidimensional parallelepiped model-a new type of non-probabilistic convex model for structural uncertainty analysis,” *Int. J. Numer. Methods Eng.*, vol. 103, no. 1, pp. 31–59, Jul. 2015.

[95] R. E. Moore, R. B. Kearfott, and M. J. Cloud, *Introduction to interval analysis*. Society for Industrial and Applied Mathematics, 2009.

[96] H. Zhang, H. Dai, M. Beer, and W. Wang, “Structural reliability analysis on the basis of small samples: An interval quasi-Monte Carlo method,” *Mech. Syst. Signal Process.*, vol. 37, no. 1–2, pp. 137–151, 2013.

[97] S. H. Chen, H. D. Lian, and X. W. Yang, “Interval eigenvalue analysis for structures with interval parameters,” *Finite Elem. Anal. Des.*, vol. 39, no. 5–6, pp. 419–431, Mar. 2003.

[98] Z. Qiu and X. Wang, “Solution theorems for the standard eigenvalue problem of structures with uncertain-but-bounded parameters,” *J. Sound Vib.*, vol. 282, no. 1–2, pp. 381–399, Apr. 2005.

[99] W. Gao, “Interval natural frequency and mode shape analysis for truss structures with interval parameters,” *Finite Elem. Anal. Des.*, vol. 42, no. 6, pp. 471–477, Mar. 2006.

[100] H. Leng, Z. He, and Q. Yuan, “Computing bounds to real eigenvalues of real-interval matrices,” *Int. J. Numer. Methods Eng.*, vol. 74, no. 4, pp. 523–530, Apr. 2008.

[101] S. Chen, H. Lian, and X. Yang, “Interval static displacement analysis for structures with interval parameters,” *Int. J. Numer. Methods Eng.*, vol. 53, no. 2, pp. 393–407, Jan. 2002.

[102] R. L. Muhanna, H. Zhang, and R. L. Mullen, “Combined Axial and Bending Stiffness in Interval Finite-Element Methods,” *J. Struct. Eng.*, vol. 133, no. 12, pp. 1700–1709, 2007.

[103] R. L. Muhanna, R. L. Mullen, and H. Zhang, “Penalty-Based Solution for the Interval Finite-Element Methods,” *J. Eng. Mech.*, vol. 131, no. 10, pp. 1102–1111, Oct. 2005.

[104] X. Guo, W. Bai, and W. Zhang, “Extreme structural response analysis of truss structures under material uncertainty via linear mixed 0-1 programming,” *Int. J. Numer. Methods Eng.*, vol. 76, no. 3, pp. 253–277, Oct. 2008.

[105] D. Degrauwe, G. Lombaert, and G. De Roeck, “Improving interval analysis in finite element calculations by means of affine arithmetic,” *Comput. Struct.*, vol. 88,

no. 3–4, pp. 247–254, Feb. 2010.

[106] G. Muscolino, R. Santoro, and A. Sofi, “Explicit frequency response functions of discretized structures with uncertain parameters,” *Comput. Struct.*, vol. 133, pp. 64–78, 2014.

[107] R. Santoro, G. Muscolino, and I. Elishakoff, “Optimization and anti-optimization solution of combined parameterized and improved interval analyses for structures with uncertainties,” *Comput. Struct.*, vol. 149, pp. 31–42, Mar. 2015.

[108] S. Tangaramvong, D. Wu, W. Gao, and F. Tin-Loi, “Response Bounds of Elastic Structures in the Presence of Interval Uncertainties,” *J. Struct. Eng.*, vol. 141, no. 1, p. 4015046, 2015.

[109] D. Wu, W. Gao, S. Tangaramvong, and F. Tin-Loi, “Robust stability analysis of structures with uncertain parameters using mathematical programming approach,” *Int. J. Numer. Methods Eng.*, vol. 100, no. 10, pp. 720–745, Dec. 2014.

[110] C. Yang, S. Tangaramvong, W. Gao, and F. Tin-Loi, “Interval elastoplastic analysis of structures,” *Comput. Struct.*, vol. 151, pp. 1–10, Apr. 2015.

[111] A. Sofi and E. Romeo, “A novel Interval Finite Element Method based on the improved interval analysis,” *Comput. Methods Appl. Mech. Eng.*, vol. 311, pp. 671–697, Nov. 2016.

[112] M. Modares, R. L. Mullen, and R. L. Muhanna, “Natural Frequencies of a Structure with Bounded Uncertainty,” *J. Eng. Mech.*, vol. 132, no. 12, pp. 1363–1371, Dec. 2006.

[113] A. Sofi, G. Muscolino, and I. Elishakoff, “Natural frequencies of structures with interval parameters,” *J. Sound Vib.*, vol. 347, pp. 79–95, 2015.

[114] Q. Li, Z. Qiu, and X. Zhang, “Eigenvalue analysis of structures with interval parameters using the second-order Taylor series expansion and the DCA for QB,” *Appl. Math. Model.*, vol. 49, pp. 680–690, Sep. 2017.

[115] W. Verhaeghe, W. Desmet, D. Vandepitte, and D. Moens, “Interval fields to represent uncertainty on the output side of a static FE analysis,” *Comput. Methods Appl. Mech. Eng.*, vol. 260, pp. 50–62, 2013.

[116] A. Sofi and G. Muscolino, “Static analysis of Euler-Bernoulli beams with interval Young’s modulus,” *Comput. Struct.*, vol. 156, pp. 72–82, 2015.

[117] A. Sofi, “Structural response variability under spatially dependent uncertainty: Stochastic versus interval model,” *Probabilistic Eng. Mech.*, vol. 42, pp. 78–86, Oct. 2015.

[118] C. Jiang, B. Y. Ni, X. Han, and Y. R. Tao, “Non-probabilistic convex model process: A new method of time-variant uncertainty analysis and its application to structural dynamic reliability problems,” *Comput. Methods Appl. Mech. Eng.*, vol. 268, pp. 656–676, 2014.

[119] C. Jiang, B. Y. Ni, N. Y. Liu, X. Han, and J. Liu, “Interval process model and non-random vibration analysis,” *J. Sound Vib.*, vol. 373, pp. 104–131, 2016.

[120] D. Wu and W. Gao, “Uncertain static plane stress analysis with interval fields,” *Int. J. Numer. Methods Eng.*, vol. 110, no. 13, pp. 1272–1300, Jun. 2017.

[121] E. Vanmarcke and M. Grigoriu, “Stochastic Finite Element Analysis of Simple Beams,” *J. Eng. Mech.*, vol. 109, no. 5, pp. 1203–1214, Oct. 1983.

[122] S. Chakraborty and P. C. Sam, “Probabilistic safety analysis of structures under hybrid uncertainty,” *Int. J. Numer. Methods Eng.*, vol. 70, no. 4, pp. 405–422, Apr.

2007.

[123] C. Wang, W. Gao, C. Song, and N. Zhang, “Stochastic interval analysis of natural frequency and mode shape of structures with uncertainties,” *J. Sound Vib.*, vol. 333, no. 9, pp. 2483–2503, 2014.

[124] B. Xia and D. Yu, “An interval random perturbation method for structural-acoustic system with hybrid uncertain parameters,” *Int. J. Numer. Methods Eng.*, vol. 97, no. 3, pp. 181–206, Jan. 2014.

[125] D. Wu, W. Gao, F. Tin-Loi, and Y. L. Pi, “Probabilistic interval limit analysis for structures with hybrid uncertainty,” *Eng. Struct.*, vol. 114, pp. 195–208, 2016.

[126] B. Wu, W. Gao, D. Wu, and C. Song, “Probabilistic interval geometrically nonlinear analysis for structures,” *Struct. Saf.*, vol. 65, pp. 100–112, Mar. 2017.

[127] G. Muscolino and A. Sofi, “Stochastic analysis of structures with uncertain-but-bounded parameters via improved interval analysis,” *Probabilistic Eng. Mech.*, vol. 28, pp. 152–163, 2012.

[128] G. Muscolino and A. Sofi, “Bounds for the stationary stochastic response of truss structures with uncertain-but-bounded parameters,” *Mech. Syst. Signal Process.*, vol. 37, no. 1–2, pp. 163–181, 2013.

[129] G. Muscolino, R. Santoro, and A. Sofi, “Reliability analysis of structures with interval uncertainties under stationary stochastic excitations,” *Comput. Methods Appl. Mech. Eng.*, vol. 300, pp. 47–69, 2016.

[130] D. M. Do, W. Gao, C. Song, and S. Tangaramvong, “Dynamic analysis and reliability assessment of structures with uncertain-but-bounded parameters under stochastic process excitations,” *Reliab. Eng. Syst. Saf.*, vol. 132, pp. 46–59, 2014.

[131] D. M. Do, W. Gao, C. Song, and M. Beer, “Interval spectral stochastic finite element analysis of structures with aggregation of random field and bounded parameters,” *Int. J. Numer. Methods Eng.*, vol. 108, no. 10, pp. 1198–1229, Dec. 2016.

[132] D. M. Do, W. Gao, and C. Song, “Stochastic finite element analysis of structures in the presence of multiple imprecise random field parameters,” *Comput. Methods Appl. Mech. Eng.*, vol. 300, pp. 657–688, Mar. 2016.

[133] D. Wu and W. Gao, “Hybrid uncertain static analysis with random and interval fields,” *Comput. Methods Appl. Mech. Eng.*, vol. 315, pp. 222–246, Mar. 2017.

[134] I. Babuška and M. Motamed, “A fuzzy-stochastic multiscale model for fiber composites: A one-dimensional study,” *Comput. Methods Appl. Mech. Eng.*, vol. 302, pp. 109–130, Apr. 2016.

[135] X. Du, “Unified Uncertainty Analysis by the First Order Reliability Method,” *J. Mech. Des.*, vol. 130, no. 9, p. 091401, Sep. 2008.

[136] J. Guo and X. Du, “Reliability sensitivity analysis with random and interval variables,” *Int. J. Numer. Methods Eng.*, vol. 78, no. 13, pp. 1585–1617, Jun. 2009.

[137] C. Jiang, W. X. Li, X. Han, L. X. Liu, and P. H. Le, “Structural reliability analysis based on random distributions with interval parameters,” *Comput. Struct.*, vol. 89, no. 23–24, pp. 2292–2302, 2011.

[138] M. S. Chowdhury, C. Song, W. Gao, and C. Wang, “Reliability analysis of homogeneous and bimaterial cracked structures by the scaled boundary finite element method and a hybrid random-interval model,” *Struct. Saf.*, vol. 59, pp. 53–66, Mar. 2016.

[139] J. Wu, Z. Luo, N. Zhang, and Y. Zhang, “A new uncertain analysis method and its application in vehicle dynamics,” *Mech. Syst. Signal Process.*, vol. 50–51, pp. 659–675, 2015.

[140] X. Feng, J. Wu, and Y. Zhang, “Time response of structure with interval and random parameters using a new hybrid uncertain analysis method,” *Appl. Math. Model.*, vol. 64, pp. 426–452, Dec. 2018.

[141] S. Yin, D. Yu, H. Yin, and B. Xia, “Interval and random analysis for structure-acoustic systems with large uncertain-but-bounded parameters,” *Comput. Methods Appl. Mech. Eng.*, vol. 305, pp. 910–935, 2016.

[142] A. S. Balu and B. N. Rao, “Multicut-High Dimensional Model Representation for Structural Reliability Bounds Estimation Under Mixed Uncertainties,” *Comput. Civ. Infrastruct. Eng.*, vol. 27, no. 6, pp. 419–438, Jul. 2012.

[143] X. Yang, Y. Liu, Y. Zhang, and Z. Yue, “Probability and convex set hybrid reliability analysis based on active learning Kriging model,” *Appl. Math. Model.*, vol. 39, no. 14, pp. 3954–3971, Jul. 2015.

[144] M. M. (Marcin M. . Kamiński, *The stochastic perturbation method for computational mechanics*. Chichester, UK: Wiley, 2013.

[145] J. Jakeman, M. Eldred, and D. Xiu, “Numerical approach for quantification of epistemic uncertainty,” *J. Comput. Phys.*, vol. 229, no. 12, pp. 4648–4663, Jun. 2010.

[146] M. Kamiński, “Generalized perturbation-based stochastic finite element method in elastostatics,” *Comput. Struct.*, vol. 85, no. 10, pp. 586–594, May 2007.

[147] Y. Xu, Y. Qian, and G. Song, “Stochastic finite element method for free vibration

characteristics of random FGM beams," *Appl. Math. Model.*, vol. 40, no. 23–24, pp. 10238–10253, Dec. 2016.

[148] G. Falsone and N. Impollonia, "A new approach for the stochastic analysis of finite element modelled structures with uncertain parameters," *Comput. Methods Appl. Mech. Eng.*, vol. 191, no. 44, pp. 5067–5085, 2002.

[149] R. Chowdhury and S. Adhikari, "High dimensional model representation for stochastic finite element analysis," *Appl. Math. Model.*, vol. 34, no. 12, pp. 3917–3932, Dec. 2010.

[150] X. Du, "Reliability-based design optimization with dependent interval variables," *Int. J. Numer. Methods Eng.*, vol. 91, no. 2, pp. 218–228, Jul. 2012.

[151] J. Wu, Y. Zhang, L. Chen, and Z. Luo, "A Chebyshev interval method for nonlinear dynamic systems under uncertainty," *Appl. Math. Model.*, vol. 37, no. 6, pp. 4578–4591, 2013.

[152] J. Wu, Z. Luo, Y. Zhang, and N. Zhang, "An interval uncertain optimization method for vehicle suspensions using Chebyshev metamodels," *Appl. Math. Model.*, vol. 38, no. 15–16, pp. 3706–3723, Aug. 2014.

[153] G. Li, Z. Lu, L. Li, and B. Ren, "Aleatory and epistemic uncertainties analysis based on non-probabilistic reliability and its kriging solution," *Appl. Math. Model.*, vol. 40, no. 9–10, pp. 5703–5716, May 2016.

[154] M. Beer, S. Ferson, and V. Kreinovich, "Imprecise probabilities in engineering analyses," *Mech. Syst. Signal Process.*, vol. 37, no. 1–2, pp. 4–29, 2013.

[155] C. R. Johnson, *Matrix theory and applications*. American Mathematical Society, 1990.

[156] A. S. Drud, “CONOPT—A Large-Scale GRG Code,” *ORSA J. Comput.*, vol. 6, no. 2, pp. 207–216, May 1994.

[157] A. Brooke, D. Kendrick, A. Meeraus, R. Raman, and R. Rosenthal, *GAMS a User’s Guide*. Washington DC: GAMS Development Corporation, 2007.

[158] The MathWorks, *MATLAB and Statistics Toolbox Release 2015b*. Natick, Massachusetts, United States: The MathWorks, Inc., 2015.

[159] L. Kocis and W. J. Whiten, “Computational investigations of low-discrepancy sequences,” *ACM Trans. Math. Softw.*, vol. 23, no. 2, pp. 266–294, Jun. 1997.

[160] OneSteel, *Hot-rolled structural & welded sections*, 5th ed. OneSteel Market Mills: Australia, 2010.

[161] H. Zhang, “Interval importance sampling method for finite element-based structural reliability assessment under parameter uncertainties,” *Struct. Saf.*, vol. 38, pp. 1–10, Sep. 2012.

[162] R. J. Pimenta, G. Queiroz, and S. M. C. Diniz, “Reliability-based design recommendations for sinusoidal-web beams subjected to lateral-torsional buckling,” *Eng. Struct.*, vol. 84, pp. 195–206, Feb. 2015.

[163] K. A. Crookston, T. Mark Young, D. Harper, and F. M. Guess, “Statistical reliability analyses of two wood plastic composite extrusion processes,” *Reliab. Eng. Syst. Saf.*, vol. 96, no. 1, pp. 172–177, Jan. 2011.

[164] S. Sriramula and M. K. Chryssanthopoulos, “Quantification of uncertainty modelling in stochastic analysis of FRP composites,” *Compos. Part A Appl. Sci. Manuf.*, vol. 40, no. 11, pp. 1673–1684, Nov. 2009.

[165] T. P. Philippidis, D. J. Lekou, and D. G. Aggelis, “Mechanical property

distribution of CFRP filament wound composites," *Compos. Struct.*, vol. 45, no. 1, pp. 41–50, May 1999.

[166] R. B. D'Agostino and M. A. Stephens, *Goodness-of-fit techniques*. M. Dekker, 1986.

[167] M. Beer, Y. Zhang, S. T. Quek, and K. K. Phoon, "Reliability analysis with scarce information: Comparing alternative approaches in a geotechnical engineering context," *Struct. Saf.*, vol. 41, pp. 1–10, 2013.

[168] D. Wu, W. Gao, J. Feng, and K. Luo, "Structural behaviour evolution of composite steel-concrete curved structure with uncertain creep and shrinkage effects," *Compos. Part B Eng.*, vol. 86, pp. 261–272, Feb. 2016.

[169] R. A. Ibrahim, "Structural Dynamics with Parameter Uncertainties," *Appl. Mech. Rev.*, vol. 40, no. 3, p. 309, Mar. 1987.

[170] B. N. Singh, A. K. S. Bisht, M. K. Pandit, and K. K. Shukla, "Nonlinear free vibration analysis of composite plates with material uncertainties: A Monte Carlo simulation approach," *J. Sound Vib.*, vol. 324, no. 1–2, pp. 126–138, Jul. 2009.

[171] W. Gao, "Natural frequency and mode shape analysis of structures with uncertainty," *Mech. Syst. Signal Process.*, vol. 21, no. 1, pp. 24–39, 2007.

[172] M. M. Kamiński and J. Szafran, "Random Eigenvibrations of Elastic Structures by the Response Function Method and the Generalized Stochastic Perturbation Technique," *Arch. Civ. Mech. Eng.*, vol. 9, no. 4, pp. 5–32, Jan. 2009.

[173] D. H. Oh and L. Librescu, "Free vibration and reliability of composite cantilevers featuring uncertain properties," *Reliab. Eng. Syst. Saf.*, vol. 56, no. 3, pp. 265–272, 1997.

[174] B. Rong, X. Rui, and L. Tao, “Perturbation Finite Element Transfer Matrix Method for Random Eigenvalue Problems of Uncertain Structures,” *J. Appl. Mech.*, vol. 79, no. 2, p. 021005, Mar. 2012.

[175] A. Shaker, W. G. Abdelrahman, M. Tawfik, and E. Sadek, “Stochastic finite element analysis of the free vibration of laminated composite plates,” *Comput. Mech.*, vol. 41, no. 4, pp. 493–501, Dec. 2007.

[176] C. Soize, “Stochastic modeling of uncertainties in computational structural dynamics - Recent theoretical advances,” *J. Sound Vib.*, vol. 332, no. 10, pp. 2379–2395, 2013.

[177] C. Jiang, Z. Zhang, X. Han, and J. Liu, “A novel evidence-theory-based reliability analysis method for structures with epistemic uncertainty,” *Comput. Struct.*, vol. 129, pp. 1–12, 2013.

[178] L. Chen and S. S. Rao, “Fuzzy finite-element approach for the vibration analysis of imprecisely-defined systems,” *Finite Elem. Anal. Des.*, vol. 27, no. 1, pp. 69–83, 1997.

[179] J. Ma, J. Chen, W. Gao, and T. Zhai, “Non-stationary stochastic vibration analysis of fuzzy truss system,” *Mech. Syst. Signal Process.*, vol. 20, no. 8, pp. 1853–1866, Nov. 2006.

[180] C. Jiang, R. G. Bi, G. Y. Lu, and X. Han, “Structural reliability analysis using non-probabilistic convex model,” *Comput. Methods Appl. Mech. Eng.*, vol. 254, pp. 83–98, 2013.

[181] R. E. Williamson, R. H. Crowell, and H. F. Trotter, *Calculus of vector functions*. Prentice-Hall, 1972.

[182] M. Stein, “Large Sample Properties of Simulations Using Latin Hypercube Sampling,” *Technometrics*, vol. 29, no. 2, pp. 143–151, May 1987.

[183] ANSYS, *ANSYS Mechanical APDL Structural Analysis Guide*, Release 15. ANSYS, 2013.

[184] D. Engwirda, “Locally optimal Delaunay-refinement and optimisation-based mesh generation,” University of Sydney, 2015.

[185] W. K. Liu, T. Belytschko, and a Man, “Random Field Finite Elements,” *Int. J. Numer. Methods Eng.*, vol. 23, no. February, pp. 1831–1845, 1986.

[186] S. Adhikari and a. S. Phani, “Random Eigenvalue Problems in Structural Dynamics: Experimental Investigations,” *AIAA J.*, vol. 48, no. 6, pp. 1085–1097, 2010.

[187] C. Jiang, X. Y. Long, X. Han, Y. R. Tao, and J. Liu, “Probability-interval hybrid reliability analysis for cracked structures existing epistemic uncertainty,” *Eng. Fract. Mech.*, vol. 112–113, pp. 148–164, 2013.

[188] B. Van den Nieuwenhof and J. P. Coyette, “Modal approaches for the stochastic finite element analysis of structures with material and geometric uncertainties,” *Comput. Methods Appl. Mech. Eng.*, vol. 192, no. 33–34, pp. 3705–3729, 2003.

[189] M. Grigoriu, “On the spectral representation method in simulation,” *Probabilistic Eng. Mech.*, vol. 8, no. 2, pp. 75–90, Jan. 1993.

[190] B. Sudret and A. Der Kiureghian, “Stochastic Finite Element Methods and Reliability A State-of-the-Art Report,” Berkeley, 2000.

[191] T. J. R. Hughes, *The finite element method : linear static and dynamic finite element analysis*. Dover Publications, 2000.

[192] G. Stefanou, “The stochastic finite element method: Past, present and future,” *Comput. Methods Appl. Mech. Eng.*, vol. 198, no. 9–12, pp. 1031–1051, 2009.

[193] A. Olsson, G. Sandberg, and O. Dahlblom, “On Latin hypercube sampling for structural reliability analysis,” *Struct. Saf.*, vol. 25, no. 1, pp. 47–68, 2003.

[194] H. C. Noh, “A formulation for stochastic finite element analysis of plate structures with uncertain Poisson’s ratio,” *Comput. Methods Appl. Mech. Eng.*, vol. 193, no. 45–47, pp. 4857–4873, 2004.

[195] N. Chen, D. Yu, B. Xia, and M. Beer, “Uncertainty analysis of a structural–acoustic problem using imprecise probabilities based on p-box representations,” *Mech. Syst. Signal Process.*, vol. 80, pp. 45–57, Dec. 2016.

[196] G. Muscolino, A. Sofi, and F. Giunta, “Dynamics of structures with uncertain-but-bounded parameters via pseudo-static sensitivity analysis,” *Mech. Syst. Signal Process.*, vol. 111, pp. 1–22, Oct. 2018.

[197] J. B. Chen and J. Li, “The extreme value distribution and dynamic reliability analysis of nonlinear structures with uncertain parameters,” *Struct. Saf.*, vol. 29, no. 2, pp. 77–93, 2007.

[198] C. Jiang, X. P. Huang, X. Han, and D. Q. Zhang, “A Time-Variant Reliability Analysis Method Based on Stochastic Process Discretization,” *J. Mech. Des.*, vol. 136, no. 9, p. 091009, 2014.

[199] Y. Shi, Z. Lu, K. Zhang, and Y. Wei, “Reliability Analysis for Structures With Multiple Temporal and Spatial Parameters Based on the Effective First-Crossing Point,” *J. Mech. Des.*, vol. 139, no. 12, p. 121403, 2017.

[200] X. Du, “Time-Dependent Mechanism Reliability Analysis With Envelope

Functions and First-Order Approximation," *J. Mech. Des.*, vol. 136, no. 8, p. 081010, Jun. 2014.

[201] P. D. Spanos and I. A. Kougioumtzoglou, "Survival Probability Determination of Nonlinear Oscillators Subject to Evolutionary Stochastic Excitation," *J. Appl. Mech.*, vol. 81, no. 5, p. 051016, Jan. 2014.

[202] I. A. Kougioumtzoglou and P. D. Spanos, "Nonlinear MDOF system stochastic response determination via a dimension reduction approach," *Comput. Struct.*, vol. 126, pp. 135–148, Sep. 2013.

[203] I. A. Kougioumtzoglou and P. D. Spanos, "Response and First-Passage Statistics of Nonlinear Oscillators via a Numerical Path Integral Approach," *J. Eng. Mech.*, vol. 139, no. 9, pp. 1207–1217, Sep. 2013.

[204] Z. Wang and W. Chen, "Time-variant reliability assessment through equivalent stochastic process transformation," *Reliab. Eng. Syst. Saf.*, vol. 152, pp. 166–175, 2016.

[205] B. Goller, H. J. Pradlwarter, and G. I. Schuëller, "Reliability assessment in structural dynamics," *J. Sound Vib.*, vol. 332, no. 10, pp. 2488–2499, 2013.

[206] I. P. Mitseas, I. A. Kougioumtzoglou, P. D. Spanos, and M. Beer, "Nonlinear MDOF system Survival Probability Determination Subject to Evolutionary Stochastic Excitation," *Strojniški Vestn. - J. Mech. Eng.*, vol. 62, no. 7–8, pp. 440–451, Jul. 2016.

[207] J. Li, J. Chen, W. Sun, and Y. Peng, "Advances of the probability density evolution method for nonlinear stochastic systems," *Probabilistic Eng. Mech.*, vol. 28, pp. 132–142, 2012.

[208] J. Xu and F. Kong, “An adaptive cubature formula for efficient reliability assessment of nonlinear structural dynamic systems,” *Mech. Syst. Signal Process.*, vol. 104, pp. 449–464, 2018.

[209] C. Andrieu-Renaud, B. Sudret, and M. Lemaire, “The PHI2 method: A way to compute time-variant reliability,” *Reliab. Eng. Syst. Saf.*, vol. 84, no. 1, pp. 75–86, 2004.

[210] G. I. Schuëller, H. J. Pradlwarter, and P. S. Koutsourelakis, “A critical appraisal of reliability estimation procedures for high dimensions,” *Probabilistic Eng. Mech.*, vol. 19, no. 4, pp. 463–474, Oct. 2004.

[211] W. Gao and N. J. Kessissoglou, “Dynamic response analysis of stochastic truss structures under non-stationary random excitation using the random factor method,” *Comput. Methods Appl. Mech. Eng.*, vol. 196, no. 25–28, pp. 2765–2773, 2007.

[212] J. Ma, W. Gao, P. Wriggers, J. Chen, and S. Sahraee, “Structural dynamic optimal design based on dynamic reliability,” *Eng. Struct.*, vol. 33, no. 2, pp. 468–476, Feb. 2011.

[213] R. E. (Robert E. . Melchers, *Structural reliability analysis and prediction*. John Wiley, 1999.

[214] J. Ma, W. Gao, P. Wriggers, T. Wu, and S. Sahraee, “The analyses of dynamic response and reliability of fuzzy-random truss under stationary stochastic excitation,” *Comput. Mech.*, vol. 45, no. 5, pp. 443–455, Apr. 2010.

[215] J. Ma, P. Wriggers, W. Gao, J. J. Chen, and S. Sahraee, “Reliability-based optimization of trusses with random parameters under dynamic loads,” *Comput. Mech.*, vol. 47, no. 6, pp. 627–640, Jun. 2011.

[216] B. Wu, D. Wu, W. Gao, and C. Song, “Time-variant random interval natural frequency analysis of structures,” *J. Sound Vib.*, vol. 414, pp. 284–298, 2018.

[217] V. N. Vapnik, *The Nature of Statistical Learning Theory*. New York, NY: Springer New York, 2000.

[218] H. Drucker, C. J. C. Burges, L. Kaufman, A. Smola, and V. Vapnik, “Support vector regression machines,” in *Proceedings of the 9th International Conference on Neural Information Processing Systems*, 1996, pp. 155–161.

[219] Chih-Wei Hsu and Chih-Jen Lin, “A comparison of methods for multiclass support vector machines,” *IEEE Trans. Neural Networks*, vol. 13, no. 2, pp. 415–425, Mar. 2002.

[220] A. J. Smola and B. Schölkopf, “A tutorial on support vector regression,” *Stat. Comput.*, vol. 14, no. 3, pp. 199–222, Aug. 2004.

[221] S. Y. Kung, *Kernel Methods and Machine Learning*. Cambridge: Cambridge University Press, 2014.

[222] N. Cristianini and J. Shawe-Taylor, *An Introduction to Support Vector Machines and Other Kernel-based Learning Methods*. Cambridge University Press, 2000.

[223] L. Wang, J. Zhu, and H. Zou, “The doubly regularized support vector machine,” *Stat. Sin.*, vol. 16, no. 2, pp. 589–615, 2006.

[224] H. Zou and T. Hastie, “Regularization and variable selection via the elastic net,” *J. R. Stat. Soc. Ser. B (Statistical Methodol.*, vol. 67, no. 2, pp. 301–320, Apr. 2005.

[225] C. Campbell and Y. Ying, “Learning with Support Vector Machines,” *Synth. Lect. Artif. Intell. Mach. Learn.*, vol. 5, no. 1, pp. 1–95, Feb. 2011.

[226] L. Wang, J. Zhu, and H. Zou, “Hybrid huberized support vector machines for

microarray classification and gene selection," *Bioinformatics*, vol. 24, no. 3, pp. 412–419, Feb. 2008.

[227] M. Dunbar, J. M. Murray, L. A. Cysique, B. J. Brew, and V. Jeyakumar, "Simultaneous classification and feature selection via convex quadratic programming with application to HIV-associated neurocognitive disorder assessment," *Eur. J. Oper. Res.*, vol. 206, no. 2, pp. 470–478, Oct. 2010.

[228] G. M. Fung and O. L. Mangasarian, "A Feature Selection Newton Method for Support Vector Machine Classification," *Comput. Optim. Appl.*, vol. 28, no. 2, pp. 185–202, Jul. 2004.

[229] V. Jeyakumar, G. Li, and S. Suthaharan, "Support vector machine classifiers with uncertain knowledge sets via robust optimization," *Optimization*, vol. 63, no. 7, pp. 1099–1116, Jul. 2014.

[230] F. Portera and A. Sperduti, "Support Vector Regression with a Generalized Quadratic Loss," in *Biological and Artificial Intelligence Environments*, Dordrecht: Springer Netherlands, 2005, pp. 209–216.

[231] O. L. Mangasarian and D. R. Musicant, "Lagrangian Support Vector Machines," *J. Mach. Learn. Res.*, vol. 1, no. Mar, pp. 161–177, 2001.

[232] B. Scholkopf *et al.*, "Input space versus feature space in kernel-based methods," *IEEE Trans. Neural Networks*, vol. 10, no. 5, pp. 1000–1017, 1999.

[233] H. Xiong, M. N. S. Swamy, and M. O. Ahmad, "Optimizing the Kernel in the Empirical Feature Space," *IEEE Trans. Neural Networks*, vol. 16, no. 2, pp. 460–474, Mar. 2005.

[234] J. Gao, P. W. Kwan, and D. Shi, "Sparse kernel learning with LASSO and Bayesian

inference algorithm," *Neural Networks*, vol. 23, no. 2, pp. 257–264, Mar. 2010.

[235] Y. Feng, S.-G. Lv, H. Hang, and J. A. K. Suykens, "Kernelized Elastic Net Regularization: Generalization Bounds, and Sparse Recovery," *Neural Comput.*, vol. 28, no. 3, pp. 525–562, Mar. 2016.

[236] Q. Fan, Z. Wang, H. Zha, and D. Gao, "MREKLM: A fast multiple empirical kernel learning machine," *Pattern Recognit.*, vol. 61, pp. 197–209, Jan. 2017.

[237] H. Su, X. Li, B. Yang, and Z. Wen, "Wavelet support vector machine-based prediction model of dam deformation," *Mech. Syst. Signal Process.*, vol. 110, pp. 412–427, Sep. 2018.

[238] H. Dai and Z. Cao, "A Wavelet Support Vector Machine-Based Neural Network Metamodel for Structural Reliability Assessment," *Comput. Civ. Infrastruct. Eng.*, vol. 32, no. 4, pp. 344–357, Apr. 2017.

[239] Q. Wu, "Hybrid wavelet ν-support vector machine and chaotic particle swarm optimization for regression estimation," *Expert Syst. Appl.*, vol. 38, no. 12, pp. 14624–14632, Nov. 2011.

[240] Ning Ye, Ruixiang Sun, Yingan Liu, and Lin Cao, "Support vector machine with orthogonal Chebyshev kernel," in *18th International Conference on Pattern Recognition (ICPR'06)*, 2006, pp. 752–755.

[241] J. Zhao, G. Yan, B. Feng, W. Mao, and J. Bai, "An adaptive support vector regression based on a new sequence of unified orthogonal polynomials," *Pattern Recognit.*, vol. 46, no. 3, pp. 899–913, Mar. 2013.

[242] S. Ozer, C. H. Chen, and H. A. Cirpan, "A set of new Chebyshev kernel functions for support vector machine pattern classification," *Pattern Recognit.*, vol. 44, no.

7, pp. 1435–1447, Jul. 2011.

[243] V. Hooshmand Moghaddam and J. Hamidzadeh, “New Hermite orthogonal polynomial kernel and combined kernels in Support Vector Machine classifier,” *Pattern Recognit.*, vol. 60, pp. 921–935, Dec. 2016.

[244] V. N. Vapnik, *Statistical learning theory*. Wiley, 1998.

[245] Z.-B. Pan, H. Chen, and X.-H. You, “Support vector machine with orthogonal Legendre kernel,” in *2012 International Conference on Wavelet Analysis and Pattern Recognition*, 2012, pp. 125–130.

[246] M. Tian and W. Wang, “Some sets of orthogonal polynomial kernel functions,” *Appl. Soft Comput.*, vol. 61, pp. 742–756, Dec. 2017.

[247] C. Wu, X. Ma, and T. Fang, “A complementary note on Gegenbauer polynomial approximation for random response problem of stochastic structure,” *Probabilistic Eng. Mech.*, vol. 21, no. 4, pp. 410–419, Oct. 2006.

[248] D. Kim, T. Kim, and S.-H. Rim, “Some identities involving Gegenbauer polynomials,” *Adv. Differ. Equations*, vol. 2012, no. 1, p. 219, 2012.

[249] L. C. Padierna, M. Carpio, A. Rojas-Domínguez, H. Puga, and H. Fraire, “A novel formulation of orthogonal polynomial kernel functions for SVM classifiers: The Gegenbauer family,” *Pattern Recognit.*, vol. 84, pp. 211–225, Dec. 2018.

[250] K. Cheng, Z. Lu, Y. Wei, Y. Shi, and Y. Zhou, “Mixed kernel function support vector regression for global sensitivity analysis,” *Mech. Syst. Signal Process.*, vol. 96, pp. 201–214, 2017.

[251] B. Schölkopf and A. J. Smola, *Learning with kernels : support vector machines, regularization, optimization, and beyond*. MIT Press, 2002.

[252] M. Gönen and E. Alpaydın, “Multiple Kernel Learning Algorithms,” *J. Mach. Learn. Res.*, vol. 12, no. Jul, pp. 2211–2268, 2011.

[253] N. Deng, Y. Tian, and C. Zhang, *Support vector machines : optimization based theory, algorithms, and extensions*. CRC Press, Taylor & Francis Group, 2013.

[254] J. Bergstra and Y. Bengio, “Random Search for Hyper-Parameter Optimization,” *J. Mach. Learn. Res.*, vol. 13, no. Feb, pp. 281–305, 2012.

[255] L. B. Jack and A. K. Nandi, “FAULT DETECTION USING SUPPORT VECTOR MACHINES AND ARTIFICIAL NEURAL NETWORKS, AUGMENTED BY GENETIC ALGORITHMS,” *Mech. Syst. Signal Process.*, vol. 16, no. 2–3, pp. 373–390, Mar. 2002.

[256] A. R. Yildiz, “A comparative study of population-based optimization algorithms for turning operations,” *Inf. Sci. (Ny).*, vol. 210, pp. 81–88, Nov. 2012.

[257] J. Snoek *et al.*, “Scalable bayesian optimization using deep neural networks,” in *International Conference on Machine Learning*, 2015, pp. 2171–2180.

[258] J. Snoek, H. Larochelle, and R. P. Adams, “Practical Bayesian Optimization of Machine Learning Algorithms,” in *Advances in Neural Information Processing Systems 25*, F. Pereira, C. J. C. Burges, L. Bottou, and K. Q. Weinberger, Eds. Curran Associates, Inc., 2012, pp. 2951–2959.

[259] MathWorks, “Statistical and machine learning toolbox: user’s guide (2017b).” MathWorks, 2017.

[260] Q. Pan and D. Dias, “An efficient reliability method combining adaptive Support Vector Machine and Monte Carlo Simulation,” *Struct. Saf.*, vol. 67, pp. 85–95, Jul. 2017.

[261] M. Moustapha, J.-M. Bourinet, B. Guillaume, and B. Sudret, “Comparative Study of Kriging and Support Vector Regression for Structural Engineering Applications,” *ASCE-ASME J. Risk Uncertain. Eng. Syst. Part A Civ. Eng.*, vol. 4, no. 2, p. 04018005, Jun. 2018.

[262] I. . Sobol’, “On the distribution of points in a cube and the approximate evaluation of integrals,” *USSR Comput. Math. Math. Phys.*, vol. 7, no. 4, pp. 86–112, Jan. 1967.

[263] P. Kersaudy, B. Sudret, N. Varsier, O. Picon, and J. Wiart, “A new surrogate modeling technique combining Kriging and polynomial chaos expansions - Application to uncertainty analysis in computational dosimetry,” *J. Comput. Phys.*, vol. 286, pp. 103–117, 2015.

[264] T. Chatterjee and R. Chowdhury, “An efficient sparse Bayesian learning framework for stochastic response analysis,” *Struct. Saf.*, vol. 68, pp. 1–14, 2017.

[265] B. Xia, Y. Qin, D. Yu, and C. Jiang, “Dynamic response analysis of structure under time-variant interval process model,” *J. Sound Vib.*, vol. 381, pp. 121–138, 2016.

[266] C. Birk, L. Liu, and C. Song, “Coupled acoustic response of two-dimensional bounded and unbounded domains using doubly-asymptotic open boundaries,” *J. Comput. Phys.*, vol. 310, pp. 252–284, Apr. 2016.